A STRONGLY COUPLED SIMULATION MODEL OF POSITIVE DISPLACEMENT MACHINES FOR DESIGN AND OPTIMIZATION

A Dissertation

Submitted to the Faculty

of

Purdue University

by

Thomas Ransegnola

In Partial Fulfillment of the

Requirements for the Degree

of

Doctor of Philosophy

December 2020

Purdue University

West Lafayette, Indiana

THE PURDUE UNIVERSITY GRADUATE SCHOOL
STATEMENT OF DISSERTATION APPROVAL

Dr. Andrea Vacca, Chair

School of Agr. & Biological Engineering, School of Mechanical Engineering

Dr. Farshid Sadeghi

School of Mechanical Engineering

Dr. Samuel Midkiff

School of Electrical and Computer Engineering

Dr. Carlo Scalo

School of Mechanical Engineering

Approved by:

Dr. Jay P. Gore

Head of the School Graduate Program

To my great-grandfather who always wanted a ‘Dr. Ransegnola,’
and to my family and friends who helped make it happen.

All models are wrong, but some are useful.

– George E.P. Box

ACKNOWLEDGMENTS

To start, none of this would be possible if not for my advisor, Professor Andrea Vacca. Andrea has been and will continue to be a role model of mine, not only as an exemplary researcher but also as a person. I owe him a debt a gratitude for all the knowledge and passion he has shared, and especially for teaching me skills I did not even know I would need. I would also like to thank the late Professor Monika Ivantsynova, who taught me the importance of being confident in your opinions but prepared to defend them. Her legacy will continue to thrive in the fluid power community, thanks to the Maha Research Center she created. Finally, I would like to thank Professors Sadeghi, Midkiff, and Scalo, who's classes and advice have helped prepare me for the engineering problems I have faced and will face in the future.

This acknowledgement would not be complete without mentioning the team at Maha that supported me throughout all the long days and late nights: Harish, Annalisa, Shanmukh, Lizhi, Xinran, Andrew, Rene, Yash, Srinath and countless others. I want to give special thanks to Sangbeom, Rituraj, Federico, Divya, Matteo, and Swarnava who where always there for a discussion on the whiteboard and Teams or a mid-day distraction. While we did work together these people are not my coworkers, they're my friends.

Outside of work, I knew I could count on my friends to keep me grounded. Regardless if they were close like Tim, Garrett, Coleton, and Caleb, or hundreds of miles away like Bill, Greg, Scott, Ethan, Del, Adam, Jonathan, Peter, Geoff, Cara, Chloe, and Joe.

Last but certainly not least, my family was my support structure. I would not have made it this far if not for the unwavering support of my parents. Through good times and bad, they have always helped me to see the light at the end of the tunnel. And to Jason and Monica, who were right there with them cheering me on.

TABLE OF CONTENTS

Page

LIST OF TABLES

LIST OF FIGURES

Figure Page

Figure Page

Figure Page

Figure Page

Figure Page

SYMBOLS

ψ	Scalar Quantity
$\widetilde{\psi}$	Dimensionless Quantity
$\overline{\psi}$	Average Quantity
$\hat{\psi}$	Unit Vector
$\underline{\psi}$, ψ_i	(Column) Vector Quantity
$\underline{\underline{\psi}}$, ψ_{ij}	Matrix Quantity
$\underline{\psi}^\intercal$, $\underline{\underline{\psi}}^\intercal$	Vector/Matrix Transpose
$\lvert\underline{\psi}\rvert$,$\lvert\underline{\underline{\psi}}\rvert$	2-Norm (Magnitude)
$\lvert\lvert\underline{\psi}\rvert\rvert_n$,$\lvert\lvert\underline{\underline{\psi}}\rvert\rvert_n$	n-Norm
$\mathrm{tr}\left(\underline{\underline{\psi}}\right)$	Trace
$\cdot$	Inner (dot) product
$\times$	Outer (cross) product
$\circ$	Hadamard (element-wise) product
N_ψ	Number/Count of a quantity ψ
ε	Tolerance/Error
ς	Damping Ratio
d	Damping Coefficient, $N\,s/m$
h	(Gap) height, m
b	Depth, m
L	Length, m
A	Area, m^2
V	Volume, m^3
Q	Volume flow, m^3/s
m	Mass, kg
$\dot{m}$	Mass flow, kg/s

v	velocity, m/s
p	Pressure, Pa
Δp	Pressure Difference, Pa
T	Temperature, K
ρ	Density, kg/m^3
μ	Dynamic Viscosity, $Pa\,s$
ν	Kinematic Viscosity, m^2/s
c	Speed of sound, m/s
K_T	Isothermal Bulk Modulus, Pa
α_i	Void (volume) fraction
f_i	Mass fraction
β	Bunsen's coefficient
n	Polytropic process index
k	Ratio of specific heats
σ	Stress, bar
σ_y	Yield Stress, bar
γ	Strain, $-$
$\dot{\gamma}$	Strain Rate, $1/s$
$\widetilde{\mathcal{H}}$	Dimensionless material hardness
λ	Auto-correlation length, m
Λ	Roughness directionality (Auto-correlation length ratio)
χ_u	Released gas percentage
χ_v	Released vapor percentage
$\underline{\underline{IM}}$	Fluid-Structure Influence Operator, m/Pa
$\underline{\underline{K}}$	Finite Element Stiffness Matrix, N/m^4
$\underline{\underline{C}}$	Finite Element Damping Matrix, Ns/m^4
$\underline{\underline{M}}$	Finite Element Mass Matrix, Ns^2/m^4
ϕ	Mixed Lubrication flow factor
R_q	Root mean square roughness, m

$\underline{\underline{I}}$	Inertial Tensor, $kg\,m^2$
$\underline{\underline{\mathcal{R}}}$	Rotation Matrix
Ψ	First (z) Euler Rotation Angle - Yaw, rad
Θ	Second (y') Euler Rotation Angle - Pitch, rad
Φ	Third (x'') Euler Rotation Angle - Roll, rad
E	Young's Modulus, bar
ζ	Poisson's ratio
E^*	Effective Young's Modulus $\frac{E}{(1-\zeta^2)}$, bar
$\mathcal{T}$	Time constant/Period, s
δ	(Rigid) Penetration depth, m
η	Efficiency
μ_d	Dynamic friction coefficient
e	Eccentricity, m
C	Clearance, m
ϵ	Eccentricity ratio e/C
$\mathfrak{W}$	Work, J
$\mathfrak{Q}$	Heat, J
$\mathfrak{U}$	Internal Energy, J
$\mathfrak{H}$	Enthalpy, J
$\mathfrak{u}$	Specific Internal Energy, J/kg
$\mathfrak{h}$	Specific Enthalpy, J/kg
Ω	Volume domain
$d\Omega$	Differential volume of domain Ω
Γ	Surface domain
$d\Gamma$	Differential surface of domain Γ
$\hat{i}, \hat{j}, \hat{k}$	Cartesian unit vectors in x,y,z
$\hat{r}, \hat{\varphi}, \hat{k}$	Cylindrical unit vectors in r,φ,z
SF	Karp-Flatt program serial fraction
S	Parallel program speedup

ABBREVIATIONS

EGM	External Gear Machine
EGP	External Gear Pump
APM	Axial Piston Machine
PD	Positive Displacement
EHA	Electro-Hydraulic Actuator
CFD	Computational Fluid Dynamics
VOF	Volume of Fluid
FEM	Finite Element Method
ODE	Ordinary Differential Equation
PDE	Partial Differential Equation
FSI	Fluid-Structure Interaction
IF	Inertial Frame
BF	Body-fixed Frame
FFI	Fluid-Forces-Interaxis mode
API	Application programming interface
LP	Lumped Parameter
DP	Distributed Parameter

ABSTRACT

Ransegnola, Thomas Ph.D., Purdue University, December 2020. A Strongly Coupled Simulation Model of Positive Displacement Machines for Design and Optimization. Major Professor: Andrea Vacca, School of Mechanical Engineering.

Positive displacement machines are used in a wide variety of applications, ranging from fluid power where they act as a transmission of power, to lubrication and fluid transport. As the core of the fluid system responsible for mechanical–hydraulic energy conversion, the efficiencies of these units are a major driver of the total efficiency of the system. Furthermore, the durability of these units is a strong decider in the useful life of the system in which they operate.

The key challenge in designing these units comes from understanding their working principles and designing their lubricating interfaces, which must simultaneously perform a load carrying and sealing function as the unit operates. While most of the physical phenomena relevant to these machines have been studied previously in some capacity, the significance of their mutual interactions has not. For this reason, the importance of these mutual interactions is a fundamental question in these machines that this thesis answers for the first time. In analysis of two different machine types, it is confirmed that mutual interactions of both physical phenomena and neighboring fluid domains of the unit contribute significantly to the overall performance of the machine. Namely, these analyses demonstrate load sharing owing to mutual interactions on average of 20% and as high as 50%, and mutual flow interactions of at least 10%.

In this thesis, the behavior of the thin films of fluid in the lubricating interfaces of the units, the bodies that make up these films, and the volumes which interface with them will be considered. The resulting coupled problem requires a model that can consider the effects of motion of all floating bodies on all films and volumes, and

collect the resulting loads applied by the fluid as it responds. This will require a novel 6 degree of freedom dynamics model including the inertia of the bodies and the transient pressure and shear loads of all interfaces of the body and the fluid domain.

During operation, fluid cavitation and aeration can occur in both the displacement chambers of the machine and its lubricating interfaces. To capture this, a novel cavitation algorithm is developed in this thesis, which considers the release of bubbles due to both gas trapped within the fluid and vaporization of the operating fluid in localized low pressure regions of the films. In the absence of cavitation, this model will also be used to find the pressures and flows over the film, communicating this information with the remainder of the fluid domain.

Due to the high pressures that form in these units, the bodies deform. The resulting deformation changes the shape of the films and therefore its pressure distribution. This coupled effect will be captured in one of two ways, the first relying on existing geometric information of the unit, and the other using a novel analytical approach that is developed to avoid this necessity. In either case, the added damping due to the shear of the materials will be considered for the first time. Additionally in regions of low gap height, mixed lubrication occurs and the effects of the surface asperities of the floating bodies cannot be neglected. Accurate modeling of this condition is necessary to predict wear that leads to failure in these units. This work will then develop a novel implementation for mixed lubrication modeling that is directly integrated into the cavitation modeling approach.

Finally, effort is made to maintain a generic tools, such that the model can be applied to any positive displacement machine. This thesis will present the first toolbox of its kind, which accounts for all the mentioned aspects in such a way that they can be captured for any machine. Using both multithreaded and sequential implementations, the tool will be capable of fully utilizing a machine on which it is run for both low latency (design) and high throughput (optimization) applications respectively. In order to make these applications feasible, the various modules of the tool will be strongly coupled using asynchronous time stepping. This approach is made possible

with the development of a novel impedance tensor of the mixed universal Reynolds equation, and shows marked improvements in simulation time by requiring at most 50% of the simulation time of existing approaches.

In the present thesis, the developed tool will be validated using experimental data collected from 3 fundamentally different machines. Individual advancements of the tool will also be verified in isolation with comparison to the state of the art and commercial software in the relevant fields. As a demonstration of the use of the tool for design, detailed analysis of the displacing actions and lubricating interfaces of these same units will be performed. These validations demonstrate the ability of the tool to predict machine efficiencies with error averaging around 1% over all operating conditions for multiple machine types, and capture transient behavior of the units. To demonstrate the utility as a virtual optimization tool, design of a complete external gear machine design will be performed. This demonstration will start from only analytical parameters, and will track a route to a complete prototype.

1. INTRODUCTION

Hydraulic pumps are typically positive displacement (PD) machines that are the key elements for a wide range of engineering applications. In fluid power (FP) systems, these units are used for the transmission of mechanical energy through the use of pressurized fluid, and are commonly used in aerospace (e.g. flight control, landing gears), off-highway (e.g. agricultural, construction equipment), industrial equipment, and automotive braking and transmission applications. They are also used in automotive and aerospace applications for fuel injection and lubrication, and for injection molding and fluid transport in the chemical and food industries. In some application, such as FP, they are used because their power density surpasses that of other solutions. For others, they are the only possibility.

1.1 Working Principle

In order to model these machines, it is important to understand their operating principles, especially when attempting to generalize their behavior. Considering this, the simplest form of positive displacement is first examined in Figure 1.1.

Unlike hydrodynamic pumps, which transmit energy via fluid inertia, hydrostatic pumps transmit energy via pressurized flow. Regardless of the machine type, its general function (for machines with finite displacement chambers) is to realize a cyclic contraction and expansion of fluid volumes within the unit. By connecting these volumes to the delivery and suction ports during contraction and expansion respectively, positive displacement is achieve regardless of fluid resistance to the resulting flow. In practice, though, this form of machine is not feasible. In this thesis, two common types of PD machines will be taken as example, both achieving the same underlying functionality via different geometric means. First in Section 1.1.1, the

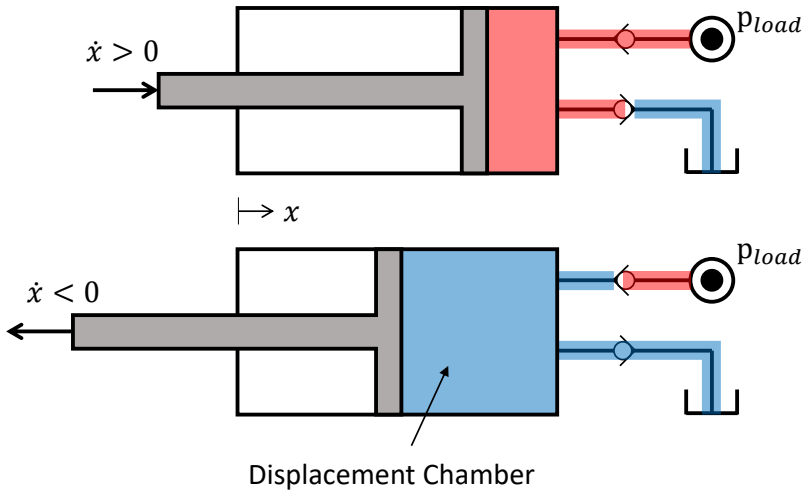

Figure 1.1. Simplified demonstration of positive displacement against a pressure load

axial piston machine will be introduced. Then in Section 1.1.2, the external gear machine is introduced.

As an inevitability of their working principle, PD machines have components in relative motion to one-another. In order to maintain efficient performance as pressure is increased, the clearances between these moving components is typically kept small (∼1-50 μm) to avoid excessive leakage flow. Embracing this, machine designers typically allow a controlled amount of flow through these gaps, using the operating pressure as well as the geometry of the film to build a reaction force which carries the loads on the floating bodies as they shift within these clearances (micro-motion). Even in the absence of relative motion, manufacturing constraints may require the separation of components, presenting a leakage path from high to low pressure. The implication of either is the introduction of thin films of fluid, the modeling of which is a key challenge for these units.

1.1.1 Axial Piston Machines

The axial piston machine (APM) extends the premise of Figure 1.1 by using a series of reciprocating pistons in parallel, phase offset with respect to each other so as to provide a more continuous flow. One of the most common types of APM is the swash-plate type unit shown in Figure 1.2. Input power is taken in the form of a drive shaft, rotating the cylinder block. This in turn carries the pistons over an inclined swash plate to realize a reciprocating motion with respect to the bore. During the suction and delivery strokes, the valve plate directs flow into and out of the fluid volumes (trapped within the bore and the piston) to the inlet and outlet respectively. A detailed analysis of the functioning of these units is available in [1].

Performance of these units is dominated by their three main lubricating interfaces. These interfaces are demonstrated in Figure 1.3, along with the terminology used throughout this work for the various components of the machine. First, the slipper-swashplate interface maintains a finite fluid film by lifting the slipper away from the swashplate aided by a hydrostatic pocket of fluid. In doing so, this interface forces the piston to follow the sinusoidal path caused by the inclined swashplate. Due to this inclination, though, a net force exists that is orthogonal to the axis of the machine which must be carried by the piston-cylinder interface. In turn, the piston-cylinder interface transmits this forces to the bore in which it sits. This force is offset from the central axis of the cylinder block, and leads to a net opposing torque that must be provided by the prime mover of the machine. Finally, the displacement chambers of the machine must be carefully connected to the outlet and inlet porting volume of the unit at the appropriate angular regions to realize the displacing flow. As a result, a third interface forms between the rotating cylinder block and the stationary valve plate used to direct this flow. Due to the planar tilting moment of the cylinder block, an inclination in this interface is possible, leading to a pressure distribution in this interface to prevent contact.

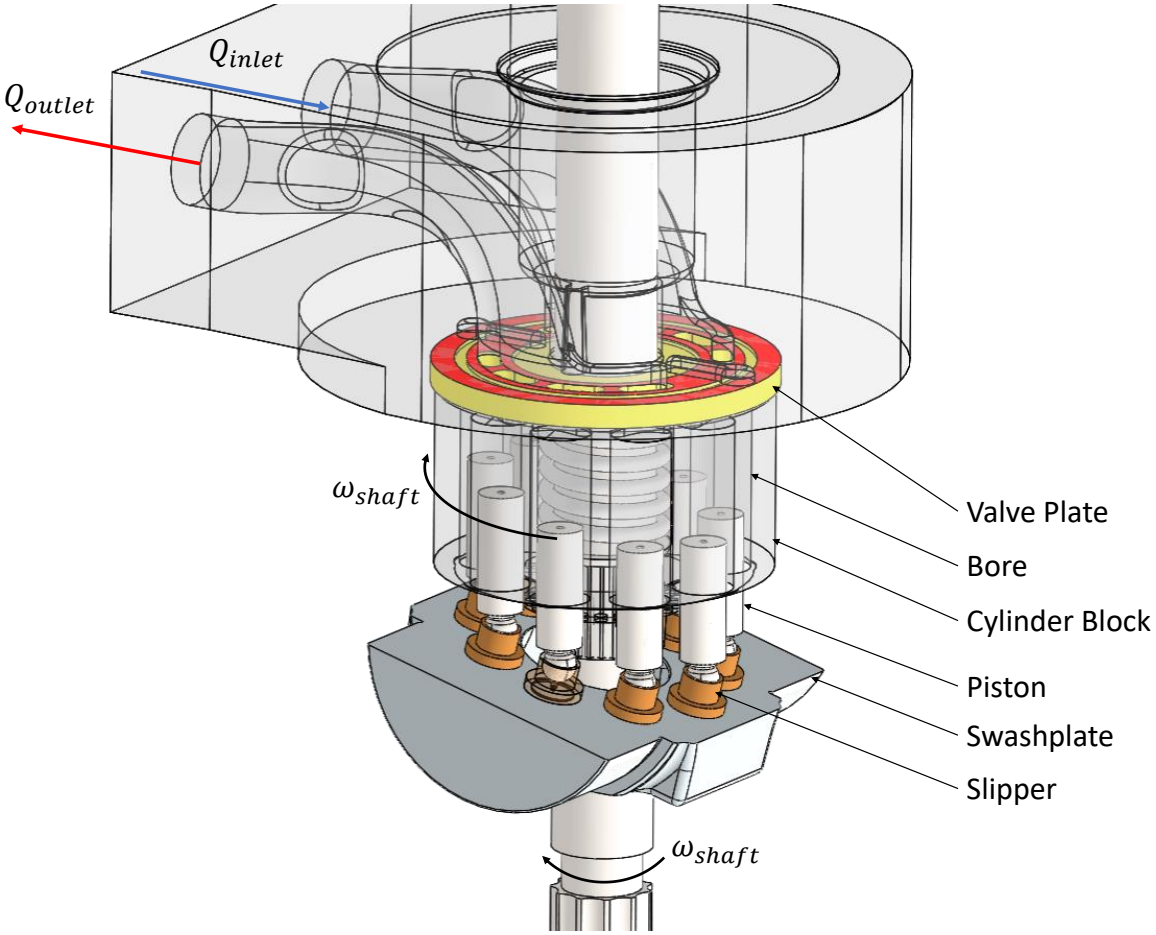

Figure 1.2. Components of a typical axial piston machine (Ref P1) during pumping

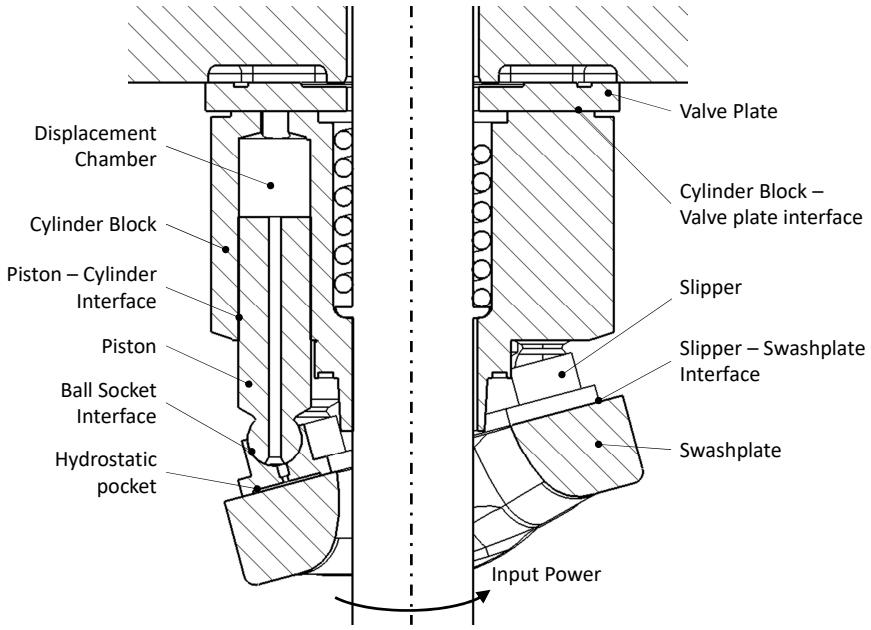

Figure 1.3. Components of an Axial Piston Machine of Swashplate Type

1.1.2 External Gear Machines

Unlike the axial piston machine, the displacing action of an external gear machine cannot be directly related to the simplified machine presented in Figure 1.1. All the same, though, the unit delivers fluid by realizing a reduction of volume on the delivery side, followed by an expansion of volume on the suction side. In the case of the external gear machine (EGM), this is accomplished by a pair of meshing gears. By connecting the region of meshing where the net volume decreases and increases to the delivery and suction sides respectively, positive displacement is achieved. In these units, the major challenges come from the design of the gears and associated relief grooves to direct the flow, as well as the bearing and lateral balancing lubricating interfaces. Similar to the APM, these interfaces isolate regions of high and low pressure and carry internal forces due to the pressure imbalance. Similar to the APM, a detailed analysis of the working of these units is available in [1].

An important design decision for these units is the choice of lateral sealing. For low pressure applications, which make up the majority of the EGM market, lateral compensation is not used. In these designs, the sealing between adjacent volumes of the machine is controlled by the clearances of the gear and pump body depth. Unlike the strategy demonstrated in Figure 1.1, the relief grooves are machined directly into the end cover and body of the unit, and no lateral compensation element is present (i.e. no lateral plate).

For high pressure applications, though, this clearance is not sufficient and a floating element must be used to maintain adequate sealing, typically coming in two forms. First in Figure 1.4 a lateral compensating plate is used. By connecting a controlled portion of the balance side of this plate to high and low pressure, a force proportional to operating pressure is applied to the plate. By offsetting the center of pressure on the balance side, a tilt of the plate can also be induced. In the lateral lubricating interface between the gears and this plate, a film pressure forms to respond to this

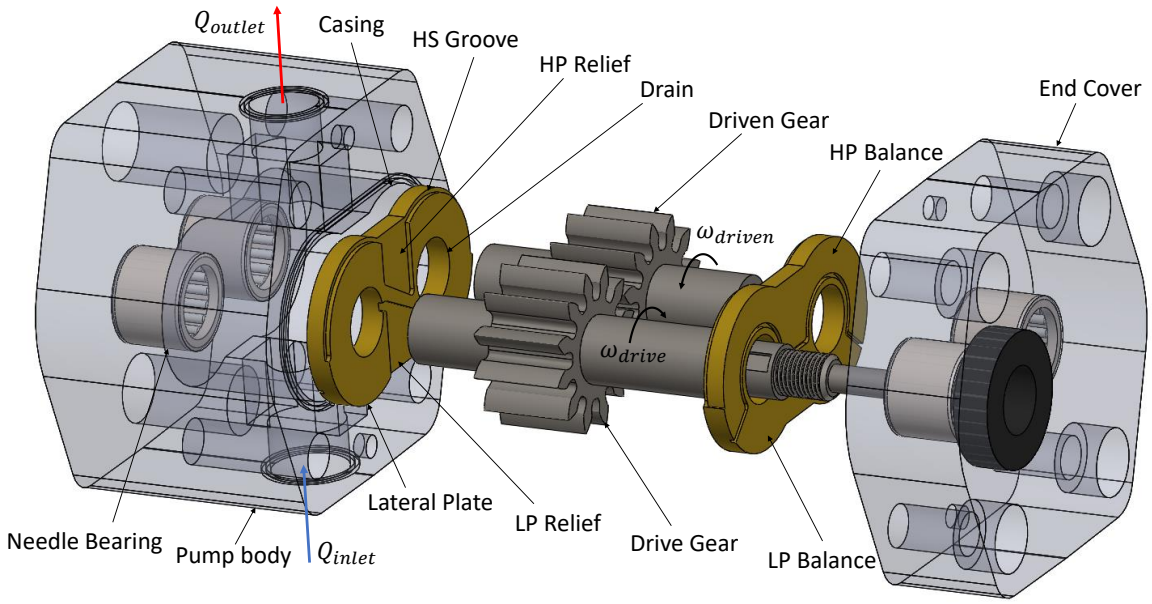

Figure 1.4. Exploded view of a typical pressure compensated external gear machine (Ref E3) during pumping

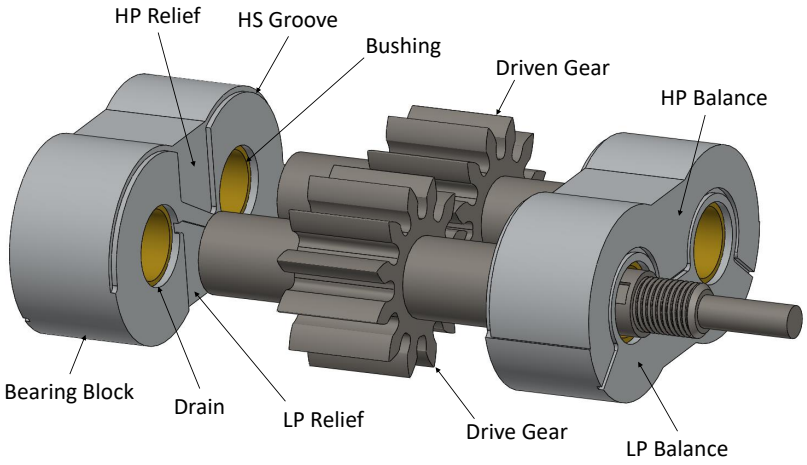

Figure 1.5. Alternate form of pressure compensation in external gear machines using bearing blocks

offset force, balancing the element in a quasi-steady equilibrium. To balance radial loads in these units, bearings are placed in the pump body and end-cover.

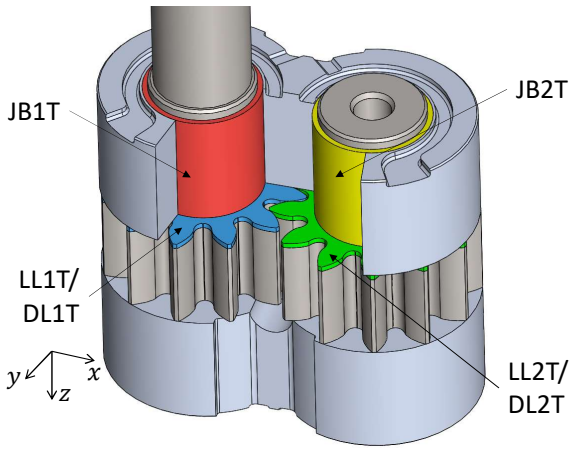

Figure 1.6. Lubricating interfaces of EGM

The alternative solution is to use a bearing block, demonstrated in Figure 1.5. These blocks performs the same lateral sealing functions as the lateral plates, but with a significantly larger depth so that the bearings can be housed in the same component. The benefit of this approach is that it decouples the radial location of the gears from the pump body, insofar as the bearing block clearance will allow.

In either balance configuration, the type of bearing used is another important design choice. Demonstrated in Figure 1.5, journal bearings are most common, providing 'infinite' life when well designed and capable of carrying large radial loads. However for challenging demands on the units, such as low speed applications, designers may elect for rolling contact bearings such as the needle bearings shown in Figure 1.4.

Figure 1.6 displays the main lubricating interfaces of a pressure compensated EGM. These interfaces perform a load carrying function in the unit, and for this reason they represent a large source of mechanical loss. Specifically, the lateral lubricating interface must cary axial loading of the floating element (regardless of the balance strategy employed) in order to main adequate sealing. Due to the differing pressure distribution over the gears, a net radial force is applied. This force must be carried by the radial bearings. From this figure, it is clear that the micro-motions of the bodies

creates an interaction between the lateral interface and the journal bearing interface, which cannot be captured by solving the two interfaces in isolation.

1.1.3 Reference Machines

In the present thesis, a total of 5 reference units are taken. These units, named in Table 1.1, correspond to 3 different working principles. Within the category of EGM, two different compensation strategies to maintain adequate sealing are explored, with varying applications.

Table 1.1.
Reference units selected for modelling in this work, with names used to reference them throughout the thesis

Name	**Type**	**Applications**	**Lubricating Gap Features**
Ref E1	EGP	Medium-high pressure pump	Lateral compensation with bearing blocks, Journal Bearings
Ref E2	EGM	Medium-high pressure pump/motor	Lateral compensation with bearing blocks, Journal Bearings
Ref E3	EGM	Electro-Hydraulic Actuator pump/motor	Lateral compensation with lateral plates, Needle Bearings
Ref G1	Gerotor	Automotive pump	No lateral compensation, Journal Bearings
Ref P1	Swashplate type APM	High pressure mobile hydraulic pump/motor	Standard Piston-Cylinder, Hydrostatic Slipper-Swashplate, Hydrostatic Block-Valveplate

1.2 Motivations

As the main source of mechanical–hydraulic energy conversion of fluid systems, PD machines play an important role in a wide variety of engineering applications. A 2012 study [2] found that while a properly designed hydraulic unit performs at greater than 90% efficiency, poorly designed units can have efficiencies less than 50%. Furthermore, the inevitability of floating components in relative motion separated by only thin films of fluid presents difficulty in designing robust units. A fundamental challenge for improving both the efficiency and robustness of most PD machines comes from the designing of these lubricating interfaces. Because of the complexity in modeling the interfaces, they are commonly modeled using approximations or empirical relations to support an iterative prototype-test-adjust design procedure. The implication of this is manufacturers requiring lead-times on the order of years to generate functioning designs. A motivation of this work, then, is the need to provide rapid high-fidelity performance feedback to designers of these machines, so that they can achieve better functioning units (with respect to efficiency and robustness) within more reasonable prototyping timelines.

As the market for PD machines evolves, manufacturers must adjust to unforeseen system requirements by exploring novel designs. This means that the insight gained by prototype-test-adjust procedures of existing designs cannot be directly applied, and manufacturers require modeling tools to investigate these novelties. The nature of the current modeling approaches for PD machines, especially as pertains to their lubricating interfaces, are rigid in their applicability to novel geometries. The inability to explore novel designs that this introduces is a key inhibitor in the advancement of PD machines. For this reason, another motivation of this work is the need for more freedom for designers to apply high fidelity, validated models to novel machine designs.

Even with a model in hand, its usefulness is strongly limited by the scope of its use. More specifically, many of the existing high fidelity tools available to design-

ers require long simulation times and heavy pre- and post-processing steps. These constraints restrict, if not preclude, their use in virtual prototyping applications. The final motivation for this work, then, is the high simulation times and heavy the human-in-the-loop interactions of existing PD models. If these points are addressed, simulation-based design can feasibly be integrated into the optimization and prototyping workflows of PD manufacturers.

1.3 State of the Art

While the operating principle of PD machines is straightforward, it is clear from the state of the art that their modeling is not trivial. A detailed review of the state of the art in gear-type PD machines was performed by Rundo [3], but can be roughly split into the three basic approaches introduced here.

First, ongoing effort has focused on studying the kinematic behavior of these machines. In [4] Manring and Kasaragadda derived an analytical equation for the kinematic flow ripple of symmetric spur external gear pump (EGP). In [5] Zhao and Vacca performed a similar analysis, including both symmetric and asymmetric spur gears, which was extended in [6] to include the effect of helix angle. Other works have derived similar techniques to investigate novel non-involute gear profiles [7, 8]. It is also possible to broaden the applicability of these kinematic models, as is done by Manring [4], by modify the perfect porting assumption so as to better predict the nominal flow behavior of the machine. In [1], Ivantysyn and Ivantysynova perform kinematic analyses on many types of PD machines available including both gear type and piston type machines. A detailed understanding of the kinematics of a unit can allow for informed modification of their nature. For example in works such as Edge [9], the kinematics of an APM were modified with a cam and piston-follower in such a way as to reduce the pressure ripple of the unit. While these studies are helping in understanding the working principle of a unit, they restrict study to a perfect fluid, and cannot capture the effects of operation with compressible and viscous fluids.

Furthermore, they neglect the effects of leakages through the clearances of the unit and any micro-motion of the bodies within the unit.

With recent advances in the computational power of desktop computers, direct application of the Navier-Stokes equations over the entire fluid domain of the machine using computational fluid dynamics (CFD) approaches has become possible. Many works have used this approach to capture the local pressurization and flow behavior, with most of the recent CFD analyses of PD machines using the simulation tool Simerics MP+ (formerly PumpLinx) discussed in detail by Ding et al. [10]. Of these works, Frosina et al. [11] and Heisler et al. [12] used CFD approaches to study the flow and pressure behaviors of high pressure spur and helical EGPs respectively. Similar approaches have been applied to gerotors [13] and APMs [14], showing the ability of these tools to capture flow in complex geometries and harsh operating conditions. In Zhao et al. [15] Simerics MP+ was used to compare the results of a CFD and lumped parameter modeling approach for a continuous contact helical EGP, providing a useful validation approach for assessing model simplification. In general, these tools are powerful for gaining detailed insight into the operation of a unit, with works such as [16] using CFD to offer design improvements. CFD approaches also allow for the exploration of novel designs, such as the macroscopic surface structures studied by Kumar et al. [17]. Finally, they can be used to precisely study important details of the machine behavior such as the turbulent flow through constrictions (such as tooth tip geometry) in Castilla et al [18], non-standard tooth geometry in Riemslagh et al. [19], and the variation of multi-phase performance with operating condition in Mithun et al. [20].

With these tools, though, this insight comes at large computational expense. In order to mitigate this cost, simplifications are often employed including fixing degrees of freedom of the floating bodies. The accuracy of these tools, then, rely on estimation of the position of the gears and balancing elements. Additionally, these tools are subject to numerical restrictions on the discretization, such as the necessity for a

continuous fluid domain. Often, they also cannot support a fine enough mesh to capture multi-physical effects such as fluid-structure interaction of the bodies.

In response to this, the third approach begins by forming control volumes within the machine. In this lumped parameter approach, interconnected discrete control volumes, with constant properties throughout, are selected so as to capture pressure variation within the unit without the computational expense of CFD analysis. Foster [21] demonstrated that the analytical lumped parameter assumption retained agreement with experiment. Similar works by Eaton et al. [22] and Manco' and Nervegna [23] further justify the applicability if this assumption. Similar tools have been developed for APMs, such as Corvaglia and Rundo [24] and show similar agreement with CFD simulation of the same unit. These tools allow for great opportunities for optimization and design of these machines, such as porting optimization [25, 26] and pressure ripple reduction [27,28]. Works such as Casoli et al. [29] show how these tools can be extended to model complex flow-physics such as the multi-phase conditions that can exist in these units. Still, though, these approaches cannot resolved the detailed behavior of the lubricating interfaces, which are typically approximated analytically [30,31]. In forming these models, though, similar assumptions to that of CFD approaches are taken including fixing degrees of freedom of the bodies and using only approximate models of the lubricating interfaces. As a result, they typically require tuning of model parameters from CFD.

With the computational expense spared by this lumped assumption, these tools are capable of accounting for micro-motion of the unit. Works by Borghi et al. [32] and Battarra and Mucchi [33] improve model agreement between the lumped parameter assumption and experiment for both spur and helical EGMs when this micro-motion is considered. Similar tools [34, 35] show the necessity of capturing micro-motion in APMs. Though approximation, these models can attain highly detailed dynamic simulations of the micro-motions of the bodies subject to their film simplifications.

This thesis draws on the simulation model HYGESim, previously developed by Vacca and Guidetti [36]. The work is based on a lumped parameter assumption,

which allows for rapid study of the instantaneous pressurization and main flow characteristics of an EGM. By balancing the computational load, the model is capable of considering these pressures to find the resulting micro-motion of the gears as they shift within the bearings. This shifting, found using Booker's mobility method [37] for journal bearings, is then used to capture the resulting change in flow and pressurization behavior. This model was initially developed for spur gears, but was adapted to capture the helix angle of a helical EGP in [38]. This thesis will be supported both by the parametric gear generator module of HYGESim [5], as well as the numerical geometric module for discretizing the gear pump control volumes [15]. In [39], Zhao and Vacca extended the lumped parameter and geometric modules to apply to continuous contact helical gears, with validation against detailed CFD simulations of the unit. The HYGESim tool was extended to account for the manufacturering errors present in EGMs in Rituraj et al. [40, 41]. The same authors accounted also for the thermal modelling of these units in [42].

While these models provide unique insight into the shifting of the gears of the unit, the use of lumped parameter models alone cannot capture the fine details of the behavior of these machines. Moreover, each of the works mentioned above derive a model for a single machine, with assumptions and flow simplifications specific to that unit. As a standalone tool, then, the scope of their use is limited. The accuracy of the lumped parameter model can be extended, though, by coupling its solution to more detailed distributed parameter models. These tools rely on lumped parameter models for the lumped volumes, and use their results as a boundary condition for more detailed study of the lubricating interfaces of the machine modeling using Reynolds equation. For external gear machines, such a model was developed by Dhar and Vacca [43], based on the output of [36] as a boundary condition to model the fluid-structure interaction within the lateral lubricating interfaces of an EGM. In [44], Dhar and Vacca extended this tool to further consider the change in temperature of the interface and its associated thermal deformations. In [45], Thiagarajan and Vacca showed that, through the use of this simulation model and the similar

distributed parameter tool developed by Pellegri and Vacca [46] for modeling of the journal bearings of EGMs, the accurate prediction of mechanical efficiency in EGMs could be achieved. In [47], Wieczorek and Ivantysnova developed the simulation tool CASPAR, providing the ability to study each interface of the APM including micro-motion of fluid-structure-thermal interactions. Pelosi and Ivantysynova [48] developed a model for fluid-structure interaction in the piston–cylinder interface. In [49], the same authors extended the tool to model the effects of heat transfer and associated thermal deformation in the film. In [50], they also investigated the implications of various constraints for the fluid-structure interaction problem.

Similar tools have also been developed by Schenk and Ivantysynova [51] and Zecchi and Ivantysynova [52] for the slipper–swashplate and cylinder block–valve plate interfaces respectively. Pellegri and Vacca [46] showed agreement with experimental results when modeling the the axial gap of a gerotor. These works demonstrate the ability of the coupled lumped-distributed parameter modelling approach to provide insight and capture complex multi-physical phenomena of a wide variety of machines that cannot be captured by other means. The limitation is that all these works developed standalone models of a single interface. This means that modeling between both the lumped fluid domain and the other gaps of the machine can only be weakly coupled, with information available only after simulation and not during. While the film flow–pressure relationship can be captured by co-simulation, the effects of shear and pressure forces from the films cannot be integrated into the net loading of the bodies considered in the lumped simulation leading to an incomplete force balance. Since these models take mobility approaches to balance the forces, the intertia of the bodies is also neglected. Additionally, these standalone models cannot be easily adapted to model a new geometry. Finally, they neglect the interplay of the various gaps of the units, whose behavior impacts all associated floating bodies and therefore all other films that interface with it.

In [53], Thiagarajan and Vacca modeled the impact of surface asperities on the flow and load sharing of the lateral lubricating interfaces of EGMs. In [54], Thiagarajan

et al. demonstrated the ability of the same tool to capture the behavior of low viscocity working fluids, with experimental validation for an aerospace fuel pump. A similar study was performed by Morgridge et al. [55], considering the effects of elasto-hydrodynamic lubrication at the interface of a single tooth with the lateral lubricating interface of an EGM. Mixed lubrication and cavitation modeling is also available in axial piston machines, including mixed lubrication by Fang and Shirakashi [56] in the piston-cylinder interface as well as Elrod cavitation in Hashemi et al. [57] in slipper-swashplate interface. Shang and Ivantysynova [58] used the insights provided by these models to develop a procedure for scaling of APMs considering the impact on the these lubricating interfaces. Ivantysyn et al. [59] showed the ability of these tools to predict the resulting wear of the slipper-swashplate interface of an APM. Similar to the CFD approaches, then, these tools can be used to answer fundamental questions in the understanding of these machines. Again, though, these studies are limited to the single films for which they are applied, and cannot be generalized to gain insight on the impact of a complete unit.

While some works have examined the nature of the piston-slipper assembly to spin within the cylinder bore [60], this aspect of the units presents challenge in modeling. First, it requires the ability model coupled interactions of the piston-cylinder and slipper-swashplate interfaces, which was demonstrated above to be a weak point in the existing approaches. Additionally, it requires detailed modeling of the ball-socket interface between the two. In [61], Faraz at all examined stress distribution in a spherical joint by imposing mechanical equilibrium on the bodies which was then related to the friction of the body via Couloumb friction. Kang [62] performed a similar analysis of a spherical joint under dynamic loading, relating a Hertzian pressure distribution to a resulting friction force using Couloumb friction. Other works use commercial finite element software [63, 64] or experimental analysis [65] to gain information on the dynamics of these contacts. The limitation of these works when applied to a hydraulic machine, however, is the consideration of only a constant Coulomb friction

coefficient. Following the approach of Weiss [66], the present work assumes Stribeck friction [67] at the interface of the ball and socket.

To capture mixed lubrication in thin films, Brown [68] generated random surface roughness and ran simulations using Reynolds equation. While this captures the interaction of the asperities with the flow, it requires a detailed numerical discretization to resolve this roughness, thus over-resolving the nominal geometry. To alleviate this, Patir and Cheng [69] derived an averaged Reynolds equation accounting for imperfect surfaces through the use of flow factor in pressure driven flow conditions. In [70], the authors extended the model to consider the effects of a constant relative sliding of the two films. In [71], Chengwei and Linqing defined a factor which accounts for the discrepancy between the expected and rigid gap heights for rough surfaces in contact for use with Patir and Cheng's model. Meng et al. [72] provided a simple way to find this factor for arbitrary film roughness distribution. The benefit of these approaches is that they remove the need to use a mesh fine enough to resolve the exact geometry of the rough film, without sacrificing accuracy. Furthermore they can be coupled with works such as Lee and Ren [73], where similar empirical models can be used to relate the load sharing by the asperities of the bodies to the rigid body position of the rough surfaces, removing the need for numerical considerations of the asperity deformation. These models have been applied only to incompressible films with uniform body velocities, however, so their application is limited only to simple or approximated geometries. Subject to these assumptions, this model can be used to capture the effects of mixed lubrication that occur during sub-optimal operation such as wear in dynamically loaded bearings [74,75], texturing and misalignment [76], and low viscosity working fluids [77] at lower computational cost. This shows a wide range of applicability of these empirical modeling approaches, with good agreement against more detailed simulation.

In terms of design and optimization of these units, both kinematic and lumped parameter models are well suited due to their lighter computational load. Such a kinematic optimization was performed by [5] to design asymmetric spur gears. In [78]

Devendran and Vacca used the kinematics of asymmetric spur EGPs to find an optimal solution for a variable displacement unit. In [79] the same authors extended the approach to use a lumped parameter approach to better capture the performance of a real unit. This work, as well as other similar works such as [80, 81], demonstrate the potential for design improvement when coupling a fast simulation tool with an optimization algorithm to perform virtual prototype design of EGPs. In [82], Chacon and Ivantysynova used the tools discussed above for the development of a virtual prototyping procedure for APMs. The application of this procedure led to a functioning prototype with only this virtual design approach, acting as a proof of concept of design by simulation. Finally, an outcome of this thesis which was published [6] and will be discussed in Section 5.2 used the lumped parameter model HYGESim discussed above to compare the potentials for helical and spur EGMs for fluid power applications. The limitations of these optimization procedures is that they are subject to the approximations of the models they use. Furthermore, geometric considerations are commonly simplified in parameterization of the design, due in large part to the limited number of design evaluations that are affordable. The benefit, though, is that modelling improvements of the evaluation functions can also directly improve the feasible of these design optimizations.

During operation of these units cavitation is common, occurring in regions where the pressures fall below the fluid's saturation and vapor pressures respectively. The resulting bubbles of both released gas and vaporized working fluid cause damage to components and drastically decrease the effective bulk modulus and density of the resulting solution, impacting unit performance. In [83], Braun and Hannon performed a detailed review of the state of cavitation modeling in general for fluid film bearings. Since all of the lubricating interfaces of PD machines can be viewed as special cases of more general fluid film bearings, the insight these works provide is helpful. To capture the detailed dynamics of the released bubbles, 3D computational fluid dynamic (CFD) models solve the Rayleigh–Plesset–Poritsky (RPP) equation [84], the governing equation which describes the formation and collapse of the released gas

bubbles. This is typically solved with either the Navier-Stokes equations in works such as [85–87] and commercial software such as Simerics-MP+ or more commonly Reynolds equation [88,89]. These approaches are important for tracking the formation and collapse, as well as the transport of individual bubbles.

The modeling of the complete dynamics of these bubbles, though, requires detailed information of the fluid inlet and outlet port and line geometries. Furthermore, the coupled solving of the formation and transport of the bubbles introduces a large computational load. This detailed modeling is not necessary, however, to capture the resulting performance of the lubricating film and to predict the regions where either gaseous or vaporous cavitation occurs. To alleviate this computation load, many works neglect the details of this cavitation, with pressures saturated at the cavitation value. This is discussed in great detail in Hamrock et al. [90] for various types of bearings, specifically as pertains to journal bearings. While this solution is fastest numerically and easiest to implement, the drawback is that all information of cavitation is lost. Additionally, this approach cannot be applied to study the effects of starved boundary conditions.

In the lumped parameter approaches described above, the effects of this cavitation can be modeled by observing the bulk behavior of a mixture of liquid, released gas, and vapor in the lumped volume. In [29], Casoli et al. successfully captured the resulting flow and pressure behavior of an APM under cavitating conditions, using equilibrium gas laws which neglect the dynamics of the cavitation. A similar approach was applied in [91] by del Campo et al. for external gear machines. In [92], Zhou et al. developed a cavitation model for hydraulic oils considering the transients of bubble release and rupture, which was applied in [93] to external gear machines. Similar model implementations of both these equilibrium and empirical dynamic models are available in commercial software such as Simcenter Amesim [94] and Simerics-MP+. In [95], Shah et al. performed further study of external gear pumps, while including the dynamics of a fixed amount of bubbles whose radius is dictated by the RPP equation simplified for lumped control volumes. The use of these models helps to

extend the feasibility of the lumped parameter assumptions, where the prediction of cavitation and aeration is made possible. In doing so, they retain rapid simulation while still capturing dynamic cavitation effects. The drawback of these approaches is that they typically offer only limited modeling of the transport of the bubbles, neglecting the exchange of bubbles between the main displacement chambers and the lubricating interfaces.

In study of the lubricating films, a modified Reynolds equation has been applied to solve for the behavior in the complete film region of the bearing. In regions of incomplete film, a similar volume of fluid (VOF) approach to the lumped domain is taken, modeling the bulk properties of the ruptured film as the combination of the fluid, vapor, and gas components. Application of this approach started first in journal bearings with Jakobsson and Floberg [96] and Olsson [97] (JFO), who developed a set of boundary conditions at the rupture and reformation of the fluid films consistent with conservation of mass. In [98, 99] Elrod developed an algorithm, based on these boundary conditions, which could automatically satisfy the JFO boundary conditions in a single "universal" differential equation. The use of this model allows for the modeling of cavitation in these films with a single equation, capturing the effects on both the flow and load carrying of the units. The main drawback of this approach is the numerical instability inherent to this model, making its implementation difficult.

To address this, many works have attempted to develop algorithms which decrease computation time and improve robustness of the universal equation including Multigrid techniques [100], Gauss-Seidel iterative schemes [101], but most using alternating direction implicit (ADI) method [102–104]. Others propose modifications to the original formulation presented by Elrod, in order to smooth the discontinuity inherent to this approach [105, 106]. More recent works apply this model to capture effects such as starvation in piston-ring/liners [107] and journal bearings with oiling grooves/textures [108, 109] and dynamic loading [110, 111]. These approaches show that, when a robust implementation is achieved, the use of this tool can be applied to

a wide variety of applications. They typically accomplish this stability, though, via model simplifications or complex numerical schemes that increase computation time.

1.4 Research Objectives

The state of the art in analysis of PD machines has identified a wide range of successful modeling approaches. These approaches span from instantaneous feedback of kinematic models to high fidelity resolution of their inner workings, having also identifying the compromises in between. Furthermore, the state of the art highlights the fundamental challenge in modeling these machines: (i) the use of a compressible working fluid means that real machines deviate from their kinematic performance (ii) fluid pressures from inter-dependant regions of the unit impart high forces on the floating bodies of the machines (iii) the pressures throughout the unit are highly sensitive to the micro-motions and deformations that result from this loading (iv) the extreme loading can lead to solid contact (wear) and cavitation (damage, poor performance) in the unit. In addressing these issues, the state of the art has developed a strong understanding of the nature of these challenges and the modeling approaches that can be employed to study them.

What these approaches lack, however, is the ability to develop a single, comprehensive analysis of any positive displacement machine. For the sake of simulation time, these approaches typically consider a single feature of the PD machine in isolation, or with the remaining aspects simplified. As a result, it is not known to what extent the mutual interactions of these aspects of the machine impact its performance. In making these assumptions, they also narrow the applicability (to varying geometries) of the approaches they develop. The solution to this is two-fold; first, the simplifications made to treat a single interface in isolation must be relaxed. Second, and in order to make the first feasible, the computational performance of these models must be improved.

The research objective of this thesis is to develop and validate a novel standalone simulation model, based on the coupled lumped-distributed parameter modeling approach discussed above, which facilities the study of any PD machine. Specifically, this work will relax the following model assumptions which restricted this goal.

First with respect to the dynamics of the bodies, all of the previous works from kinematic to detailed CFD analysis have placed at least some limitations on the degrees of the freedom of the floating bodies of these units. Instead, the modeling approach of this thesis will make no assumption on the geometry of the unit, and a novel 6 degree of freedom dynamics model for an arbitrary rigid body is developed. Based on these dynamics, all lubricating interfaces are modeled in the same simulation. As opposed to the isolated modeling approach performed previously, here shifting of the floating bodies leads to pressure and shear forces over all films that in turn impact the dynamics of the bodies.

Due to the resulting gap geometry, as well as flow constrictions in the lumped modeling, cavitation throughout the fluid domain can occur. For the first time, the resulting bubble exchange will be captured by a novel cavitation model of the lubricating films, which directly interfaces with the lumped parameter model. When the forces are not sufficient to carry the loads, the resulting mixed lubrication will be directly implemented into this film model via a novel integration of the cavitation and mixed lubrication modeling, consider its impact on both flow and film forces. The film pressures that are found with this model are used to calculate the resulting body deformation using either a finite element method (FEM) approach or a novel analytical-based deformation model, both of which consider the shear of the bodies for the first time. This allows for the model to close the fluid-structure problem even without external external modeling software or known geometry.

For the first time, a model of any unit, not just a single unit, will be developed as an application programming interface (API) applicable to any PD machine with finite displacement chambers. Here, both the physical and computational merits of a modeling choice are prioritized. This thesis will consist of the physical, numerical,

and software implications of coupling the solving of all the lubricating films of a units together with the main solver of these displacement chambers and floating bodies. Summarizing, the goals of this thesis are as follows

1. To develop a distributed parameter model that directly couples the solution of all lubricating films with the lumped parameter model, considering the effects of cavitation, mixed lubrication, and body dynamics over the entire fluid–solid domain.

2. To implement these models as a modular toolbox that can be used to model the performance of any PD machine.

3. To validate the results of this toolbox by implementing both an EGM and an APM model and comparing the resulting simulations against experimental data of reference machines and the relevant state of the art.

4. To demonstrate the application of this model to design a prototype EGM for an electro-hydraulic actuator, including virtual design optimization of its main design parameters followed by detailed design of its lubricating interfaces.

1.5 Structure of the thesis

Throughout this document, the general modeling suite which is developed will be referred to as Multics. The specific application of this suite to external gear machines will be referred to as Multics HYGESim. The information flow of this tool is demonstrated in Figure 1.7. Similarly, the application of the suite to axial piston machine will be referred to as Multics CASPAR, with information flow demonstrated in Figure 1.8.

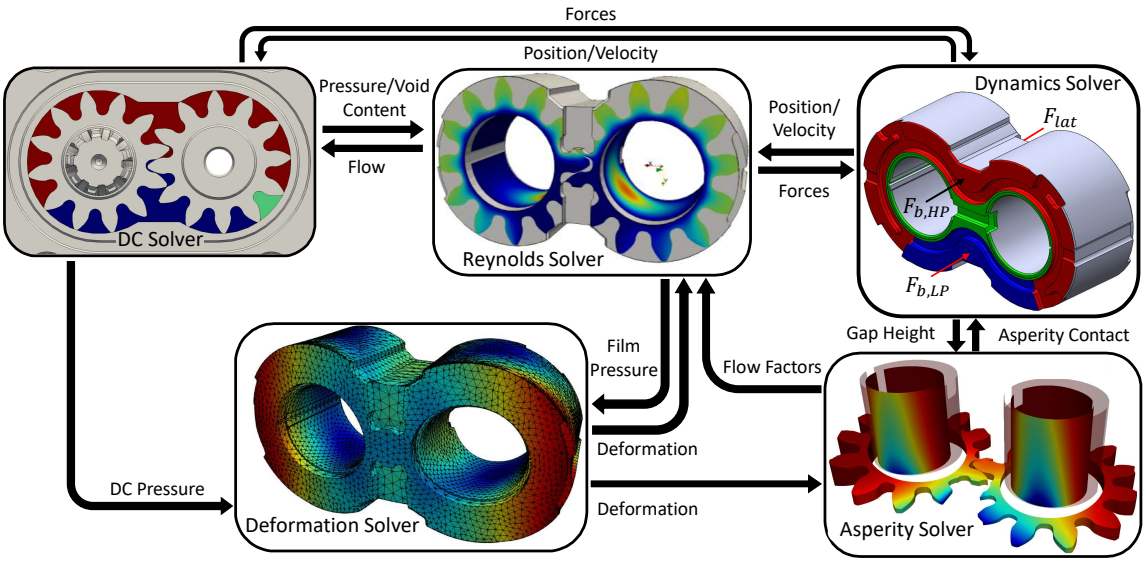

Figure 1.7. Information flow for Multics HYGESim

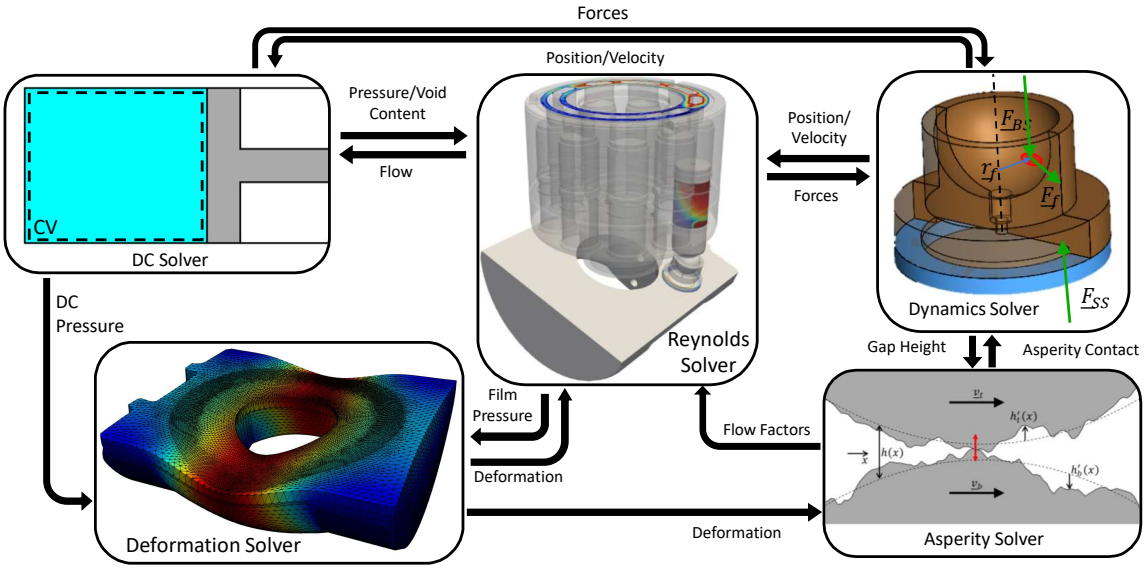

Figure 1.8. Information flow for Multics CASPAR

These figures highlight the highly coupled information exchange across the modules. In the sections to come, the details of this information exchange as well as the

role of each module will be explored. To do this, as well as to accomplish the goals stated above, the structure of the thesis is as follows

- Chapter 2 will describes the lumped parameter model used to capture the main displacing behavior of the machine (DC Solver), as well as the dynamics of the floating bodies (Dynamics Solver) and simple approximations of the lubricating interfaces.

- Chapter 3 will build on the lumped parameter model to solve the complete, distributed parameter behavior of the lubricating interfaces (Reynolds Solver), including the coupled effects of fluid–structure interaction (Deformation Solver), the dynamics of the bodies (Dynamics Solver), mixed lubrication (Asperity Solver), and cavitation/aeration (Reynolds Solver). It will also discuss how the model is implemented and coupled to other films as well as the lumped parameter model.

- Chapter 4 will use the toolbox developed in the previous chapters to build models of a pressure compensated external gear machine and axial piston machine, and provide validation by comparing the simulation results against experimental measurements of reference machines as well as representative results from literature.

- Chapter 5 will demonstrate the potentials of the model, using both the analytical approximation-based model for design optimization and the distributed models for detailed analysis of the lubricating films of an EGM.

2. LUMPED PARAMETER MODELING

This chapter introduces each component which makes up the lumped parameter model. As was mentioned in Chapter 1, the use of CFD modeling of these units offers high fidelity results, but at the expense of high computational demand. Considering this, the present model can be seen as a novel formulation, based on the lumped parameter model HYGESim [36] developed by Dr. Andrea Vacca's research group over the past decade, for any positive displacement machine. In doing so, the shortcomings identified in Section 1.3 have also been addressed with respect to lumped parameter modeling. The work presented in this thesis focuses mostly on the lubricating interface module, with modifications made to the remaining components to facilitate a strong coupling of the two. Due to the increased computational demand that this leads to, care was taken in implementation of both the lumped and distributed parameter components. The novel contributions to the lumped component of the model are as follows

- Development of the model API with focus on generality and object-oriented programming to facilitate application to any machine.
- Derivation of a full 6 degree of freedom inertial motion model of the bodies, using an impedance based force balance to capture the inertia of the bodies.
- The novel inclusion of the forces and torques on the floating bodies due to the thin-film shear and pressure buildup.

While the tools developed here are applicable to many PD machines, this thesis focuses on two very different machines, the EGM and APM. These two are chosen intentionally to challenge the tool with the generality required to model machines with drastically different working principles. To do this, the hydraulic diagram of the

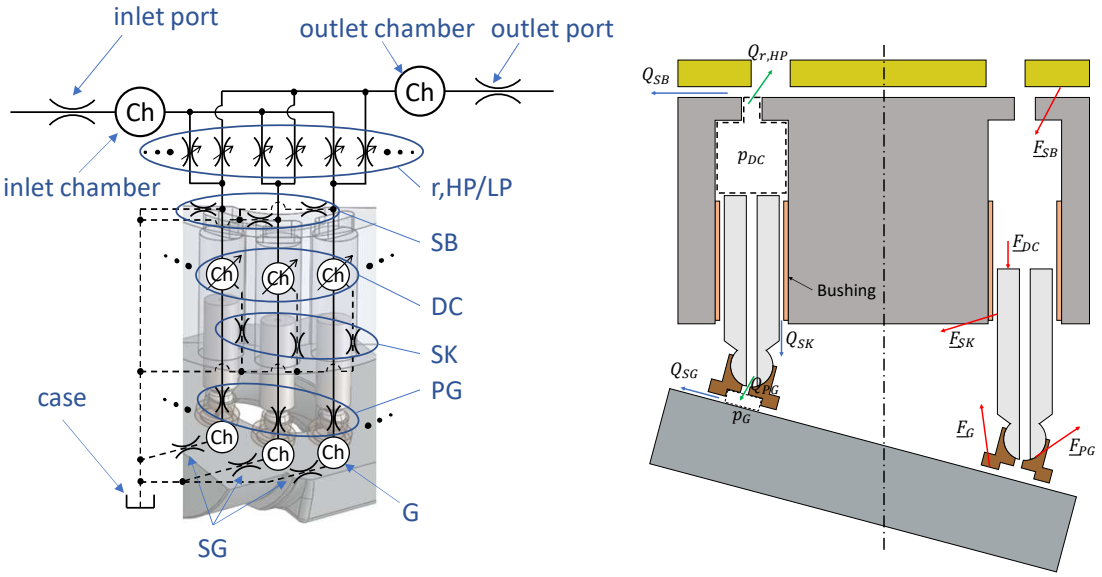

(a) Schematic view (b) Cross-section view

Figure 2.1. Loading and flow paths of an axial piston machine with (a) the hydraulic circuit of a single displacement chamber connected to high pressure through the outlet port and to low pressure by a series of leakages and the inlet port (b) the representation of the circuit as a cross section of the unit

machine must be understood. Starting first with the APM, Figure 2.1 demonstrates the hydraulic connectivity of the machine. As the pistons reciprocate in the bore, flow leaks through the thin gap between the piston and bore Q_{sk}. As this displacing action occurs, the valve plate directs flow to the delivery $Q_{r,HP}$ and from the suction port $Q_{r,LP}$, with some of the pressurized fluid leaking through the gap between the block and valve plate Q_{sb}. Finally, the hydrostatic balance, via the slipper chamber p_g connected to the displacement chamber Q_{pg}, comes at the expense of a leakage across the thin sealing land Q_{sg}. Each of these thin films exert a force which, in response to the net pressure from the displacement chamber, carry the floating bodies. A summary of how each of these components is modeled is included in Table A.1.

Next for the EGM, a hydraulic schematic is demonstrated in Figure 2.2. This Figure includes both the hydraulic system view in 2.2(a) (adapted from [112]) as well as a cross-sectional view 2.2(b). Similar to the APM, the displacing action of the fluid trapped between the teeth of the gear (TSVs) of the EGM drives flow to the delivery and suction ports through the depths of the gears via the HV and LV connections respectively. As the teeth begin to mesh, though, these connections close, and the transition from high to low pressure is controlled by the placement of relief grooves. The grooves, recessed in the lateral surface above and below the meshing teeth, direct flow to delivery (HG) and suction (LG). For a single-flank pump, such as the one shown in Figure 2.1(b), the existence of backlash between the two gears permits a fluid exchange between the TSVs via the FG connection. Instead for a dual-flank pump, the teeth make contact on both flanks, and effectively act like isolated displacement chambers. The high pressure side of the relief grooves extend into the casing (HS), whose purpose is to permit back-flow which pressurizes the TSV at a consistent angle regardless of the operating pressure or speed. In do so, the loads on the gears and balance elements are consistent and can be designed for. The resulting radial loads are carried by bearings (typically journal bearings), which build pressure to react the applied loads at the expense of a leakage Q_{JB}. Any axial loads cause the plate to move either towards or away from the gears, causing pressure to build in the film between the bushing and gears to oppose it. In a well designed unit, an equilibrium is found which ensures minimal lateral leakages over the teeth Q_{LL} and into the drain volume and journal bearing Q_{DL}. Finally, the clearance between the teeth of the gears and the casing of the unit is small, minimizing the radial gap that leads to a leakage over the tooth tips Q_{RL}. Again, the model assumptions are collected in Table A.2.

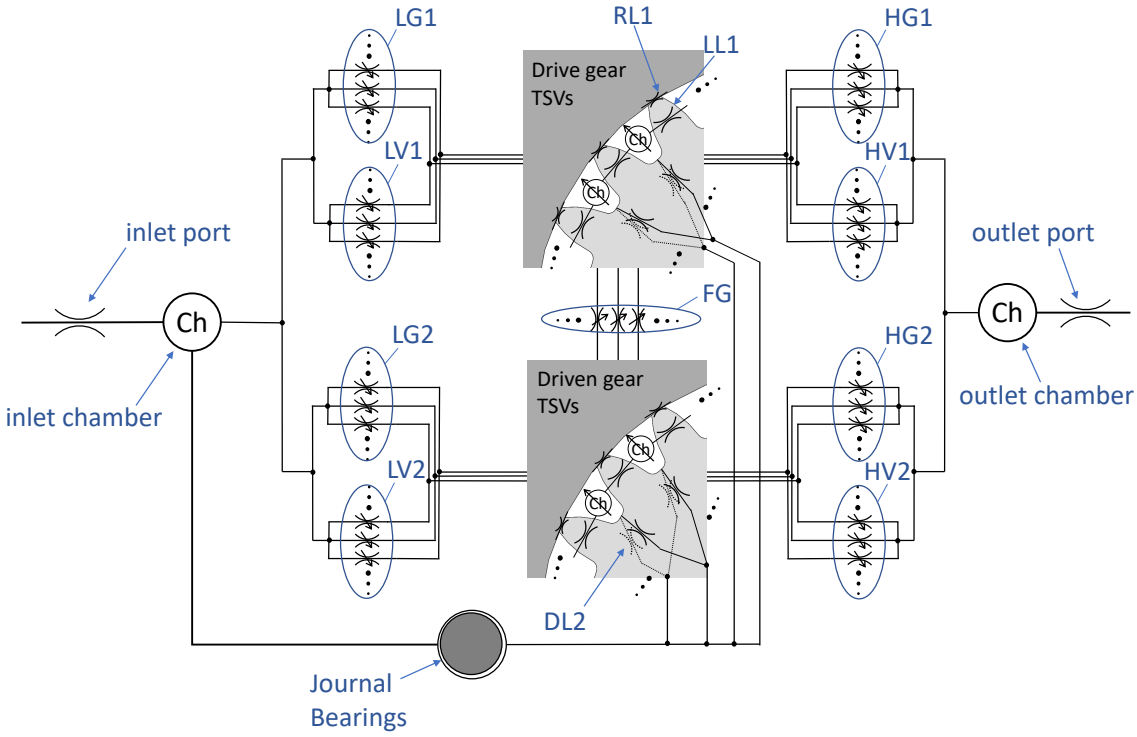

(a) Schematic view

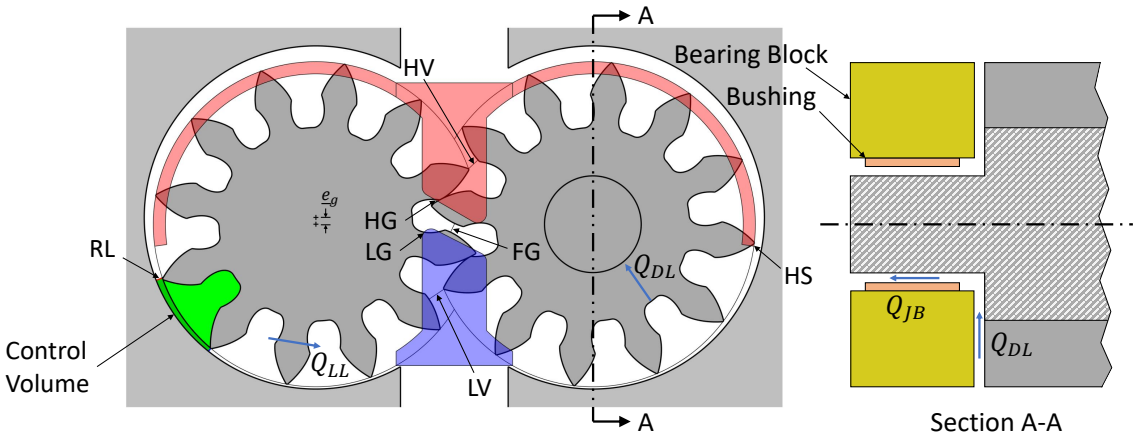

(b) Cross-section view

Figure 2.2. (a) Flow paths of an external gear machine with displacement chambers connected to adjacent chambers as well as the inlet and outlet volumes a series of leakages and orifices (b) the representation of the circuit as a cross section of the unit

2.1 Fluid Dynamic Module

In the present section, the lumped parameter fluid dynamic model is derived. With no information on the relevant assumptions for a given unit, each component is derived as a standalone object. This ensures modularity, because each component is isolated from the functionality of all others, and relies only on 'black-box' input/output across components. As was demonstrated in Figures 2.1 and 2.2, these components are connected in a circuit to form the complete model of a given unit.

2.1.1 Displacement Chambers

In the lumped parameter model, the fluid domain of the unit is split into a series of control volumes. In a lumped control volume, the pressure and temperature is assumed to be constant, with any released vapor/gas bubbles assumed to be homogeneous mixture throughout the volume. The validity of this assumption is supported by many of the previous works discussed in Chapter 1, with comparison against both detailed CFD simulation and experimental validation. In order to solve for the pressures in the volume, the integral form of continuity equation is applied

$$\frac{\partial}{\partial t}\left(\int_{\Omega}\rho\, d\Omega\right)+\int_{\Gamma}\rho\,\underline{v}\cdot\underline{d\Gamma}=0 \tag{2.1}$$

Since the properties of the fluid are assumed to be constant throughout the whole volume, this equation breaks down to relate the net change in mass of the chamber to the mass fluxes into the volume at each boundary

$$\frac{\partial \rho V}{\partial t}=V\frac{\partial \rho}{\partial t}+\rho\frac{\partial V}{\partial t}=\sum_{i}\dot{m}_{in,i} \tag{2.2}$$

The change in density, for a control volume whose density can change with both pressure and temperature, is given by

$$\rho=\rho(p,T)\implies\frac{\partial \rho}{\partial t}=\left.\frac{\partial \rho}{\partial p}\right|_{T}\frac{\partial p}{\partial t}+\left.\frac{\partial \rho}{\partial T}\right|_{p}\frac{\partial T}{\partial t}=\frac{\rho}{K_T}\frac{\partial p}{\partial t}+\left.\frac{\partial \rho}{\partial T}\right|_{p}\frac{\partial T}{\partial t} \tag{2.3}$$

Substituting this relation into 2.2 and rearranging yields the governing equation for pressure in the chamber, the thermal pressure build-up equation

$$\frac{\partial p}{\partial t} = \frac{K_T}{V}\left(\frac{1}{\rho}\sum_i \dot{m}_{\text{in,i}} - \frac{\partial V}{\partial t}\right) - \frac{K_T}{\rho}\frac{\partial \rho}{\partial T}\bigg|_p \frac{\partial T}{\partial t} \tag{2.4}$$

Similarly for the temperature in the volume, conservation of energy is applied

$$\frac{\partial}{\partial t}\left(\int_\Omega \left(\mathfrak{u} + \frac{1}{2}|v|^2 + gz\right)\rho\, d\Omega\right) + \int_\Gamma \left(\mathfrak{h} + \frac{1}{2}|v|^2 + gz\right)\rho \underline{v}\cdot \underline{d\Gamma} = \dot{\mathfrak{Q}}_{\text{in}} + \dot{\mathfrak{W}}_{\text{on }\Omega} \tag{2.5}$$

Neglecting body forces and assuming the volume is large enough that its change in momentum is negligible, then in the absence of external shaft or compressor work Equation 2.5 breaks down to balancing the total energy with the advection of enthalpy from the adjacent volumes, the expansion work, and any external heat flux

$$\frac{\partial m\mathfrak{u}}{\partial t} = \frac{\partial m\mathfrak{h}}{\partial t} - \frac{\partial pV}{\partial t} = m\frac{\partial \mathfrak{h}}{\partial t} + \mathfrak{h}\frac{\partial m}{\partial t} - p\frac{\partial V}{\partial t} - V\frac{\partial p}{\partial t} = -p\frac{\partial V}{\partial t} + \dot{\mathfrak{Q}}_{\text{in}} + \sum_i (\mathfrak{h}\dot{m})_{\text{in,i}} \tag{2.6}$$

Collecting terms and inserting Equation 2.4 yields the governing equation for the specific enthalpy of the volume

$$m\frac{\partial \mathfrak{h}}{\partial t} = \dot{\mathfrak{Q}}_{\text{in}} + V\frac{\partial p}{\partial t} - \mathfrak{h}\frac{\partial m}{\partial t} + \sum_i (\mathfrak{h}\dot{m})_{\text{in,i}} \tag{2.7}$$

Implementation of this relation directly can prove challenging. Instead by relating the specific enthalpy to the temperature via the specific heat capacity

$$\frac{\partial \mathfrak{h}}{\partial t} = c_p\frac{\partial T}{\partial t} + \frac{\partial \mathfrak{h}}{\partial p}\frac{\partial p}{\partial t} \tag{2.8}$$

and substituted into Equation 2.7, an express the rate of change of the temperature in the volume is given by

$$mc_p\frac{\partial T}{\partial t} + \frac{\partial \mathfrak{h}}{\partial p}\frac{\partial p}{\partial t} = \dot{\mathfrak{Q}}_{\text{in}} + V\frac{\partial p}{\partial t} - \mathfrak{h}\frac{\partial m}{\partial t} + \sum_i (\mathfrak{h}\dot{m})_{\text{in,i}} \tag{2.9}$$

Observing that the rate of change of mass in the volume comes only from influx of adjacent volumes, and rearranging yields the governing equation of temperature in the chamber

$$\frac{\partial T}{\partial t} = \frac{\dot{\mathfrak{Q}}_{\text{in}} - \mathfrak{h}\sum_i \dot{m}_{\text{in,i}} + \sum_i (\mathfrak{h}\dot{m})_{in,i}}{c_p\,\rho\,V} + \frac{1}{c_p\,\rho}\left(1 - \frac{1}{V}\frac{\partial \mathfrak{h}}{\partial p}\right)\frac{\partial p}{\partial t} \tag{2.10}$$

In the absence of temperature variation, $\frac{\partial T}{\partial t}$ terms drop and the isothermal pressure build up equation is recovered.

$$\frac{\partial p}{\partial t} = \frac{K_T}{V}\left(\frac{1}{\rho}\sum_i \dot{m}_{in,i} - \frac{\partial V}{\partial t}\right) \qquad \frac{\partial T}{\partial t} = 0 \tag{2.11}$$

Otherwise, these equations show the interdependence of temperature in the volume, as well as that of the adjacent volumes.

To model fluid properties of the volume above saturation conditions, two options are available. First, several empirical relations for modeling fluid properties, including the Barus [113] and Roeland [114] viscosity models and the Dowson and Higginson [115] density model (which is also used to find bulk modulus). While these models are helpful when no other resources are available, the present thesis will make use of tabulated properties as a function of pressure and temperature, provided by the supplier of a typical ISO VG 46 oil.

2.1.2 Fluid Cavitation and Aeration

Below the saturation pressure of gas (commonly air) trapped in the liquid, it cannot retain all of the dissolved gas, which begins to come out of solution in the form of undissolved gaseous bubbles. If the pressure is further reduced to the vapor pressure of liquid it will begin to evaporate, so that bubbles of the vaporous state of the liquid will also be present. Vaporous and gaseous cavitation in these volumes is accounted for in one of three ways. In all of the following approaches, the cavitation is subjected to the lumped parameter assumption such that the mixture of gas bubbles as well as the liquid and vaporous states of the oil are treated as a well mixed homogeneous bulk fluid. All fluid properties are then taken as the equivalent properties of this bulk fluid, with weighted contribution of each component dictated by the model choice.

First and most commonly, the equilibrium model described in [29] is used. This model, based on Henry's law, neglects the transients of the formation and collapse

of the bubbles, and models the properties of the bulk mixture of liquid, vapor, and released gas at equilibrium. Increasing the complexity, [93] is an implementation based on Singhal's full cavitation model [86] adapted for lumped parameter modeling, both of which use empirically determined parameters to define the time constants of phase change of the gaseous and vaporous bubbles to capture the transient of the production of the bubbles. Finally the most computationally complex model is given by Shah [95], where the fluid volume is initialized with a large number of bubbles. The instantaneous radii are these bubbles are solved using Rayleigh-Plesset equation, adapted for use in lumped parameter modeling. In either of the latter two models, bubbles are advected between the volumes via the various flow models to come. This aspect, as well as the added complexity of the models makes their implementation more computationally cumbersome. Considering this, they are typically used when cavitation issues are predicted by the equilibrium model and require detailed study. Unless otherwise specified, all results in this thesis will use the equilibrium cavitation model derived here.

To demonstrate this model, it is necessary to define the 4 equilibrium conditions that are possible. First, Figure 2.3(d) demonstrates the condition where the fluid pressure p is greater than the saturation pressure of its trapped gas p_{sat} and only liquid is present. Below this pressure the solubility of the liquid decreases and gas is released, as is shown in Figure 2.3(c). If the pressure is further reduced, the liquid will vaporize. Hydraulic oils typical for lubrication applications, however, are a solution of various substances rather than a single substance. Considering this, vaporization occurs over a range of pressures, with the lightest molecules in the solution beginning to vaporize at $p_{\text{vap,h}}$ leaving a mixture of released gas, vapor, and liquid as is shown in Figure 2.3(b). When the pressure reaches $p_{\text{vap,l}}$ the heaviest molecules of the liquid have vaporized, leaving only vapor and entirely released gas as is demonstrated in Figure 2.3(a). In the analysis to follow, the mixture of liquid, released gas, and vapor present in a given volume as a function of pressure will be referred to as the effective bulk fluid, assumed here to be a well-mixed homogeneous combination of the three.

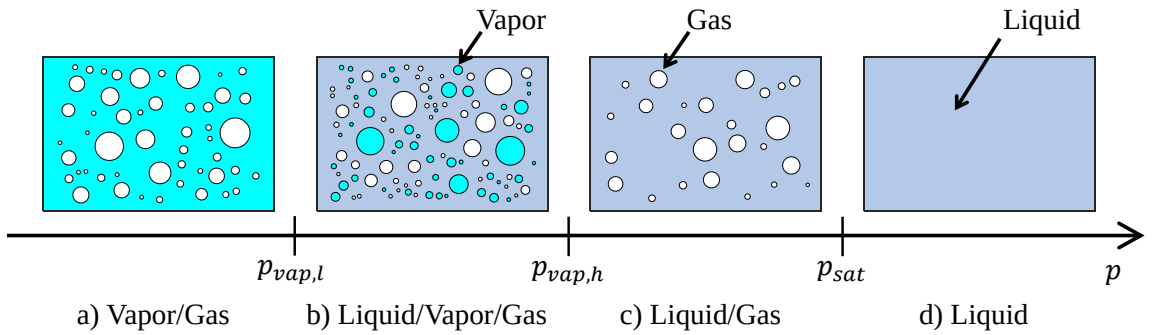

Figure 2.3. Diagram of equilibrium phases of bulk fluid containing liquid (blue), released gas (white), and vapor (cyan) as a function of pressure

It is the properties of this bulk fluid that will then be used in modeling the behavior of the films.

In regions of full film where $p \geq p_{\text{sat}}$, this approach has no restriction on the fluid property model used. Since the gas is fully dissolved in the fluid it does not contribute to it's the bulk fluid volume, only acting as a constant offset to the mass of the fluid. Therefore, the tabulated fluid properties discussed above are directly applicable here.

Above the saturation pressure, the bulk fluid (f) is comprised of liquid (l) as well as gas (g) that dissolves in the liquid up to the saturation limit at the pressure of its tank. As the film pressure decreases below this saturation pressure, the liquid cannot retain all of the dissolved (d) gas and it is released in the form of undissolved (u) gaseous bubbles. If the pressure is further reduced past the vapor pressure of the fluid, the fluid begins to evaporate and vaporous (v) working fluid is also present. In these conditions, the bulk fluid's density is the volume occupied by a mixture of the three components in a differential fluid element

$$\rho_f = \frac{dm_l + dm_v + dm_g}{dV_l + dV_v + dV_u} \tag{2.12}$$

Notice here that since the dissolved gas does not contribute to the volume occupied by the fluid, only the undissolved portion is considered in the fluid volume.

$$dV_f = dV_l + dV_v + dV_u \tag{2.13}$$

To describe the composition of the bulk fluid, void (volume) fractions α_i are defined

$$\alpha_i = \frac{dV_i}{dV_f} \text{ for } i = l, g, v, u, d \tag{2.14}$$

which can be related to the mass fractions

$$s_i = \frac{dm_i}{dm_f} = \alpha_i \frac{\rho_i}{\rho_f} \text{ for } i = l, g, v, u, d \tag{2.15}$$

For film pressures between the saturation and vapor pressure, gaseous cavitation occurs as the dissolved air begins to come out of the solution. To evaluate this condition, it is first necessary to identify the saturation pressure. For a given gas content, this saturation pressure can be found with Henry's law at equilibrium, using Bunsen's coefficient β for the corresponding gas-liquid pair.

$$\frac{dV_{\text{sat}}}{dV_{l0}} = \frac{\alpha_{g0}}{\alpha_{l0}} = \beta \frac{p_{\text{sat}} - p_{\text{vap,h}}}{p_{\text{atm}}} \implies p_{\text{sat}} = \frac{\alpha_{g0}}{\beta \alpha_{l0}} p_{\text{atm}} + p_{\text{vap,h}} \tag{2.16}$$

Notice here that the entrained air is assumed to be released at the high vapor pressure of the liquid when the liquid begins to vaporize, rather than vacuum, following similar approximations made in [29,94]. Equation 2.16 is then used to calculate the minimum pressure required to dissolve all the gas, for a given amount of saturated gas in the mixture α_{g0}. In this condition, the fluid volume is given entirely by the liquid, and the volume of gas that can be dissolved at this pressure can be calculated. The saturation density ρ_{sat} is then given by evaluating the liquid density at p_{sat}. This equation can also be used to find the expected volume of gas trapped in a reference liquid kept at p_{sat} such as an open tank.

Below this saturation pressure ($p_{\text{vap,h}} < p < p_{\text{sat}}$), the liquid cannot retain all dissolved gas, and undissolved gas bubbles form. In this case, the constant mass

$dm = dm_l + dm_g$ is distributed over a volume occupied by both the liquid and gas bubbles so that Equation 2.12 takes the form

$$\rho_f = \frac{\rho_{\text{sat}}}{\alpha_{l0} \exp\left(\frac{p_{\text{sat}}-p}{K}\right) + \chi_u \alpha_{g0} \left(\frac{T}{T_0}\right) \left(\frac{p_0}{p}\right)^{1/n_g}} \tag{2.17}$$

where the amount of gas that is released is linearly related to the pressure via Henry's law

$$\begin{aligned} \chi_u = \frac{\alpha_{u0}}{\alpha_{g0}} &= \begin{cases} 0, & p \geq p_{\text{sat}} \\ \frac{p_{\text{sat}}-p}{p_{\text{sat}}-p_{\text{vap,h}}}, & p_{\text{vap,h}} < p < p_{\text{sat}} \\ 1, & p \leq p_{\text{vap,h}} \end{cases} \\ \frac{d\chi_u}{dp} &= \begin{cases} 0, & p \geq p_{\text{sat}} \\ \frac{-1}{p_{\text{sat}}-p_{\text{vap,h}}}, & p_{\text{vap,h}} < p < p_{\text{sat}} \\ 0, & p \leq p_{\text{vap,h}} \end{cases} \end{aligned} \tag{2.18}$$

and the saturation density of the fluid is used

$$\rho_{sat} = (1 - \alpha_{g0})\rho_{l0} + \alpha_{g0}\rho_{g0} = \alpha_{l0}\rho_{l0} + \alpha_{g0}\rho_{g0} \tag{2.19}$$

Note here that this equation considers both the release of gas, as well as the polytropic expansion of the instantaneous undissolved component with index n_g from a reference condition to the given pressure

$$\frac{p}{\rho_g^{n_g}} = \frac{p_0}{\rho_{g0}^{n_g}} \implies p = p_0 \left(\frac{\rho_g}{\rho_{g0}}\right)^{n_g} \tag{2.20}$$

The reference condition will be taken as $(p_0, T_0) = (p_{\text{sat}}, T_0)$ where T_0 is the reference operating temperature. The liquid and gas void fractions are then found by dividing the local density of the differential volume by its value at saturation

$$\begin{aligned} \alpha_l &= \frac{\rho_f}{\rho_{sat}} \\ \alpha_u &= 1 - \alpha_l \end{aligned} \tag{2.21}$$

If the pressure is further reduced past the high vapor pressure ($p_{\text{vap,l}} < p \leq p_{\text{vap,h}}$), the liquid itself begins to evaporate. As was stated above, it is assumed that once

this pressure is reached all dissolved gas has been released ($\chi_u = 1$), so that similar to above the bulk fluid density includes volume contributions of the liquid, vapor, and all undissolved gas. Then from [29] the bulk fluid density is given by

$$\rho_f = \frac{\rho_{\text{sat}}}{\alpha_{l0}(1-\chi_v)\exp\left(\frac{p_{\text{sat}}-p}{K}\right) + \frac{T}{T_0}\left(\frac{\rho_{l0}}{\rho_{v0}}\alpha_{l0}\chi_v\left(\frac{p_{\text{vap,h}}}{p}\right)^{1/n_v} + \alpha_{g0}\left(\frac{p_{\text{sat}}}{p}\right)^{1/n_g}\right)} \tag{2.22}$$

where it is assumed that the mass of the molecules in the oil are evenly distributed over the range so that the mass of liquid that is evaporated is linearly related to the pressure

$$\begin{aligned}
\chi_v = \frac{f_v}{f_{l0}} &= \begin{cases} 0, & p \geq p_{\text{vap,h}} \\ \frac{p_{\text{vap,h}}-p}{p_{\text{vap,h}}-p_{\text{vap,l}}}, & p_{\text{vap,l}} < p < p_{\text{vap,h}} \\ 1, & p \leq p_{\text{vap,l}} \end{cases} \\
\frac{d\chi_v}{dp} &= \begin{cases} 0, & p \geq p_{\text{vap,h}} \\ \frac{-1}{p_{\text{vap,h}}-p_{\text{vap,l}}}, & p_{\text{vap,l}} < p < p_{\text{vap,h}} \\ 0, & p \leq p_{\text{vap,l}} \end{cases}
\end{aligned} \tag{2.23}$$

Similar to above, this equation considers the instantaneous evaporation of the liquid molecules, as well as the polytopic expansion of both the gaseous and vaporous bubbles. The gas and vapor density are updated with Equation 2.20, which can be used to update the mass fractions with χ_v given

$$\begin{aligned}
f_u &= f_{g0} \\
f_v &= \chi_v f_{l0} \\
f_l &= f_{l0} - f_v
\end{aligned} \tag{2.24}$$

so that Equation 2.15 can be used to find the corresponding void fractions.

If the pressure is reduced below the low saturation pressure $p \leq p_{\text{vap,l}}$, the entirety of the liquid has evaporated, leaving only the vaporous and gaseous bubbles so that Equation 2.22 simplifies to

$$\rho_f = \frac{\rho_{\text{sat}}}{\frac{T}{T_0}\left(\frac{\rho_{l0}}{\rho_{v0}}\alpha_{l0}\left(\frac{p_{\text{vap,h}}}{p}\right)^{1/n_v} + \alpha_{g0}\left(\frac{p_{\text{sat}}}{p}\right)^{1/n_g}\right)} \tag{2.25}$$

Table 2.1.
Reference fluid properties used in this thesis for typical ISO VG 46 oil

Bunsen Coefficient β	0.085
High vapor pressure $p_{\text{vap,h}}$	-0.5 bar_g
Low vapor pressure $p_{\text{vap,l}}$	-0.6 bar_g
Saturation pressure p_{sat}	0 bar_g
Reference liquid bulk modulus $K_{l,0}$	1.3 GPa
Reference liquid density $\rho_{l,0}$	850 kg/m^3
Reference liquid dynamic viscosity $\mu_{l,0}$	0.026 Pa s
Reference gas/vapor density $\rho_{g,0} = \rho_{v,0}$	1.2 kg/m^3
Reference gas/vapor kinematic viscosity $\nu_{g,0} = \nu_{v,0}$	15.68 mm^2/s

Again, the mass and void fractions can be found using Equation 2.24 and then 2.15.

Using this default static model, Figure 2.4 shows the resulting fluid properties of the bulk fluid used throughout the lumped parameter simulation, for the same tabulated ISO VG 46 oil mentnioned above with relevant properties detailed in Table 2.1. First in Figure 2.4(a), the bulk fluid density is shown with variation in pressure. The bulk modulus at these three conditions is then given by the density equations via its definition

$$K_f = \rho_f \frac{dp}{d\rho_f}\bigg|_T \tag{2.26}$$

as outlined in [29] and demonstrated in Figure 2.4(b). The dynamic viscosity of the bulk fluid, is given by the volume contributions of each to the bulk fluid

$$\mu_f(p,T) = \sum_i \left(\alpha_i(p)\mu_i(T)\right) \text{ for } i = l,u,v \tag{2.27}$$

The kinematic viscosity is then given by the bulk dynamic viscosity and density

$$\nu_f(p,T) = \mu_f/\rho_f \tag{2.28}$$

and is depicted in Figure 2.4(c).

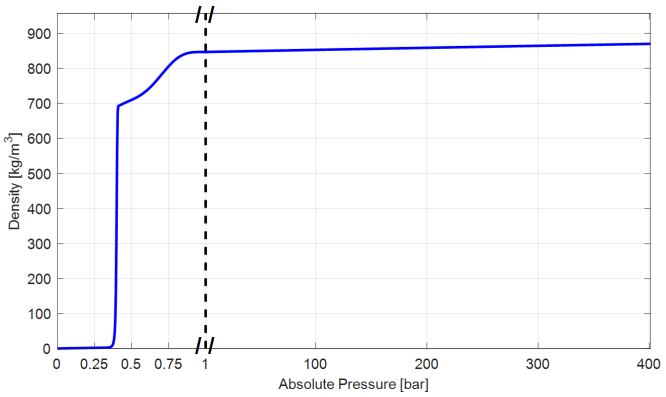

(a) Density

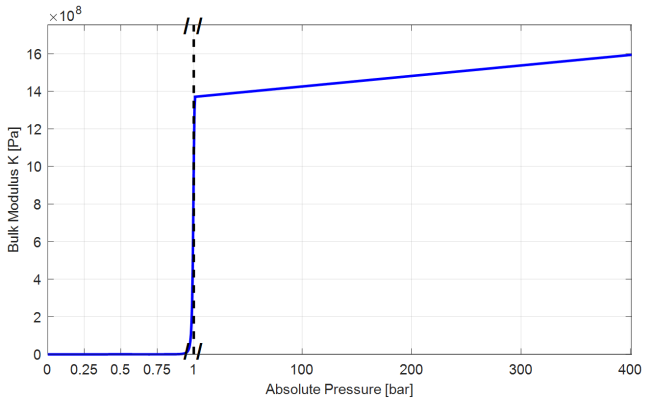

(b) Bulk Modulus

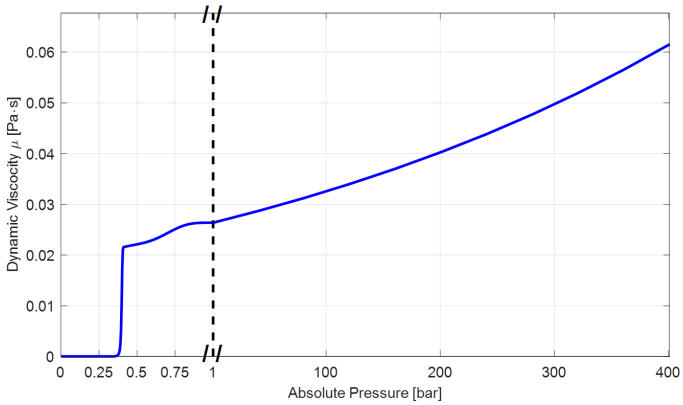

(c) Dynamic Viscosity

Figure 2.4. Properties of the resulting bulk fluid mixture as a function of pressure for (a) Equivalent density (b) Equivalent Bulk Modulus (c) Equivalent Dynamic Viscosity

2.1.3 Flow Throttling

In order to ensure that the assumptions of constant lumped pressures and temperatures in a given volume is reasonable, it is important to define their boundaries to reflect the physical flow constrictions of the unit. In effect, this choice creates a network of chambers, connected to one another via these constrictions. The flow passing through these boundaries can then be modeled using the orifice equation, demonstrated in Figure 2.5. This equation is derived by first assuming that the fluid is locally incompressible and steady, such that Bernoulli's equation relates the upstream flow conditions to that of the throat (including the associated minor loss ψ_l) where

$$\frac{p_u}{\rho g} + \frac{\overline{v}_u^2}{2g} + z_u = \frac{p_t}{\rho g} + \frac{\overline{v}_t^2}{2g} + z_t + \frac{\psi_l}{2g}\overline{v}_t^2 \tag{2.29}$$

Figure 2.5 shows that the entrance effects of the orifice must be included, but downstream of the throat the adverse pressure gradient causes the flow to break down to turbulence and the pressure is effectively that of the throat $p_t \approx p_d$. Applying continuity, then, the velocity at the throat and orifice can be related to that of the upstream $A_u\overline{v}_u = A_o\overline{v}_o = A_t\overline{v}_t$ so that neglecting change in elevation

$$p_u - p_d = \frac{\rho}{2}\left(\overline{v}_t^2(1+\psi_l) - \overline{v}_u^2\right) = \frac{\rho}{2}\overline{v}_o^2\left[\left(\frac{A_o^2}{A_t^2}\right)(1+\psi_l) - \left(\frac{A_o^2}{A_u^2}\right)\right] \tag{2.30}$$

Rearranging, the orifice equation is found where the mass flux can be expressed as

$$\dot{m}_o = \rho A_o \overline{v}_o = \psi_o A_o \sqrt{2\rho(p_u - p_d)} \tag{2.31}$$

with introduction of the orifice coefficient

$$\psi_o \equiv \Bigg[\underbrace{\left(\frac{A_o^2}{A_t^2}\right)(1+\psi_l)}_{\text{Discharge}} - \underbrace{\left(\frac{A_o^2}{A_u^2}\right)}_{\text{Velocity of Approach}} \Bigg]^{-1/2} \tag{2.32}$$

This orifice coefficient is well explored, accounting for to the ratio of the unknown throat diameter to that of the physical flow constriction, the head loss in the constriction process, and the entrance effects of the orifice owing to the velocity of approach.

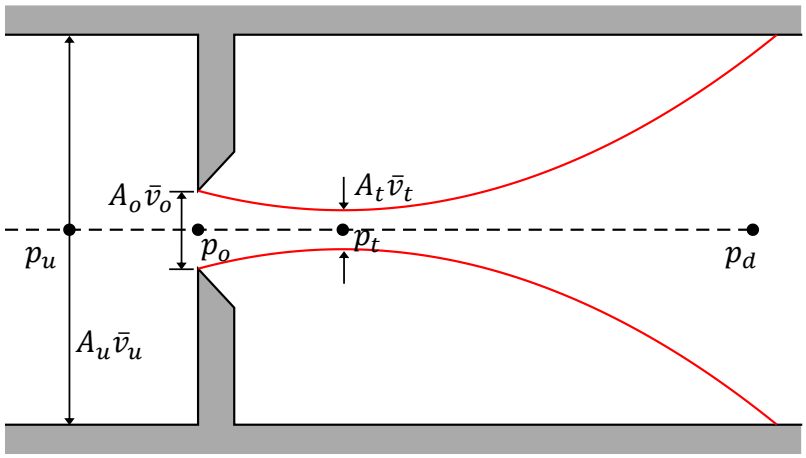

Figure 2.5. Flow through a sharp orifice, demonstrating the vena-contracta of the flow downstream from the physical flow constriction

From empirical evidence, as well as inspection from its definition, the discharge coefficient is a function of the flow. In the present work, emperical relations based on Merritt [116] are used to relate the orifice coefficient to the Reynolds number depending on the geometry of the orifice used.

However because this constriction may become very small compared to the volume of fluid that must pass through, it is possible for the flow to reach sonic conditions at the throat of the orifice. In this model, it is assumed that the properties at the throat are equal to that of the average pressure and upstream temperature, similar to that of an isentropic nozzle, and the flow is saturated at the corresponding choked mass flux

$$\dot{m}_t = \text{sign}(\Delta p)\, A_o \,\min\left[\psi_o \sqrt{2|\Delta p|\,\rho\big|_{\bar{p},T_{\text{up}}}},\, \sqrt{(K\rho)\,\big|_{\bar{p},T_{\text{up}}}}\right] \tag{2.33}$$

By expressing the rate of change of temperature in the volume in terms of the net enthalpy influx, the energy lost to heat through this is orifice is easily implemented. Treating the flow as adiabiatic, then by taking the specific enthalpy at the upstream fluid state (p_{up},T_{up}) location, the energy is advected to the downstream volume as some combination of heat and enthalpy at the downstream state.

$$\dot{\mathfrak{H}} = \dot{m}\mathfrak{h}|_{p_{up},T_{up}} \tag{2.34}$$

Similarly, the vapor and gas fractions of the upstream chamber can be taken to consider the advection of bubbles to the downstream volume where

$$\dot{\alpha}_{v,u} = \dot{m}\alpha_{v/u,up} \tag{2.35}$$

2.1.4 Leakages

To model leakages, two approaches are possible. First, the exact flows may be modeled using the distributed parameter models that will be presented in detail in Chapter 3. For rapid simulation (e.g. for optimization) though, the use of this tool is infeasible, and it is helpful to have analytical approximations of the flows. Taking the EGM for example, Figure 2.6 shows how a radial gap exists between the teeth of the gears and the body of the pump. Since the gap height is much smaller than the radius of the gear ($h_{\text{gap}} \ll r_{\text{gear}}$), this can be treated as a flow between parallel plates. Additionally since the depth of the gear is much larger than the gap ($h_{\text{gap}} \ll b_{\text{gap}}$), pressure variation in the y-direction and therefore axial flow can be neglected.

To model this, the flow is assumed to be steady, with change in density and temperature assumed to be locally small so that change in properties can be neglected. With these assumptions, the Navier–Stokes equations simply to

$$\frac{d^2 v_x}{dz^2} = -\frac{1}{\mu}\frac{dp}{dx} \tag{2.36}$$

No slip boundary conditions are applied to both moving bodies $v_x(h) = v_{x,t}$,$v_x(0) = v_{x,b}$. Then integrating this equation twice yields the modified Couette–Poiseuille equation

$$\underline{v}(z) = \left(v_{x,b} + \frac{v_{x,t} - v_{x,b}}{h_{\text{gap}}} z - \frac{\Delta p}{2\mu L_{\text{gap}}} z(h_{\text{gap}} - z)\right)\hat{i} \tag{2.37}$$

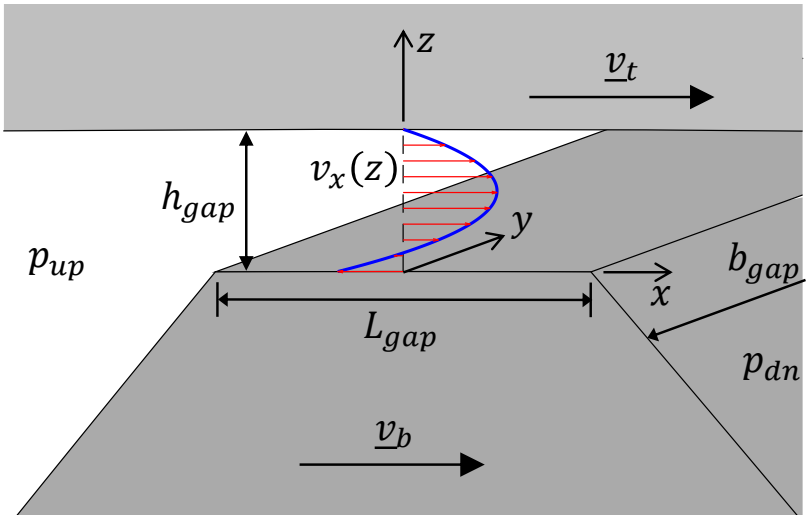

Figure 2.6. Tooth tip leakage exaggerated gap in external gear machines as Cartesian Couette-Poiseuille flow, and resulting velocity profile

The net flow across the gap is then given by the integral of this velocity of the whole gap so that

$$\dot{m}_l = \int_0^{b_{\text{gap}}} \int_0^{h_{\text{gap}}} \rho \left(\underline{v}(z) \cdot \hat{i} \right) dz dy = \rho|_{\overline{p},T_{\text{up}}} b_{\text{gap}} \left(\frac{(v_{x,t} - v_{x,b})h}{2} - \frac{h_{\text{gap}}^3}{12\mu|_{\overline{p},T_{\text{up}}}} \frac{\Delta p}{L_{\text{gap}}} \right) \tag{2.38}$$

The pressure profile can then be recovered from this solution after applying boundary conditions, linearly varied so that the total pressure drop $\Delta p = p_{\text{dn}} - p_{\text{up}}$ is realized

$$p(x) = p_{\text{up}} + \Delta p \left(\frac{x}{L_{\text{gap}}} + \frac{1}{2} \right) \tag{2.39}$$

Note that while it is sufficient in the present work, this equation considers only the nominal geometry of the unit and cannot capture the leakage behavior of a unit with manufacturing errors. This component is equally applicable in these cases, however, with inclusion of the complete leakage model described in [41, 112].

Taking the APM as example, Figure 2.6 shows how a gap exists between the floating slipper and the swash plate. Following similar assumptions as the Cartesian gap, the flow in an axisymmetric cylindrical gap is given for $\Delta p = p_o - p_i$ by

$$\underline{v}(z) = \left(\frac{1}{2\mu} \frac{\Delta p}{r \ln(r_i/r_o)} z(h_{\text{gap}} - z) \right) \hat{r} + \left(\frac{\omega r}{h_{\text{gap}}} z \right) \hat{\varphi} \tag{2.40}$$

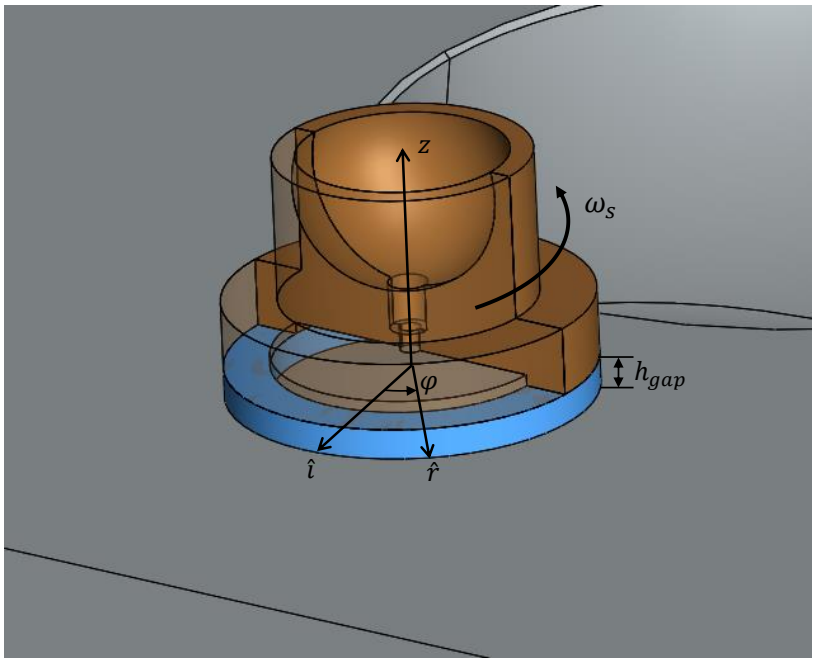

Figure 2.7. Radial slipper-swashplate exaggerated leakage gap in axial piston machines as cylindrical Couette-Poiseuille

so that flow across the boundary is

$$\dot{m}_l = \int_0^{2\pi} \int_0^{h_{\text{gap}}} \rho \left(\underline{v}(z) \cdot \hat{r}\right) r dz d\varphi = -\frac{\pi h_{\text{gap}}^3}{6\nu|_{\overline{p},T_{\text{up}}}} \Delta p \left(\ln\left(\frac{r_i}{r_o}\right)\right)^{-1} \tag{2.41}$$

In both the Poiseuille and Couette terms of these equations, the flow is treated as steady. This is justified using the results of [117], who showed that the time constant for a purely Couette flow, and similarly for a purely Poiseuille flow, to fully develop is

$$\mathcal{T}_{\text{CP}} \sim \frac{h^2}{\nu} \tag{2.42}$$

For a typical gap height of $h = 10\,\mu m$ and kinematic viscosity $\nu = 30\,mm^2/s$ this time is on the order of 3.4×10^{-6} seconds, or 0.04 degrees of shaft rotation at 2000 rpm, and can therefore neglecting the transients can be justified.

While this justifies the assumption of steady flow, it is possible that the two bodies are in relative motion in the film-normal direction as well, such that the squez-

ing causes excess pressure to build. Starting from the incompressible 1D Cartesian Reynolds equation, where again parallel gaps are assumed, an ODE in pressure is formed

$$\frac{d}{dx}\left(\frac{h^3}{12\mu}\frac{dp}{dx}\right) = \frac{dh}{dt} \tag{2.43}$$

and it is demonstrated that the case of squeezing in the films introduces a particular solution to the homogeneous pressure solution that can be extracted from 2.39. The general solution to the ODE is then simply the sum of the two. The particular squeeze solution is given by

$$\begin{aligned} \frac{dp_s}{dx} &= \frac{12\mu}{h^3}\frac{dh}{dt}x + C_1 \\ p_s &= \frac{6\mu}{h^3}\frac{dh}{dt}x^2 + C_1 x + C_2 \end{aligned} \tag{2.44}$$

However the homogeneous solution is linear, such that the general solution is still a parabola

$$p_g = \frac{6\mu}{h^3}\frac{dh}{dt}x^2 + C_1' x + C_2' \tag{2.45}$$

Applying the boundary conditions $p(-L_{\text{gap}}/2) = p_{\text{up}}$, $p(L_{\text{gap}}/2) = p_{\text{dn}}$

$$\begin{aligned} p(x) &= p_{\text{up}} + \Delta p\left(\frac{1}{2} + \frac{x}{L_{\text{gap}}}\right) + \left(\frac{6\mu x^2}{h^3} - \frac{3\mu L_{\text{gap}}^2}{2h^3}\right)\frac{dh}{dt} \\ \frac{dp}{dx} &= \frac{\Delta p}{L_{\text{gap}}} + \frac{12\mu x}{h^3}\frac{dh}{dt} \end{aligned} \tag{2.46}$$

For a squeezing gap, the flows are appended by the volume of fluid displaced by the squeezing action is evenly distributed to both the inlet and outlet volume

$$Q\left(\pm\frac{L_{\text{gap}}}{2}\right) = \frac{b_{\text{gap}}h^3}{12\mu}\frac{dp}{dx}\bigg|_{\pm\frac{L_{\text{gap}}}{2}} = \frac{b_{\text{gap}}h^3}{12\mu}\frac{\Delta p}{L_{\text{gap}}} \mp \frac{b_{\text{gap}}L_{\text{gap}}}{2}\frac{dh}{dt} \tag{2.47}$$

By way of example, in the EGM Figure 2.2(b) shows that this squeezing can be implemented indirectly by choice of control volume. Due to the finite clearance between the gears and the tooth tips, an additional variable volume is formed. By including this trapped volume in the total volume of the chamber (including half of the gap volume for each tooth), this squeezing is accounted for in the pressure build-up of the chamber and need not be expressly added here. In effect, it is treated as an internal flow, with 2.41 accounting for the external component of the flow.

An important observation, though, is the fact that sign of the Couette component depends on the frame of reference taken. This means that, with respect to the frame of reference fixed to the gear, the tooth is stationary ($u_t = 0$) and the casing sweeps the fluid towards the inlet ($u_b = -r\omega_g$). Thus when solving for the net mass flux into a control volume, the relative velocities of the bodies must always be defined with respect to the control volume. By preventing this variable volume definition from passing the extremes of the casing, a perceived (artificial) suction or pumping action of the tooth space volume as it enters and exits the casing respectively corrects for this body fixed flow reference, conserving mass and reflecting the true physics of the problem.

A similar procedure can be applied to the cylindrical film, starting first with the axi-symmetric cylindrical Reynolds equation

$$\frac{d}{dr}\left(\frac{rh^3}{12\mu}\frac{dp}{dr}\right) = r\frac{dh}{dt} \tag{2.48}$$

So that after integrating and applying the boundary conditions at this inner radius $p(r_i) = p_i$ and outer radius $p(r_o) = p_o$

$$\begin{aligned} p(r) &= \frac{1}{\ln\frac{r_i}{r_o}}\left[\ln(r)\left(p_i - p_o\right) + \ln(r_o)p_i - \ln(r_i)p_o\right] \\ &+\frac{3v_z\,\mu}{h^3}\left[r^2 + \frac{1}{\ln\frac{r_i}{r_o}}\left(\ln(r)\left(r_o^2 - r_i^2\right) + \ln(r_o)r_i^2 - \ln(r_i)r_o^2\right)\right] \\ \frac{dp}{dr} &= \frac{1}{r\,\ln\frac{r_i}{r_o}}\left(p_i - p_o\right) + \frac{3v_z\,\mu}{h^3}\left[2r + \frac{1}{r\,\ln\frac{r_i}{r_o}}\left(r_o^2 - r_i^2\right)\right] \end{aligned} \tag{2.49}$$

Following the Cartesian case, the control volume can be carefully drawn at the 'mean flow' radius so that the squeeze term is accounted for in the pressure buildup of the two volumes with definition. To do this, the radius is found such that the squeeze contribution to the pressure gradient (and therefore the flow) is zero and

$$\overline{r} = \sqrt{\frac{r_o^2 - r_i^2}{2\ln\left(\frac{r_o}{r_i}\right)}} \tag{2.50}$$

so that the external flow is given exactly by 2.41.

Similar to the turbulent orifice, both the cylindrical and Cartesian flows are treated as adiabatic so that the enthalpy flux to the downstream volume is given by 2.34 and bubble advection is given by 2.35, where the external component of the flow is used for each.

2.2 Dynamics Module

A key strength of the lumped parameter modeling approach is the decreased computational load required to solve for the pressure distribution of the fluid domain. As a result, the model can afford to consider not only the nominal positions of the floating components, but allow them to vary. In order to accomplish this, it is important to capture all loads applied to the floating bodies, to properly capture their micro-motion behavior. This section details the various loading types considered in this model.

In the previous versions of this model developed by Dr. Vacca's group, a mobility-based solution was used for body dynamics. Here, mobility is defined as the dynamic systems relationship of a velocity response to an input force. In effect, this approach assumes that the velocity can instantly adjust to meet the force demand. However for implementation with the distributed films, this approach requires a root finding loop to find the appropriate velocity, rendering it computationally expensive. Furthermore, this approach neglects the inertia of the bodies, which need not be negligible. Finally, the nature of these mobility methods mean they cannot be extended to study mutual interactions of multiple interfaces and cannot directly couple with the LP modules.

Instead in this model, a impedance-based solution is taken, where the dynamic relation is instead of a force response to an input velocity. The implication of this causality switch is the possibility of a net force imbalance, resulting in net linear and angular acceleration of the body governed by Newton's 2^{nd} law. This approach is also favorable numerically, as it forces a solution that is first order continuous

$\psi_{\text{impedance}} \in \mathcal{C}^1(t)$ instead of $\psi_{\text{mobility}} \in \mathcal{C}^0(t)$, yielding a well-behaved solution for numerical integration. In each of the sections to come then, force will be found for a given position and velocity, which is then collected to find the net acceleration of the body.

2.2.1 Pressure Loading

In the case of the APM, the pressure loading on the piston is directly given by the area exposed to the DC pressures. Similarly, the slipper pocket pressure acts directly on the slipper–piston assembly

$$\underline{F}_{DC} = p_{DC}\underline{A}_{DC} \tag{2.51}$$

These are demonstrated for the piston-slipper assembly in Figure 2.8.

In the case of an EGM, the projection geometry is considerably more complex. Again, though, the premise is the same and pressure forces act on the net area exposed to the given pressure. This concept is demonstrated in Figure 2.9, where both a drive ($\underline{A}_{115}$) and driven ($\underline{A}_{225}$) gear TSV projection is shown in magenta. Due to the discretization applied to this unit, a region of the gear tooth will be exposed to the delivery ($\underline{A}_{1D}$) and suction ($\underline{A}_{1S}$) volumes for some angular positions, demonstrated by the red and blue regions respectively. While not shown in this figure, the driven gear will also have area shared by these volumes as well ($\underline{A}_{2D/S}$). Notice that in all of these projections, there are regions of the tooth profile where pressure acts in both directions on the profile, negating its effect on the net force and moment applied to the body.

In the meshing zone of the gears, the pressures within a TSV affect not only their associated gear, but the meshing gear as well. This is shown in green in the figure, where the pressure of drive gear TSV applies a force to the driven gear ($\underline{A}_{211}$). Again, the opposite is true and the driven TSV will apply force to the drive gear as well.

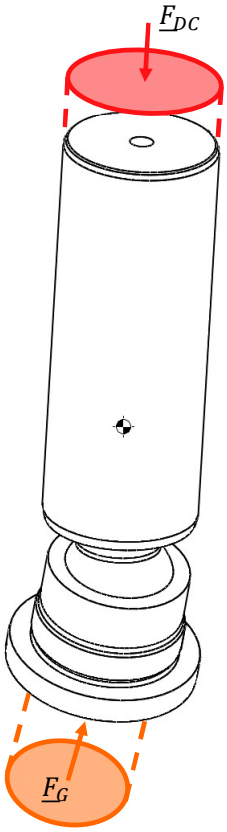

Figure 2.8. DC and Hydrostatic Pocket pressure projection for Ref P1 axial piston machine

With these projection areas defined, the net loading on each gear is then given

$$\underline{F}_{p,i} = p_D \underline{A}_{i,D} + p_S \underline{A}_{i,S} + \sum_{j=1}^{N_{\text{teeth}}} \left(p_{1,j} \underline{A}_{i,1,j} + p_{2,j} \underline{A}_{i,2,j} \right) \tag{2.52}$$

with tooth space volume area vector $\underline{A}_{i,j,k}$ read as the projection area of TSV k of the j^{th} gear onto the i^{th} gear, and similarly the pressure $p_{j,k}$ as the pressure in TSV k of the j^{th} gear. Due to the imbalance of pressures on the gears, a net pressure moment is applied to each. Since the pressure is uniform over each of these projections, the

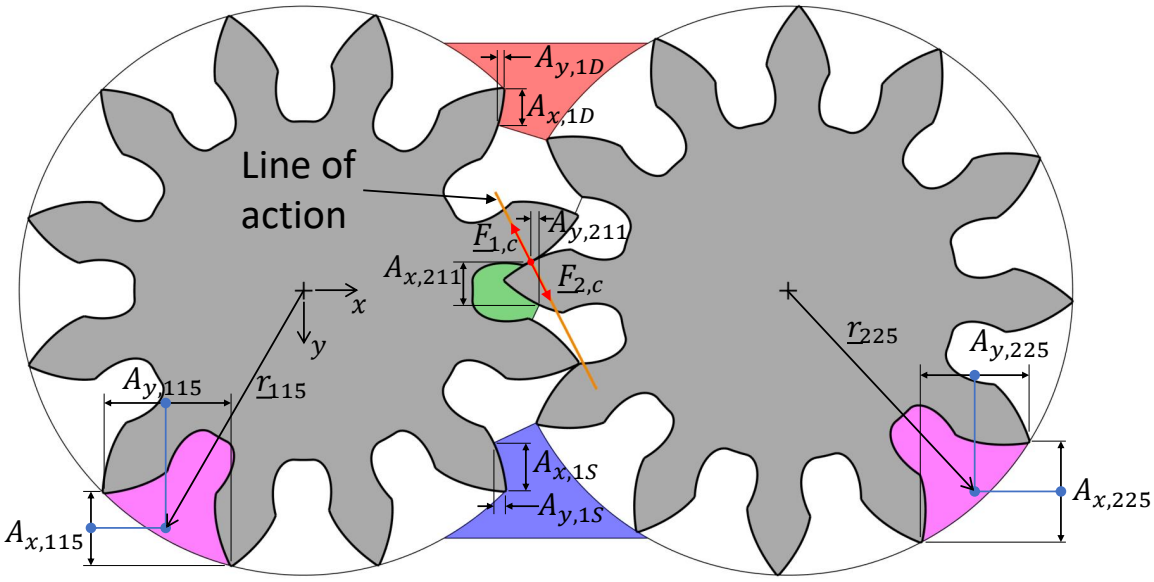

Figure 2.9. TSV pressure projection for Ref E3 external gear machine

point at which it acts on the body is given by the center of the projection plane, and the net moment due to pressure on a gear is given by

$$\underline{M}_{p,i} = \underline{r}_{i,D} \times (p_D \underline{A}_{i,D}) + \underline{r}_{i,S} \times (p_S \underline{A}_{i,S}) + \sum_{j=1}^{N_{\text{teeth}}} \left(\underline{r}_{i,1,j} \times (p_{1,j} \underline{A}_{i,1,j}) + \underline{r}_{i,2,j} \times (p_{2,j} \underline{A}_{i,2,j}) \right) \tag{2.53}$$

where similar to the area vector, the position vector $\underline{r}_{i,j,k}$ reads as the center of pressure of the projection of TSV k of the j^{th} gear onto the i^{th} gear (defined with respect to the center of gear i).

The driven gear's only mechanical contact is the drive gear, and so the entirety of its moment (including all torque losses) is opposed by a resulting contact force $\underline{F}_{2,c}$ with the drive gear's meshing teeth. The moment on the drive gear is given by the equal and opposite contact force on the drive gear, as well as the net pressure imbalance on the drive gear, all of which is carried by the prime mover. By the nature of the involute profile of the gears, the contact always occurs along the line of action, with force always act along the same line.

2.2.2 Analytical Film Forces

In Section 2.1.4, the analytical approximations of leakage flow were derived. The impact of these gaps comes not only from their flows, but also their resulting pressure and shear forces on the bodies. To find the shear stresses applied to either body, the velocity profiles derived in Section 2.1.4 are used. For the Cartesian gap, shear stress on the top and bottom bodies are given by differentiating Equation 2.37 so that

$$\underline{\tau}|_{\text{wall,t}} = -\mu \frac{d\underline{v}}{dz}\bigg|_{z=h_{\text{gap}}} = \left(-\mu \frac{v_{x,t} - v_{x,b}}{h_{\text{gap}}} - \frac{\Delta p}{2L_{\text{gap}}} h_{\text{gap}}\right) \hat{i} \tag{2.54}$$

$$\underline{\tau}|_{\text{wall,b}} = \mu \frac{d\underline{v}}{dz}\bigg|_{z=0} = \left(\mu \frac{v_{x,t} - v_{x,b}}{h_{\text{gap}}} - \frac{\Delta p}{2L_{\text{gap}}} h_{\text{gap}}\right) \hat{i} \tag{2.55}$$

The resulting shear force applied to either body is then the integral of this shear stress over the whole gap region

$$\underline{F}_{\tau,t/b} = \int_0^{L_{\text{gap}}} \int_0^{b_{gap}} \underline{\tau}|_{\text{wall,t/b}} \, dydx = L_{\text{gap}} \, b_{\text{gap}} \, \underline{\tau}|_{\text{wall,t/b}} \tag{2.56}$$

For the cylindrical gap, differentiating Equation 2.40 yields the shear stresses.

$$\underline{\tau}|_{\text{wall,t}} = -\mu \frac{d\underline{v}}{dz}\bigg|_{z=h_{\text{gap}}} = -\left(\frac{1}{2\mu \, r \ln(r_i/r_o)} \frac{\Delta p}{} h_{\text{gap}}\right) \hat{r} - \left(\frac{\omega r}{h_{\text{gap}}}\right) \hat{\varphi} \tag{2.57}$$

$$\underline{\tau}|_{\text{wall,b}} = \mu \frac{d\underline{v}}{dz}\bigg|_{z=0} = -\left(\frac{1}{2\mu \, r \ln(r_i/r_o)} \frac{\Delta p}{} h_{\text{gap}}\right) \hat{r} + \left(\frac{\omega r}{h_{\text{gap}}}\right) \hat{\varphi} \tag{2.58}$$

so that the net shear forces is again given by the integral over the gap, where the asymmetric nature means that the leakage applies no net force

$$\underline{F}_{\tau,t/b} = \int_0^{2\pi} \int_{r_i}^{r_o} \underline{\tau}|_{\text{wall,t/b}} \, r dr d\varphi = 0 \tag{2.59}$$

It is possible that the center of the cylindrical mesh is also translating. While this does not introduce a net mass flow when integrated over the whole surface, it does introduce an addition shear component. Since this is simply a linear velocity, it is given by the shear term of the Cartesian film

$$\underline{F}_{\tau,t,v} = \int_0^{2\pi} \int_{r_i}^{r_o} -\mu \frac{\underline{v}_c}{h_{gap}} r dr d\varphi = -\frac{\pi \mu (r_0^2 - r_i^2)}{h_{\text{gap}}} \underline{v}_c \tag{2.60}$$

$$\underline{F}_{\tau,b,v} = \int_0^{2\pi} \int_{r_i}^{r_o} \mu \frac{\underline{v}_c}{h_{gap}} r dr d\varphi = \frac{\pi \mu (r_0^2 - r_i^2)}{h_{\text{gap}}} \underline{v}_c \tag{2.61}$$

Observe that as the gap height tends to zero, Newton's law predicts infinite shear stress from the Couette terms. Certainly this is not the case, and it is common practice to saturate the gap height at some small value $h \ll C$.

To account for the pressure that builds in a film with arbitrary squeeze, the pressure solutions found in Section 2.1.4 are considered. Starting first with the Cartesian film, integrating the pressure over the gap surface defines the resulting impedance relationship of the gap relating the gap force to the instantaneous position and velocities of the bodies

$$\underline{F}_{t/b} = \pm b_{\text{gap}} L_{\text{gap}} \left(\underbrace{\frac{p_{\text{up}} + p_{\text{dn}}}{2}}_{\text{Mean pressure}} - \underbrace{\frac{\mu L_{gap}^2}{h^3} \frac{dh}{dt}}_{\text{Squeeze}} \right) \hat{k} \tag{2.62}$$

Again as was discussed in 2.1.4, the careful choice of control volume allows for the mean pressure term to be indirectly accounted for in the pressure projection of the control volume. The squeeze term, however, is added to the net load applied by the film.

Similarly for the cylindrical film, integrating over the cylindrical surface yields

$$\frac{|F_z|}{\pi} = \underbrace{p_o r_o^2 - p_i r_i^2 + \frac{(p_i - p_o)(r_i^2 - r_o^2)}{2 \ln \frac{r_i}{r_o}}}_{\text{'Mean' pressure}} - \underbrace{\frac{3 \mu v_z}{2h^3} \left[(r_o^4 - r_i^4) + \frac{(r_i^2 - r_o^2)^2}{\ln \frac{r_i}{r_o}} \right]}_{\text{Squeeze}} \tag{2.63}$$

While more complicated than the Cartesian case, this equation still relates the force and squeeze as a function of gap height, fluid viscosity, and a geometric constant, and the 'mean' pressure of the gap.

2.2.3 Bearing Modeling

As was mentioned previously, the lubricating films provide a bearing function which maintains design gaps in the films. Considering this, they cannot be neglected even in the simplified lumped model. Instead, they are approximated using analytical solutions to their pressure distributions. In [118], Child's et al. developed an

'impedance' approach where the force response of various hydrodynamic bearings can be related to the squeeze velocity they experience. Assuming an incompressible and aligned journal bearing, the instantaneous force that a journal bearing film applies the journal can be related analytically to its instantaneous eccentricity and velocity. This is accomplished by defining impedance tensors, which relate a pure squeezing motion to a resulting force. An arbitrary journal rotating about its translating central axis must first be converted to the pure squeeze frame by calculating its pure squeeze velocity

$$\underline{v}_s = \underline{v} - \overline{\underline{\omega}} \times \underline{e} \tag{2.64}$$

and eccentricity ratio

$$\underline{\epsilon}_s = \frac{1}{C_b} \begin{bmatrix} \cos\left(\angle \underline{v}_s\right) & \sin\left(\angle \underline{v}_s\right) \\ -\sin\left(\angle \underline{v}_s\right) & \cos\left(\angle \underline{v}_s\right) \end{bmatrix} \underline{e} \tag{2.65}$$

The resulting pure squeeze force given by the impedance tensors is then returned to the fixed frame to find the load applied to the journal

$$\underline{F}_b = -2\mu L_b \left(\frac{r_b}{C_b}\right)^3 |\underline{v}_s| \begin{bmatrix} \cos\left(\angle \underline{v}_s\right) & -\sin\left(\angle \underline{v}_s\right) \\ \sin\left(\angle \underline{v}_s\right) & \cos\left(\angle \underline{v}_s\right) \end{bmatrix} \underline{W}_s \tag{2.66}$$

The appropriate impedance tensor to use depends on the geometry of the bearing considered. While not required, it is common to have journal bearings in EGMs to carry radial loads on the gears due to the net pressure and shear forces of the unit. Due to geometric constraints, these bearings are typically 'short' $\left(\frac{L_b}{2r_b} < 1\right)$. Considering this, they can be modeled using Ockvirk's short bearing impedance tensor given in [119]

$$\psi_1 = 2(1-\epsilon^2)^{-1/2} \arccos\left(-\epsilon_{s,x}(1-\epsilon_{s,y}^2)^{-1/2}\right) \tag{2.67}$$

$$\psi_2 = \frac{L_b}{2r_b}(1-\epsilon^2)^{-2} \tag{2.68}$$

$$W_{\text{x,short}} = \left((1-\epsilon^2+3\epsilon_{s,x}^2)\psi_1 + 6\epsilon_{s,x}\right)\psi_2 \tag{2.69}$$

$$W_{\text{y,short}} = \left(3\epsilon_{s,x}\psi_1 + 4 + \frac{2\epsilon_{s,x}^2}{1-\epsilon_{s,y}^2}\right)\epsilon_{s,y}\psi_2 \tag{2.70}$$

In order to apply the analytical film assumption to APMs, the piston's tilting about its central axis must be assumed small as compared to the clearance of the unit. In this case, its behavior will resemble that of a journal bearing.Unlike typical journal bearings in EGMs though, the piston is long and therefore more closely resembles the Sommerfeld long journal bearing $\left(\frac{L_b}{2r_b} > 1\right)$. Considering this, the long bearing impedance tensor given in [119] is used where

$$\psi_1 = \sqrt{\left(1 + \frac{\epsilon^2}{2}\right)^2 - (1 + \frac{\epsilon^2}{4})\epsilon_{s,y}^2} \tag{2.71}$$

$$\psi_2 = 2(1-\epsilon^2)^{-1/2} \arccos\left(-\left(1 + \frac{\epsilon^2}{2}\right) x(\psi_1^2 - \epsilon_{s,y}^2)^{(-1/2)}\right) \tag{2.72}$$

$$\psi_3 = \frac{3}{2}\left((1-\epsilon^2)\left(1 + \frac{\epsilon^2}{2}\right)\right)^{-1} \tag{2.73}$$

$$W_{\text{x,long}} = \left((2 + \epsilon^2 - 3\epsilon_{s,y}^2)\psi_2 + 4\epsilon_{s,x}\psi_1\right)\psi_3 \tag{2.74}$$

$$W_{\text{y,long}} = (3\epsilon_{s,x}\psi_2 + 4\psi_1)\epsilon_{s,y}\psi_3 \tag{2.75}$$

Since these impedance definitions consider only the pressure forces of the interface, it is necessary to include additional shear terms. Again because of the assumption of small tilting, there is negligible wedge effect in the axial direction, and the axial shear force is thus an integral of the constant surface velocity over the circumferentially varying gap height. Following the approach suggested by Rituraj et al. [120], the circumferential shear of the bearing is determined as a modification of the nominal Ockvirk shear solution to account for the aspect ratio of the film. Note that as a machine rotates, the length of the interface can change (e.g. piston-cylinder interface of APM). Considering this, both the impedance tensors and the shear relation are dynamically adjusted to select the appropriate tensor and aspect ratio (if necessary). The net force of the bearing is then accounted for with Gauss quadrature, allowing for slight variations in eccentricity along the axial length $\epsilon(z)$ to induce a net moment from the film.

$$\underline{F}_b = \int_{-L/2}^{L/2}\left[\left(2\mu|\underline{v}|\left(\frac{r_p}{c}\right)^3\right)\underline{W} + \int_0^{2\pi}\frac{\mu}{h}\,\underline{v}_s r_p\,d\varphi\right]dz \tag{2.76a}$$

Table 2.2.
Impedance tensor case study parameters

Reference Dynamic Viscocity μ_{fluid}	0.0594 Pa s
Gear Nominal Mass m	0.338 kg
Rotation Speed ω_s	2000 rpm
Shaft Radius r_{bearing}	10 mm
Bearing Depth b_{bearing}	19 mm
Bearing Clearance C_{bearing}	60 μm
Applied Load F_s	$[0\ 1.5\ 0]^T$ kN

$$\underline{M}_b = \int_{-L/2}^{L/2} \left[\underline{r}_{cg} \times \left(2\mu |\underline{v}| \left(\frac{r_b}{c} \right)^3 \right) \underline{W} + \int_0^{2\pi} (\underline{r}_{cg} + r_b \hat{r}) \times \frac{\mu}{h} \underline{v}_s r_b \, d\varphi \right] dz \qquad (2.76b)$$

The benefit of using an impedance method is shown in Figure 2.10, comparing an example of the dynamic results obtained by the Ockvirk solution mobility and impedance methods with varying mass. The relevant simulation parameters for this study are given in Table 2.2. This figure shows that while all solutions converge to the steady Ockvirk analytical solution, the path that they take to this point is a significant function of the inertia of the body. For the transient loads of a PD machine, then, this inertia is not negligible and will impact the resulting micro-motion of the bodies. Here, the mass of the bodies taken as reference is the mass of the driven gear of Ref E3, showing a non-negligible effect for modeling of the unit.

To account for the rolling contact bearings that are used in PD machines, an example of which is given in Figure 2.11(a), an impedance relationship must be derived here. From Johnson [121], the indentation depth of two rolling cylinders with parallel axis in steady rolling is given by Hertzian contact. Certainly the bodies do not penetrate in reality, and it is worth clarifying that here indentation depth δ is defined as the maximum depth of penetration of the rigid profiles before deforming in the contact. With this, the needle bearing is equivalent to that of a cylinder rolling on

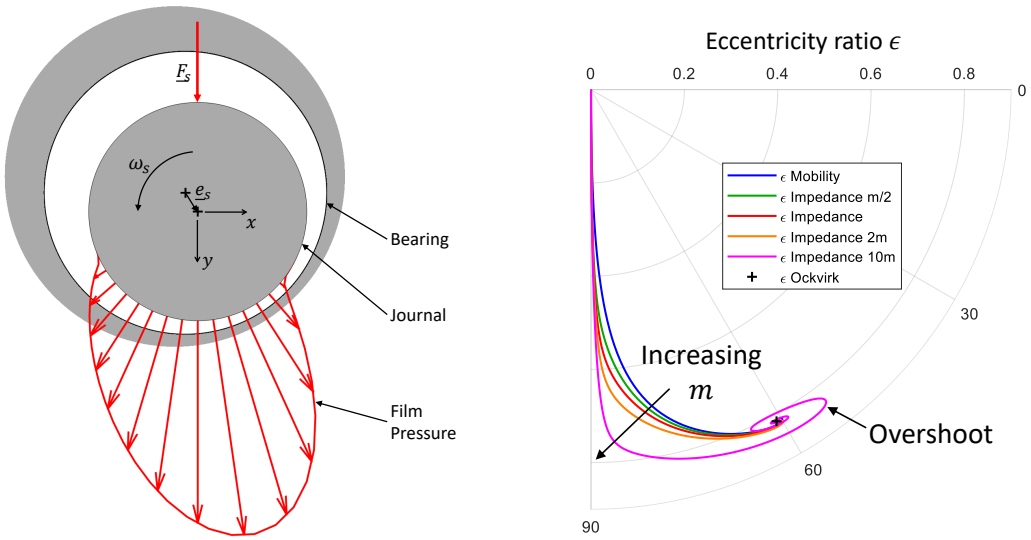

(a) Instantaneous Journal Loading

(b) Journal Trajectory

Figure 2.10. (a) Instantaneous pressure and external loading of an eccentric rotating journal with exaggerated clearance (b) the time varying journal center position predicted by both the mobility and impedance methods, and their asymptotic tending to the steady Ockvirk π-film solution

a flat plane (with $R_p \to \infty$ for flat plane suggested by [121]), so that the force from one needle of the bearing is linearly dependant on the rigid indentation depth

$$F_\delta \approx \frac{\pi}{4} E^* b_{needle} \delta \tag{2.77}$$

The total stiffness of the bearing is then given by the collection of forces of all needles in the bearing. Notice, however, that the bodies deform at both the inner and outer race interfaces, demonstrated in Figure 2.11(b). Assuming that the deformations are small enough that these interfaces do not interact, then for a given shaft eccentricity only half of the deformation yields force output on the shaft so the impedance relationship is given by

$$\underline{F}_b \approx \sum_{i=1}^{N_{\text{needle}}} -\frac{\pi}{8} E^* b_{\text{needle}} \max\left(0, \underline{e}_s \cdot \hat{r}_{n,i}\right) \hat{r}_{n,i} = -k_{\text{needle}} \underline{e}_s \tag{2.78}$$

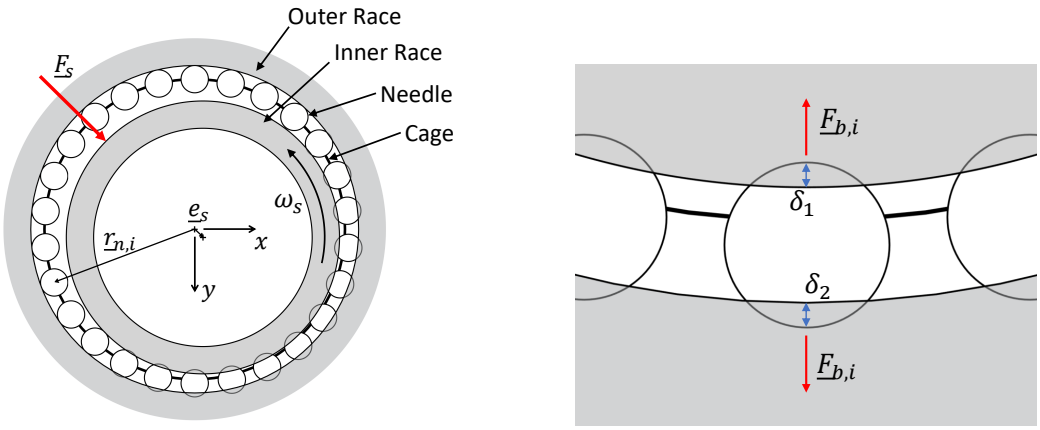

(a) Eccentric needle bearing

(b) Single Needle

Figure 2.11. (a) Typical needle bearing configuration with exaggerated eccentricity (b) Demonstration of multiple penetrations $\delta_{1/2}$ for a single needle in bearing

It turns out that this expression is not a function of the phase of the needles with respect to the angle of eccentricity $\left(\angle \underline{r}_{n,i} - \angle \underline{e}_s\right)$, so this system can be resolved into an equivalent linear spring, whose constant is a function only of the number and length of the needles and the material properties

$$k_{needle} = \frac{\pi}{8} E^* b_{\text{needle}} \sum_{i=0}^{N_{\text{needle}}-1} \max\left(0, cos\left(i \frac{2\pi}{N_{\text{needle}}}\right)\right)^2 \tag{2.79}$$

To account for the damping associated with this bearing, an optional definition of the damping ratio ς of the body is available, so that

$$d_{\text{needle}} = 2\varsigma\sqrt{m_{\text{body}} k_{\text{needle}}} \tag{2.80}$$

and the net force of the bearing considers also the velocity of the bodies involved

$$\underline{F}_b = -k_{\text{needle}} \underline{e}_s - d_{\text{needle}} \dot{\underline{e}}_s \tag{2.81}$$

2.2.4 Rigid Body Motion

With the loads on the body defined, it is necessary to find the resulting acceleration of the body. Because the model must work for an arbitrary unit, no assumptions can be made on the shape or constraints of the bodies. To model the dynamics, then, Newton's 2^{nd} law is applied to conserve linear and angular momentum in the arbitrary body. First, the linear momentum must be defined in a fixed inertial frame (IF) so that

$$m\frac{d}{dt}\underline{v}_{IF} = \sum_i \underline{F}_{i,IF} \tag{2.82}$$

Instead the angular momentum is defined with respect to the center of mass of the body, and is therefore conserved in the body-fixed (BF) frame traveling with the center of mass. This has the added convenience of an inertial tensor that need not be transformed as the body moves, so that

$$\underline{\underline{I}}_{BF}\frac{d}{dt}\underline{\omega}_{BF} = \sum_i \underline{M}_{i,BF} \tag{2.83}$$

The inertial tensor here is the collection of the products of inertia in each direction, where

$$\underline{\underline{I}} = \begin{bmatrix} I_{xx} & -I_{xy} & -I_{xz} \\ -I_{yx} & I_{yy} & -I_{yz} \\ -I_{zx} & -I_{zy} & I_{zz} \end{bmatrix} \tag{2.84}$$

These expressions can calculated either analytical for simple geometry or directly from CAD, demonstrated for I_{xx} and I_{xy} as

$$\begin{aligned} I_{xx} &= \int_\Omega \left(y^2 + z^2\right) dm \\ I_{xy} = I_{yx} &= \int_\Omega x\, y\, dm \end{aligned} \tag{2.85}$$

Because of this coordinate system distinction, and because the applied loads are typically applied in the body-fixed frame, a coordinate transformation is necessary to relate the two. This transformation can be a seen as the result of 3 sequential rotations, known as the Euler angles. In the present thesis, the most common 'ZYX'

convention is followed, where the body is first 'Yawed' about the z-axis by an angle Ψ, then 'Pitched' about the transformed y'-axis by an angle Θ, and finally 'Rolled' about the resulting x''-axis by an angle Φ so that

$$\begin{aligned} \underline{r}_{BF} &= \underline{\underline{\mathcal{R}}}_x(\Phi)\underline{\underline{\mathcal{R}}}_y(\Theta)\underline{\underline{\mathcal{R}}}_z(\Psi)\,\underline{r}_{IF} \\ &= \underbrace{\begin{bmatrix} 1 & 0 & 0 \\ 0 & \cos\Phi & -\sin\Phi \\ 0 & \sin\Phi & \cos\Phi \end{bmatrix}}_{\text{Roll}} \underbrace{\begin{bmatrix} \cos\Theta & 0 & \sin\Theta \\ 0 & 1 & 0 \\ -\sin\Theta & 0 & \cos\Theta \end{bmatrix}}_{\text{Pitch}} \underbrace{\begin{bmatrix} \cos\Psi & -\sin\Phi & 0 \\ \sin\Psi & \cos\Psi & 0 \\ 0 & 0 & 1 \end{bmatrix}}_{\text{Yaw}} \underline{r}_{IF} \end{aligned} \tag{2.86}$$

Since these rotation matrices are skew-symmetric with determinant +1, this relationship is easily inverted by observing that the inverse of the matrix is simply a rotation in the opposite direction

$$\begin{aligned} \underline{r}_{IF} = \left(\underline{\underline{\mathcal{R}}}_x(\Phi)\underline{\underline{\mathcal{R}}}_y(\Theta)\underline{\underline{\mathcal{R}}}_z(\Psi)\right)^{-1} \underline{r}_{BF} &= \underline{\underline{\mathcal{R}}}_z(\Psi)^{-1}\underline{\underline{\mathcal{R}}}_y(\Theta)^{-1}\underline{\underline{\mathcal{R}}}_x(\Phi)^{-1}\,\underline{r}_{BF} \\ &= \underline{\underline{\mathcal{R}}}_z(-\Psi)\underline{\underline{\mathcal{R}}}_y(-\Theta)\underline{\underline{\mathcal{R}}}_x(-\Phi)\,\underline{r}_{BF} \end{aligned} \tag{2.87}$$

The net loading of the body can then be found by collecting the forces in both reference frames and

$$\underline{F}_{\text{net,IF}} = \left(\sum_i \underline{F}_{IF,i}\right) + \underline{\underline{\mathcal{R}}}_z(-\Psi)\underline{\underline{\mathcal{R}}}_y(-\Theta)\underline{\underline{\mathcal{R}}}_x(-\Phi)\left(\sum_j \underline{F}_{BF,j}\right) \tag{2.88}$$

$$\underline{M}_{\text{net,BF}} = \underline{\underline{\mathcal{R}}}_x(\Phi)\underline{\underline{\mathcal{R}}}_y(\Theta)\underline{\underline{\mathcal{R}}}_z(\Psi)\left(\sum_i \underline{M}_{IF,i}\right) + \left(\sum_j \underline{M}_{BF,j}\right) \tag{2.89}$$

By consider the location of each force, the moment due to the j^{th} force offset from the center of mass of the body is

$$\underline{M}_{BF,j} = \underline{r}_{BF,j} \times \underline{F}_{BF,j} \tag{2.90}$$

with appropriate coordinate transformations to facilitate inertial frame definitions of the position and/or force vector.

This formulation is not directly integrable as presented, since there is no expression which relates the sum of the moments to progress the Euler angles. By observation of the coordinate systems, however, the following expression can be used to relate the

instantaneous rate of change of the Euler angles to the angular velocities, closing the problem of body position

$$\underline{\omega}_{BF} = \begin{bmatrix} \dot{\Phi} \\ 0 \\ 0 \end{bmatrix} + \underline{\underline{\mathcal{R}}}_x(-\Phi) \begin{bmatrix} 0 \\ \dot{\Theta} \\ 0 \end{bmatrix} + \underline{\underline{\mathcal{R}}}_x(-\Phi)\underline{\underline{\mathcal{R}}}_y(-\Theta) \begin{bmatrix} 0 \\ 0 \\ \dot{\Psi} \end{bmatrix} \tag{2.91}$$

2.3 Geometric Module

Throughout the previous modules outlined in this chapter, the control volume discretization is referenced by both the surfaces and the volume for both fluid-dynamic and micro-motion contexts. To extract this required information, a geometric module of the model is required. The geometric module is intentionally treated as a black-box in this thesis, and its existence assumed for whichever pump is being considered. This is because it will inevitably be pump specific, but is a pre-processing step that can be treated as a separate analysis. Details of the geometric module used in the EGM can be found in [15], and are briefly explained here.

The module starts directly from the CAD of the unit, and extracts the gear and groove profiles. With the resulting gear profile, it defines the delimiting segments mentioned in Section 2.1. The purpose of the geometric module is to extract the relevant information from the geometry of the unit necessary to facilitate the lumped simulation of the displacing action of the unit. For some units, such as piston-type machines, the distinction between these finite displacement chambers is trivially given by each piston-bore pair. Others, such as typical gerotors, the volumes are delimited by sealing lands, making for intuitive separation points of the volume. In some machines, such as external or internal gear machines, there is no consistent delimitation of the fluid volumes. In either of the latter cases, the geometric module must define the fluid volume into an inter-connected set of volume in such a way that it appropriately captures the displacing action of the unit.

In order to conserve mass and to respect the fundamental rules outline by Zhao and Vacca [15], the segments are adjusted slightly before exporting the resulting

information in an N-dimensional table for interpolation online in the simulation. For the case of EGM, this table is a function of the drive gear shaft angle and the center distance of the two gears, but in general these dimensions correspond to mechanical degrees of freedom of any pump. As an alternative to CAD, the geometric module can take input of an analytical gear profile, generated by symbolically performing the cutting process of the gear and passing the resulting tooth profile. The latter functionality will be required for the optimization procedure in coming chapters. This gear generator module is described in detail in [5].

Similarly for APMs, the tool AVAS outlined in [122] is used. While the delimitation of volume in these units is straightforward, determination of the flow restrictions formed in the porting is not. To overcome this, AVAS examines the instantaneous flow path of the porting of the APM directly from the 3D drawings of the unit. In doing so, it extracts the instantaneous point of flow constriction to both the outlet and inlet porting given by the 3D flow paths. By repeating this procedure over a range of shaft angles, the instantaneous connectivity of the $A_{r,HP}$ and $A_{r,LP}$ connections can be collected into a similar lookup table for use simulation.

2.4 Implementation

The various inter-connected modules of the proposed model form a stiff non-linear system of ordinary differential equations of the form

$$\frac{d}{dt}\underline{\psi} = \underline{f}\left(t, \underline{\psi}\right) \tag{2.92}$$

For the lumped parameter implementation, LSODA [123] provides a powerful method switching ODE solver to integrate the system of equations. In each function evaluation of LSODA, the function $\underline{f}\left(t, \underline{\psi}\right)$ is evaluated by collecting the flows and forces in the chambers and bodies respectively, so that the instantaneous properties of the chamber and acceleration of the bodies can be found. This information is then used by LSODA to progress the solution and provide updated state-variables $\underline{\psi}$ for subsequent function evaluations. For this reason, they are treated as known quantities for

a single function evaluation. For the distributed parameter implementation to follow, the use of this integrator is unfavorable since the simulation time of is not monotonically increasing. Instead in this case, available integrators for the LP domain include the multi-step variable coefficient backwards difference formula implemented in the GNU Scientific Library [124], variable order Runge-Kutta explicit integration, and a semi-implicit Adams–Bashforth predictor-corrector. These integrators have been proven to be successful for systems of equations with varying stiffness, and all have the important property of constant forward progress that is necessary in this approach. While these solvers are generally not capable of matching the computation time of LSODA, the distributed parameter films dominate simulation time and the impact of the lumped parameter portion is negligible.

3. DISTRIBUTED PARAMETER MODELING

This chapter details the development of the distributed parameter modeling approach. Similar to Chapter 2, this thesis can be seen as a novel formulation for modeling any lubricating interface, again addresses the shortcomings identified in Section 1.3 relevant to distributed parameter modeling. This work takes as reference the collection of lubricating film models developed by Dr. Vacca and Dr. Ivantysynova's research groups over decades, with notable contributions from Pellosi [48], Shang [125], Schenk [51], Zecchi [52], Dhar [44], Thiagarajan [54], and Pellegri [46]. The major inspiration of this work is that, while a large effort has been made to improve the modeling of each lubricating interface of EGM, gerotor, and APM considered in the above works, their improvements typically focused on a single interface. In reality, though, the dynamics of the single body reflect in all films it interacts with, and balance is achieved by the simultaneous response of all these films. However because each of the aforementioned models were developed as standalone tools, direct combination of all was not possible. Furthermore, the increased computational demand required to solve all films simultaneously means that care must be taken in the distribution of computational loads. This will imply prioritizing not only fidelity, but also efficiency of a given modeling approach. Considering this, the novel contributions to the distributed parameter modeling are as follows

- Development of the distributed parameter model within the same API as the lumped model, with heavy focus on modularity and parallelizable object-oriented programming. In doing so, a novel strong coupling of the lubricating and lumped parameter models within a single complete simulation is achieved.

- Consideration of the coupled effects of all lubricating films on all related floating body.

- Development of a numerically stable cavitation algorithm for lubricating films.
- Direct integration of this cavitation algorithm with the mixed lubrication model.
- Development of transient FEM and analytical based solutions to the fluid-structure problem.
- Definition of a numerical impedance tensor for the mixed universal Reynolds equation to facilitate asynchronous time stepping of the lumped and distributed domains.

3.1 Universal Flow Solver

The analysis begins with the compressible Reynolds equation for thin films, derived from the Navier-Stokes equations assuming

- a Newtonian fluid
- laminar flow such that viscous forces dominate inertial and body forces
- negligible pressure gradient and flow in the film-normal direction

so that the conservation of mass and momentum in the film is governed by

$$\underline{\nabla} \cdot \left(\frac{\rho h^3}{12\mu} \underline{\nabla} p \right) = \underline{\nabla} \cdot (\rho h \underline{v}) + \frac{\partial \rho h}{\partial t} \tag{3.1}$$

As was mentioned in Section 2.1, there are many possible ways to model the variation of fluid properties with pressure and temperature. Similar to the lumped parameter model, this analysis will make use of tabulated fluid properties of a typical ISO VG 46 hydraulic oil. If the temperature in the film is allowed to reached a steady value such that isothermal operation can be assumed, then neglecting transients of cavitation, the density is a function only of pressure $\rho = \rho(p)$. Inverting this relation shows that $p = p(\rho)$, which can then be differentiated with respect to an arbitrary quantity ψ

$$\frac{\partial p}{\partial \psi} = \frac{\partial p}{\partial \rho} \frac{\partial \rho}{\partial \psi} \tag{3.2}$$

to relate the change in pressure and density. Using the definition of the isothermal bulk modulus

$$K = \rho \frac{\partial p}{\partial \rho}\bigg|_T \tag{3.3}$$

and substituting this into the original form of Reynolds Equation 3.1, the pressure gradient can be recast as a density gradient to form the universal Reynolds equation

$$\underline{\nabla} \cdot \left(\frac{Kh^3}{12\mu} \underline{\nabla} \rho \right) = \underline{\nabla} \cdot (\rho h \underline{v}) + \frac{\partial \rho h}{\partial t} \tag{3.4}$$

The term 'universal' comes from the fact that, by accounting for density of the bulk mixture properly, the equation can be directly applied in regions of full film and cavitated ruptured film. While it is possible to solve the original Reynolds Equation 3.1 directly, the sharp gradients in fluid properties at the interface of the ruptured film make numerical integration difficult. This is because change in pressure cannot be related to change in fluid properties within a given iteration, and a computationally expensive non-linear implicit solver is required. The benefit of the universal Reynolds Equation 3.4 is the presence of the integrated quantity ρ in each term, yielding a better behaved solution that can be directly updated by a time-march. Furthermore the strongest sensitivity, between pressure and density, is removed for the governing equation leading to more stable behavior of the equation.

In order to implement this approach, though, it is necessary to relate the solution in terms of density to that of pressure to update the fluid properties and for use in the force calculations to follow. To do this, the cavitation/aeration model introduced in Section 2.1.2 is inverted to find pressure for a known density.

Above the saturate density $\rho_{\text{sat}} = \rho(p_{\text{sat}})$, the pressure-density relationship is given directly by interpolation of the same tabulated fluid properties used in the LP model. Below this pressure, the volume occupied by the bulk fluid is given by the liquid and undissolved gas components. As was demonstrated in Figure 2.4(a), small changes in pressure in this region will lead to large changes of the bulk fluid properties. These changes, however, are due primarily to the highly compressible gas, and therefore the change in density of the liquid is negligible. Considering this, the fluid density

is fixed at its value at saturation $\rho_{l0} = \rho(p_{\text{sat}})$. As was proven success in [29, 93, 95], the transient of the release of dissolved gas is neglected, where instead Henry-Dalton equilibrium equation is used to model the asymptotic behavior of the bulk fluid in the differential volume dV. While the more detailed approaches discussed for the LP domain are possible for the films as well, their use implies a significant increase in computation time. For this reason, the present work elects to use the lighter-weight equilibrium model over the entire fluid domain, retaining cavitation information while preserving the feasibility of multiple interfaces in a single simulation.

This is further supported by works outside of lumped parameter systems as outlined by Braun and Hannon [83], which find that most forms of cavitation have very short time constants. Furthermore, it concludes that gaseous cavitation typically results in the generation of a stable cavity in the film. While the release of the gas is fast, changes in this stable cavity will be slow. Thus, its expansion can be assumed to be isothermal so that the polytropic index $n_g = 1$. Under these assumptions, the density of the bulk fluid, as derived in Section 2.1.2, is provided with the exception that the liquid density has been treated as constant. This implies that

$$\exp\left(\frac{p_0 - p}{K_l}\right) \approx 1 \tag{3.5}$$

and the bulk fluid density given in Equation 2.17 is simplified to

$$\rho_f = \frac{\rho_{\text{sat}}}{\alpha_{l0} + \chi_u \alpha_{g0} \frac{p0}{p}} \tag{3.6}$$

By inverting this equation, the pressure of the fluid can be expressed as a function of the bulk fluid density

$$p = p_{\text{sat}} \left[\frac{\alpha_{l0}}{\alpha_{g0}} \frac{(p_{\text{sat}} - p_{\text{vap,h}})}{p_{\text{sat}}} \left(\frac{\rho_{\text{sat}}}{\alpha_{l0}\rho_f} - 1\right) + 1\right]^{-1} \tag{3.7}$$

This function is valid only in the range $p \in (p_{\text{vap,h}}, p_{\text{sat}})$, or $\rho_f \in (\rho_{\text{vap,h}}, \rho_{\text{sat}})$, stopping at the points of discontinuity in χ_u. As the entrained gas of the liquid α_{g0} approaches null, and there is not trapped gas, the range $(p_{\text{vap,h}}, p_{\text{sat}})$ narrows so that

the equation is never used. With the pressure known, the bulk modulus can be found by taking the derivative with respect to the bulk fluid density

$$\frac{K_f}{\rho_f} = \left(\frac{\partial \rho}{\partial p}\right)\bigg|_T = \frac{(p_{\text{sat}} - p_{\text{vap,h}})\rho_{\text{sat}}}{\alpha_{g0}\rho_f^2}\left[\frac{(p_{\text{sat}} - p_{\text{vap,h}})(\rho_{\text{sat}} - \alpha_{l0}\rho_f)}{\alpha_{g0}\, p_{\text{sat}}\, \rho_f} + 1\right]^{-2} \tag{3.8}$$

The mass fraction of the undissolved gas can then be related to the void fraction using Equation 2.15, where the density of the gas is given by an expansion to the given pressure as is shown in Equation 2.20.

When the film pressure reaches the vapor pressure, $p \leq p_{\text{vap,h}}$, all the gas has been released and the fluid begins to evaporate. Unlike the case of gaseous cavitation, it was discussed in [83] that the vaporous cavitation component is a very dynamic, transitory phenomenon. In this condition, then, it is not appropriate to treat the gas as isothermal and the compression and expansion of the vaporous bubbles is treated as an isentropic process. If the vaporous working fluid is treated as an ideal gas, Shapiro [126] gives that the kinetic theory of gasses can be applied to state that its ratio of specific heats k_v is related to the degrees of freedom of its molecules

$$k_{\text{ideal}} = 1 + \frac{2}{N_{\text{DOF}}} \tag{3.9}$$

Since hydraulic oil molecules (which are typically used for PD machines) contain long, complex chains of atoms, the molecule will have a very large number of degrees of freedom N_{DOF}. Without information on the exact chemical makeup of the working fluid it is assumed, as is suggested in Shapiro [126], that the ratio of specific heats approaches unity. The ratio of specific heats $k_v \approx 1$ is then taken for this thesis, and similarly its polytropic index $n_v = k_v = 1$. With this, the density is simplified from Equation 2.22, with constant liquid density ρ_{l0},

$$\rho_f = \frac{\rho_{\text{sat}}}{\alpha_{l0}(1-\chi_v) + \frac{\rho_{l0}}{\rho_{v0}}\alpha_{l0}\chi_v\frac{p_{\text{vap,h}}}{p} + \alpha_{g0}\frac{p_{\text{sat}}}{p}} \tag{3.10}$$

Again, this equation is inverted to solve for pressure as a function of fluid density

$$p = \frac{\psi_{v1} + \psi_{v2}\,\rho_f - \sqrt{\psi_{v3}\,\rho_f^2 + 2\psi_{v4}\,\rho_f + \psi_{v1}^2}}{2\rho_f} \tag{3.11}$$

where

$$\begin{aligned}
\psi_{v1} &= \left(p_{\text{vap,h}} - p_{\text{vap,l}}\right)\rho_{\text{sat}} \\
\psi_{v2} &= p_{\text{vap,h}}\left(\frac{\rho_{l0}}{\rho_{v0}}\right) + p_{\text{vap,l}} \\
\psi_{v3} &= \psi_{v2}^2 - 4\left(\frac{\rho_{l0}}{\rho_{v0}}\right)p_{\text{vap,h}}^2 - 4\left(\frac{\alpha_{g0}}{\alpha_{l0}}\right)p_{\text{sat}}\left(p_{\text{vap,h}} - p_{\text{vap,l}}\right) \\
\psi_{v4} &= \rho_{\text{sat}}\left[\left(\frac{\rho_{l0}}{\rho_{v0}}\right)p_{\text{vap,h}}^2 + \left(1 - \frac{\rho_{l0}}{\rho_{v0}}\right)p_{\text{vap,h}}\,p_{\text{vap,l}} - p_{\text{vap,l}}^2\right]
\end{aligned} \tag{3.12}$$

Similar to above, this function is valid only in the range $p \in (p_{\text{vap,l}}, p_{\text{vap,h}}]$ or $\rho_f \in (\rho_{\text{vap,l}}, \rho_{\text{vap,h}}]$. In this region, the bulk modulus can be found by differentiation so that

$$\frac{K_f}{\rho_f} = \left(\frac{\partial\rho}{\partial p}\right)\bigg|_T = \frac{\psi_{v1}^2 + \psi_{v4}\,\rho_f - \psi_{v1}\sqrt{\psi_{v3}\,\rho_f^2 + 2\psi_{v4}\,\rho_f + \psi_{v1}^2}}{2\rho_f^2\sqrt{\psi_{v3}\,\rho_f^2 + 2\psi_{v4}\,\rho_f + \psi_{v1}^2}} \tag{3.13}$$

Finally, when the pressure falls below the low vapor pressure $p \leq p_{\text{vap,l}}$, all liquid has evaporated, and the fluid is comprised of only vapor and gas. In this condition, Equation 3.10 simplifies with $\chi_v = 1$ and

$$\rho_f = \frac{\rho_{sat}}{\frac{\rho_{l0}}{\rho_{v0}}\alpha_{l0}\frac{p_{\text{vap,h}}}{p} + \alpha_{g0}\frac{p_{\text{sat}}}{p}} \tag{3.14}$$

This can then be inverted to find the pressure as a function of density for $p \in (0, p_{\text{vap,l}}]$ or $\rho_f \in (0, \rho_{\text{vap,l}}]$

$$p = \frac{\rho_f}{\rho_{\text{sat}}}\left[p_{\text{vap,h}}\left(\frac{\rho_{l0}}{\rho_{v0}}\right) + p_{\text{sat}}\left(\frac{\alpha_{g0}}{\alpha_{l0}}\right)\right] \tag{3.15}$$

By differentiating this, the bulk modulus is given as

$$\frac{K_f}{\rho_f} = \left(\frac{\partial\rho}{\partial p}\right)\bigg|_T = \frac{1}{\rho_{\text{sat}}}\left[p_{\text{vap,h}}\left(\frac{\rho_{l0}}{\rho_{v0}}\right) + p_{\text{sat}}\left(\frac{\alpha_{g0}}{\alpha_{l0}}\right)\right] \tag{3.16}$$

demonstrating that the bulk modulus is directly equal to the pressure $K_f = p$.

Over the whole operating range, Figure 3.1 shows the varying fluid properties calculated by this model over the cavitated and full film region. First in Figure 3.1(a), the instantaneous bulk fluid density is given, showing the sharp drop as the bubbles begin to release as compared to that of the pure liquid above saturation pressure. The resulting bulk modulus is given in Figure 3.1(b), explaining the sharp drop that

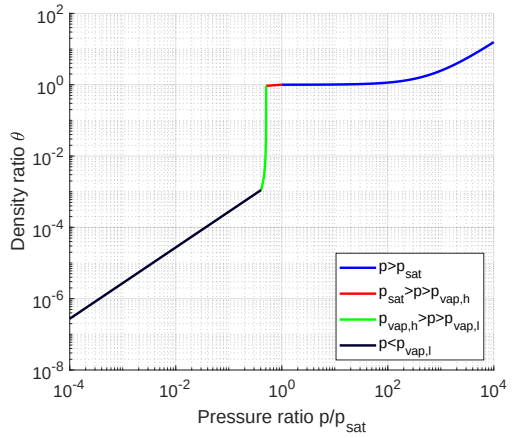

(a) Density Ratio

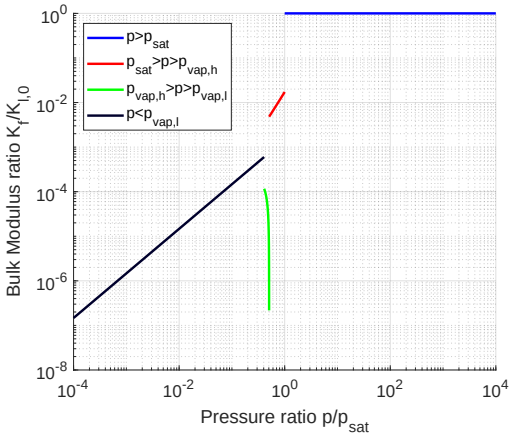

(b) Bulk Modulus Ratio

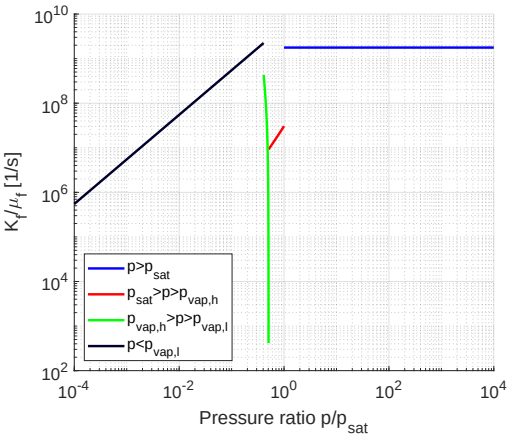

(c) Bulk Modulus to Viscosity Ratio

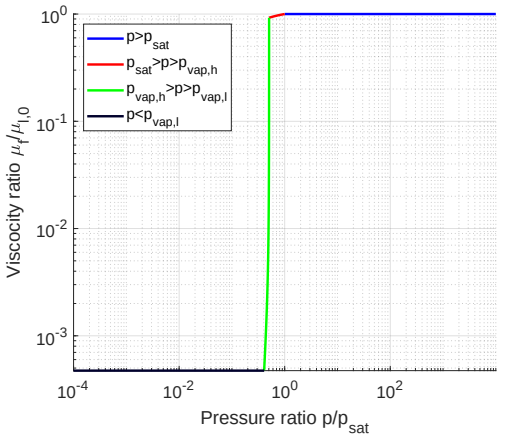

(d) Dynamic Viscosity Ratio

Figure 3.1. Equivalent properties of the bulk fluid for simulation (a) density ratio (b) bulk modulus ratio (c) ratio of bulk modulus to viscosity (d) dynamic viscosity ratio

occurs due to these bubbles. In Figure 3.1(d), the dynamic viscosity calculated with Equation 2.28 is shown. From Equation 3.4, though, it is not this viscosity that defines the diffusive of the density in the film, but rather the ratio of the bulk modulus to this density as is shown in Figure 3.1(c).

Note here that while the bubble release functions $\chi_{u/v}$ are necessary in deriving the model, they result in a 1st order discontinuous derivative of density reflected in Figure 3.1, and thus present an issue for numerical solution. The sharp discontinuities occur when these functions meet, and the slope of the density-pressure curve changes drastically. Physically, these properties describe the effective bulk fluid property, so they describe not only the compressibility of the instantaneous make-up of the fluid but the immediate release and absorption of the gas and vapor within. Therefore, at the transition from one region to the next, the instantaneous rate of release of the gas or vapor changes, leading to discontinuity in the rate of change of properties of the bulk fluid. Furthermore, this leads to a drastic drop in fluid properties starting at p_{sat} of many orders of magnitude, disabling the pressure (density) driven flow terms Equation 3.4 with respect to the shear flow terms. Since this drop must occur exactly at the point of film rupture, it is this property of the model that allows the scheme to inherently respect the JFO boundary conditions. In order to overcome the discontinuity, previous works including [29, 94] have approximated the functions with higher order continuous polynomials. In this work, however, hyperbolic tangent blending functions are used to smoothly transition the otherwise discontinuous properties from one formulation to the next. This achieves the effect of maintain physical accuracy, with only local deviation to accommodate numerical solution.

With the fluid model defined, Figures 3.2-3.4 demonstrate the behavior of each term of the Reynolds equation, comparing the results of the compressible and incompressible Reynolds to motivate the choice of compressible fluid. The incompressible form is recovered from Equation 3.1 by assuming ρ constant such that it drops from all terms. To consider cavitation in this case, it is common [90] to saturate pressure at the point where cavitation begins, effectively imposing the Reynolds boundary condition at the edge of film rupture

$$\left.\frac{\partial p}{\partial n}\right|_{p=p_{\text{sat}}} = 0 \tag{3.17}$$

In the analysis to follow, the incompressible form of the equation will hold density and viscosity constant, applying pressure saturation in regions of pressure $p < p_{sat}$.

This will be compared to the fully compressible form, with fluid properties tabulated for the typical ISO VG 46 oil demonstrated in Figure 3.1 that would be used in these PD units. In either, fixed pressure boundaries are applied to either side of the 1D film, with the different cases created by manipulating the shape and velocities of the bodies.

In a uniform parallel gap, or one without relative body motion, pressure simply diffuses from the boundaries as is demonstrated in Figure 3.2. Notice in the left column that in the absence of cavitated pressures, the resulting pressure profiles are almost identical for compressible and incompressible, with the slight change in density for the compressible case contributing negligible difference. In the right column, however, the case where p_{sat} is reached yields very different results. The issue with this is an apparent sharp gradient out the outlet boundary of the film, causing a significant over-prediction of the flow at the boundary. To this point, in general once pressure saturation occurs the solution no longer conserves mass in the film, which makes its use undesirable for prediction of film leakages.

Pressure generation in these films comes from two forms. First in Figure 3.3, pressure is generated in regions where fluid is dragged into a converging gap. Conversely, pressure drops in regions where fluid is dragged into a diverging gap. Similar to the case of diffusion, there is very little difference in result for the converging wedge; in both cases pressure builds in response to compression of the fluid. A subtle difference in result is found, due to an extra source term via the density wedge $h\frac{\partial \rho}{\partial t}$, allowing for slightly more pressure to build as compared to the incompressible case. This is expected, as the fluid plots in Figure 2.4 demonstrated that the properties change very slowly with pressure above the saturation pressure. Instead in the diverging gap, the pressure saturation approach fails to describe the breakdown of the film, and a flat region of saturation pressure is returned. The issue with this is demonstrated for $x > 0.95$, where the outlet pressure boundary is able to lift the pressure above p_{sat}. By saturating the pressure, the reformulation of the film can happen immediately, when in reality the compressible formulation cannot recover until the last internal

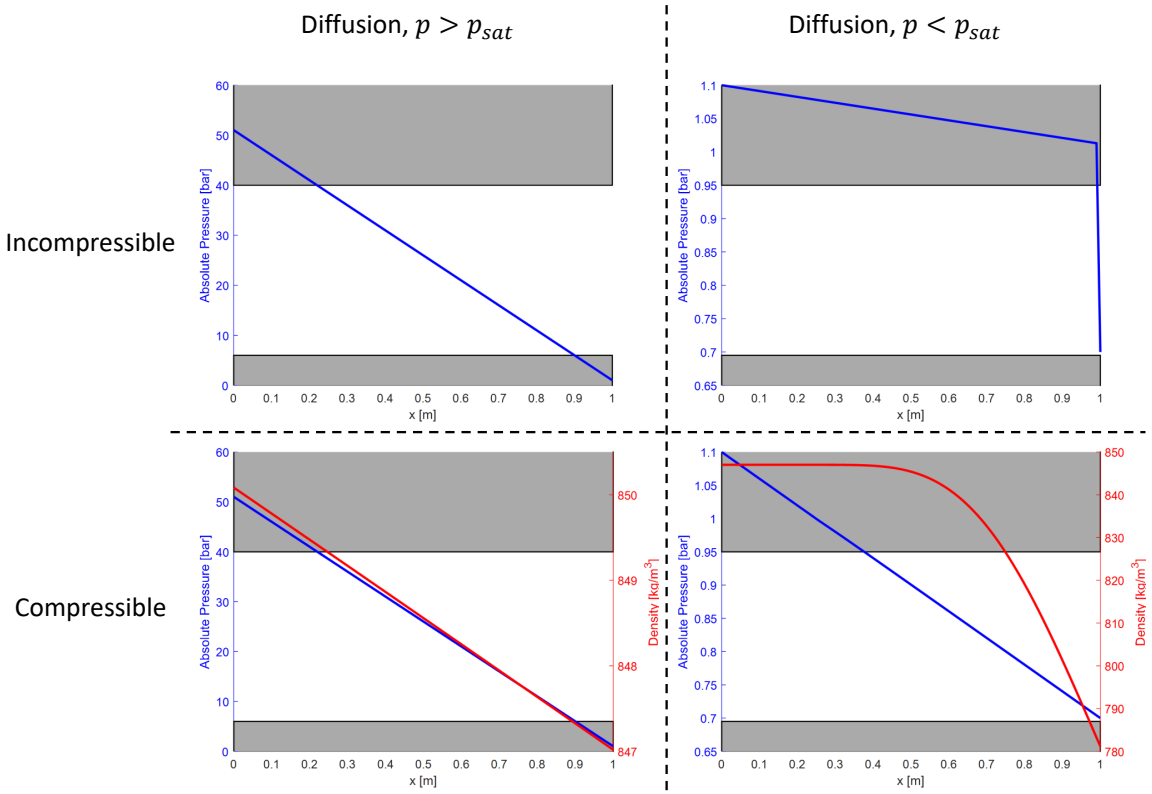

Figure 3.2. Pressure diffusion in an exaggerated parallel gap, comparison of incompressible and compressible Reynolds in cavitated and non-cavitated conditions

element in the mesh. The implications of this observation are the inability of the pressure saturation approach to predict even the shape of the ruptured film, only to warn that cavitation is expected.

The other source of pressure generation comes from squeeze, as is shown in Figure 3.4. For an expanding gap, the same issue discussed above is present, where the film is simply saturated and is not brought further below into regions of low density as is demonstrated in the compressible case. The more extreme example in this case comes from the converging gap, where the incompressible performed well in the other examples. Due to the large gap length, this case is an extreme example of the pitfall of the incompressible Reynolds, namely that the entirety of the displaced mass must be

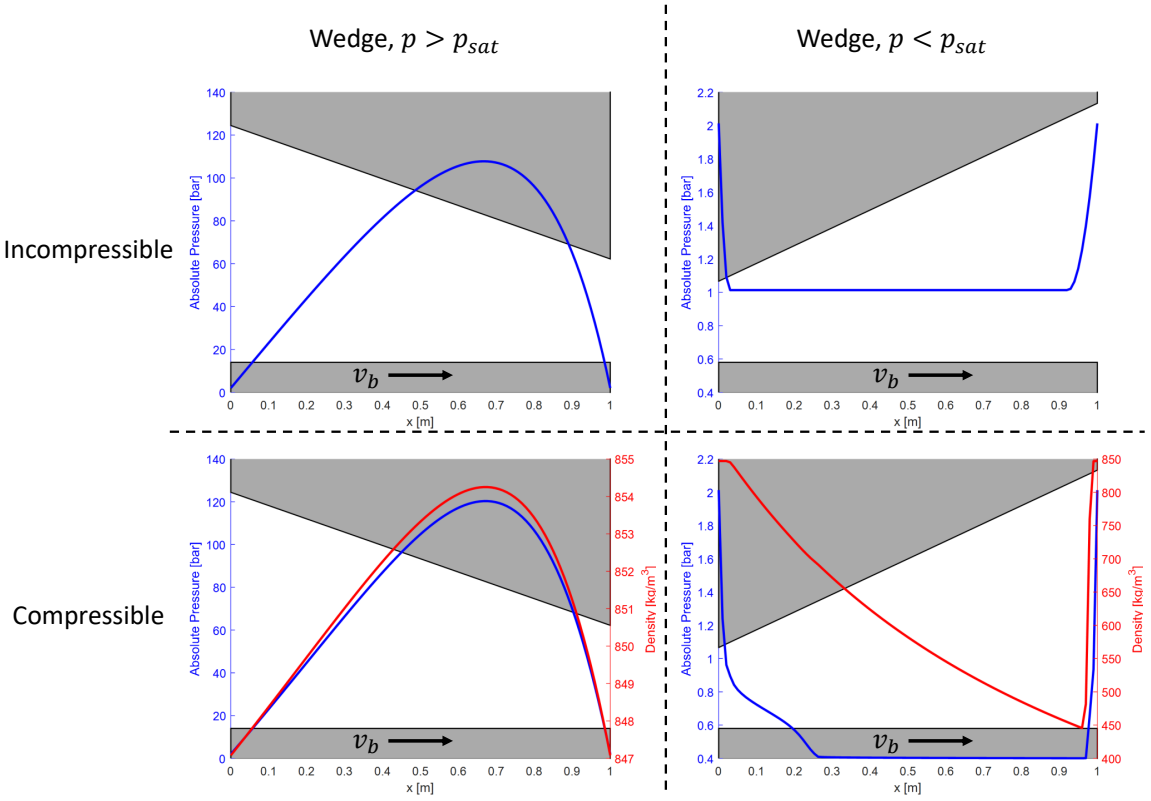

Figure 3.3. Film wedge effects in an exaggerated non-parallel gap, comparison of incompressible and compressible Reynolds in cavitated and non-cavitated conditions

discharged via a pressure driven flow. This requires a large pressure gradient, where the compressible fluid instead allows the density to increase slightly with little effect on the film pressure. This example shows that the incompressible form of Reynolds equation can drastically over-predict the stiffness of film, leading to both unphysical behavior and numerical instability.

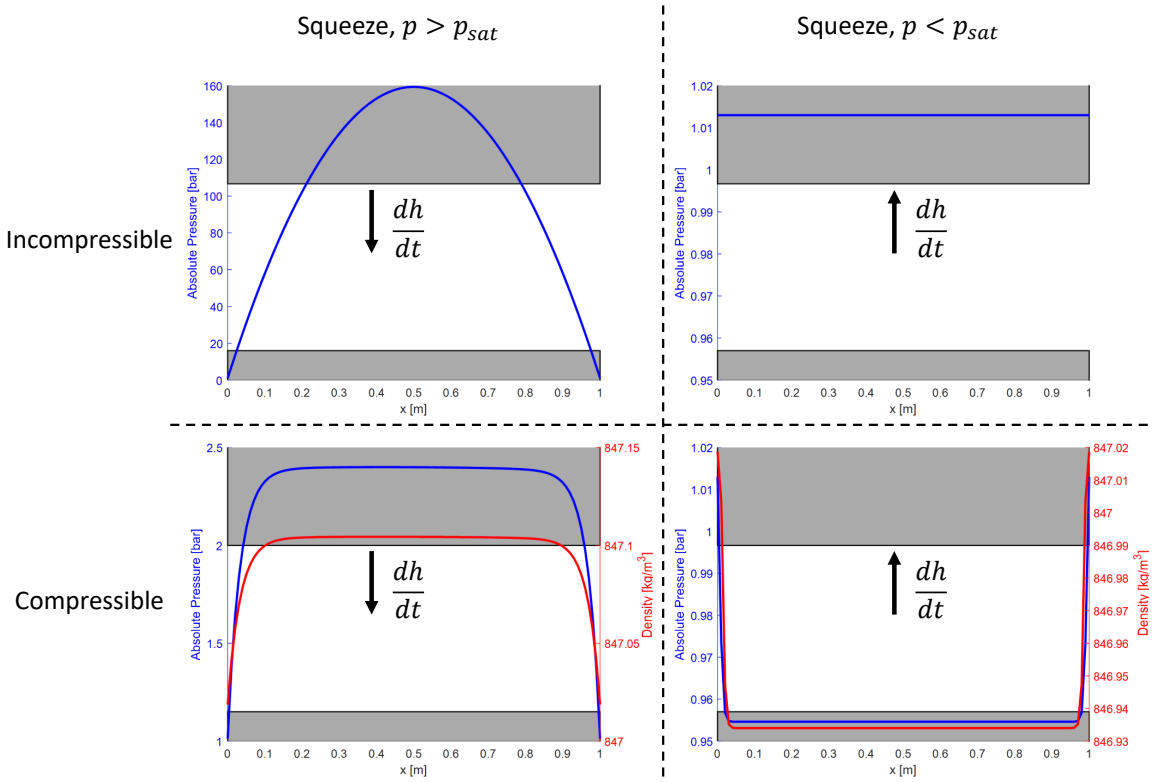

Figure 3.4. Film squeeze effects in an exaggerated translating gap, comparison of incompressible and compressible Reynolds in cavitated and non-cavitated conditions

3.2 Modification for Mixed Lubrication

In reality, the nominal surface smooth expected in design is not realizable in manufacturing. Figure 3.5, taken from Hamrock [90], shows that as the Hersey number (dimensionless velocity) decreases, the hydrodynamic effects become too weak to carry load and the film enters the mixed lubrication regime. In this regime, fluid lubricant is still present in the film, however a portion of the load is carried by direct contact of asperities of the two bodies. If the dimensionless velocity is further reduced, the asperities carry the majority of the load in a regime called boundary friction.

Depending of the manufacturing process used surface finish will vary, affecting the transition across these regimes. As the nominal film approaches the magnitude

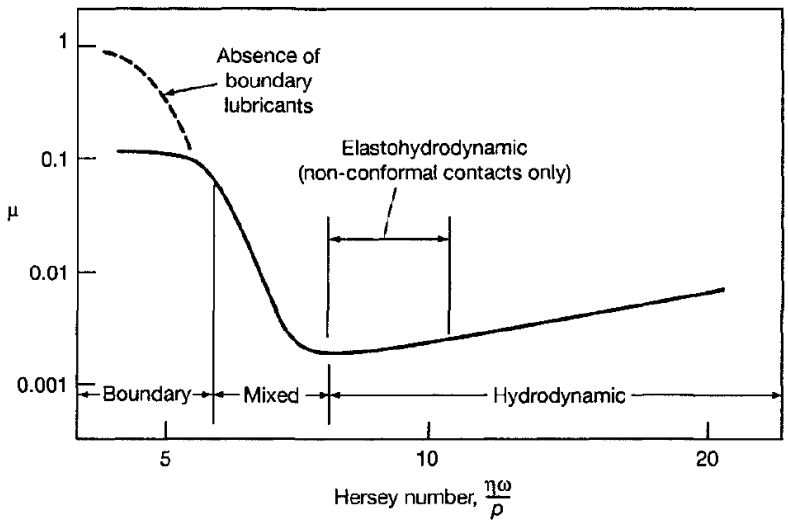

Figure 3.5. Demonstration of the lubrication regimes (from Hamrock [90])

of the roughness, the effects of these surface asperities become non-negligible not only in terms of contact but to the film flows as well. In [53], Thiagarajan and Vacca demonstrated how the application of Patir and Cheng's partial film lubrication model [69,70] allowed for accurate prediction of flow in the lateral lubricating interface of EGMs. As was stated earlier, more detailed deterministic models are available in the state of the art. The use of these models however, requires a fine enough mesh to resolve the individual asperities. This leads to a significantly higher computational cost to model a single film. With the overall goal of including multiple films in a single simulation, then, the present model elects to use the empirical approach developed in [69,70]. This approach retains the ability to capture mixed lubrication effects while maintaining the feasibility of strong coupling.

In the present section, the aforementioned model is extended to the universal Reynolds equation derived in Section 3.1. This analysis begins with the corrected film flow (per unit width) given by Patir and Cheng [69, 70]

$$\overline{\underline{q}} = \overline{\underline{v}}\,\overline{h} + \frac{\phi_s}{2} R_q \left(\underline{v}_t - \underline{v}_b\right) - \underline{\phi}_p \circ \left(\frac{h^3}{12\mu} \underline{\nabla} p\right) \tag{3.18}$$

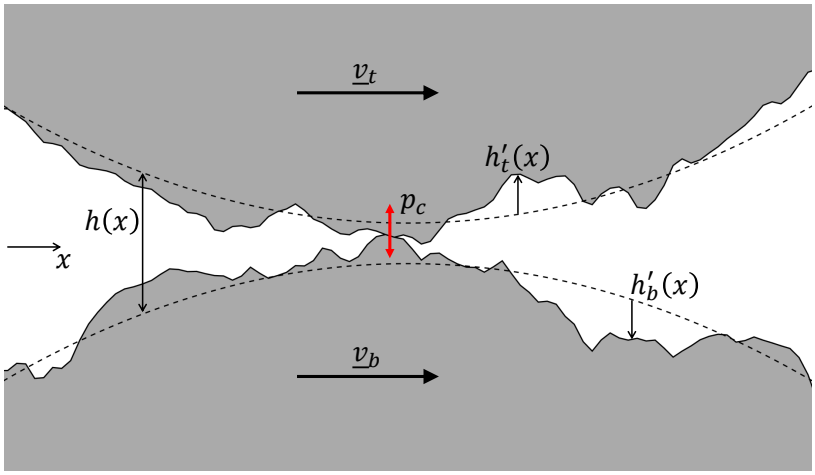

Figure 3.6. Cross section of a rough 2D film, comparing the nominal dashed profile and the real film surface with non-zero roughness

where the pressure flow factors $\underline{\phi}_p$ corresponds to the added flow resistance that is introduced by the fluid turning around the asperities in the two directions, and the shear flow factor ϕ_s accounts for the additional fluid dragged by the asperities.

It is worth noting, aided by Figure 3.6, the distinction between the nominal (smooth) gap distributions of the top and bottom bodies and the averaged gap $\overline{h}$. Here, $\overline{h}$ is the expectation of gap height under the probability density distribution $f_{h'}(s)$ of the asperities on both surfaces

$$\overline{h} \equiv E[h + h_t' + h_b'] = \int_{-h}^{\infty} (h+s) f_{h'}(s) ds \tag{3.19}$$

where the probability distribution of the net gap deviation

$$h' = h_t' + h_b' \tag{3.20}$$

is expressed in terms of the net roughness

$$R_q = \sqrt{R_{q,t}^2 + R_{q,b}^2} \tag{3.21}$$

In order to relate this term to the the rigid gap, then, this integral is expanded so that

$$\overline{h} = \int_{-h}^{\infty} (h+s) f_{h'}(s) ds = \int_{-h}^{\infty} s f_{h'}(s) ds + h \int_{-h}^{\infty} f_{h'}(s) ds \tag{3.22}$$

If only a constant surface velocities and incompressible fluid is considered, there is no need to expressly define this quantity, only its change with nominal gap, leading to the definition of the contact flow factor derived in [71]

$$\phi_c \equiv \frac{\partial \overline{h}}{\partial h} = \int_{-h}^{\infty} f_{h'}(s) dy \tag{3.23}$$

Instead in this approach for an arbitrary film, an expression relating $\overline{h}$ to h is required, leading to the definition of a new roughness flow factor

$$\phi_R \equiv \frac{1}{R_q} \int_{-h}^{\infty} s f_{h'}(s) ds \tag{3.24}$$

so that the two are used to relate the expected and nominal gap via the roughness

$$\overline{h} = \int_{-h}^{\infty} s f_{h'}(s) ds + h \int_{-h}^{\infty} f_{h'}(s) ds = \phi_R R_q + \phi_c h \tag{3.25}$$

Substituting this into 3.18 and multiplying by the fluid density gives the averaged mass flow (per unit depth) as a function only of the nominal gap

$$\underline{\dot{m}} = \rho \underline{\overline{q}} = \rho \underline{\overline{v}} (\phi_R R_q + \phi_c h) + \rho \frac{\phi_s}{2} R_q \left(\underline{v}_t - \underline{v}_b \right) - \underline{\phi}_p \circ \left(\frac{\rho h^3}{12 \mu} \underline{\nabla} p \right) \tag{3.26}$$

From continuity, the divergence of this mass flow must balance the instantaneous rate of change of mass in the control volume (per unit area), and Reynolds equation is recovered accounting for mixed lubrication

$$\underline{\nabla} \cdot \left(\underline{\phi}_p \circ \left(\frac{\rho h^3}{12 \mu} \underline{\nabla} p \right) \right) = \underline{\nabla} \cdot \left(\rho \underline{\overline{v}} (\phi_R R_q + \phi_c h) \right) + \underline{\nabla} \cdot \left(\rho \frac{\phi_s}{2} R_q \left(\underline{v}_t - \underline{v}_b \right) \right) + \frac{\partial \rho \overline{h}}{\partial t} \tag{3.27}$$

Finally applying the pressure-density transformation derived in Section 3.1, and transforming the average gap that appears with 3.25, the universal Reynolds equation with mixed lubrication effects is found

$$\underline{\nabla} \cdot \left(\underline{\phi}_p \circ \left(\frac{K h^3}{12 \mu} \underline{\nabla} \rho \right) \right) = \underline{\nabla} \cdot \left(\rho \underline{\overline{v}} (\phi_R R_q + \phi_c h) \right) + \underline{\nabla} \cdot \left(\rho \frac{\phi_s}{2} R_q \left(\underline{v}_t - \underline{v}_b \right) \right) + \frac{\partial \rho (\phi_R R_q + \phi_c h)}{\partial t} \tag{3.28}$$

To define the pressure and shear flow factors, Patir and Cheng [69, 70] performed detailed simulation of the original Reynolds function as a function of the magnitude and directionality of the surface roughness, at a high enough resolution to resolve

the asperities. Here the directionality of the roughness is given by the ratio of the auto-correlation lengths in the two directions

$$\Lambda = \frac{\lambda_{0.5,x}}{\lambda_{0.5,y}} \tag{3.29}$$

where the auto-correlation length $\lambda_{0.5}$ corresponds to the length at which the auto-correlation of the profile is half of its maximum. From these simulations, empirical relations for the flow factors were extracted. In [53], Thiagarajan and Vacca found that the roughness in the lateral lubrication interface of EGMs was isotropic ($\Lambda = 1$) before and after operation, and well modeled by a Gaussian distribution. Following these findings, this is assumed to be a general observation of lubricating interfaces of PD machines so that the flow factors are given by the empirical relations corresponding to isotropic roughness. For all relations, the flow coefficients are defined in terms of the dimensionless gap height, normalized by the effective roughness of the surface

$$\widetilde{h} = \frac{h}{R_q} \tag{3.30}$$

First the pressure flow factors for an Gaussian distribution are given by [69], which are independent of direction for an isotropic surface so that

$$\phi_{p,x} = \phi_{p,y} \approx 1 - 0.9 \exp\left(-0.56\widetilde{h}\right) \tag{3.31}$$

Similarly from [70], the shear factor of an isotropic surface is defined

$$\phi_s \approx \frac{R_{q,t}^2 - R_{q,b}^2}{R_q^2} \begin{cases} 1.899\,\widetilde{h}^{0.98} \exp\left(0.05\widetilde{h}^2 - 0.92\widetilde{h}\right), & \widetilde{h} \leq 5 \\ 1.126 \exp\left(-0.25\widetilde{h}\right), & \widetilde{h} > 5 \end{cases} \tag{3.32}$$

For a Gaussian distribution of roughness, [71] derived the exact analytical solution to the contact factor. However since the solution contains the error function, a polynomial approximation was provided which is favorable for numerical implementation

$$\phi_c = \frac{1}{2}\left(1 + \mathrm{erf}(\widetilde{h})\right) \approx \begin{cases} \exp\left(0.0401\widetilde{h}^3 - 0.304\widetilde{h}^2 + 0.782\widetilde{h} - 0.6912\right), & 0 \leq \widetilde{h} < 3 \\ 1, & \widetilde{h} \geq 3 \end{cases} \tag{3.33}$$

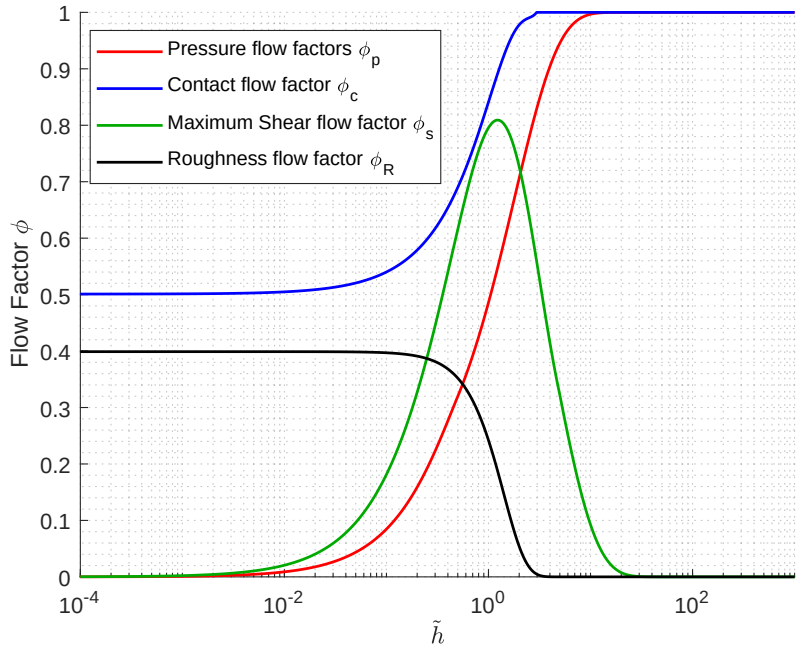

Figure 3.7. Variation of mixed lubrication flow factors with dimensionless gap height, for shear flow taken at its maximum when the bottom surface is smooth $R_{q,b} = 0$ so $R_q = R_{q,t}$

The roughness flow factor defined in 3.24 can be found by substituting the Gaussian probability density function, yielding the exact solution in terms of the dimensionless gap height

$$\phi_R = \frac{1}{R_q}\int_{-h}^{\infty} \frac{s}{\sqrt{2\pi R_q^2}} \exp\left(\frac{s^2}{2R_q^2}\right) ds = \frac{1}{\sqrt{2\pi}} \exp\left(-\frac{\widetilde{h}^2}{2}\right) \tag{3.34}$$

Using these expressions, Figure 3.7 demonstrates the variation of flow factors as a function of dimensionless gap height. This demonstrates that at large gap heights, the flow factors decay such that the original universal Reynolds is recovered. As the gap is decreased, however, these factors accouting for the resulting change in flow behavior accounting for the asperity interaction.

3.3 Fluid-Structure Interaction

As was discussed in [50] as well as [45] for APMs and EGMs respectively, the choice of constraint has a strong effect on the resulting deformation, and therefore pressure, behavior of the film. Therefore, it is important to select the constraint of each body to reflect the true physics of the component. When possible, it is also best to validate the assumption against experimental results.

During operation, the pressures that build in these films can rise well above the operating pressure of the unit. In these conditions, the deformation of the bodies on either side of the film due to these large pressures is not negligible. Furthermore, since the gaps are on the order of microns, similar to the deformation, their inclusion makes significant changes to the gap geometry which alter the resulting film pressure distribution. This forms a fluid-structure interaction (FSI) that must be solved together to accurate reflect the pressure distribution in the film.

Since the goal of this thesis is promote exploration of novel units and working princples, the geometry of the bounding bodies of these interfaces may not be known. For this reason, the present section discusses two modeling options available for use in this tool. First, the deformation of the bodies can be determined using a finite element structural solver in the form of an influence operator. Since this approach requires existing knowledge of the geometry of the bodies, an analytical approximation of this deformation is discussed as an alternative. In either case, the transient response of these bodies is considered here for the first time.

3.3.1 Influence Operator

In the present thesis, the material of the bounding bodies is assumed to be uniform and isotropic, with small strain such that linear elastic behavior can be assumed. The displacement $\underline{u}$ of the relevant film surfaces can be found by imposing mechanical

equilibrium in each body. Neglecting body forces, this is accomplished by setting the divergence of the stress tensor $\underline{\underline{\sigma}}$, a function only of strain $\underline{\underline{\gamma}}$, to zero.

$$\text{div}\left(\underline{\underline{\sigma}}(\underline{\underline{\gamma}})\right) = \underline{0} \tag{3.35a}$$

$$\underline{u}(\underline{x}) = \underline{u}_D \,\forall\, \underline{x} \in \Gamma_D \tag{3.35b}$$

$$\underline{\underline{\sigma}}\left(\underline{\underline{\gamma}}(\underline{x})\right)\, \hat{\underline{n}} = p(\underline{x})\, \hat{\underline{n}} \,\forall\, \underline{x} \in \Gamma_N \tag{3.35c}$$

For arbitrary body, the surface domain Γ_D corresponds to the region of the body where displacement is constrained. Since the body (i.e. the gears or the lateral bushings for EGM; piston, slipper, valve plate, and cylinder block for APM) is fully submerged in the fluid domain, the surface domain Γ_N corresponds to the remainder of the exposed area of the body on which a non-uniform pressure distribution is applied in the surface-normal direction.

Subject to the assumptions outlined above, the linearity of this problem allows its solution to be expressed in terms of solutions of sub-problems with traction boundary (3.35c) split

$$\underline{\underline{\sigma}}(\underline{x})\, \hat{\underline{n}} = \hat{\underline{n}} \,\forall\, \underline{x} \in \Gamma_{n,i}, \tag{3.36a}$$

$$\underline{\underline{\sigma}}(\underline{x})\, \hat{\underline{n}} = \underline{0} \,\forall\, \underline{x} \in \Gamma_N - \Gamma_{n,i} \tag{3.36b}$$

$$\Gamma_N = \cup_i \Gamma_{n,i} \tag{3.36c}$$

so unit pressure is applied to segmented subsets $\Gamma_{n,i}$ of the total surface domain Γ_N. The solution to each of these sub-problems $\hat{\underline{u}}_i$ can then be treated as a basis of the solution space, which scales linearly to describe the deformation for arbitrary pressure applied to its associated segment. Collecting these sub-problems, the exact displacement solution $\underline{u}$ to the original problem can then be determined by superimposing all these basis vectors, scaled by the pressure applied on each segment of Γ_N less the atmospheric pressure p_0 where displacement is defined as zero

$$\underline{u}(\underline{x}) = \sum_i \hat{\underline{u}}_i(\underline{x})\, [p_i - p_0] \tag{3.37}$$

Recording only the surface-normal component of each sub-problem's displacement at discrete points, an influence matrix $\underline{\underline{IM}}$ can be generated. This matrix acts as a deformation map and relates an applied surface pressure on the body to a resulting film deformation Δh by summing over the pressure contribution of each subset of the domain Γ_N

$$\hat{h}_i = \underline{\hat{u}}_i \cdot \underline{\hat{n}} \tag{3.38a}$$

$$IM_{ji} = \hat{h}_i(\underline{x}_j) = \underline{\hat{u}}_i(\underline{x}_j) \cdot \underline{\hat{n}}(\underline{x}_j) \tag{3.38b}$$

$$\Delta h_j = \sum_i IM_{ji} \left[p_i - p_0\right] \tag{3.38c}$$

The creation of this influence matrix can be performed as a pre-processing step, with the results read during simulation instead of being solved online. To find this deformation map a finite element method (FEM) is used, where the solution is expressed in terms of predetermined shape functions $\underline{\underline{N}}$ with unknown degrees of freedom $\underline{d}$. With the assumption of small displacement, the stiffness matrix of the system is constant and each sub-problem defined in Equation 3.36 is given only by a differing forcing vector $\underline{f}_i$

$$\underline{\underline{K}}\,\underline{d}_i = \underline{f}_i \tag{3.39a}$$

$$\underline{\hat{u}}_i(\underline{x}) = \underline{\underline{N}}(\underline{x})\underline{d}_i \tag{3.39b}$$

With the small time steps required to resolve the film behavior, though, the transient of the deformation subjected to a dynamic pressure load cannot be neglected. To account for this, the existing influence matrix approach cannot be applied directly, and the present thesis derives a novel form with consideration of the dynamics of the solid elements. Momentum must still be conserved, where the force balance of Equation 3.35a now considers additional terms related to the inertia and strain rates of the differential element

$$\operatorname{div}\left(\underline{\underline{\sigma}}(\underline{\underline{\gamma}}, \dot{\underline{\underline{\gamma}}})\right) = \rho\ddot{\underline{u}} \tag{3.40}$$

The fixed boundaries and surface tractions remain the same. Considering this, the FEM formulation must be extended to consider the dynamic behavior of the body

with introduction of the mass $\underline{\underline{M}}$ and damping $\underline{\underline{C}}$ of the system. Similar to above, these matrices can be treated as constant due to the assumption of small displacement so that

$$\underline{\underline{M}}\,\ddot{\underline{d}}_i + \underline{\underline{C}}\,\dot{\underline{d}}_i + \underline{\underline{K}}\,\underline{d}_i - \underline{f}_i(t) = 0 \tag{3.41a}$$

$$\hat{\underline{u}}_i(t, \underline{x}) = \underline{\underline{N}}(\underline{x})\underline{d}_i(t) \tag{3.41b}$$

To capture the velocity dependence, Rayleigh damping is applied

$$\underline{\underline{C}} = \alpha\underline{\underline{M}} + \beta\underline{\underline{K}} \tag{3.42}$$

With the assumption of small displacement in the body, it is assumed that the shape of the deformed body is that of the undeformed. Considering this, the mass of the body can be isolated to the separate rigid body dynamics module in Section 2.2.4. Instead it can be assumed here that, due to the magnitude of the pressure loading on the bodies, inertial effects of the solid elements deviating from the rigid solution are negligible. The dynamic system of Equation 3.41a then simplifies to

$$\beta\underline{\underline{K}}\,\dot{\underline{d}}_i + \underline{\underline{K}}\,\underline{d}_i - \underline{f}_i(t) = 0 \tag{3.43}$$

For this simplified system, the instantaneous degrees of freedom of each sub-problem are given by the first order ordinary differential equation

$$\underline{d}_i = \underline{\underline{K}}^{-1}\left(\underline{f}_i(t) - \beta\underline{\underline{K}}\,\dot{\underline{d}}_i\right) = \underline{d}_i^{(\infty)}(t) - \beta\dot{\underline{d}}_i \tag{3.44}$$

Here the term $\underline{d}_i^{(\infty)}(t)$ describes the 'steady' solution at that instant to which the solution tends, evaluated from Equation 3.39a. Slowing the approach to this solution is the damping term $\beta\dot{\underline{d}}_i$. This damping term is then discretized at time step (k) using an implicit backward difference stencil for velocity so that

$$\underline{d}_i^{(k)} = \underline{d}_i^{(\infty)}(t) - \frac{\beta}{\Delta t}\left(\underline{d}_i^{(k)} - \underline{d}_i^{(k-1)}\right) \tag{3.45}$$

Applying Equation 3.41b followed by Equation 3.38a, this relationship can be transformed to describe the evolution of the displacement basis which is then project onto the constant film-normal direction so

$$\left(1 + \frac{\beta}{\Delta t}\right)\hat{h}_i^{(k)} = \hat{h}_i^{(\infty)} + \frac{\beta}{\Delta t}\hat{h}_i^{(k-1)} \tag{3.46}$$

By summing this equation over each sub-problem, Equation 3.38c can be used to transform this into an update of the net deformed gap

$$\left(1+\frac{\beta}{\Delta t}\right)\underline{\underline{IM}}\,\underline{p}_*^{(k)} = \underline{\underline{IM}}\left[\underline{p}^{(k)} - p_0\right] + \frac{\beta}{\Delta t}\underline{\underline{IM}}\,\underline{p}_*^{(k-1)} \tag{3.47}$$

with definition of the 'perceived pressure'

$$\underline{\Delta h}^{(k)} = \underline{\underline{IM}}\,\underline{p}_*^{(k)} \tag{3.48}$$

Note that while this equation draws an analog to the static influence matrix case (Equation 3.38c), this perceived pressure $\underline{p}_*$ no longer corresponds to the instantaneous pressure $\underline{p}$ over the faces of the body. Instead, it embeds the delay in response of the body to a change in loading and only asymptotically approaches the true pressure over the domain. The transient deformation is implemented by updating this perceived pressure vector on each iteration, with Equation 3.48 then used to relate this pressure to the instantaneous film-normal deformation

$$\underline{p}_*^{(k)} = \frac{\underline{p}^{(k)} - p_0 + \frac{\beta}{\Delta t}\underline{p}_*^{(k-1)}}{1+\frac{\beta}{\Delta t}} \tag{3.49}$$

In order to verify this approach, a simplified case study is taken using Ansys Static/Transient Structural. The relevant details of this study are given in Table 3.1. As was discussed above, the rigid body translation of this body is accounted for in the rigid body dynamics module, and so this loading condition is designed such that the body's center of mass is fixed. This solid foundation loading condition is demonstrated in Figure 3.8(a), where the bottom face of the body is fixed. Over a small portion of the top face, a uniform 10 MPa pressure is applied. Note that the study of one pressure segment is sufficient, as the superposition property discussed above means that more complex pressure loading will follow this same behavior.

For the giving loading condition, the same study was run in both Ansys Static Structural and Transient Structural. The resulting face-normal deformation of the body is demonstrated in Figure 3.8(b). First, this case was run in Static Structural with linear-elastic steel as the material using the small strain solver. These results

Table 3.1.
Transient deformation case study parameters

Density	7850 kg/m^3
Young's Modulus	200 GPa
Poisson's ratio	0.3
Rayleigh Damping Coefficient β	10^{-4} s
Patch Offset L_{off}	3 mm
Patch Length L_{p}	7 mm
Foundation Length L_{fnd}	40 mm
Patch Depth b_{p}	8 mm
Foundation Depth L_{fnd}	20 mm
Foundation Height h_{fnd}	5 mm

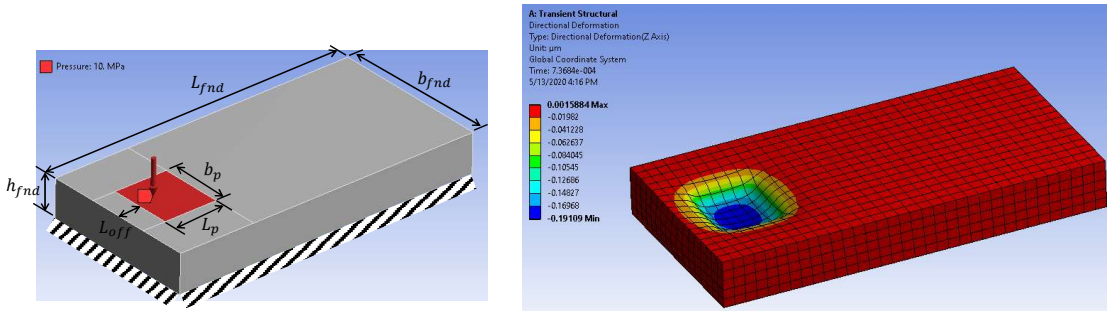

(a) Loading Condition

(b) Resulting Deformation

Figure 3.8. Transient deformation case study in Ansys (a) Loading and boundary conditions of object (b) resulting deformation

then correspond exactly to the $\underline{\underline{IM}}$ operator of this problem. This same problem was then repeated in Transient Structural, using typical parameters for constant Rayleigh damping for the steel material used here. By using these same parameters with the $\underline{\underline{IM}}$ and Equation 3.48, Figure 3.9(a) compares the maximum deformation

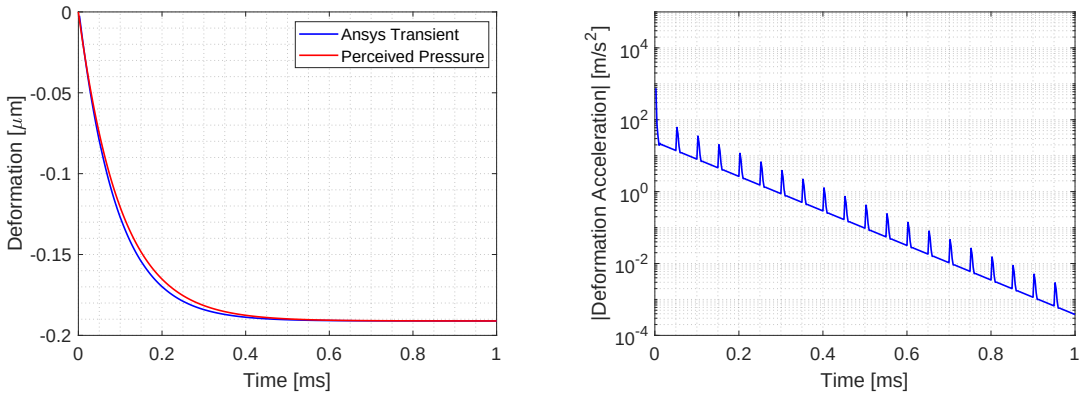

(a) Transient Deformation

(b) Material Acceleration

Figure 3.9. Transient deformation results comparison (a) Maximum Deformation (b) Material Acceleration

that results in each case. While the entire surface domain follows this same trend, only this maximum deformation point is plotted for clarity.

The figure highlights the ability of the perceived pressure approach to capture the deformation curve attained from detailed transient simulation without the additional storage and computational expenses. While the settle time of the curves are identical, there is some slight deviation in the trajectory of the point. To explain the slight disagreement, Figure 3.9(b) includes the acceleration of the solid element (neglected in the perceived pressure approach) at this maximal point given by the Ansys Transient simulation. This figure demonstrates that in reality, the solid elements are inertial and experience some acceleration. For reference in this problem, the norm of the mass matrix $|\underline{\underline{M}}|_2 = 4.6$, while the norm of the stiffness matrix is $|\underline{\underline{K}}|_2 \sim 10^{12}$. Thus while there is a relative large acceleration of the bodies, the shear and stiffness of the problem are dominant and thus this acceleration contributes only a slight deviation to the resulting trajectory of the elements. With this result as demonstration, the approximation of the perceived pressure approach is acceptable.

The limitation of the influence matrix approach comes from both the numerical and computational point view. First, the solid domain can typical be resolved by a mesh that is far coarser than that required for the fluid domain. In order to map the pressure of the film to the solid domain, then, an interpolation must be performed. Once the deformations at the solid body are found, they must be again interpolated to map back to the fluid domain. As a result, this approach requires an additional 2 (likely sparse) matrix-vector multiplications

$$\underline{\Delta h}^{(k)} = \underline{\underline{Q}}^{(k)^{-1}} \underline{\underline{IM}}\, \underline{\underline{Q}}^{(k)}\, \underline{p}_*^{(k)} \tag{3.50}$$

Furthermore, the interpolation errors introduced compound on the error of the solution. Since this influence matrix is dense, but typically with much coarser than the fluid domain discretization $N_{\text{fluid}} > N_{\text{solid}}$, it is not advantageous to combine these three matrices due to the added computational and memory demands. For example the present thesis uses linear barycentric interpolation, so the resulting density of the interpolation matrix is very low for reasonably large solid domain. The interpolation matrix density for an interpolant requiring k entries is given by

$$\rho_Q = \frac{kN_{\text{fluid}}}{N_{\text{fluid}}N_{\text{solid}}} = \frac{k}{N_{\text{solid}}} \ll 1 \tag{3.51}$$

with linear barycentric interpolation requiring $k = 3$ neighbors. For clarity, it is pointed out that the inverse of this matrix need not be computed directly, nor does a linear system need to be solved. Instead, the reverse interpolation matrix is formed as a seperate interpolation matrix, which is then equally sparse. Since linear interpolation is used in both matrices, the solutions are consistent across domains. The benefit of keeping the interpolation matrices separate is the ability to perform the influence calculation in $\mathcal{O}\left(2\rho_Q N_{\text{fluid}}^2 + N_{\text{solid}}^2\right)$, as opposed to $\mathcal{O}\left(N_{\text{fluid}}^2\right)$ for the merged matrices, when the operations are optimally ordered. Note that in practice, these interpolation matrices need not be formally constructed and change with time. In the present thesis, this is accounted for by directly integrating these interpolation operations into the perceived pressure and gap updates.

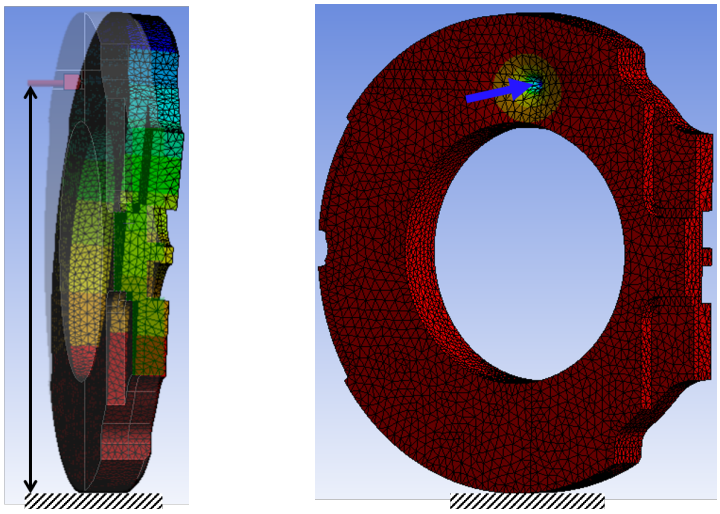

(a) Bending (b) Micro Deformation

Figure 3.10. Cantilever Plate effect of LP constraint boundary condition of lateral balancing element of Ref E2 EG (a) Macroscopic bending (b) Local (Micro) deformation

3.3.2 Analytical Approximation

While this approach is useful for simulations of an existing unit, it is a rigid constraint for a designer attempting to develop a new unit. In effect, the designer must develop the entire assembly of the unit before beginning to design the key interfaces. As a solution, this thesis presents an alternate approach by observing that the influence matrix captures two compounding effects, namely the local (micro) and global (macro) effects of a fluid pressure applied to the surface of a body. This is demonstrated qualitatively in Figure 3.10(a), where the pressure acts at a distance from the constraints of the body inducing a bending of the body. Locally, the pressure applies an added deformation of the region in direct contact with the pressure as is shown in Figure 3.10(b).

Macro Deformation

Considering first the macro deformation, the example of the lateral plate is continued, using Figure 3.10 as reference. As will be demonstrated in Section 3.4.4, the radial force imbalance on the plate tends to enforce a fixed constraint at the interface of the low pressure side of the casing. Hence, the plate can be approximated as a cantilever rectangular plate of the same nominal thickness. While the geometry of a rectangular plate varies from that of the lateral balancing plate, the shear forces in the corners are zero and since body forces are neglected, this material has no effect on the solution. Here is is assumed that the plate is thin, such that the $x-y$ planar displacements can be neglected, and that the z displacement is a function only of x and y. The displacement of the plate's neutral plane to the applied forces and moments can then be related to the flexural rigidity D of the plate. This equation can be seen as the extension of the 1D Euler-Bernoulli beam to the planar deformation of the thin plate

$$\begin{bmatrix} M_x \\ M_y \\ M_{xy} \end{bmatrix} = D \begin{bmatrix} 1 & \nu & 0 \\ \nu & 1 & 0 \\ 0 & 0 & (1-\nu) \end{bmatrix} \begin{bmatrix} \frac{\partial^2 u}{\partial x^2} \\ \frac{\partial^2 u}{\partial y^2} \\ \frac{\partial^2 u}{\partial x \partial y} \end{bmatrix} \tag{3.52}$$

As was discussed Shin and Lee [127], expression of the exact solution of this problem is difficult for arbitrary loading. Following their findings, a 0-th order approximation of the plate bending is taken, where symmetry is assumed and the dependence on the deformation along the x direction (as defined in Figure 3.11(a)) is neglected, so that displacement u_z is a function only of y. Considering this, the problem breaks down to a 1D Euler-Bernouli beam, governed by

$$w(x) = \frac{d^2}{dx^2}\left(EI_{xx}\frac{d^2 u_z}{dx^2}\right) \tag{3.53}$$

In order to solve for this bending, all pressures that act on the plate are collected into applied forces by their application area. They are then resolved into point forces acting at the centroid $y_{c,i}$ of the given application area, inducing a bending of the plate. Due to linearity of the problem, the net deformation is directly given by the

sum over all of these individual point forces, and more complex considerations are avoided. The solution to this equation, for the case of the cantilever beam with arbitrary point loading, and $u_Z(r_{\text{plate}}) = \frac{d}{dz}u_Z\big|_{r_{\text{plate}}} = 0$, is

$$u_z(y) = \sum_i^{N_f} \left[\frac{A_i p_i}{6E\psi_I \overline{I}_{xx}} \begin{cases} (r_{plate} - y)^2(2r_{plate} + y - 3y_{ci}) & y > y_{c,i} \\ (r_{plate} - y_{ci})^2(2r_{plate} + y_{ci} - 3y) & y \leq y_{c,i} \end{cases} \right] \tag{3.54}$$

Observe here the presence of a factor $\psi_I < 1$ which acts to decrease the flexural rigidity of the plate. The purpose of this is two-fold; first Figure 3.11(b) demonstrates that the nominal cross-section of the beam varies along its length due to its circular shape and the existence of bores for the shafts. Furthermore, Figure 3.10 demonstrates how the given cross-section of the plate is not rectangular, with recessed machined into the plate to direct flow and retain seals. This factor is specific to the geometry of the plate but, as is demonstrated in Figure 3.10, is preserved with change in both material properties and load magnitude and location, so the resulting relation can be used in place of a more detailed FEM approach. To demonstrate the feasibility of this approach, the same loading condition was considered with both Ansys Static Structural (Figure 3.10(a)) as well as the macro-def approach discussed here.

This comparison is given in Figure 3.11(a). For the numerical result, the deformation at each node is plotted as a single point, demonstrating that the deviation from the analytical curve is small and follows the trend of the analytical solution. The highest deviation occurs in the y-region which includes the bore, but the approximation is demonstrated to be reasonable even there.

A similar analyse is performed for the gears, where again a 0-th order approximation is used to model the gears as a simply supported beam. Based on the location of the pressure peak of the Reynolds film, the point of application of a pin and roller on the gear is adjusted, as well as a distributed load from the TSV pressures. This loading condition is demonstrated in Figure 3.12.

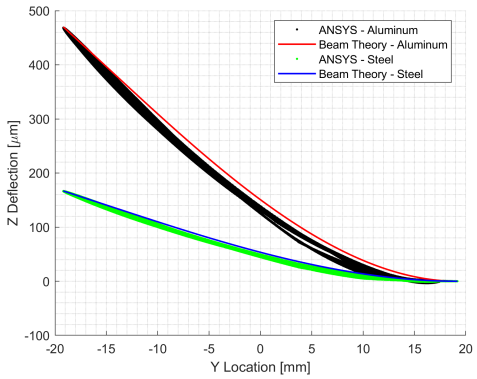

(a) Comparison of numerical FEM and analytical deflection

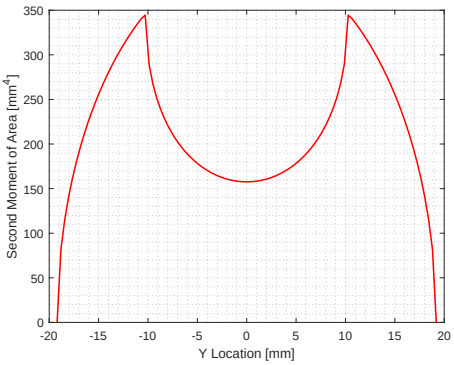

(b) Second Moment of area of nominal rectangular plate cross-sections

Figure 3.11. Plate bending considerations with (a) comparison of numerical simulation and analytical approximation of plate deflection (b) demonstration of second moment of area variation along plate

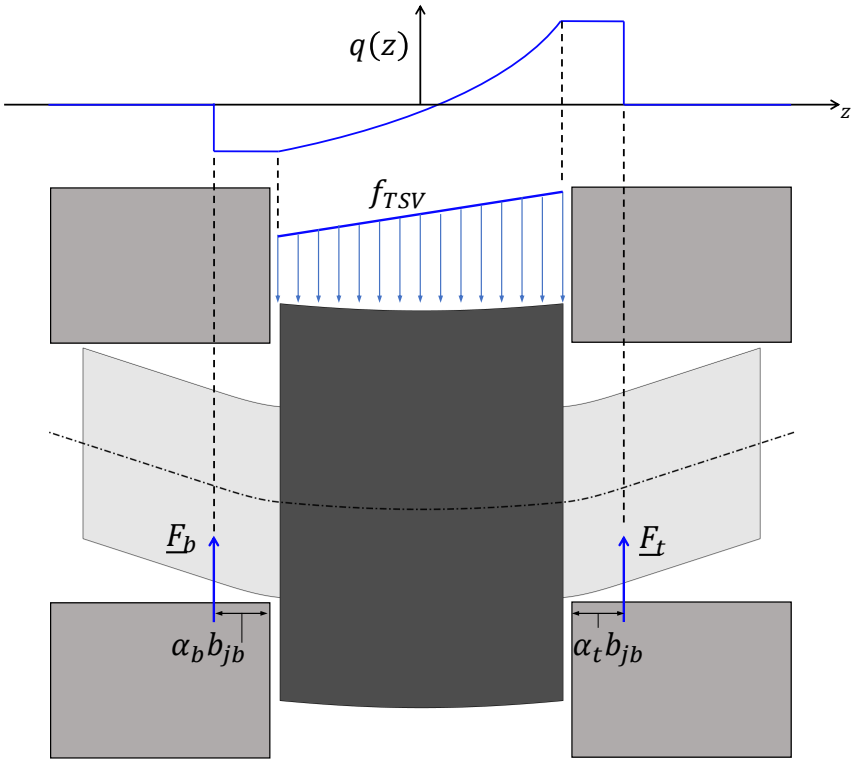

Figure 3.12. Simply support effect of journal bearings and gears of EGM, with 1000x exaggerated effect of macro-deformation on resulting gear shape

Micro Deformation

For the local effects, it is assumed that the micro-deformation is much smaller than the length scales of the bodies. In this condition, with the global effects removed, the micro-deformation caused by each element can be modeled as a uniform pressure applied to a differential area of an infinite elastic half-space. This is demonstrated in Figure 3.13 for two possible material configurations.

First in Figure 3.13(a), the case of a single material is demonstrated, where the film pressure acts directly on the elastic half space. In this case, the influence of the i^{th} element's pressure, with size Δx_i by Δy_i, on the surface deformation of the j^{th} element ofset from i by $\langle x_j, y_j, 0\rangle$ is reported in Johnson [121] and originally published by Love [128]

$$\begin{aligned}\Delta h_j = \frac{p_i}{2\pi E^*}\Bigg[&(2x_j+\Delta x_i)\ln\left(\frac{(2y_j+\Delta y_i)+\sqrt{(2y_j+\Delta y_i)^2+(2x_j+\Delta x_i)^2}}{(2y_j-\Delta y_i)+\sqrt{(2y_j-\Delta y_i)^2+(2x_j+\Delta x_i)^2}}\right)\\ &(2y_j+\Delta y_i)\ln\left(\frac{(2x_j+\Delta x_i)+\sqrt{(2y_j+\Delta y_i)^2+(2x_j+\Delta x_i)^2}}{(2x_j-\Delta x_i)+\sqrt{(2y_j+\Delta y_i)^2+(2x_j-\Delta x_i)^2}}\right)\\ &(2x_j-\Delta x_i)\ln\left(\frac{(2y_j-\Delta y_i)+\sqrt{(2y_j-\Delta y_i)^2+(2x_j-\Delta x_i)^2}}{(2y_j+\Delta y_i)+\sqrt{(2y_j+\Delta y_i)^2+(2x_j-\Delta x_i)^2}}\right)\\ &(2y_j-\Delta y_i)\ln\left(\frac{(2x_j-\Delta x_i)+\sqrt{(2y_j-\Delta y_i)^2+(2x_j-\Delta x_i)^2}}{(2x_j+\Delta x_i)+\sqrt{(2y_j-\Delta y_i)^2+(2x_j+\Delta x_i)^2}}\right)\Bigg]\end{aligned} \tag{3.55}$$

While singularities exist in this solution at the corners of the pressure indenter, this is harmless by definition of the pressure application area. By placing the edges of the area directly between adjacent elements, information will never be required at these points.

For some films, such as the journal bearings of an EGM or the piston-cylinder interface of an APM, Figure 3.13(b) shows how N_{layer} finite thickness layers of elastic material are added to the half space to capture the bushings pressed into these interfaces. Due to lack of availability of a model for rectangular loading, the solution derived in [129] is used, which relates the surface deformation to a circular loading of

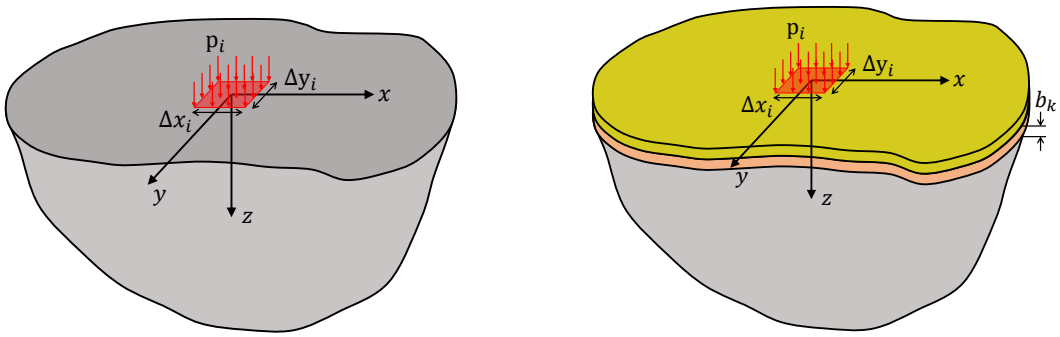

(a) Single Material (b) Multi-Material Finite-Layered

Figure 3.13. Local deformation domain for with rectangular pressure applied by mesh element for (a) continuous single material elastic half space (b) finite thickness elastic material layers on top of an infinite elastic half space

uniform pressure, which propagates though a set a finite thickness elastic layers before reaching the elastic half space. The surface deformation is given by the analytical relation given by [129], where the radius of the circular region is selected to satisfy the net area of the application point. The radius is mapped to an elliptic region to take account of the aspect ratio of the rectangle

$$u_{z,i}(x,y) = -p_i \Delta r_i \int_0^\infty \frac{D_0}{s} J_1(s\Delta r_i) J_0\left(s\Delta r_i \sqrt{\left(\frac{x}{\Delta x_i}\right)^2 + \left(\frac{y}{\Delta y_i}\right)^2}\right) ds \tag{3.56}$$

where

$$\Delta r_i = \sqrt{\frac{\Delta x_i \Delta y_i}{\pi}} \tag{3.57}$$

and J_i is the i^{th} order Bessel function of the first kind. Since this integral is poorly behaved for numerical integration, the MATLAB toolbox given in [130], based on Lucas's algorithm [131] for integrating indefinite integrals of products of Bessel functions, is adapted. This toolbox uses adaptive Gauss-Kronrod quadrature to evaluate the integral with piece-wise simplifications. Observe here that the response to a unit

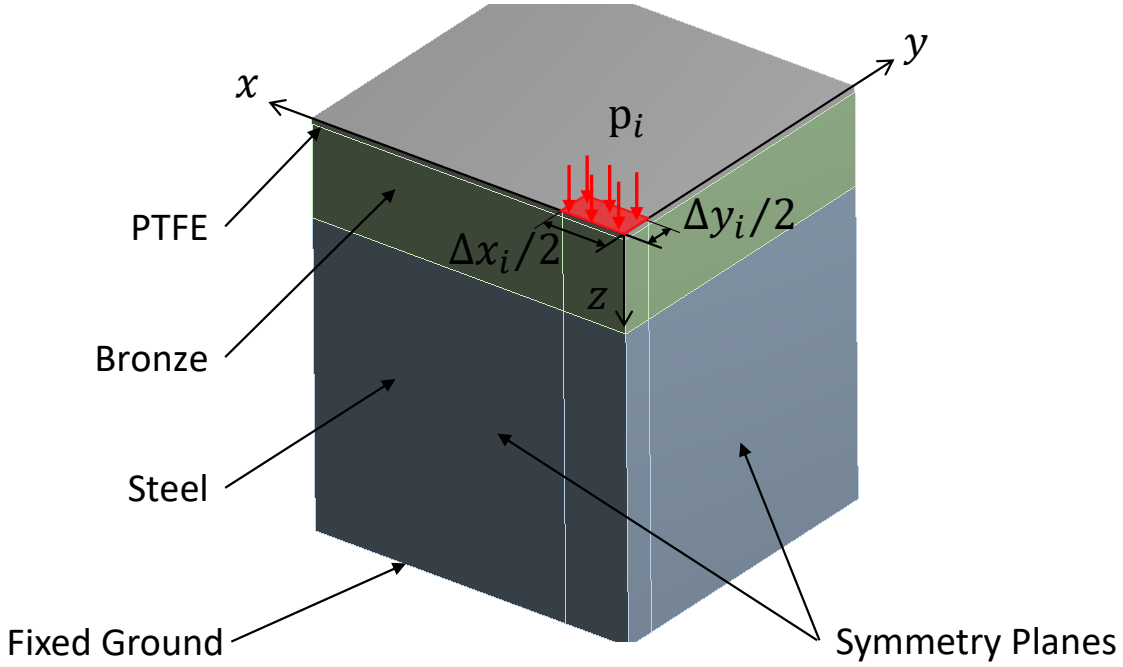

Figure 3.14. Numerical deformation sample for local deformation effects

force is still linear with pressure, and these indefinite integrals must be evaluated only during a heavy pre-processing phase and do not impact online simulation time.

To confirm these analytical expressions, the bushing of an EGM or APM is taken as reference. These bushings are typically pressed into a bore in the machine, made up of a thick steel retainer holding a soft bronze that is lined with PTFE. Assuming that the deformations are small, the PTFE is treated as elastic, so that the bushing can be treated 3 finite elastic layers on top of an elastic space that is the bore it is pressed into. For validation, the resulting deformation is compared to a numerical sample of deformation, evaluated using Ansys Static Structural, the loading of which is demonstrated in Figure 3.14. For the case of uniform material, the steel and PTFE are replaced with bronze so that the same sample is used but with uniform properties.

With these results, the agreement between the analytical and numerical solutions is given in Figure 3.15. These results show a perfect match, as expected, between

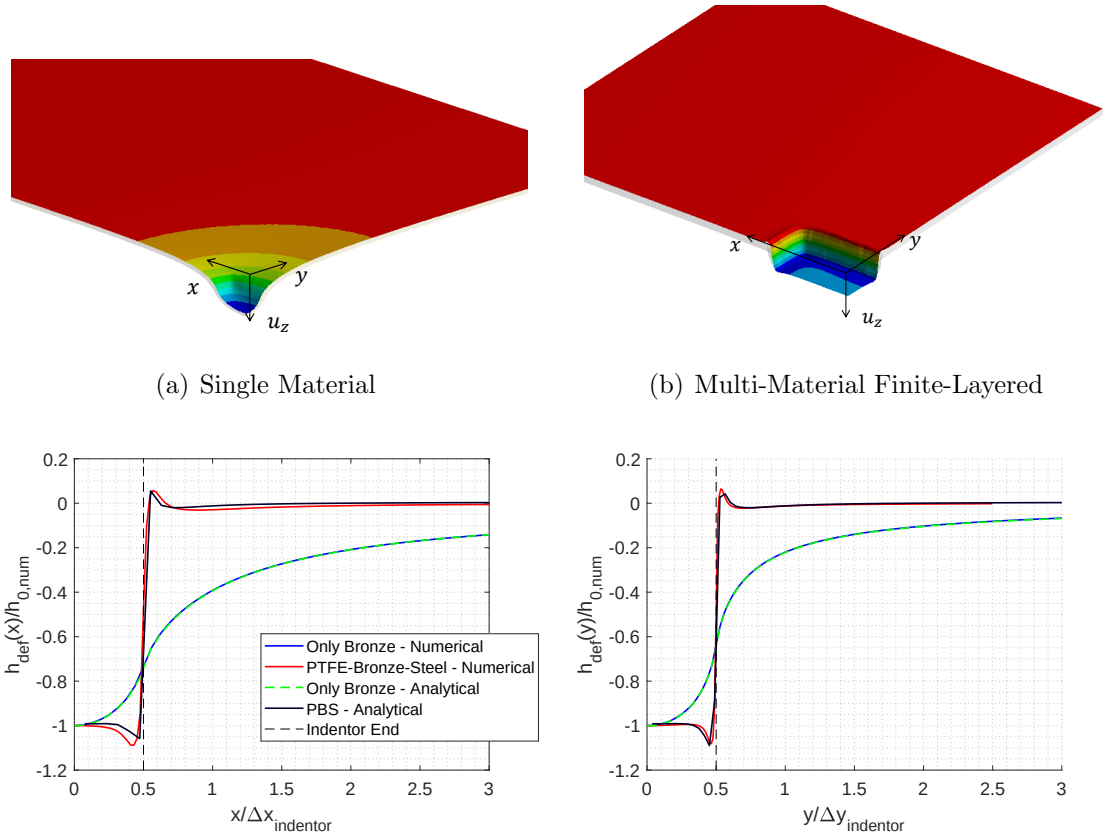

(a) Single Material

(b) Multi-Material Finite-Layered

(c) Displacement along y=0 edge

(d) Displacement along x=0 edge

Figure 3.15. Local surface displacement results for rectangular pressure applied by mesh element for (a) continuous single material elastic half space (b) finite thickness elastic material layers on top of an infinite elastic half space (c) deformation along y=0 edge (d) deformation along x=0 edge

the analytical and numerical solutions of the single material case. This is trivial, however, because both solve the same elastic equations and thus must return the same result. For the multi-material solver, though, this figure demonstrates that the use of an equivalent circular loading is sufficient to capture not only the magnitude of the deformation, but also the overshoot after the application area and resulting rapid decay. Note here that each curve is normalized by the maximum deformation predicted by the numerical case so that the curves can be better compared.

As was mentioned for the first FSI option, storage and usage of an $\mathcal{O}\left(N_{fluid}^2\right)$ matrix is cumbersome. Instead, it is observed that by isolating only the local effects, nodes far from the point of application show negligible micro-deformation. Considering this, entries whose influence are significantly smaller than the norm of the matrix are neglected

$$IM_{ij} = \begin{cases} IM_{ij}, & |IM_{ij}| \geq \varepsilon ||IM||_\infty \\ 0, & \text{Otherwise} \end{cases} \tag{3.58}$$

The result is a banded matrix with sparsity of around 80-90%, corresponding to a significant decrease in the computational load with indistinguishable difference in result. The limitation of this approach comes from the fact that the macro deformation must be given by an analytical solution. While this can be solved by extracting an empirical curve from more detailed FEM modeling, this approach inherently risks to introduce model simplifications that alter the result. Similar to the influence matrix case, the transients of the solid response is accounted for with application of the perceived pressure discussed in Equation 3.48.

3.4 Strong Coupling

To solve the distributed parameter model developed above, the domain is discretized using finite difference for the three fundamental domains that can occur in these machines. Though most PD machines rotate and therefore have circular regions in relative motion, the radii are typical significantly larger than the gaps ($L, b \ll h$) and can be modeled with the Cartesian domain (e.g. EGM tooth tips) demonstrated in Figure 3.16(a). Next in 3.16(b), annular gap geometry is common due to the existence of drive shafts and pistons in these machines, with thin films in the radial direction to maintain sealing. In this thesis, the annular film is unwrapped and treated as a special case of a periodic Cartesian domain. Finally 3.16(c) shows a flat circular film in cylindrical coordinates which, as was mentioned above, is very common in

(a) Cartesian Film

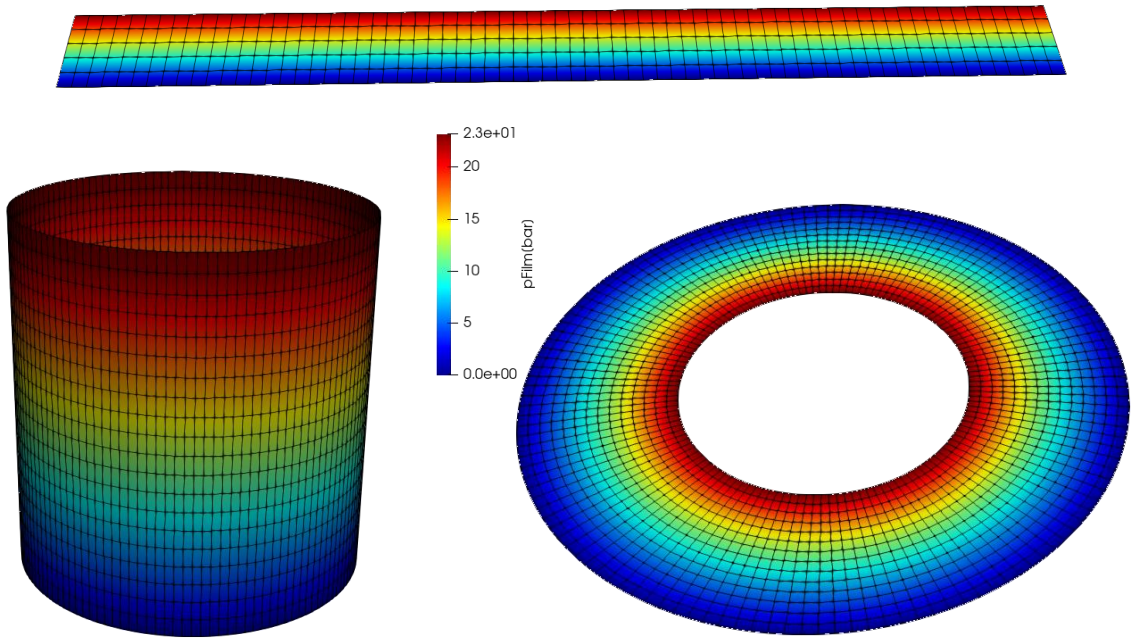

(b) Unwrapped Film

(c) Cylindrical Film

Figure 3.16. Fundamental film types for distributed parameter modeling (a) a flat Cartesian film (b) annular film which is unwrapped to a Cartesian domain (c) a flat cylindrical film in cylindrical coordinates

rotating PD machines. For each, non-uniform structured meshes are automatically generated, starting with all elements treated as internal elements that must be solved.

In order to account for the boundary conditions, which cause these films to deviate from their nominal shapes, elements are removed from the internal field. In doing so, they are no longer solved in that iteration of the Reynolds film update. To ensure that the film model can capture any PD machine, the profile of these boundaries is taken in the form of an arbitrary polygon. For simple geometry, such as a grooved journal bearing, this polygon does not vary with time. For other more complicated film geometries, like the lateral lubricating interface of an EGM, there are many boundaries whose profiles are complex and vary with shaft angle. In this case, the profiles are updated with nearest neighbor interpolation, based on a series of polygons

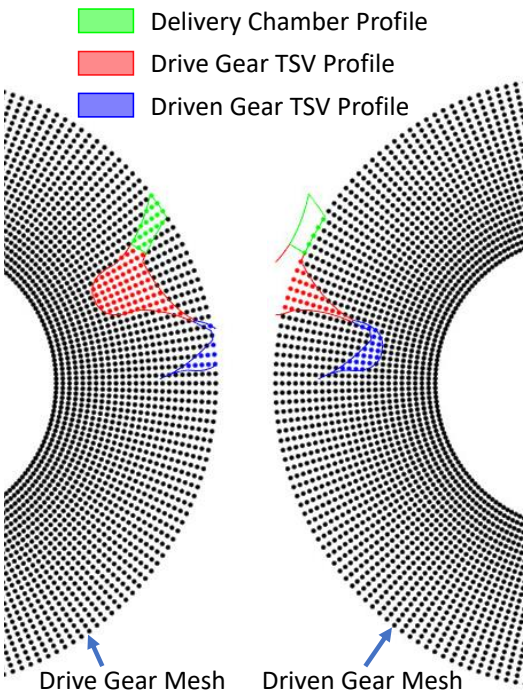

Figure 3.17. Boundary point definition by finding the mesh points within the given polygon

corresponding to specified shaft angles. These profiles are dictated by the shape of the control volumes that apply the pressures, and are therefore an output of the geometric module discussed in Section 2.3.

To determine whether a mesh element falls within the given polygon, the Winding number algorithm is used. This thesis uses an implementation based on the one given in [132], which maintains the robustness with non-simple polygons of the winding number algorithm while avoiding the use of trigonometric functions to match the efficiencies of the alternative Ray-tracing algorithm.

Regardless of the polygon complexity, all points that fall within (or outside) it are taken out of the internal field. Rather than being solved, these points have their values set to that of the lumped volume associated with the polygon. This allows the information from the lumped parameter model to be exchanged with the DP domain via the internal field elements adjacent to these boundaries. For each polygon, a

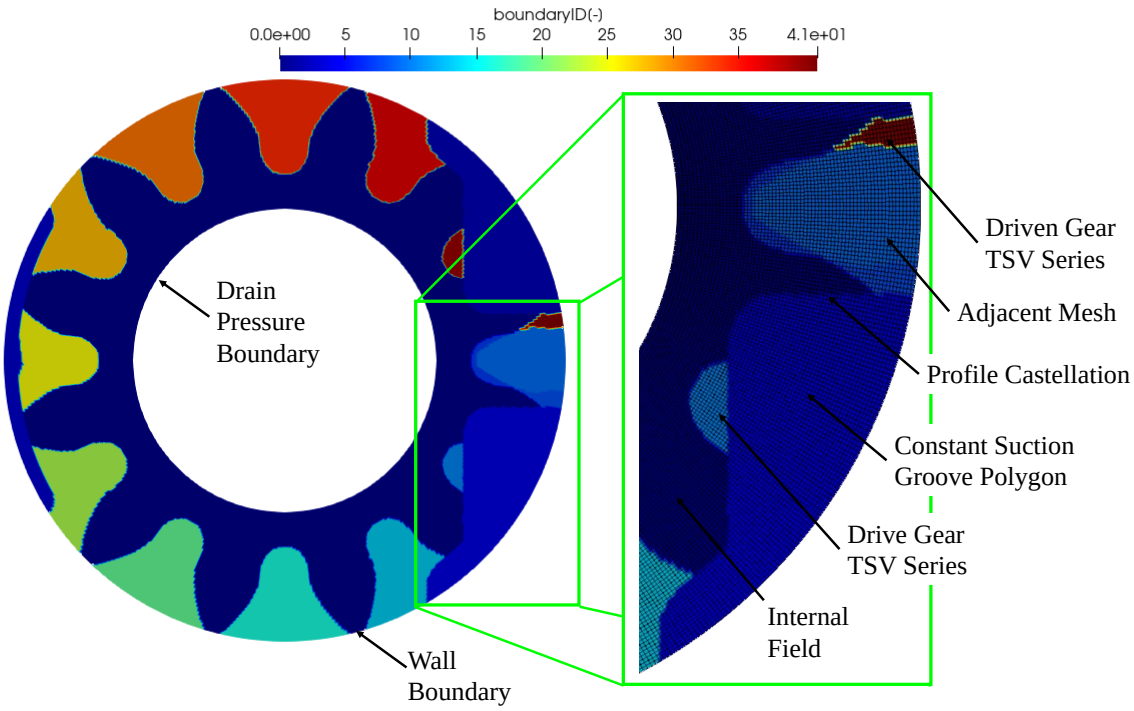

Figure 3.18. Boundary definitions on the drive gear lateral gap of an EGM as demonstration of application of complex geometry with fundamental film of Ref E2 EGM

unique boundary ID is assigned, which is used for mapping between the DP and LP domains. For the lateral gap of the Ref E2 EGM, the resulting film assignments are shown in Figure 3.18.

This figure shows many of the possible boundary cases that may occur. First, the delivery and suction grooves must be removed from the film, as they are directly connecting to the ports by an recess in the plate. Since this geometry does not change with angle, it is implemented as a constant polygon. Instead for both the drive and driven gear TSVs, the profiles change with shaft angle as dictated by the geometric module, and are therefore implemented as a time-dependant polygon series. Since

the tips of the teeth meet the casing outside of the meshing zone, a constant wall boundary condition is applied at the outer radius of the gears

$$Q_r(r_0) \sim \left.\frac{\partial p}{\partial r}\right|_{r_0} = 0 \tag{3.59}$$

Finally, the inner radius of the gear is connected to a drain volume that exists between the lateral and journal bearing gaps. What is left after all boundaries have been applied is the internal field, which forms the complex gear shape in which the pressure distribution must be solved. In this figure, castellation of the profiles is noticed when compared to the ideal boundary profile demonstrated in Figure 3.17. While the mesh could be snapped to these curves to better resolve the boundaries, Pellegri [46] observed that the resulting local skewness that this introduces in the mesh was harmful for numerical solution. Furthermore since these boundaries provide only an interface with the LP domain, and do not otherwise impact the solution, it is not necessary to exactly resolve their shapes. Instead in this thesis, castellation is mitigated by choice of fine grid which minimizes this effect.

In order to achieve the strong coupling of the lumped and distributed models, information is exchanged at each iteration at the edges of the internal field with each boundary. At the interface of each LP boundary, Dirchlet boundary conditions are applied in pressure, density, void contents, and temperatures, so that all effects considered by the lumped parameter model are transferred to the DP domain.

3.4.1 Fluid Exchange

To capture the leakages across these films, it is necessary to calculate the fluid that is exchanged with each boundary. This is accomplished using the generalized flow equation 3.26, which gives the net mass flux accounting for the change in fluid properties and the added flow resistances in cases of mixed lubrication. With the density (and thus pressure) distribution known, the flow out of the film into the i^{th}

boundary domain Ω_i is then given by the sum of the differential flows across each segment which delimits the internal field from this domain

$$\dot{m}_{\Omega_i} = \sum_{j \in \Omega_i} \underline{\dot{m}}_j \cdot \underline{d\Omega}_{i,j} \tag{3.60}$$

By considering the density of the boundaries, cavitation that occurs in the lumped volumes is also directly fed into the DP solution. Similarly by considering the enthalpy and void flux carried by this mass flow, the energy that escapes the LP domain via these films is captured using Equations 2.34 and 2.35 respectively.

Returning to Figure 3.18, the penetration of the driven gear's tooth into the domain of the drive gear's lateral gap demonstrates that is not only with the LP domain, but within different films of the DP domain. While it is reasonable to treat the remainder of the film as independent from the other films, this figure shows that their solutions are not isolated. To account for this, then, the films retrieve the properties at the requested location of their 'neighbor' on the adjacent mesh, effectively merging the films and enforcing a solution that conserves mass over the coupled domain inherently by solving the universal Reynolds equation across their union.

To ensure that the castellated interface discussed above does not prevent convergence of the film flows, the following study was performed. In this study, the boundary profile defined in Figure 3.18 was applied to meshes with varying resolution (N_{lat} nodes in mesh). For each case, a complete EGM simulation was run. The resulting flow across a TSV boundary and the drain boundary was then collected for both the drive and driven gears, and averaged over the last converged revolution. Note that in order to converge on the same flows, this approach must also lead to the same pressure build-up in the lumped and film domains. Therefore, this study tests not only the flow predictions of the film, but also the film's consistency in interfacing with the lumped domain as well as adjacent films. In Figure 3.19(a) and 3.19(b) the convergence of these flows, across the TSV and drain respectively, is demonstrated. Here error is defined with respect to the finest mesh taken. This result confirms that

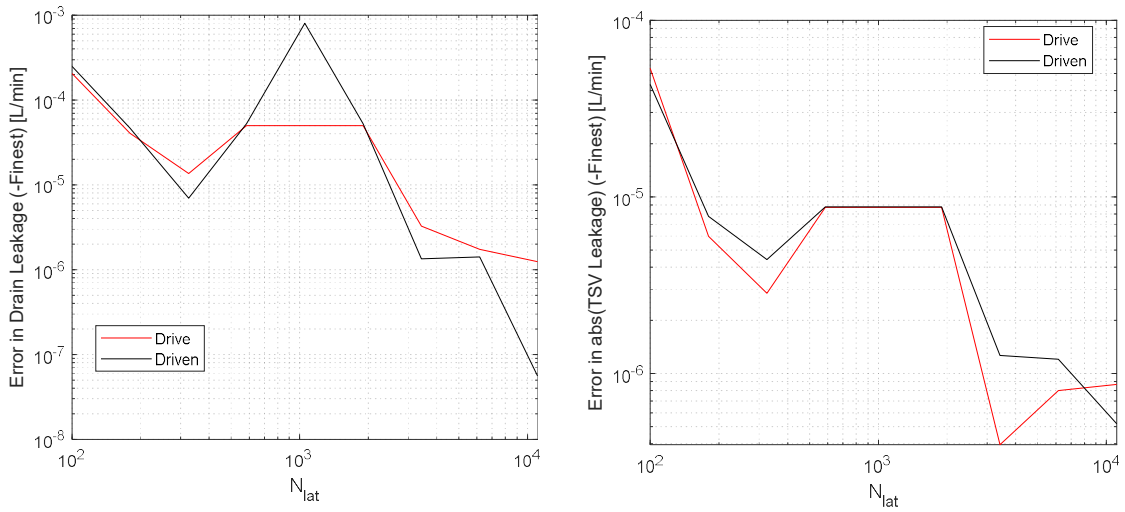

(a) TSV Leakage

(b) Drain Leakage

Figure 3.19. Flow Convergence study with change in lateral mesh resolution (a) Convergence in TSV Boundary Leakage (b) Converge of Drain Leakage

even for moderately coarse meshes ($N_{\text{lat}} \sim 10^3$), the castellated meshes are able to converge on a single flow. This gives confident that the snapping of elements, and its associated mesh skewness, need not be considered.

3.4.2 Film Forces

When applying the boundaries, elements are taken out of the internal field either because they do not reflect the actual geometry of the film, or because they are in direct contact with an LP volume. Considering this, their pressures are (optionally) not considered when evaluating the net forces of the film. It is instead assumed in this case that their influence on the dynamics of the body is accounted for in the lumped parameter pressure project component discussed in Section 2.2.1. Returning to the lateral lubricating interface of EGMs, Figure 3.20(a) shows the distribution of pressure that results during operation.

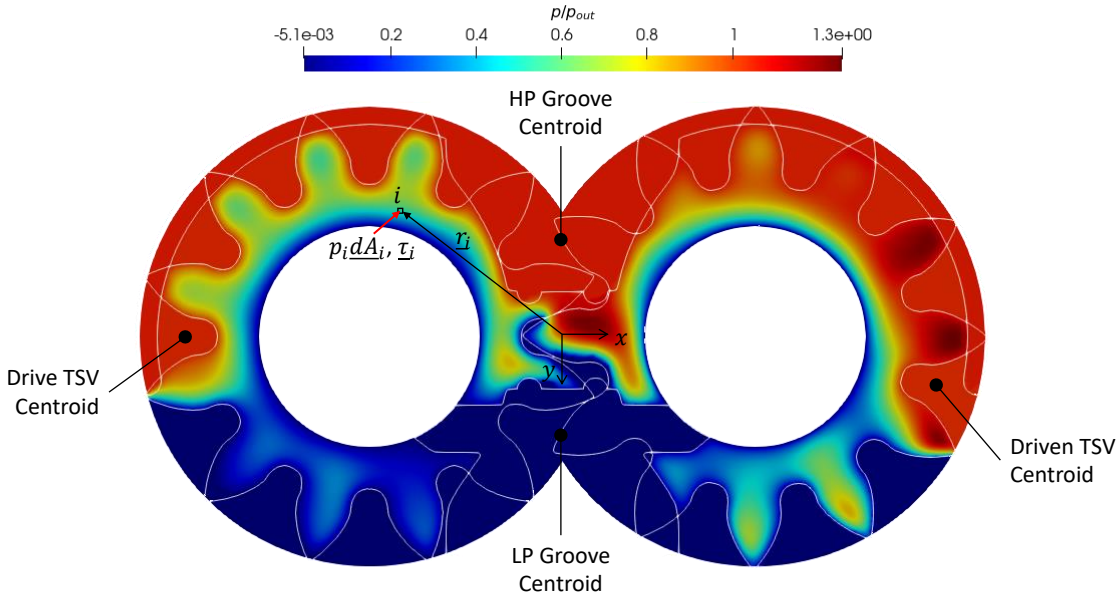

(a) Pressure Distribution of Lateral balancing element

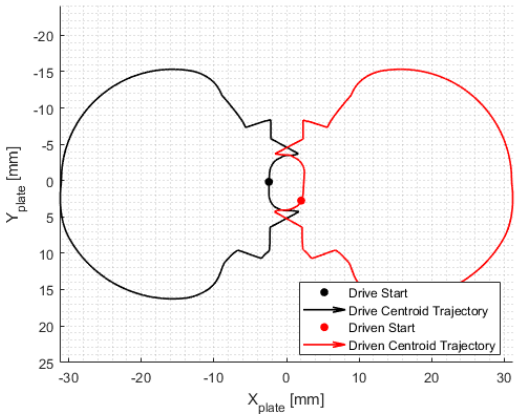

(b) Single TSV centroid for drive and driven

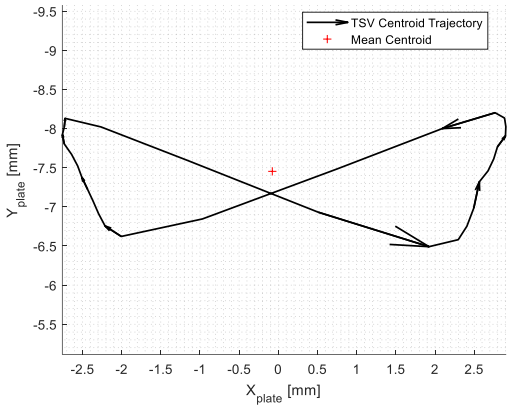

(c) Net TSV centroid

Figure 3.20. TSV pressure projection centroid into lateral balance element of a Ref E1 EGM (a) Pressure profile including film and LP regions (b) for a single TSV of drive and driven over a full shaft rotation (c) net centroid due to all TSVs

In this figure, the centroids of the TSVs as they rotate are shown. In Figure 3.20(b), the trajectory of the centroid of a single TSV of the drive and driven gear is shown over a full shaft rotation. Notice here that while the trajectories of the drive

and driven gear are a mirror image for the symmetric gears, they are phase offset due to the angle offset of the driven gear with respect to drive. This offset, as well as the pressure distribution over the TSVs leads to a net TSV centroid

$$r_{c,p} = \frac{\sum_{i=1}^{N_{\text{teeth}}} p_i A_i \underline{r}_{c,i}}{\sum_{i=1}^{N_{\text{teeth}}} p_i A_i} \tag{3.61}$$

that oscillates with time, demonstrated in Figure 3.20(c).

The remaining forces on the body are given by the contribution of each differential element within the internal field of the film, governed by the equations defined above, and shown in Figure 3.20(a). First, the film pressures act in the negative gap normal direction for both the top and bodies

$$\underline{F}_{p,t/b} = -\sum_{i=1}^{N_{int}} p_i \Delta x_i \Delta y_i \hat{n}_{t/b} \tag{3.62}$$

While Figure 3.20(a) shows the net pressure distribution as perceived by the bushing, it is important to highlight that this information is coming from two different sources. To aid in this point, Figure 3.21 contrasts the contributions of each domain. From these figures, it is clear that the body dynamics are strongly dependant on the pressurization of both domains.

Note that this feature of the films need not applied. Consider for example the cylinder block - valve plate of an APM, demonstrated in Figure 3.22(a). This figure highlights how as the unit rotates, the porting boundaries of the DCs and the outlet/inlet overlap. To isolate these complex profiles as the two overlap would require complex polygon operations and a tabulated result. Instead, the pressure contribution of the boundary nodes can be included to directly account for the complex pressure distribution. In effect, this functionality is left as a model option for the user, who can apply the more convenient approach to define the net loading over the surface of the body. On the DC side shown in Figure 3.22(b), then, the net projection due to the displacement chamber pressures is given by the radius of the bode. The additional area known to be at case pressure (A_{under}) must be applied in the +z direction to so account for the gap pressure distribution it opposes. Since the shape of the bore

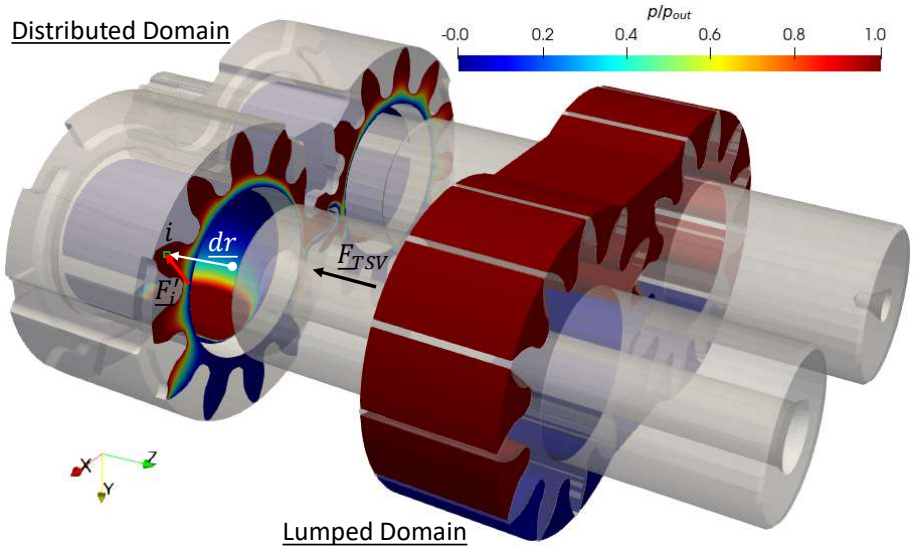

Figure 3.21. Surface Pressure contributions to lateral balancing element of EGM from distributed and lumped domains

deviates from the annular disk geometry of the gap side, the known case pressure on the gap side must also be accounted in the -z direction (A_{over}). Since the remaining regions of the body are at a uniform case pressure, their contributions cancel and do not need to be considered for the rigid body loading.

Similar to the film pressures the shear must also be applied to the bodies, where here it must be assumed that the forces of the film come only from the internal field. In order to account for the mixed lubrication effects introduced above, the shear flow factors derived in [70] are used. Again, these empirically determined coefficients relate the variation of shear that occurs as the asperities become non-negligible to the rigid gap height h, where

$$\overline{\underline{\tau}}_{t/b} = \frac{\mu(\underline{v}_t - \underline{v}_b)}{h}(\phi_f \pm \phi_{fs}) \pm \phi_{fp}\frac{h}{2}\underline{\nabla}p \tag{3.63}$$

For the Gaussian and isotropic surfaces assumed here, these coefficients are given by [70]

$$\phi_f \approx 1 - 1.4\exp(-0.66\widetilde{h}) \tag{3.64}$$

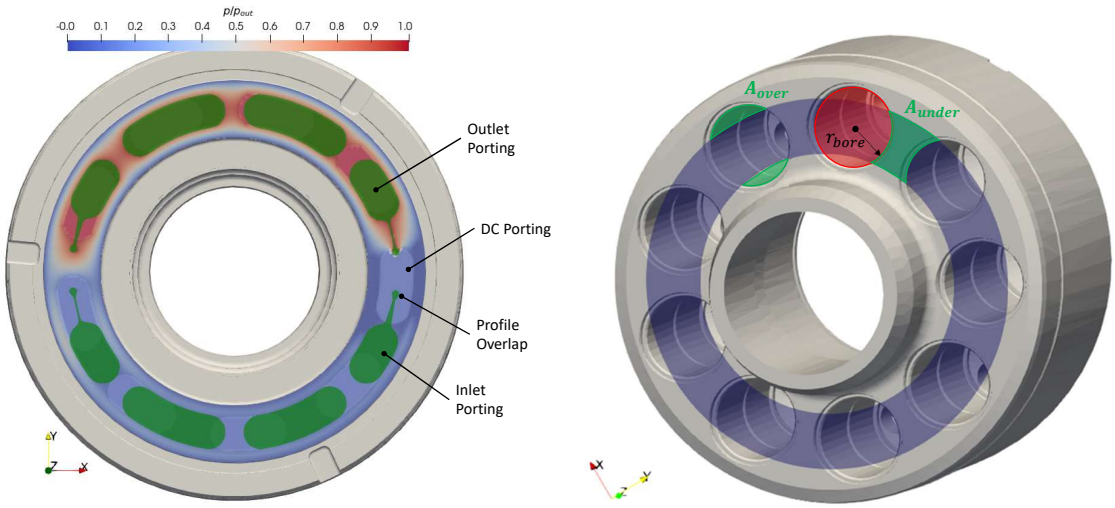

(a) Gap Side (b) DC Side

Figure 3.22. Boundary Contributions to Cylinder Block - Valve Plate interface of Ref P1 APM (a) Gap side (b) DC side

$$\phi_{fs} \approx \frac{R_{q,t}^2 - R_{q,b}^2}{R_q^2} \begin{cases} 11.1\widetilde{h}^{2.31}\exp(0.11H^2 - 2.38H), & \widetilde{h} \leq 7 \\ 0, & \widetilde{h} > 7 \end{cases} \tag{3.65}$$

$$\phi_{fp} \approx \begin{cases} \widetilde{h}\left(\ln\left(\frac{R_q(\widetilde{h}+3)}{\varepsilon_\tau}\right)\left(\frac{\widetilde{h}^2}{9}-1\right)^3 - \frac{\widetilde{h}}{180}(\frac{\widetilde{h}}{3}(\frac{\widetilde{h}}{3}(\frac{\widetilde{h}}{3}(\frac{\widetilde{h}}{3}(49\widetilde{h} \right. \right. \\ \left. \left. +60) - 405) - 160) + 345) + 132) + \frac{11}{12}\right)\frac{-35}{96}, & \widetilde{h} \leq 3 \\ \widetilde{h}\left(\ln\left(\frac{\widetilde{h}+3}{\widetilde{h}-3}\right)\left(\frac{\widetilde{h}^2}{9}-1\right)^3 - \frac{\widetilde{h}\left(\frac{\widetilde{h}^2(\frac{10}{3}\widetilde{h}^2-80)}{9}+66\right)}{45}\right)\frac{-35}{96} & \widetilde{h} > 3 \end{cases} \tag{3.66}$$

As was discussed in the lumped parameter analytical shear definitions of Section 2.2.2, infinite shear stress is avoided by saturating the rigid gap height at a small number $\varepsilon_\tau \ll R_q$. With these two, the net force on the top and bottom bodies are

$$\begin{aligned}\underline{F}_t &= \sum_{i=1}^{N_{int}} \Delta x_i \Delta y_i \left(-p_i \hat{n}_t - \phi_{fp} \frac{h}{2} \underline{\nabla} p - \frac{\mu(\underline{v}_t - \underline{v}_b)}{h} (\phi_f - \phi_{fs}) \right) \\ \underline{F}_b &= \sum_{i=1}^{N_{int}} \Delta x_i \Delta y_i \left(-p_i \hat{n}_b - \phi_{fp} \frac{h}{2} \underline{\nabla} p + \frac{\mu(\underline{v}_t - \underline{v}_b)}{h} (\phi_f + \phi_{fs}) \right)\end{aligned} \tag{3.67}$$

To find the net tilting moment of this film force, the moment arm between the force and the center of mass of each body is considered so that

$$\begin{aligned}\underline{M}_t &= \sum_{i=1}^{N_{int}} (\underline{r}_i - \underline{r}_{CG,t}) \times \left[\Delta x_i \Delta y_i \left(-p_i \hat{n}_t - \phi_{fp} \frac{h}{2} \underline{\nabla} p - \frac{\mu(\underline{v}_t - \underline{v}_b)}{h} (\phi_f - \phi_{fs}) \right) \right] \\ \underline{M}_b &= \sum_{i=1}^{N_{int}} (\underline{r}_i - \underline{r}_{CG,b}) \times \left[\Delta x_i \Delta y_i \left(-p_i \hat{n}_b - \phi_{fp} \frac{h}{2} \underline{\nabla} p + \frac{\mu(\underline{v}_t - \underline{v}_b)}{h} (\phi_f + \phi_{fs}) \right) \right]\end{aligned} \tag{3.68}$$

3.4.3 Asperity Contact

As was demonstrated in Figure 3.6, in regions of low film thickness the asperities of the two bodies that makeup the film will begin to make contact. In this condition, the results contact pressure p_c assists in carrying load on the film. To model the load sharing due to asperity contact pressures in regions of mixed lubrication, the empirical model developed in [73] is used, defining a relationship between the rigid gap and the resulting average asperity contact pressure over the film. The

$$\ln \widetilde{h} = \begin{cases} \sum_{i=0}^{4} [1 \ \Lambda^{-1} \ \Lambda^{-2} \ \Lambda^{-3}] \underline{\underline{G}}_i \, [1 \ \widetilde{\mathcal{H}}^{-1} \ \widetilde{\mathcal{H}}^{-2} \ \widetilde{\mathcal{H}}^{-3}]^{\mathsf{T}} \widetilde{p}_c^{\,i}, & \widetilde{p}_c < \widetilde{\mathcal{H}} \\ 0, & \widetilde{p}_c \geq \widetilde{\mathcal{H}} \end{cases} \tag{3.69}$$

where $\underline{\underline{G}}_i$ are the empirical coefficient matrices found by Lee and Ren [73], which act on the dimensionless material hardness

$$\widetilde{\mathcal{H}} = \frac{3\sigma_y \lambda_{0.5}}{\pi E^* R_q} \tag{3.70}$$

and roughness directionality to relate the dimensionless contact pressure

$$\widetilde{p}_c = p_c \frac{\pi E^* R_q}{\lambda_{0.5}} \tag{3.71}$$

to the log of the gap height. Evaluating this summation yields a quartic polynomial relationship between contact pressure and the log of the dimensionless gap whose coefficients are a function of the material and surface properties, and can therefore be evaluated in preprocessing

$$\ln \widetilde{h} = \psi_{\gamma,4}\widetilde{p}_c^4 + \psi_{\gamma,3}\widetilde{p}_c^3 + \psi_{\gamma,2}\widetilde{p}_c^2 + \psi_{\gamma,1}\widetilde{p}_c + \psi_{\gamma,0} \tag{3.72}$$

The use of this model, however, is cumbersome at the scale to which it must be applied here, since the known quantity is $\widetilde{h}$, and $\widetilde{p}_c$ cannot be easily extract from the polynomial. Instead, it is observed the integration of the film requires a small time step. Considering this, the change in gap at a point will be small, and its log even smaller. With this observation, the otherwise quartic polynomial can be linearized about the previous position

$$\widetilde{p}_c = \widetilde{p}_{c0} + \left.\frac{d(\widetilde{p}_c)}{d(\ln \widetilde{h})}\right|_0 (\ln \widetilde{h} - \ln \widetilde{h}_0) + \mathcal{O}\left((\ln \widetilde{h} - \ln \widetilde{h}_0)^2\right) \tag{3.73}$$

to yield a simple equation to update the contact pressure

$$\widetilde{p}_c \approx \widetilde{p}_{c0} + \frac{\ln \widetilde{h} - \psi_{\gamma,4}\widetilde{p}_{c0}^4 - \psi_{\gamma,3}\widetilde{p}_{c0}^3 - \psi_{\gamma,2}\widetilde{p}_{c0}^2 - \psi_{\gamma,1}\widetilde{p}_{c0} - \psi_{\gamma,0}}{4\psi_{\gamma,4}\widetilde{p}_{c0}^3 + 3\psi_{\gamma,3}\widetilde{p}_{c0}^2 + 2\psi_{\gamma,2}\widetilde{p}_{c0} + \psi_{\gamma,1}} \tag{3.74}$$

If the step between the two point is too large, or contact pressure crosses zero, then the exact solution can be found by finding the positive real root of the modified quartic polynomial with trailing coefficient

$$\psi'_{\gamma,0} = \psi_{\gamma,0} - \ln \widetilde{h} \tag{3.75}$$

In either case, the resulting contact pressure is added to the force and moment calculations given in Equations 3.67 and 3.68 respectively.

3.4.4 Boundary Friction

Returning to Figure 3.5, Hamrock [90] shows that the friction behavior of lubricated contact deviations from the mixed Reynolds solution in the presence of boundary lubrication. This condition occurs in areas where the hydrodynamic and hydrostatic components of a contact interface are not sufficient to hold its loading, and a

majority of the load is carried by solid contact. In regions where boundary lubrication occurs, the universal Reynolds equation cannot be applied. In PD machines these conditions are unavoidable, so the present thesis develops a separate means to model them. First for APM in the piston-slipper joint, friction between the ball and socket joint of the slipper and piston restricts relative motion between the two. For EGM, Thiagarajan et al. [54] found a hysteresis effect in the position of the lateral balancing element of an EGP. This hysteresis, they found, was due to the effects of boundary friction between the floating element and the pump body. The boundary friction occurring in both these interfaces is accounted for in this section.

Lateral Bushing of EGM

The cause of this friction in EGMs is shown in Figure 3.23. Here a net pressure imbalance over the axial area of the bushing and the forces of the journal bearings inevitably drives it into the low-pressure size of the pump body.

As a result, motion of the body is restricted by lubricated (though not notably hydrodynamic) friction. As was demonstrated in [54], inclusion of friction effects in this regions was necessary for the authors to capture hysteresis effects in the measured bushing position, confirming its importance. The present work extends this model, to consider also the frictional resistance of this contact to tilting of the bushing. To do this, the contact pressure is assumed to be uniformly shared over the contact region so that the net friction force per unit area is given by modifying the Stribeck friction relation from [133]

$$\underline{F}'_f = \left[-\frac{\sqrt{2\mathrm{e}}}{v_{st}} \Delta p (\mu_s - \mu_d) \exp\left(-\left(\frac{|\underline{v}|}{v_{st}} \right)^2 \right) - \frac{\mu_d \Delta p}{|\underline{v}|} \tanh\left(\frac{|\underline{v}|}{v_c} \right) - f_v \right] \underline{v} \qquad (3.76)$$

This curve, demonstrated in Figure 3.24, accounts for the transition from static to dynamic friction (Coulomb) friction as the breakaway velocity v_{brk} is reached and the body begins to move. The Stribeck ($v_{st} = \sqrt{2} v_{brk}$) and Coulomb ($v_c = v_{brk}/10$) velocity thresholds are defined with respect to this breakaway friction to determine the shape of the curve. The static breakaway friction with coefficient μ_s is then tran-

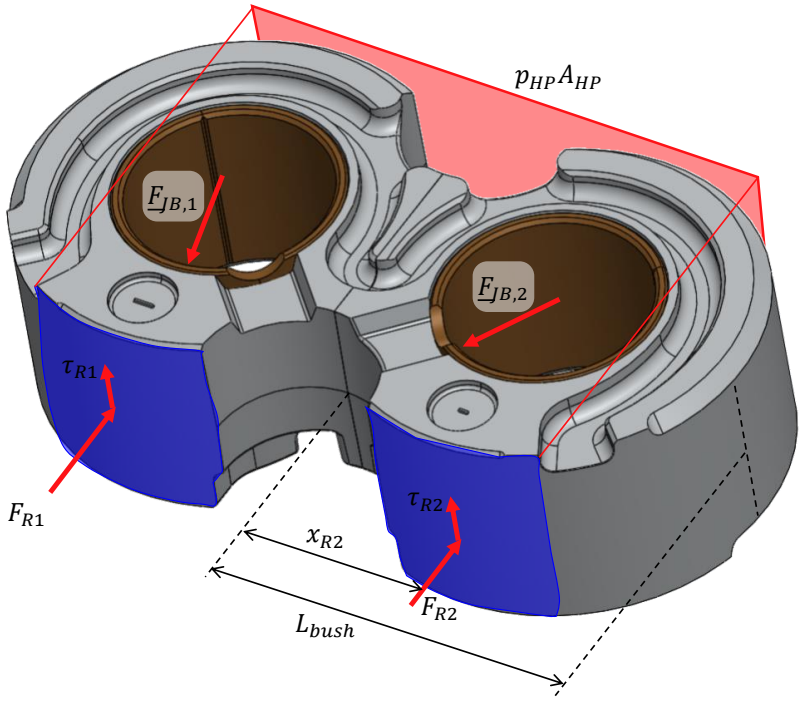

Figure 3.23. Planar free body diagram of lateral balancing element of Ref E1 EGP, showing net force imbalance

sitioned into dynamic Coulomb friction with coefficient μ_d in the opposite direction of the velocity, with shear force building as speed increases. With this, the net force and moment of the region are given by an integral over the contact surface Γ_c

$$\underline{F}_f = \iint_{\Gamma_c} \underline{F}'_f \, d\Gamma \tag{3.77a}$$

$$\underline{M}_f = \iint_{\Gamma_c} \underline{r} \times \underline{F}'_f \, d\Gamma \tag{3.77b}$$

These integrals are then evaluated numerically using Gauss quadrature.

Ball-Socket Interface of APM

In the present work, the clearance between the piston and slipper in its ball socket interface is assumed to be sufficiently small. As a a result, the combined piston-slipper

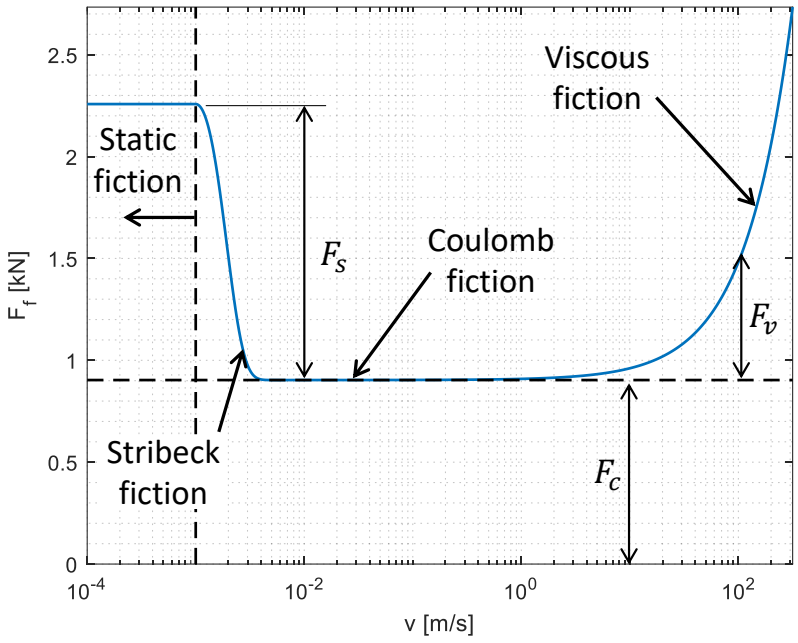

Figure 3.24. Variation of friction regime with surface velocity

behaves as a single free body . In general, though, the ball socket does not accomplish a perfect welding of the piston and slipper bodies. Considering this, it is necessary to also capture the relative tilting of the slipper to the piston. In the frame of this net piston-cylinder body, the slipper does not behave like a free body. With the assumption of small clearance, it can experience only rotational modes about the ball socket.

With the assumption of small clearance, the contact that occurs in the socket interface can be treated as an internal force. The function of the contact is to maintain the relative linear motion of the two bodies. To achieve this, a normal stress builds over a small contact region of the interface. Due to the high forces that build in this contact region, a friction force develops which opposes relative motion of the ball

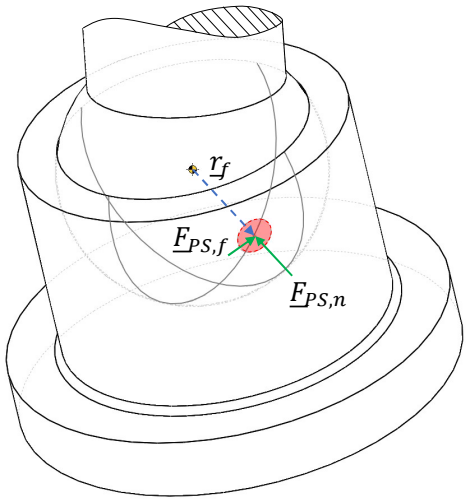

Figure 3.25. Contact in piston-slipper ball socket

and socket. As an internal force, the net contact force must exactly balances the accelerations of the two bodies to that of the net piston-slipper body, so that

$$\frac{\underline{F}_{\text{net,P}} + \underline{F}_{PS}}{m_p} = \frac{\underline{F}_{\text{net,S}} - \underline{F}_{PS}}{m_s} \tag{3.78}$$

Since the ball-socket interface is a spherical contact, the vector from the socket center to the center point of its application must be collinear with the normal component of the applied force, and is therefore known. The net loading of this contact can then be demonstrated in Figure 3.25.

From the review of the state of the art in the modeling of this contact, it is demonstrated that these interfaces are modeled with an effective friction coefficient. Since the relative velocities of these bodies is typically very small, hydrodynamic effects are negligible. Nonetheless, the contact is flooded with oil and a dry contact model is not suitable. For this reason, the same Stribeck friction equation shown in Figure 3.24 is used to model this interface. The contribution of this frictional force on both bodies is then determined by considering the moment arm at which it acts. This model provides the additional benefit of not needing detailing information of

the shape of the contact patch, maintaining simple calculations that facilitate rapid lumped parameter evaluation.

To consider the impact of relative motion of the piston and slipper on the performance of the unit, the present thesis also considers the limiting case of infinite friction force. In effect, this conditions means that there can be no relative motion in the ball-socket interface. Similar to Equation 3.78, this infinitely frictional contact moment can be expressed by the moment required to balance the angular accelerations of the body, where it is important to note the use of the common inertial frame in calculation.

$$\frac{\partial \underline{\dot{\omega}}_{p,IF}}{\partial \underline{M}_{IF}} \left(\underline{M}_{p,IF} + \underline{M}_{f,IF} \right) = \frac{\partial \underline{\dot{\omega}}_{s,IF}}{\partial \underline{M}_{IF}} \left(\underline{M}_{s,IF} - \underline{M}_{f,IF} \right) \tag{3.79}$$

Figure 3.25 demonstrates that the frictional component of this force is offset from the center of the socket, and therefore induces a net moment on both bodies. It is exactly this frictional contact that acts to constrain the relative rotation of the slipper with respect to the socket. The normal component passes through the center of the socket, and so it does not impact the slipper rotation. The net force is transmitted via this socket to the piston, and acts to communicate the slipper-swashplate loading to the piston-slipper body.

3.5 Implementation

Though the relative states of the lumped and distributed parameter regions of the fluid domain inform the solution of both, they are often governed by drastically differing time-scales. Specifically, the non-linearity of the lumped parameter system results in a stiff system of equations compared to the Reynolds films. Since film computations dominate the overall run-time, it is harmful to limit the lubricating film to match this smaller step, and asynchronous time stepping of the two offers a large potential for alleviating excessive computation expense. The implementation of this approach is illustrated in Figure 3.26(b). Here, the main timeline (A) solves

the lumped parameter problem, considering all hydraulic components as well as the dynamics of all bodies.

For each distributed parameter film an additional coupled timeline is introduced. As is demonstrated in Figure 3.26(b) , these additional (B, C, ...) timelines always lead the main timeline (A) so that film information between their steps can be interpolated. For demonstration, Figure 3.26(b) highlights 3 noteworthy time points on the more dense main (A) timeline. As is shown at time point $t_{A,2}$, this interpolation is unique within each timeline in order to collect all film states at this main time. In case a time request of the main timeline falls behind of the current bounds of a film timeline $t_{A,1}$, previous steps are also recorded for interpolation. This is an important feature that ensures continuity of the film solution as perceived by the main timeline.

Finally, the request of a time point ahead of the current bounds of a film $t_{A,3}$ triggers a time step of the film timeline (B, C, ...). The use of the Mixed Universal Reynolds Equation 3.28 gives a nonlinear advection-diffusion problem in ρ. Considering this, the time step of the scheme is controlled using the Courant–Friedrichs–Lewy (CFL) conditions of the numerical discretization. In the present work, four additional timelines (B-E) are necessary from the EGM, corresponding to the top side lateral and journal bearing gaps of the drive and driven gears respectively. This approach is equally applicable for modeling of a helical gear as well, with the introduction of 4 additional timelines. For the APM 3 additional timelines are necessary (B-D), corresponding to the piston-cylinder, slipper-swashplate, and cylinder block - valve plate interfaces.

Figure 3.26(a) shows how information of both the film forces and leakages are required in order to progress both the dynamics and fluid simulations within the main LP timeline. Both the DP and LP domains interface with the output of the geometric module and the gap preprocessing in order to update the geometry of the unit as the floating bodies shift. At each print interval of simulation, results are output to a text file for the LP film and a `.vtk` file for the DP film, which can be used with the open source software Paraview for post-processing and visualization.

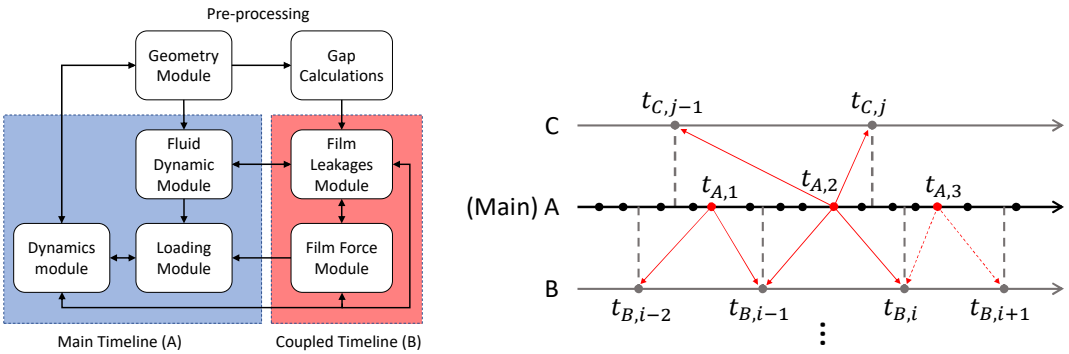

(a) Double timeline interface (b) Asynchronous timelines

Figure 3.26. Strong coupling of the Main LP timeline and the DP timeline (a) flow chart of the module interaction (b) Interfacing between asynchronous timelines

All figures that are included in thesis of film results are direct output of the code created using this software, unless otherwise specified.

3.5.1 Information Exchange

As described in Figure 3.26(a), the interface between the main lumped timeline and the films is accomplished by interpolating between the two. At each step of a film, then, the flows over all boundaries are recorded, which are then used at arbitrary main timeline (A) request. Here, a linear interpolation is chosen over higher order interpolation schemes for its consistency. If not for this property, the film flows perceived by the main timeline would change as new DP time steps were considered in the interpolant, leading to an unrealistic and numerically unfavorable solution for the main timeline.

$$\dot{m}_B(t_{A,2}) = \dot{m}_B(t_{B,i-1}) + \left(\frac{t_{A,2} - t_{B,i-1}}{t_{B,i} - t_{B,i-1}}\right)\left[\dot{m}_B(t_{B,i}) - \dot{m}_B(t_{B,i-1})\right] \tag{3.80}$$

As demonstrated in Figure 3.26(a), mass fluxes are used to exchange information with the lumped films, retrieving density and void fractions in return. While doing

this, the cavitation and aeration information of all distributed parameter films and lumped chambers are inherently accomplished.

Similar to the flow coupling, the film forces are recorded at each discrete time-step of the film. As the main timeline progresses, this information is used to linearly interpolate both forces and moments on the body. While the larger time scale alleviates a large computational load, it does so at the expense of instantaneous feedback on body acceleration in the main timeline. In most positive displacement machines, the leakage flows of the unit are much smaller than the main flows. This makes the loss of feedback acceptable for a realistic solution. However, since these interfaces perform the main load carrying functions of the unit, this lack of feedback in the dynamics module leads to numerical instability in the solution. Therefore, to provide this feedback, an additional load term $\underline{F}_{B,I}(t_{A,2})$ is considered. To define this addition, the velocity field at which the mixed Reynolds film was solved is perturbed so the gap-normal squeeze deviates by $\dot{h}'$ yielding a perturbation ρ' in the density solution. The universal Reynolds equation is linearized and collected in Appendix B.1 about the nominal solution, so that the perturbation can be locally described using Equation B.4 repeated here

$$\underline{\nabla} \cdot \left(\underline{\underline{D}}\, \underline{\nabla} \rho' \right) = \gamma + \kappa \rho' \tag{3.81}$$

In order to implement this function directly, the gradient of the diffusivity is required. To resolve this gradient, a fine mesh and temporal resolution would be required and in effect the time steps are re-synchronized negating the performance benefit. Instead, the method of weighted residual is used to express this equation in its weak form. To simplify notation, this function can be expressed in terms of an arbitrary diffusivity tensor $\underline{\underline{D}}$ and constant and linear forcing γ and κ respectively as derived in Appendix B.1. In this notation, the method of weighted residual is given by the functional

$$G(\rho', \widetilde{\rho}) = -\iint_{\Gamma} \widetilde{\rho} \left(\underline{\nabla} \cdot \left(\underline{\underline{D}}\, \underline{\nabla} \rho' \right) - \gamma - \kappa \rho' \right) d\Gamma = 0 \tag{3.82}$$

Applying the divergence theorem to the first term of this functional, the weak form of this problem is recovered. Notice here that due to the homogeneous boundary condition of the perturbation, all boundary terms drop

$$\iint_{\Gamma} \left(\underline{\underline{D}}\,\underline{\nabla}\rho'\right) \cdot \underline{\nabla}\widetilde{\rho}\, d\Gamma + \iint_{\Gamma} \widetilde{\rho}\gamma\, d\Gamma + \iint_{\Gamma} \widetilde{\rho}\kappa\rho'\, d\Gamma = 0 \tag{3.83}$$

In order to solve this problem in the four domains considered here, a function f mapping the unit square domain Γ' to the physical domain Γ is defined. Each problem discussed below will use a different map of this form, given in Appendix B.2

$$f : \Gamma'(\xi, \eta) \mapsto \Gamma(x_1, x_2) \text{ for } \xi, \eta \in [-1, 1] \tag{3.84a}$$

$$\underline{\underline{J}} = \begin{bmatrix} \frac{\partial x_1}{\partial \xi} & \frac{\partial x_1}{\partial \eta} \\ \frac{\partial x_2}{\partial \xi} & \frac{\partial x_2}{\partial \eta} \end{bmatrix} \tag{3.84b}$$

In this unit domain, the problem is solved using a pseudospectral method. As such, the solution to the problem is expressed in terms of a sum of basis functions $N_i(\xi, \eta)$ with unknown weights $\underline{a}$. With the Galerkin method used here, similar definition is used for the test function with weights $\widetilde{\underline{a}}$

$$\rho'(\xi, \eta) = \underline{N}(\xi, \eta)^T \underline{a},\ \widetilde{\rho}(\xi, \eta) = \underline{N}(\xi, \eta)^T \widetilde{\underline{a}} \tag{3.85}$$

Substituting this approximation into the weak form of Equation 3.83 yields the definition of the discrete functional. The Jacobian $\underline{\underline{J}}$ of the map f is used so that this functional can be expressed in terms of an integral over the unit domain

$$\widetilde{G}(\underline{a}, \widetilde{\underline{a}}) = \widetilde{\underline{a}}^T \left[\left(\iint_{\Gamma'} \left(\nabla \underline{N}\, \underline{\underline{J}}^{-1} \underline{\underline{D}}\, \underline{\underline{J}}^{-T} \nabla \underline{N}^T + \underline{N} \kappa \underline{N}^T \right) \left|\underline{\underline{J}}\right| \, d\Gamma' \right) \underline{a} + \iint_{\Gamma'} \underline{N} \gamma \left|\underline{\underline{J}}\right| d\Gamma' \right] = 0 \tag{3.86}$$

The non-trivial solution to this problem forms a linear system of equations in $\underline{a}$. Since the diffusivity and forcing are an arbitrary function of the film state, the surface integrals are evaluated using Gauss–Legendre quadrature with film properties interpolated at the quadrature points. This aspect of a global method justifies its use here, namely that it requires only limited information to be interpolated from the film solution while still retaining rapid convergence. This rapid convergence allows for a

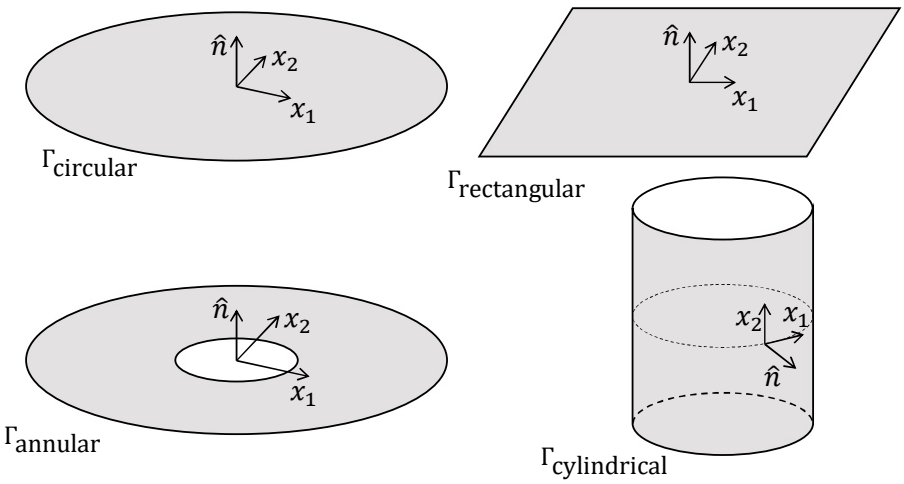

Figure 3.27. Base domain types for impedance Reynolds films

small system of equations which can be rapidly inverted as opposed to more expensive distributed parameter film steps. This approach is applied to each of the four domain types considered in Figure 3.27. Here, circular and/or annular domains can be found in the lateral interface of the EGM and the slipper swashplate and cylinder block - valve plate interfaces of APMs. Similarly cylindrical films are found in the journal bearings of EGMs and the piston-cylinder interface of APMs. Here, the rectangular domain is included in order to assist the other definitions, but could also be used to model more complex tooth-tip geometries of an EGM.

With the perturbed density found by solving the linear system of Equation 3.86, the corresponding perturbed pressure can then be determined using a linearized approximation of the bulk modulus

$$p' \approx \frac{K_0}{\rho_0}\rho' \tag{3.87}$$

The linearity of this system means that the solution to arbitrary perturbation of velocity can be expressed in terms of the superposition of perturbations in each direction. Considering this, each mechanical degree of freedom of the film is perturbed with unit magnitude, and the force response is integrated from the resulting perturbed

pressure. By collecting these solutions, a numerical impedance tensor $\underline{\underline{W}}$ is formed so that the instantaneous response to an arbitrary velocity perturbation is given by superposition. With each timestep of the film, this tensor is updated to describe the tangent impedance of the film

$$\underline{R} = [F_x\ F_y\ F_z\ M_x\ M_y\ M_z]^T = \underline{\underline{W}}\,[v_x\ v_y\ v_z\ \omega_x\ \omega_y\ \omega_z]^T \tag{3.88}$$

Finally, this impedance tensor is used to augment the interpolated force of the film so that

$$\begin{aligned}\underline{R}_B(t_{A,2}) = \underline{R}_B(t_{B,i-1}) + \left(\frac{t_{A,2} - t_{B,i-1}}{t_{B,i} - t_{B,i-1}}\right)\left[\underline{R}_B(t_{B,i}) - \underline{R}_B(t_{B,i-1})\right] \\ +\underline{\underline{W}}\left[v'_x\ v'_y\ v'_z\ \omega'_x\ \omega'_y\ \omega'_z\right]^T\end{aligned} \tag{3.89}$$

3.5.2 Parallelization

The distributed parameter component of the model is parallelized using OpenMP. While this restricts the parallelization to a single node, this is not a problem as the goal of this thesis is to a develop a tool that can be run on a single machine, and not a large cluster. Use of this program typically comes in two cases. Case one pertains to a given unit with a specific problem. In this case, the operating condition(s) that elicit the undesirable behavior are typically known, and the parallel implementation of the program provides the engineer with the simulation results in the fastest possible time. Instead the alternate use of this program is for mapping performance over a range of operating conditions, either for diagnostics or unit evaluation. In this case, the time taken for an individual simulation is less important, but the total time for the batch is. To maximize throughput, then, the sequential version of the program is run with multiple instances on the machine, so that the higher efficiency of the sequential version leads to a lower overall time. The benefit of using OpenMP is the ability to directly toggle the parallel/sequential implementations of the program with no change in the underlying source code. This eases development time as only one source is maintained, and more importantly prevents differing implementations for the sequential and parallel modes and potentials for bug introduction.

The parallel flow of the model is demonstrated in Figure 3.28 for a single DP timeline (B). This figures demonstrates the major sources of efficiency loss in the parallel implementation. Due to the nature of the initial value problem, the solution to the next time step cannot be evaluated until the current time step is complete. As a result, parallel forking (or barriers) must be placed at each time step of the timelines, leading to a large overhead.

In an attempt to mitigate these losses, the amount of barriers/forking within a single step is minimized to 3 phases. The calculation of a step of a coupled timeline step relies on barriers to ensure that the solution remains consistent. First, the pre-processing phase collects the updated boundary information from the LP volumes, as well as the rigid body positions of the floating bodies. It then applies the relaxed deformation update to the rigid gap to get the net deformed gap distribution over the film. Finally it prepares the flow factors using these updated gap heights for solving.

After these actions, it is necessary to place a barrier before the next phase to prevent the density/temperature update from using outdated gap and flow information. Similarly after the fields are updated, another barrier ensures that the force and flow calculations take place using the updated values of the states. Because the film can include arbitrary boundaries, an even workload over the threads cannot be guaranteed with a static work distribution and a guided scheduling must be used. This approach is a dynamic work distribution, where work is distributed in chunks as the threads completes its previous chunk of work. The difference as opposed to pure dynamic scheduling is that the guided scheduler starts with large chunk distribution, and dynamically scales the chunk size towards the end of the work queue. This is beneficial, as it approaches the optimal behavior of the static distribution, but pays a small efficiency price to protect against cases where one thread is given a disproportionate number of internal field elements.

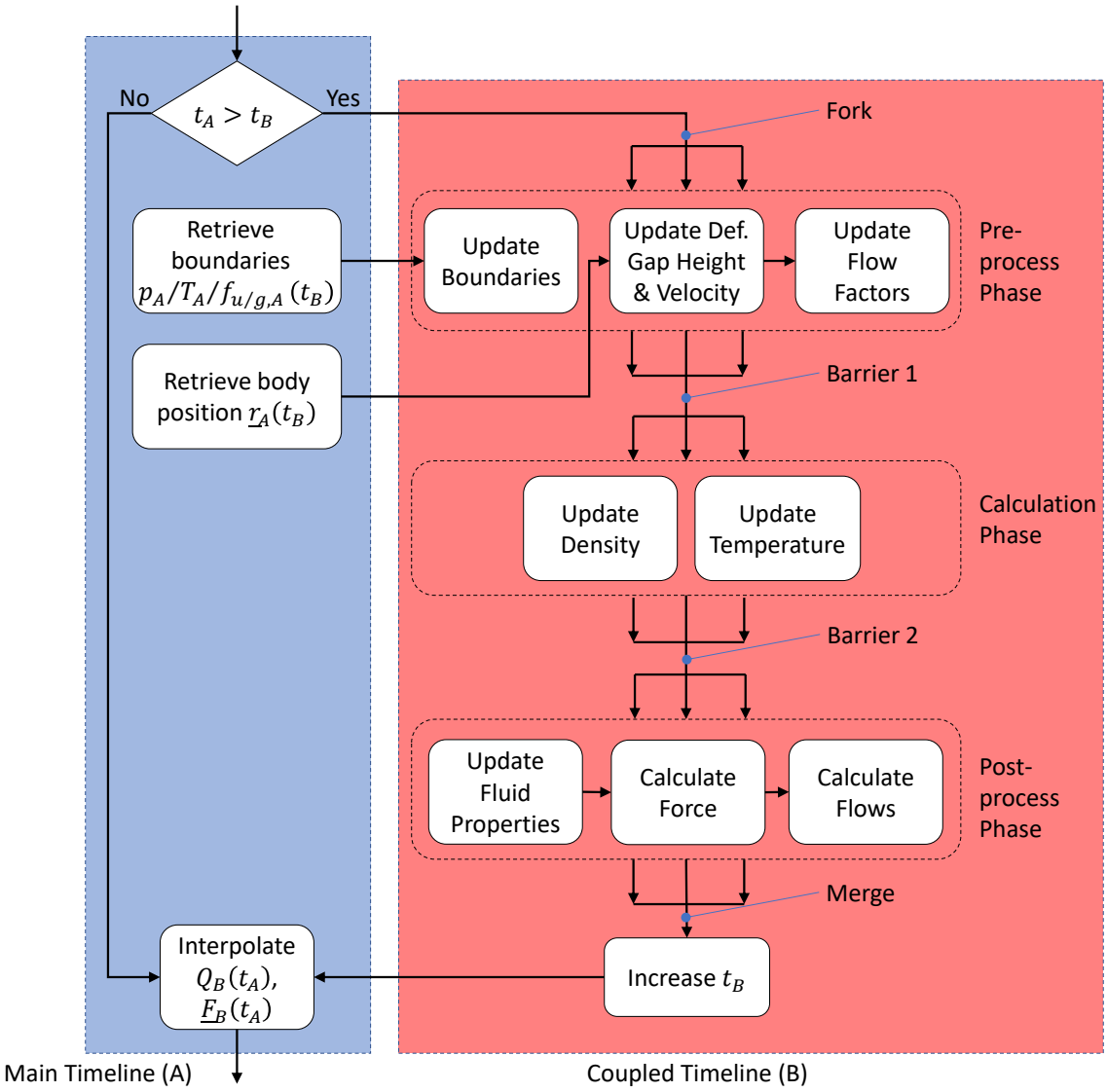

Figure 3.28. Parallel workflow and interface of the DP/LP domain coupling

3.5.3 Numerical Discretization

As mentioned above, the films are solved on a structured, non-uniform mesh using finite difference discretization. Note that while this approach will be demonstrated for the Cartesian film here, it is equally applicable for the cylindrical film with appropriate adjustment of the $\underline{\nabla}$ operator for cylindrical coordinate system. Dirichlet boundary

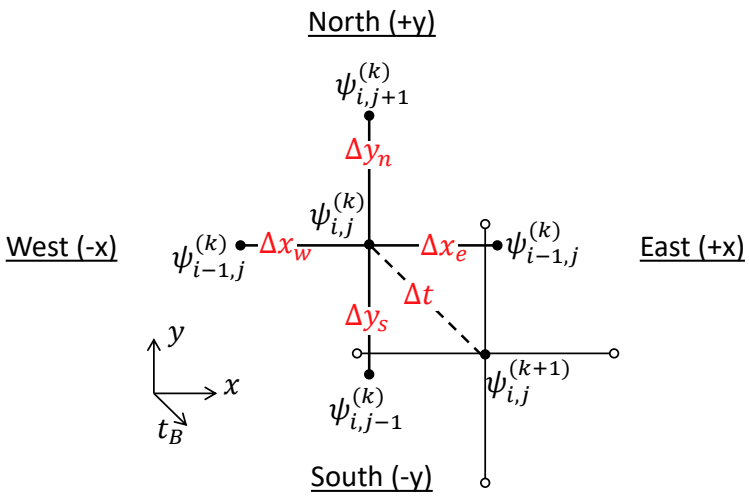

Figure 3.29. Second order finite difference stencil for given Cartesian internal field element for arbitrary field quantity

conditions are applied by removing elements from the internal field which is solved, and are instead fixed at the corresponding boundary values as demonstrated in Figure 3.18. All other boundaries, such as wall and symmetry boundaries are achieved by manipulation of the masking of the film. More specifically, the connectivity and grid spacing of the mesh is stored as a set of masks pointing to the north, south, east, and west neighbors of the given element. With these masks, the stencil given in Figure 3.29 can be constructed for each element for an arbitrary field quantity.

For example to accomplish a wall boundary condition on the north edge of a node, the mask entry is adjusted so that

$$\psi_{i,j+1} = \psi_{i,j} \tag{3.90}$$

Similar manipulation can be used to achieve all boundaries that are required in the film.

In regions of full film, the universal Reynolds equation is an ecliptic partial differential equation. Since this means that information propagates in all directions immediately, it is well suited for central differencing schemes. Considering this, the

pressure driven flow terms are evaluated using a central difference stencil. The second order accurate stencil used in this thesis is then demonstrated for the x component

$$\frac{\partial}{\partial x}\left(\phi_{p,x}\frac{Kh^3}{12\mu}\frac{\partial \rho}{\partial x}\right) = \frac{\partial}{\partial x}\left(Dx\frac{\partial \rho}{\partial x}\right) \approx \frac{Dx^{(k)}_{i+\frac{1}{2},j}\frac{\rho^{(k+1)}_{i+1,j}-\rho^{(k+1)}_{i,j}}{\Delta x_e} - Dx^{(k)}_{i-\frac{1}{2},j}\frac{\rho^{(k+1)}_{i,j}-\rho^{(k+1)}_{i-1,j}}{\Delta x_w}}{0.5(\Delta x_e + \Delta x_w)} \tag{3.91}$$

where $Dx^{(k)}_{i,j}$ is the density diffusivity in the x direction given by the leading term. This includes both fluid and film roughness and gap properties

$$Dx = \phi_{p,x}\frac{Kh^3}{12\mu} \tag{3.92}$$

In regions of film rupture, the dimensionless bulk modulus is small so that shear flow is dominant, and this pressure driven term drops out. Without this term, the partial differential equation becomes hyperbolic and information travels at a finite speed. To promote stability and accuracy of the numerical solution in these regions then, upwind differencing is used for the advective flow terms. The first order accurate stencil, again demonstrated in the x direction, is

$$\begin{aligned}\frac{\partial}{\partial x}\left(\rho\overline{v}_x(\phi_R R_q + \phi_c h)\right) + \frac{\partial}{\partial x}\left(\rho\frac{\phi_s}{2}R_q\left(v_{t,x}-v_{b,x}\right)\right) &= \frac{\partial Ax\,\rho}{\partial x} \\ &\approx \begin{cases}\frac{Ax^{(k)}_{i,j}\rho^{(k+1)}_{i,j} - Ax^{(k)}_{i-1,j}\rho^{(k+1)}_{i-1,j}}{\Delta x_w}, & Ax \geq 0 \\ \frac{Ax^{(k)}_{i+1,j}\rho^{(k+1)}_{i+1,j} - Ax^{(k)}_{i,j}\rho^{(k+1)}_{i,j}}{\Delta x_e}, & Ax < 0\end{cases}\end{aligned} \tag{3.93}$$

where $Ax^{(k)}_{i,j}$ is the advection velocity in the x direction including only film roughness and gap properties

$$Ax = \overline{v}_x(\phi_R R_q + \phi_c h) + \frac{\phi_s}{2}R_q\left(v_{t,x}-v_{b,x}\right) \tag{3.94}$$

Over the entire internal field, these stencils can be formed into differencing operators, where all known (k) terms are absorbed, acting on the next solution

$$\left(\underline{\underline{Dx}}^{(k)} + \underline{\underline{Dy}}^{(k)}\right)\underline{\rho}^{(k+1)} = \left(\underline{\underline{Ax}}^{(k)} + \underline{\underline{Ay}}^{(k)}\right)\underline{\rho}^{(k+1)} + \frac{\underline{\rho}^{(k+1)}(\underline{\phi}_R R_q + \underline{\phi}_c \underline{h})^{(k+1)} - \underline{\rho}^{(k)}(\underline{\phi}_R R_q + \underline{\phi}_c \underline{h})^{(k)}}{\Delta t} \tag{3.95}$$

which can be solved implicitly to update the solution. In effect, this forms a semi-implicit update, where the change in the fluid properties and deformation is assumed to be small so that iteration is not required and instead the (k) properties are used in the update of $(k+1)$. Additional user options for the film integrator besides this first order implicit update include: 2-step predictor-corrector implicit/explicit updates, first order backward difference update. All of these integrators follow the same update logic, with slight variation in the stencil (Equation 3.95) employed.

In order to ensure stability as the film state changes, especially given this assumption, the time step must be dynamically adjusted. To do this, CFL conditions are derived for the aforementioned numerical discretization approach. These conditions examine the region of numerical stability, ensuring that errors due both to the numerical discretization and finite precision arithmetics are not amplified. This can be ensured for the linear scheme with CFL≤ 1 for an explicit scheme, where CFL> 1 is allowable here for to the semi-implicit scheme. In order to define this CFL criteria, the linearized form of the universal Reynolds equation B.4 is taken, so that advection

$$\mathrm{CFL}_{A,i} = \Delta t \left(\frac{|v_1|}{\Delta x_1} + \frac{|v_2|}{\Delta x_2} \right) \Bigg|_i \tag{3.96}$$

and diffusion

$$\mathrm{CFL}_{D,i} = 2\Delta t \left(\frac{D}{\overline{\overline{h}}\,(x_1^2 + x_2^2)} \right) \Bigg|_i \tag{3.97}$$

conditions are given based on the two directions at each point in the mesh. Note that these CFL conditions are sensitive not only the the fluid properties and body position/velocity, but also to the resolution of the mesh. To promote mesh quality, the default mesh is created in such a way as to make the discretization as close to squares as possible. For highly advection-dominated films, these resolution can instead be manually set to bias in the direction of high speeds. Furthermore, the mesh can be augmented with grading toward regions of high sensitivity. For this reason, as well as the variation in fluid properties and velocities that result, this calculation must be repeated over each node in the mesh.

To account for squeeze effects, two additional criteria are imposed related to the net change in gap height

$$\Delta t|\dot{h}_i| \leq \epsilon_h \tag{3.98}$$

and gap squeeze

$$\Delta t^2|\ddot{h}_i| \leq 2\epsilon_v \tag{3.99}$$

allowable in a single step. Again these must be satisfied for each node in the mesh. Finally, the time step is heuristically adjust if the reliance on impedance corrections of the forces becomes too high.

The allowable CFL and tolerances $\epsilon_{v/h}$ of the simulation are taken as a user input. With this, the maximum time step where all conditions are satisfied over a film is then selected as the next time step for that DP timeline. It is worth reiterating, for clarity, that this calculation is unique to each film, which all progress their solution at differing time steps. It is also worth noting that in practice, the explicit schemes require values of CFL much less than unity due to the non-linearity of the problem.

3.5.4 Strong Scaling and Performance

In order to evaluate the performance of this program, it was run and timed in the Brown cluster at Purdue. The sequential version of the code was run on the same node, but compiled in sequential mode for fair comparison. Since changing the film resolution changes the nature of the problem, primarily with regard to regions of numerical stability, a weak scaling study of the problem cannot be performed. Instead the same mesh resolution was taken, and a strong scaling study was performed by changing the number of threads used in simulation. By recording the timing results of the same simulation run with each number of threads, the resulting performance parameters can be found. Since a single node on Brown was available for this work, this study will consider only from 1-24 threads, the maximum available on a single Dell compute node with two 12-core Intel Xeon Gold “Sky Lake” processors @ 2.60GHz.

First, the times taken for both the parallel and sequential implementations can be compared, so the resulting speedup can be found. In Figure 3.30, the speedups observed as the number of processors was varied are demonstrated. This speedup is defined by

$$S = \frac{t_{\text{sequential}}}{t_{\text{parallel}}} \tag{3.100}$$

so that the sequential time for a mesh resolution is used to find the speedup of each parallel run with that resolution. These results are compared to the behavior predicted by Ahmdal's law

$$S_A = \frac{1}{(1-s) + \frac{s}{N_{\text{thread}}}} \tag{3.101}$$

for s as the percentage of the program that can be parallelized. This figure demonstrates Amdahl's effect, where the speedup increases more slowly as number of processors increases. As the number of threads is first increased, a noticeable speedup is achieved. Further increasing the number of threads, however, yields diminishing returns in terms of speedup as it levels out. On the contrary as the mesh resolution is increased, so does the problem size. As a result, the speedup seen by the program increases, and the rate at which the speedup increases stays higher since the 'knee' occurs at higher number of processors.

This is expected, as for a given number of threads the same amount of forking work is required regardless of the problem size. However as the problem size increases, the amount of the program that can be parallelized increased. This is shown in Figure 3.30, where the same program yields significantly more parallelized code simply by increasing the problem size.

Looking next to the efficiency, Figure 3.31 shows a plot similar to Figure 3.30, where now the efficiency at each configuration is shown. This efficiency is found by relating the total resource time spent by the sequential and parallel implementations where

$$\eta_S = \frac{t_{\text{sequential}}}{N_{\text{thread}}\ t_{\text{parallel}}} = \frac{S}{N_{\text{thread}}} \tag{3.102}$$

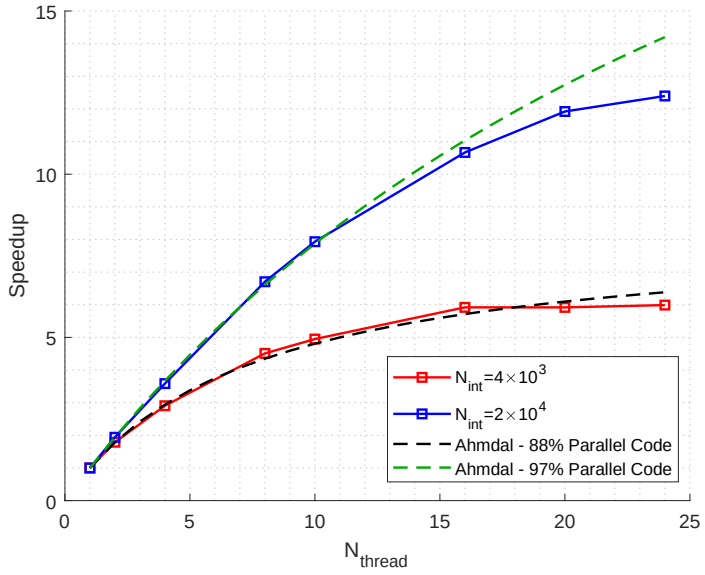

Figure 3.30. Amdahl's Effect on speedup with increase in number of threads

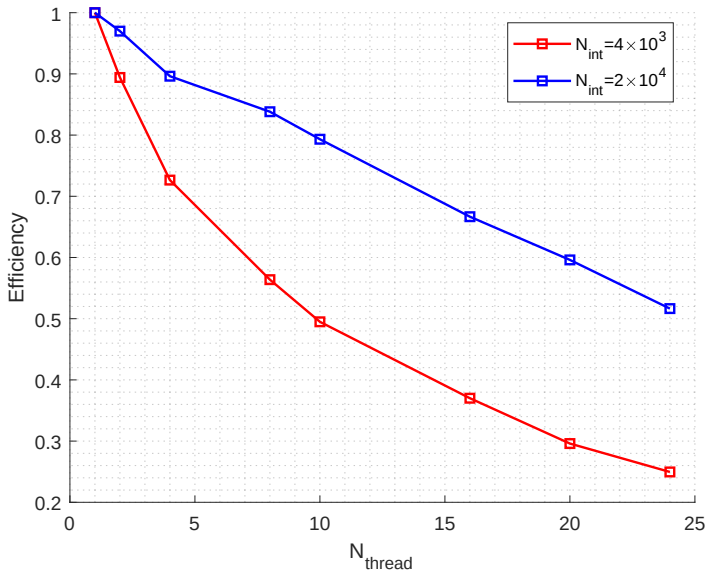

Figure 3.31. Parallel efficiency of program with increase in number of threads

These results shows that the efficiency of the program drops drastically as the number of threads is increased, explaining the corresponding plateau in the speedup of the program. It is likely that the constant forking/merging work, as well as time spent idle in the barriers, can explain this sharp drop in efficiency. As the number of thread increases, the magnitude of this work increases and decreases the overall efficiency of the program as an increasing amount of work is present which is not necessary in the sequential implementation.

To better understand this behavior, a Karp-Flatt analysis of the program can be performed. Here the fraction of the program run time where it is performing serial acts, not required in the sequential version, can be represented by

$$SF = \frac{\frac{1}{S} - \frac{1}{N_{\text{thread}}}}{1 - \frac{1}{N_{\text{thread}}}} \tag{3.103}$$

where the speedup and number of threads are used. Figure 3.32 shows that with the exception of low number of threads, the serial fraction grows as the the number of threads is increased. This observation confirms the claim made above, namely that the loss of efficiency can be blamed on the growing overhead of the problem as the number of threads is increased. Similarly, it also shows how the percentage of serial work is significantly decreased when it is compared to an increased problem size.

This strong scaling study highlights the justification for implementing only thread-wise parallelism in the tool. Namely, these result show that indeed the parallel implementation is capable of retaining high parallel efficiencies as the mesh resolution is increase. However, since the nature of these problems means that the meshes will remain in the orders of magnitude examined here, there is little potential for improvement if the number of threads is further increased.

As an additional reference, typical simulation times of the present tool are contrasted with comparable existing simulation tools for APMs and EGMs discussed in Section 1.3. For APMs, Multics CASPAR is compared to the simulation tool FSTI [48, 51, 52, 125] in Table 3.2. First comparing the lumped parameter models, it is worth noting that in the existing approach's lumped parameter module runs with

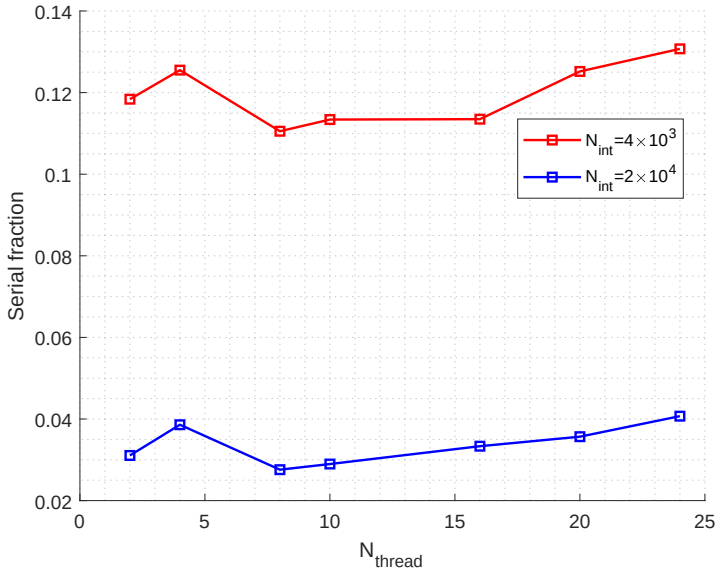

Figure 3.32. Serial fraction of program with increase in number of threads

leakage only from the film models. Since this means that the leakages are "known" (for a single weak coupling iteration), the lumped parameter simulations run very quickly with no need to converge on pressure-leakage behavior simultaneously. While this speed can be replicated with Multics CASPAR by disabling features to match the assumptions of the existing tool, a typical use of the Multics CASPAR includes analytical approximations of the films. For the improved fidelity these features offer, a slight price must be paid in simulation speed. Still, though, this "intermediate" fidelity solution is helpful. Examples of these uses include efficiency mapping, sensitivity studies, and virtual prototyping applications as will be discussed in Section 5.2.

For the distributed parameter version of the tool, this table shows that a complete simulation of Multics CASPAR reaches the same speed as an iteration of the other tools for a single iteration (iterations limited by the longest time). It is worth noting here that while the existing tool can run a simulation in similar time, it requires multiple iterations to converge on the weakly coupled lumped-distributed behavior.

Table 3.2.
Run time breakdown comparison with existing APM simulation

	Min	**Max**	**Typical**
Piston-Cylinder Interface (per iteration)	6 hr	1 week	18 hr
Slipper-Swashplate Interface (per iteration)	6 hr	2 days	12 hr
Cylinder block - Valve plate Interface (per iteration)	6 hr	2 days	12 hr
Pressure Module (per iteration)	10 s	2 min	20 s
Multics CASPAR - LP (Sequential)	10 s	1 hr	2 min
Multics CASPAR - DP (4 threads)	2 hr	3 days	20 hr

For Multics CASPAR on the other hand, this simulation represents a strongly coupled converged solution. For fair comparison, Multics CASPAR times are reported for simulation on 4 threads, the minimum number that would be expected on a typical desktop machine. As was shown above, the code retains high potential to improve on these times if more threads are made available.

Similarly for EGMs, Multics HYGESim is compared to the previous simulation tool HYGESim [36, 44, 46, 54] in Table 3.3. Here the lumped parameter model of HYGESim (previous) can run without (or with) interfacing with the Reynolds models, and thus faces the same issues mentioned for Multics CASPAR. The major speed benefits observed between this existing tool and Multics HYGESim, then, come from it being re-implemented as a standalone software package (as opposed to within another software as was done previously) rather than changes to the underlying modeling ap-

Table 3.3.
Run time breakdown comparison with existing EGM simulation

	Min	**Max**	**Typical**
Journal Bearing Interface (per iteration)	6 hr	2 days	12 hr
Lateral Lubricating Interface (per iteration)	6 hr	1 week	18 hr
Lumped Parameter (per iteration)	5 min	2 hr	30 min
Multics HYGESim - LP (Sequential)	10 s	30 min	2 min
Multics HYGESim - DP (4 threads)	2 hr	2 days	15 hr

proach. For the distributed parameter approach, on the other hand, a similar trend as was observed for Multics CASPAR is present. Namely, a single strongly coupled simulation of an EGM with Multics HYGESim can be performed in the same time as a single weak coupling iteration of the existing tools. Again 4 threads are used for the DP version of Multics HYGESim, accounting for use on a typical desktop machine.

For both the EGM and APM cases, these tables demonstrate that the core changes to the underlying approach of Multics allow for a marked decrease in the time required to attain a coupled lumped-distributed simulation result. Furthermore, the components developed in Multics introduce novel physical considerations within the same run-time. This is accomplished mainly via the ability of Multics to perform a single strongly coupled simulation of these machines, without the need for weak coupling iterations. It is also worth noting that these results are attained assuming a modest computational ability. Even with this modest resource, the simulation times of the present work is similar to single iteration of the existing approaches. Even if only

a single iteration of the weak coupling is required to converge (which is unlikely), analysis with the present model is completed in 50% of the time. This section further shows that with the availability of more parallel threads, the performance of Multics can be further improved to even surpass the time required for a single iteration of the existing tools.

4. VALIDATION

Throughout Chapters 2 and 3, the various components of the simulation suite Multics were developed and individually verified. In the present chapter, these model approaches are validated against relevant experimental measurement and state of the art. First, the novel universal Reynolds equation will be validated in isolation in Section 4.1 against both experimental results and relevant approaches in literature. With confidence in the behavior of this equation, experimental validation will then be performed on the specific applications to 3 different PD machines: EGM, APM, and Gerotor in Sections 4.2, 4.3, and 4.4 respectively.

4.1 Lubricating Films

Before proceeding with application to specific machines, it is important to validate the underlying approach. To do so, this section will compare the novel universal Reynolds equation against existing studies of common bearing geometry. This will come in the form and experimental and reference results available in literature for the Elrod cavitation algorithm on which the present thesis builds. In this section, 3 simplified cases are considered. First, the model is applied to a simple 1D slider bearing with results compared to Elrod [99] and Vijayaraghavan and Keith [103], then a plain journal bearing compared to Raimondi and Boyd [134] under steady operation and finally Brewe [110] during dynamic loading.

For the dynamic case, the time dependant density solution is solved using the finite difference scheme developed in Section 3.5.3. For both of the steady cases, the problem is solved using the same finite difference stencil. Without the time dependence, the steady problem is solved using an root finding approach adapted from Powell's Hybrid method [135] that was developed in [136].

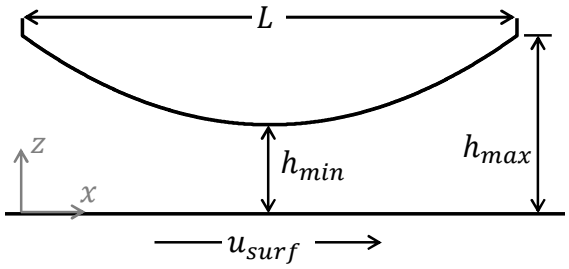

Figure 4.1. Parabolic slider bearing geometry definitions, with exaggerated gap height

4.1.1 Parabolic Slider Bearing

In [103], Vijayaraghavan and Keith extended the Elrod algorithm to include the compressibility effects of the shear flow term in the full film condition, comparing it to the infinite width parabolic slider bearing studied in Elrod [99]. To validate the present model, results will be compared to both of these works. Since constant liquid bulk modulus and viscosity are assumed in both thse works, values μ_0 and K_0 are taken respectively instead of the tabulated properties discussed previously. The density is then given by the linearized approximate approximation of the logarithmic relation

$$p \approx p_c + K_0 \left(\frac{\rho}{\rho_0} - 1 \right) \tag{4.1}$$

as is discussed in [99]. In Figure 4.1, the geometry of the slider is demonstrated, with fixed upper body and moving lower body. For this bearing, Table 4.1 demonstrates the relevant geometric and fluid properties.

With flooded inlet, results can be compared to the analytical, incompressible Reynolds solution

$$\frac{dp}{dx} = 12\mu_0 \overline{v}_x \frac{h - h_0}{h^3} \tag{4.2}$$

Table 4.1.
Fluid properties used for model validation study

Surface velocity $\underline{v}_{\text{surf}}$	$4.57\hat{i}\, m/s$
Length L	$76.2\, mm$
Minimum height $h_{\min}$	$25.4\, \mu m$
Maximum height $h_{\max}$	$50.8\, \mu m$
Liquid constant viscosity μ_0	$0.039\, Pa\, s$
Liquid constant bulk modulus K_0	$69\, MPa$
Liquid reference density ρ_0	$850\, kg/m3$
Reference saturation pressure p_0	$0\, bar_g$

with $h_0 = h(x_0)$, subject to a constant pressure inlet and Reynolds boundary outlet conditions

$$\begin{aligned} p|_{x=0} &= 0 \\ p|_{x=x_0} &= \left.\frac{dp}{dx}\right|_{x=x_0} = 0 \end{aligned} \tag{4.3}$$

The solution to this equation can then be written in terms of the unknown x_0, which is found numerical via a 1D root finding algorithm to satisfy the boundary conditions. In the compressible cavitated region, pressure is saturated at 0 and the cavitated pressure variation is neglected, an approach consistent with that of Hamrock et al. [90]. For numerical solution, the same constant inlet condition is applied, corresponding to either the flooded $\frac{\rho}{\rho_{\text{sat}}} \geq 1$ or starved $\frac{\rho}{\rho_{\text{sat}}} < 1$ inlet. Consistent with the previous works, the second derivative of pressure is fixed to zero at the boundary, corresponding to an outlet boundary condition on flow

$$\begin{aligned} \rho|_{x=0} &= \rho|_{\text{inlet}} \\ Q \sim \frac{d\rho}{dx} \therefore \left.\frac{dQ}{dx}\right|_{x=L} &\sim \left.\frac{d^2\rho}{dx^2}\right|_{x=L} = 0 \end{aligned} \tag{4.4}$$

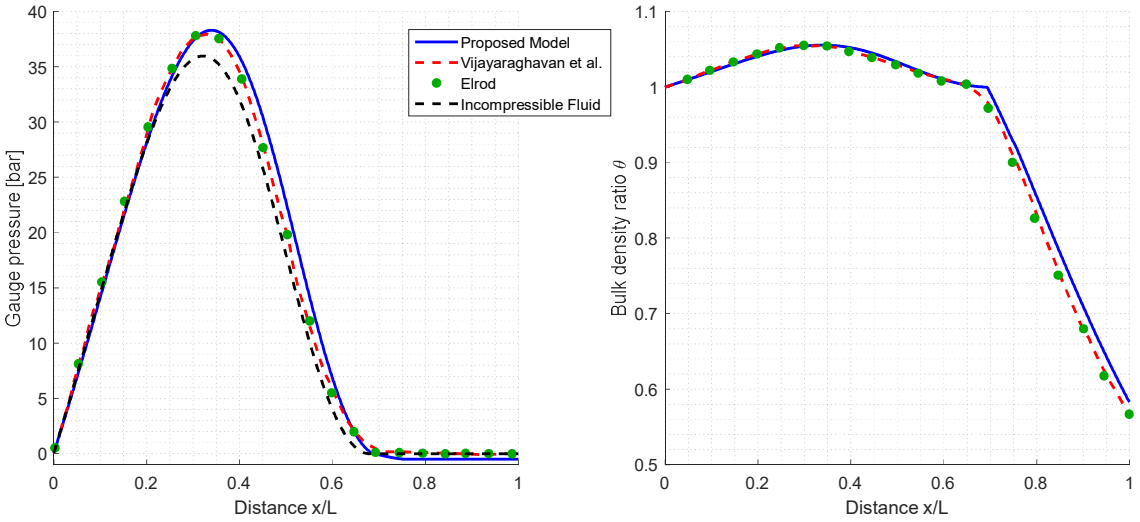

Figure 4.2. Flooded inlet ($\rho_{inlet} = 1.0001\rho_{sat}$) pressure and density ratio profile comparison of proposed model to Vijayaraghavan et al. [103] and Elrod [99] approaches, as well as the exact solution for incompressible fluid pressure

With this information defined, the flooded inlet case $\rho_{\text{inlet}} = 1.0001\rho_{\text{sat}}$ is first run. The pressure and density ratio that result in this condition are given in Figure 4.2.

While the density ratios of all three approaches appear similar, the conversion to pressures highlights the difference in result. Note here that in matching Elrod's approach, Vijayaraghavan's data presumably does not include the compressibility in the shear term, which was demonstrated to have an effect on the resulting pressure profile. Since this term is included in the proposed approach, the slight variation in resulting profile is expected. Furthermore, since both previous approaches use the discontinuous switch function to transition between upwind and central difference of the shear term in cavitated and full film regions respectively, the discretization and therefore the numerical problem to solve are different. With all models, the results show how pressure builds in the converging end, with the pressure dropping past the minimum film thickness and forming a void at the exit of the bearing.

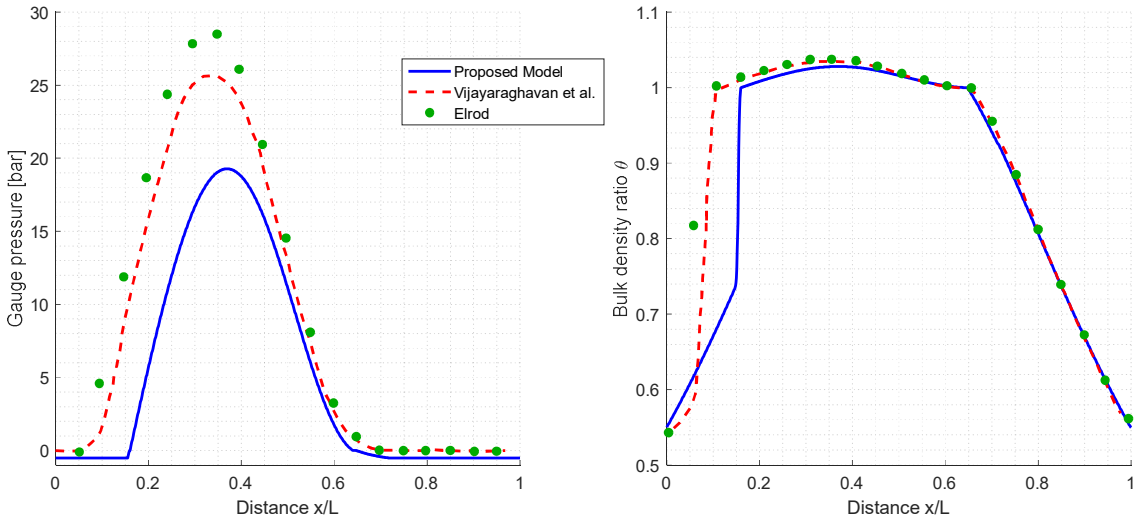

Figure 4.3. Starved inlet ($\rho_{inlet} = 0.55\rho_{sat}$) pressure and density ratio profile comparison of proposed model to Vijayaraghavan et al. [103] and Elrod [99] approaches

Similarly, the inlet condition $\rho_{\text{inlet}} = 0.55\rho_{\text{sat}}$ is run, corresponding to the same bearing with a starved inlet. The pressure and density ratio in this condition are given in Figure 4.3. Here the methods show poor agreement, even between the Elrod approaches. In case of the present work, it is likely that the disagreement comes in part from the non-zero pressure diffusion term which is neglected in the other works. As a result, the present work predicts a slower rate of reformulation of the film as compared to the Elrod approaches. All three, however, predict that same point at which the film ruptures, as well as the distribution of liquid in the film after rupture. Again, the same issues present in the flooded case will also impact agreement here. As is mentioned in [103], though, Elrod's shear flow term does not include the effects of compressibility in the full film shear term. In Figure 4.4, the proposed model is compared to Vijayaraghavan's result after including this effect, with better agreement.

Despite close results in the reference condition above, the agreement between incompressible and compressible fluid models are not always so close. In the case below, the surface velocity has been increased by a factor of 4 to provide more ability

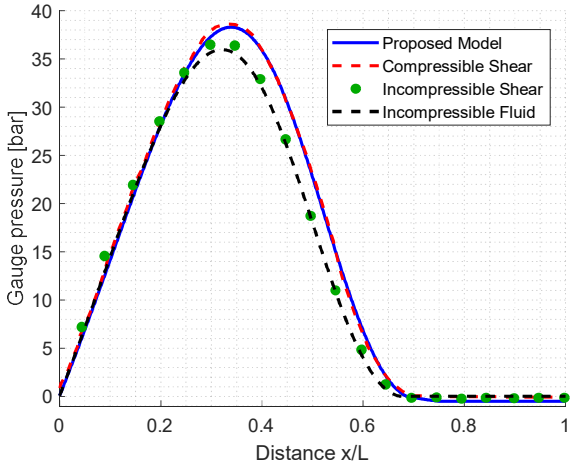

Figure 4.4. Flooded inlet pressure profile comparison of proposed model to Vijayaraghavan et al. [103] with and without inclusion of fluid compressibility in the shear term, as well as the exact solution for incompressible fluid

for hydrodynamic pressure buildup. Again, the inlet is assumed to be flooded $\rho_{\text{inlet}} = 1.0001\rho_{\text{sat}}$. Though the magnitudes of the two models are in relative agreement in this case, the peak locations and non-zero pressure region of the film are different, leading to different net force and moment prediction of the bearing. Furthermore, this figure shows the difference in results due only to a change when considering that the compressibility of the fluid itself changes with pressure.

As was mentioned above, the exact bulk modulus must be altered to facilitate numerical solution. The result of this alteration is highlighted in the zoomed portion of Figure 4.5, where a slight perturbation to the shape of the pressure curve occurs as the pressure crosses p_{sat} and the models are blended. Therefore, it is important to ensure that this blending occurs over a small enough region of pressure that it does not impact the final result. This zoomed portion also demonstrates how the pressure falls below that of saturation, and cavitation occurs. In Figure 4.6, the film content distribution is plotted against this pressure profile, demonstrating the film makeup for the case of the variable bulk modulus.

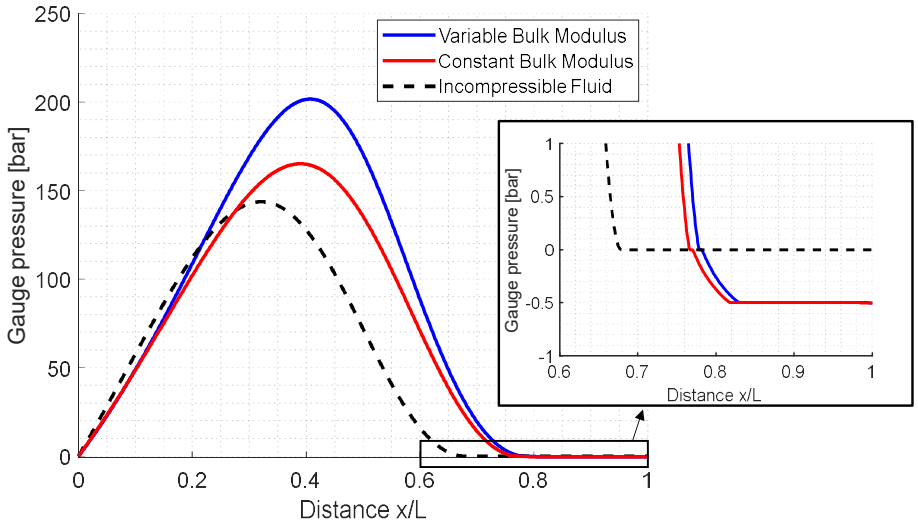

Figure 4.5. Flooded inlet pressure profile comparison of effect of variable compressibility on resulting pressure profile

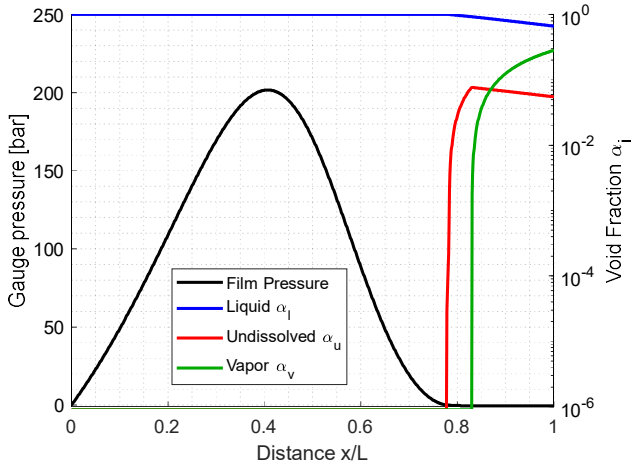

Figure 4.6. Flooded inlet pressure profile and void fractions demonstrating bulk fluid contents

This plot shows how first the trapped air is released from the liquid. However, since this release is not enough to fill the void, the pressure is further reduced until a slight evaporation of the liquid occurs. This highlights the utility of the proposed

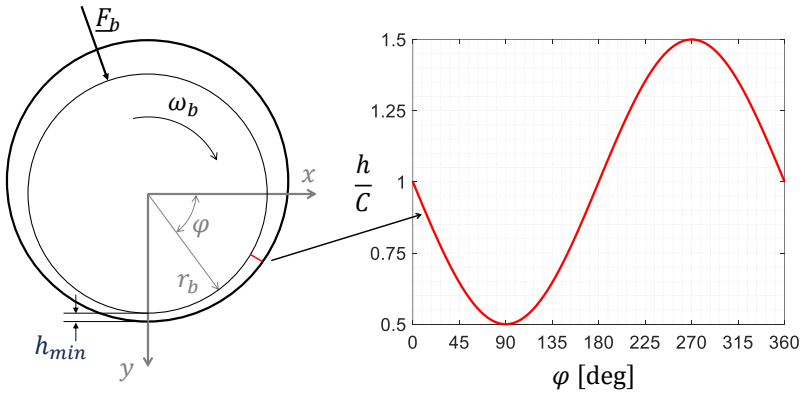

Figure 4.7. Unwrapped journal bearing film, with exaggerated radial clearance between bearing and journal

model, where not only the presence of cavitation, but a better understanding of the type and behavior of the cavitation can be studied.

4.1.2 Steady Journal Bearing

As was observed by Elrod [99], the difference between the incompressible and compressible solutions of a flooded inlet journal bearing is not detectable in a typical plot. Considering this, the proposed approach was applied to the flooded, axially fed plain journal bearing studied by Raimondi and Boyd [134]. Again since this work assumed constant viscosity and bulk modulus, the properties detailed above are maintained for validation.

The results are then compared to results obtained for incompressible fluid by [134]. In order to solve for the film pressures in the bearing, it is first unwrapped so that the circumferential $\hat{c}$ and axial $\hat{k}$ directions make up a rectangular, periodic film as is demonstrated in Figure 12. The lengths in the two directions are given by the circumference $2\pi r_b$ and axial length of the bearing L_z.

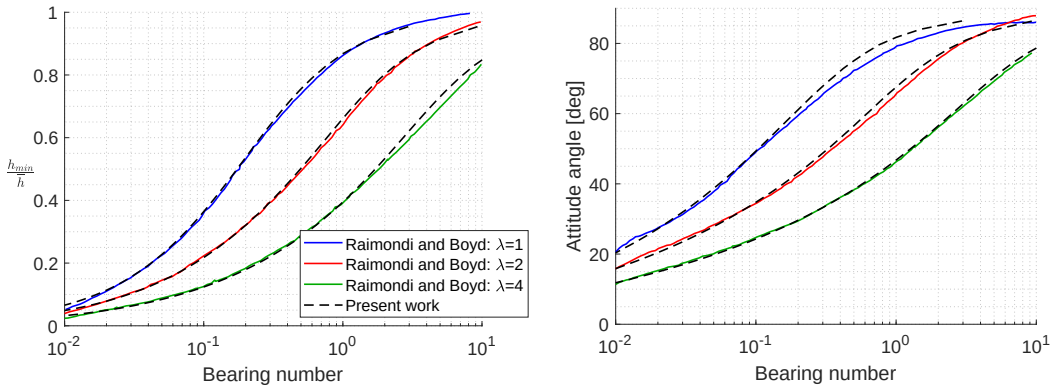

(a) Minimum Gap

(b) Attitude Angle

Figure 4.8. Comparison with Raimondi and Boyd [134] results as a function of bearing number for various bearing aspect ratios D/L (a) minimum gap thickness (b) attitude angle

From Hamrock et al. [90], the gap height of the bearing, for a given eccentricity vector $\underline{e}$ and nominal radial clearance C, can be calculated.

$$h = C - e_x \cos\varphi - e_y \sin\varphi \tag{4.5}$$

In steady conditions, the applied load is exactly opposite the net bearing force. Therefore, the attitude angle for $\omega > 0$ is

$$\Theta_F = \arctan\frac{F_{b,y}}{F_{b,x}} - \arctan\frac{e_y}{e_x} \tag{4.6}$$

Similarly, the bearing number is calculated via its definition in [134]

$$B_N = \frac{\mu_0 \omega r_b L_z}{\pi |\underline{F}_b|}\left(\frac{r_b}{C}\right)^2 \tag{4.7}$$

Using these, Figure 4.8 is constructed to compare results of the proposed model to that of [134] for the minimum gap height and attitude angle.

This result shows a good agreement between the pressure saturation and proposed approaches at various bearing aspect ratios. Notice, however, that the agreement begins to break down at higher bearing number, depending on bearing aspect ratio.

This effect was also observed above, where increasing the characteristic frequency ω, speed in the case of the slider, decreased the agreement between the incompressible and compressible solutions. This points to the fact the pressure saturation approach is appropriate for high loading situations but breaks down when the effects of the non-zero cavitation pressure are not negligible with respect to the peak pressure.

To demonstrate a typical solution, the constant fluid property assumptions are removed, and Figure 4.9(b) shows the film density distribution over the film for the gap distribution shown in Figure 4.7. The corresponding pressure profile is given by Figure 4.9(a), where the pressure and density peak at 90° corresponding to the minimum of the converging gap region, at an eccentricity ratio $\frac{|e|}{C} = 0.5$. Elsewhere, though, the contrast between the flat pressure profile and the drastically changing density profile shows key information that is discarded when using pressure saturation alone.

In the same condition, Figures 4.10(a) and 4.10(b) show the void fractions of the undissolved gas and vapor respectively. These plots demonstrate the key advantage of this approach, which provides insight of the degree of gaseous and vaporous cavitation throughout the film. These plots show that at first, the entrained gas of the liquid is released to fill the void created by the expanding region of the bearing. However, when this is not enough, the fluid evaporates and overcomes the gas and liquid bubble volume until its maximum at 270°, the peak of the expanding film region. While the gap height begins to converge here, the low bulk modulus and density of the film cause a lag in recovery of pressure. Thus, the bubbles do not come completely back into solution until after 45°, coinciding with the building of pressure.

Incorporating the effect of oiling grooves, Figures 4.11(b) and 4.11(a) for the density and pressure respectively are constructed. This simulation is run with the same bearing geometry and eccentricity ratio $\frac{|e|}{C}$, excepting supply grooves maintaining constant pressure of $5bar_g$ at the points marked in the figures. Notice here that the bearing has been loaded by a purely vertical load $\underline{F}_b = \langle 0, F_{b,y}, 0 \rangle$. The eccentricity angle was then adjusted to balance this load with the resulting film pressures, so that

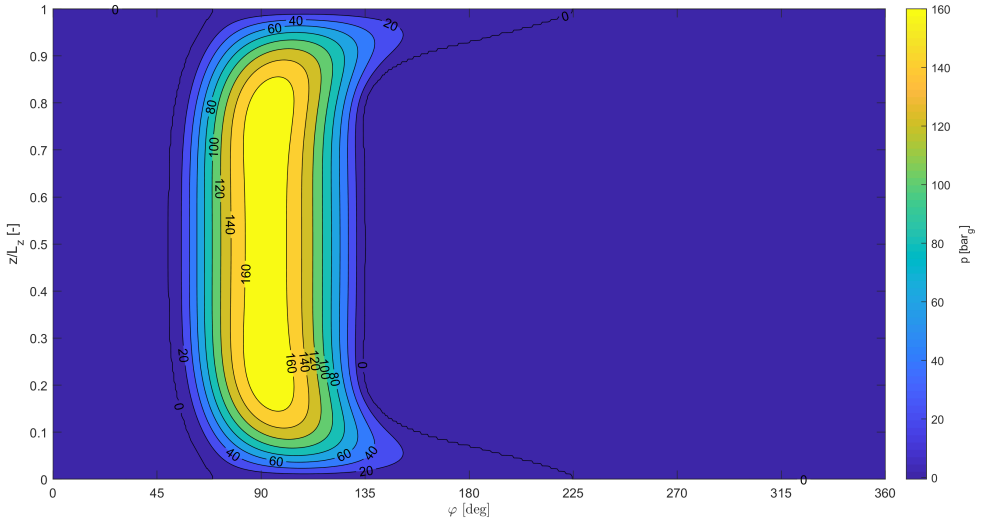

(a) Film Pressure

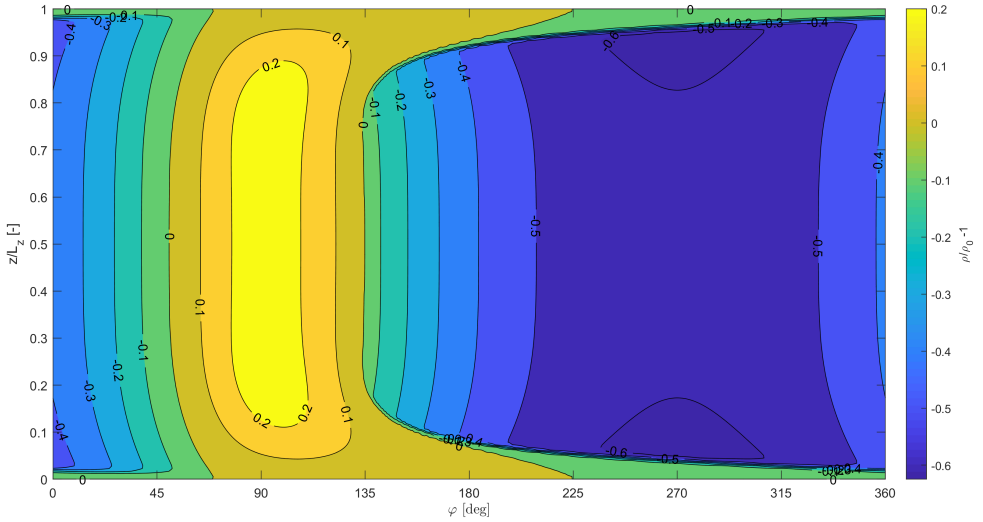

(b) Film Density

Figure 4.9. Steady film makeup for plain journal bearing at eccentricity ratio $\frac{|e|}{C} = 0.5$

the gap height distribution is shifted from that of Figure 4.7. Contrasting with Figures 4.9(a) and 4.9(b), these figures demonstrates how the downstream feeding groove

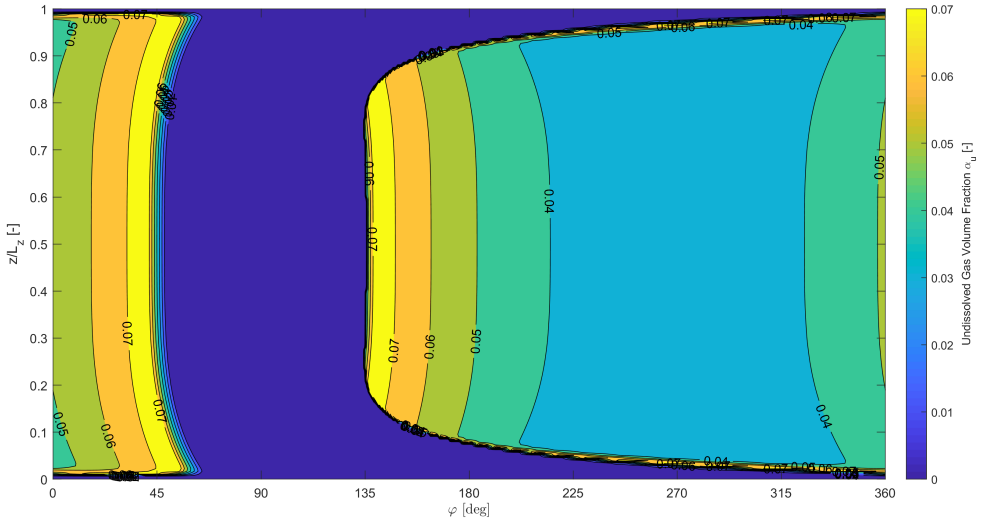

(a) Undissolved gas void fraction

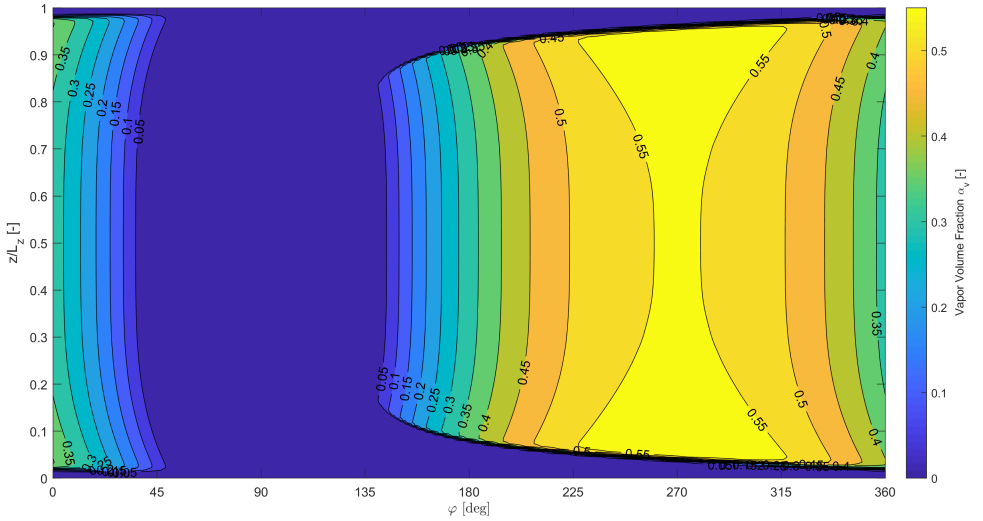

(b) Vapor void fraction

Figure 4.10. Steady ruptured film makeup for plain journal bearing at an eccentricity ratio $\frac{|e|}{C} = 0.5$

extends the region before the collapse of the film, and decreases the magnitude of the density drop in the ruptured film. Additionally, the upstream groove maintains high

pressure in the converging region of the bearing that allows it to build enough pressure to accomplish a bearing number 6 times smaller than the axially fed bearing at the same eccentricity ratio.

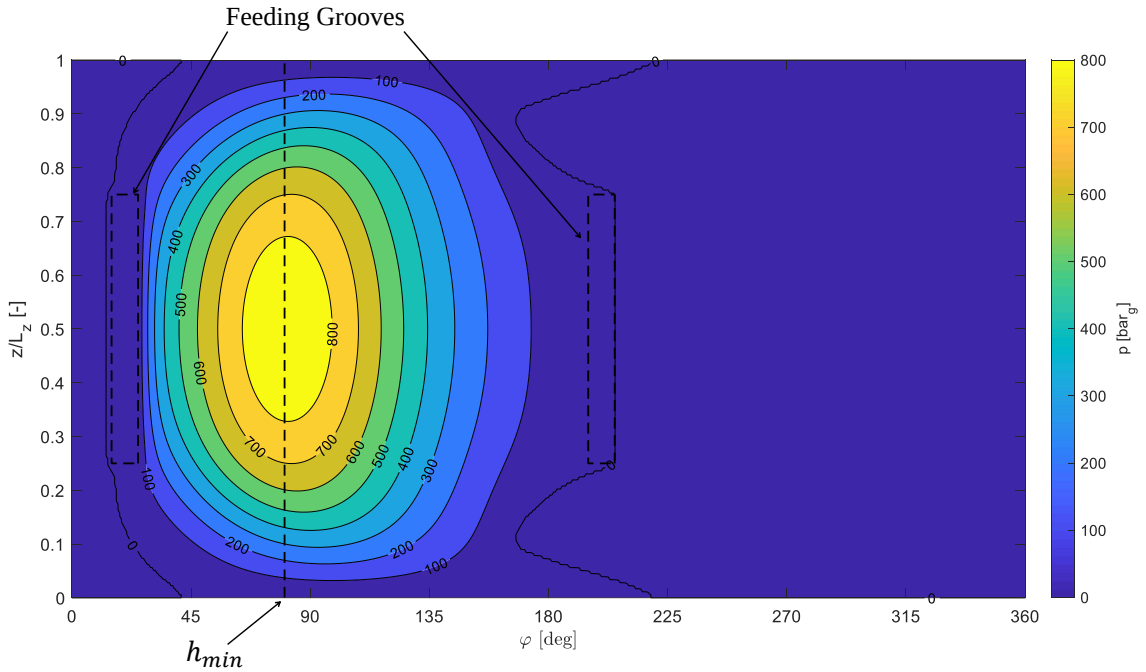

(a) Film Pressure

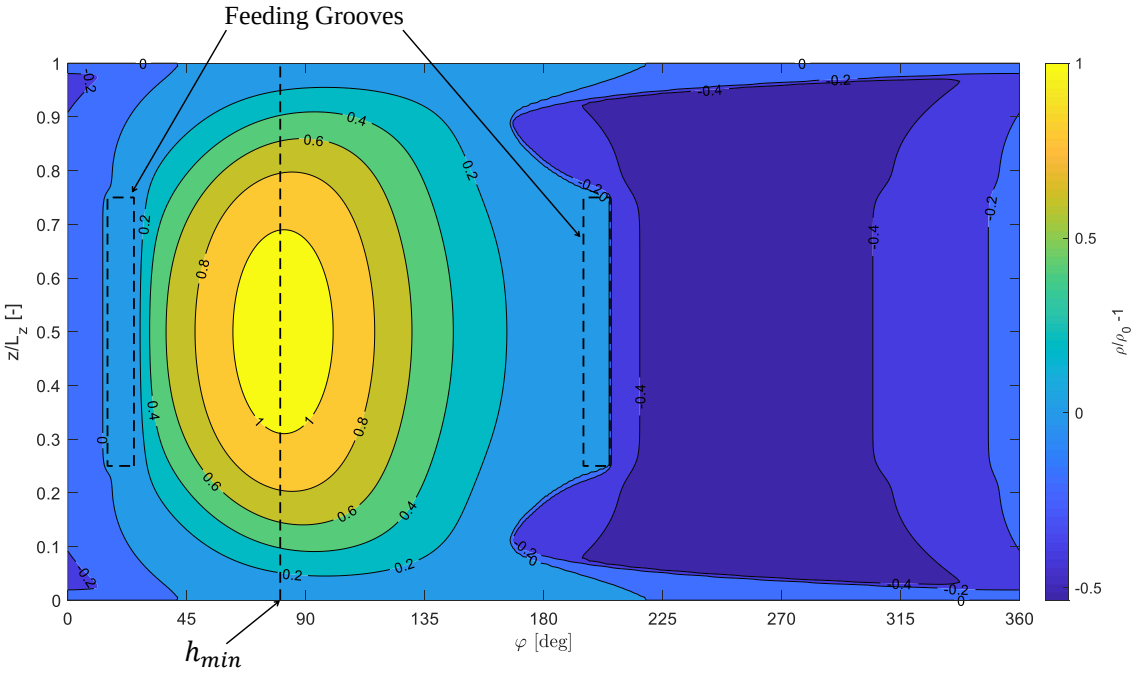

(b) Film Density

Figure 4.11. Steady film makeup for journal bearing with oiling grooves at an eccentricity ratio $\frac{|e|}{C} = 0.5$

4.1.3 Dynamic Journal Bearing

To investigate the implications of the proposed change to the universal Reynolds on the transients of the ruptured film, dynamic simulations are compared with the Elrod implementation performed by Brewe [110] for a whirling journal bearing. For these simulations, Table 3 demonstrates the parameters collected from Brewe, which are used in the results to follow. Notice here that the fluid was assumed to be degassed, such that only liquid and vaporous states of the oil are possible.

First in Figure 4.12(a), the radial load on the journal is plotted over a full orbit of the shaft center with the bearing, demonstrating the 'journal bearing hysteresis loop' observed by Brewe. This figure shows that the two models agree in the first half of the orbit, where there is no cavitation predicted and both models break down to full film Reynolds models.

The results deviate slightly in the separation phase, however. This region was also observed to be sensitive to boundary condition by Brewe, when comparing the Elrod method implementation to the pseudo-Gümbel boundary condition. The disagreement here is likely due to a key difference between the present work and Elrod's, namely that of the diffusion term in the cavitated film. In Elrod's method, the pressure is saturated over the entire cavitated front, with the diffusion term disabled. Instead in the present work, the dimensionless bulk modulus approaches 0 only at the boundary of the cavitation front, then recovers in the ruptured film. While both satisfy the JFO boundary conditions, they permit slight variation in cavitated pressure profile, which would then reflect in a difference in the resulting load on the journal.

As is demonstrated in Figure 4.12(b), the void forms 30ms into the orbit, existing until 63ms for a predicted bubble life of 33ms in line with the prediction of Brewe. As was mentioned in Brewe, this value is larger than observed in experiments, likely owing to a ruptured film that is still numerically existent that cannot be spotted by the photographs.

Table 4.2.
Bearing geometry and operating condition for dynamic journal bearing simulation

Radial clearance C	5×10^{-4} m
Bearing Radius r_b	42.5 mm
Bearing Length L_b	85 mm
Minimum eccentricity $\|e\|_{min}$	0.1
Maximum eccentricity $\|e\|_{max}$	0.8
Shaft angular velocity ω_s	-19.5 rad/s
Orbit angular velocity ω_D	-92.7 rad/s
Reference saturation pressure p_{sat}	0 bar_g
Liquid constant viscosity μ_0	0.066 Pa s
Liquid constant bulk modulus K_0	1.72 GPa
Edge pressure over saturation	1.0133 bar

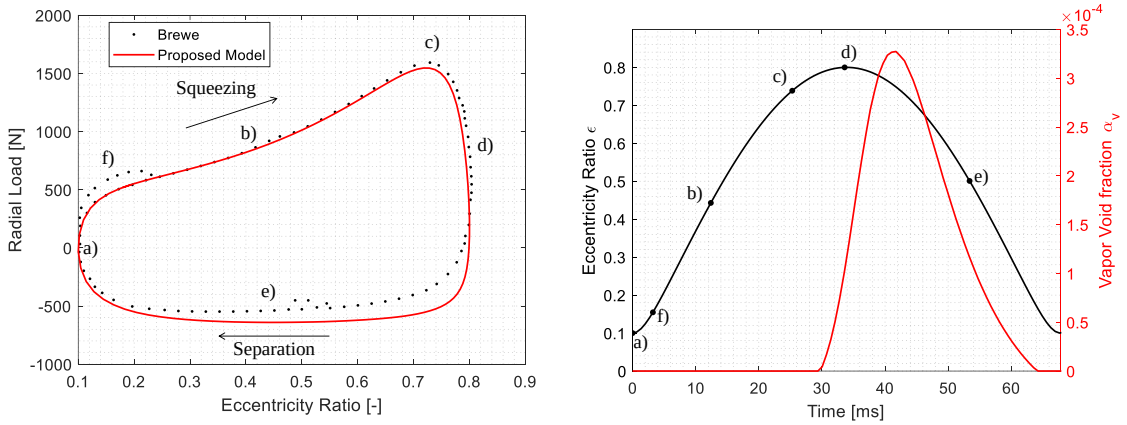

(a) Radial Load

(b) Void Content

Figure 4.12. Film Forces and Void content over a full shaft orbit, where the curve travels clockwise with simulation time

Finally, the film pressures over an orbit can be seen in Figure 4.13. Similarly, the journal position is demonstrated in Figure 4.14 over a full orbit, with the exaggerated film colored by the density ratio at the center cross-section. These figures are helpful in visualizing the circumferential motion of the pressure/density peak as it follows the shaft orbit. Notice here that the points (a)-(f) are also noted in Figure 4.12. These plots show that pressure builds during the squeezing phase of the orbit. By the time the journal reaches its highest eccentricity, though, a void has already formed in the expanded region of the bearing. During the separation phase of the orbit, this bubble is expanded until it collapses just before reaching the minimum eccentricity. This is also demonstrated in Figure 4.14 with the void fraction protruding radially outward, denoting the location of the void which forms and specifically how it follows the orbit. This is a difference with respect to Brewe's result, which predicts that the bubble should last past the minimum eccentricity and into the squeezing phase. As a result, points a) and f) do not agree with Brewe's, due to the difference in timing of the bubble life. Similarly, this discrepancy is responsible for the disagreement in load carrying in the separation phase of the orbit. As was stated above, this difference in pressure profile is likely explained by the difference in the treatment of diffusion in the cavitated film.

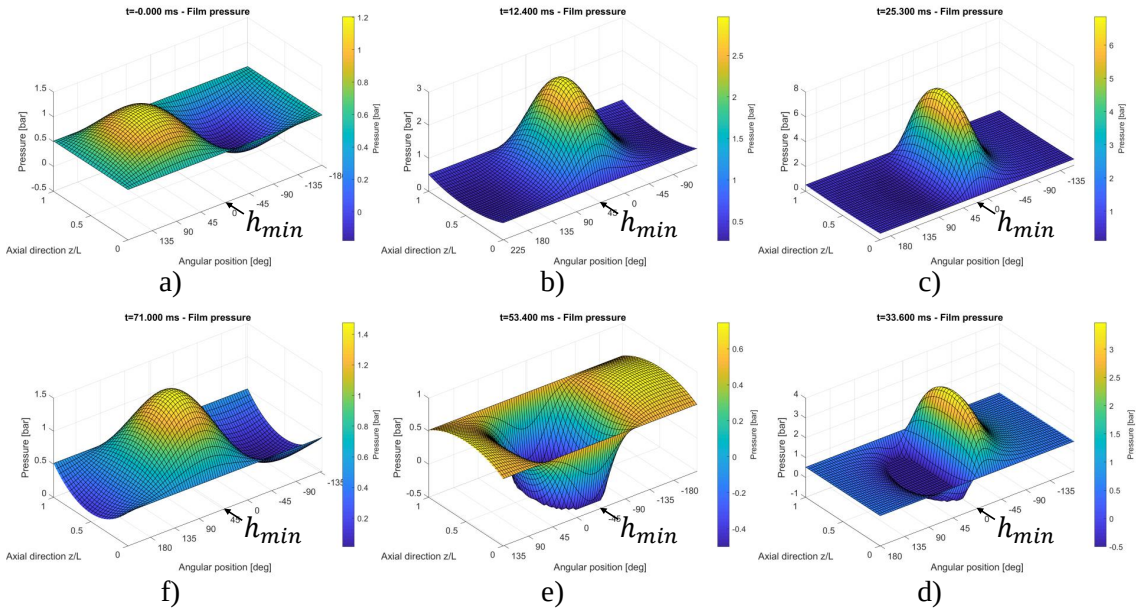

Figure 4.13. Film Pressure over an orbit of the bearing, at same times demonstrated by Brewe, where the time points (a)-(f) are viewed clockwise in increasing time

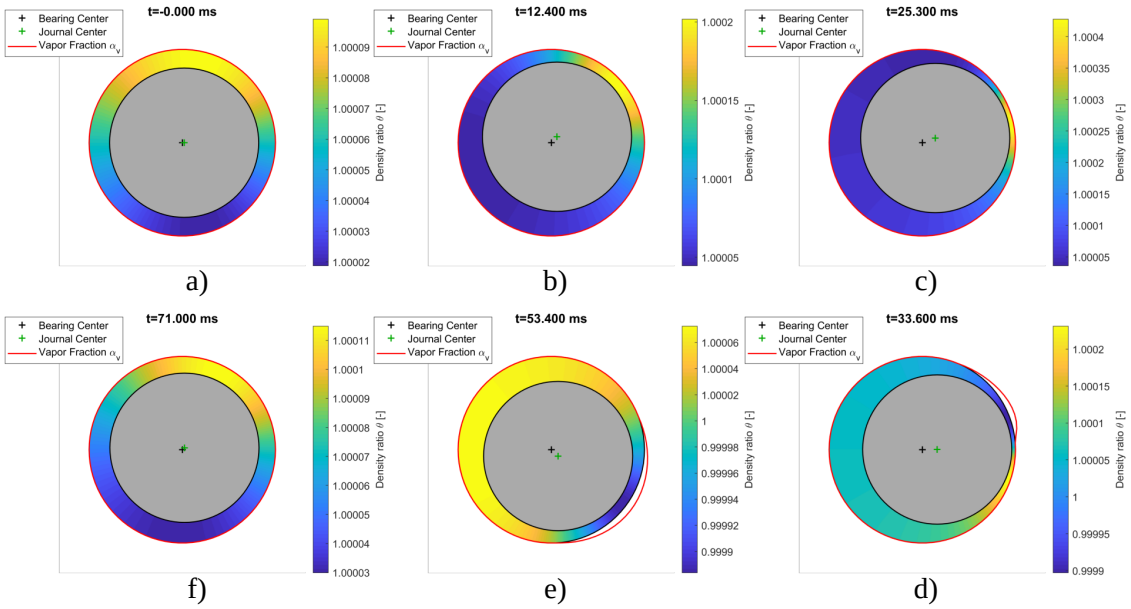

Figure 4.14. Journal trajectory over an orbit, with exagerated film colored by density ratio and void fraction protruding radially outward at the cneter journal cross-secion. Again (a)-(f) are viewed clockwise in increasing time

4.2 External Gear Machine

In the previous section, the core universal Reynolds solver of Multics was validated. As was discussed in Section 1.5, this solver as well as other elementary components of Multics are applied in the simulation tool Multics HYGESim to form a complete system of an EGM. While Table A.2 collects a complete list of the relevant models applied here, it is helpful to graphically represent the components which constitute Multics HYGESim. This is given in Figure 4.15. Here all components of the machine are treated as inertial bodies, with their dynamics solved using the rigid body and deformation modules of Multics. The tooth space volumes and porting volumes of the units are treated as lumped control volumes, with pressure dictated by the pressure buildup equations. The turbulent flows between both the tooth space volumes and the porting volumes is modeling using the orifice equation. Flow and force due to the leakage path across the tooth tips of the unit is modeled as Couette-Poiseuille flow. Finally, the flows and forces in the journal bearing and lateral lubricating interfaces solve Reynolds equation, using either analytical approximations for a LP model or the complete Reynolds film objects for a DP model. Boundary friction between the bushing/lateral plate and the casing (if lateral compensation is employed) is modeled as Stribeck friction. In the present section, model validation of Multics HYGESim will be performed using two commercial EGMs.

4.2.1 Reference Unit E1

In order to validate the performance of Multics HYGESim, experimental measurement of the Ref E1 EGM was performed at Purdue University with an ISO VG46 working fluid. The test setup is demonstrated in Figure 4.16 with both an image of the setup and the corresponding ISO schematic. In this circuit, a needle valve (represented by the orifice O2) is used to load the unit. Between the pump and the load, there is a rigid and constant diameter straight pipe with a close end termination (orifice O1) which is only used to create standing waves which are easy to reproduce

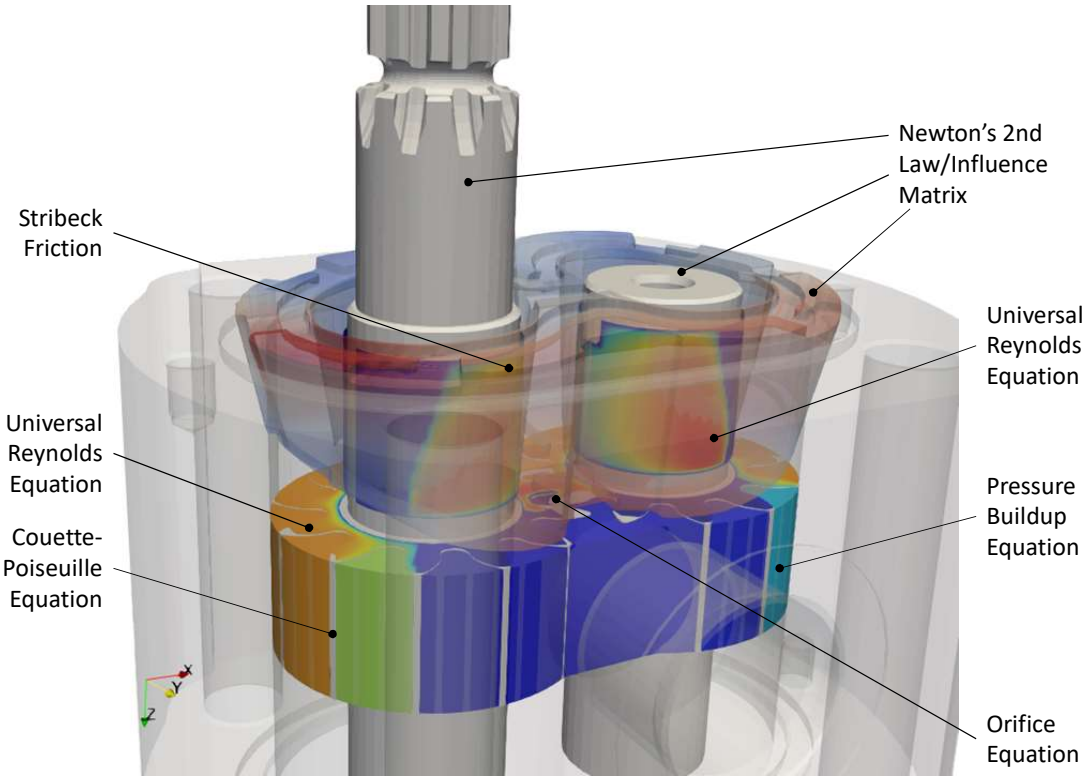

Figure 4.15. Modeling components for Multics HYGESim

in simulation for pressure ripple comparison. While it is typically the flow ripple that is of interest for a pump, the dynamics of flow meters are typically too slow to capture this ripple. Instead, it is common to measure the pressure ripple, which can be captured with high frequency pressure sensors. Since the pump is loaded by a constant orifice, the resulting pressure ripple is directly proportional to the flow ripple

$$Q \propto \sqrt{\Delta p} \tag{4.8}$$

per orifice equation 2.5, and matching of one inherently validates the other. This experimental technique was first introduced by [137]. The details of the measurement equipment used in this experiment are defined in Table 4.3.

In Figures 4.17 – 4.22, the resulting pressure ripple at various operating conditions throughout the operating range is given. In these figures, the ripple is demonstrated

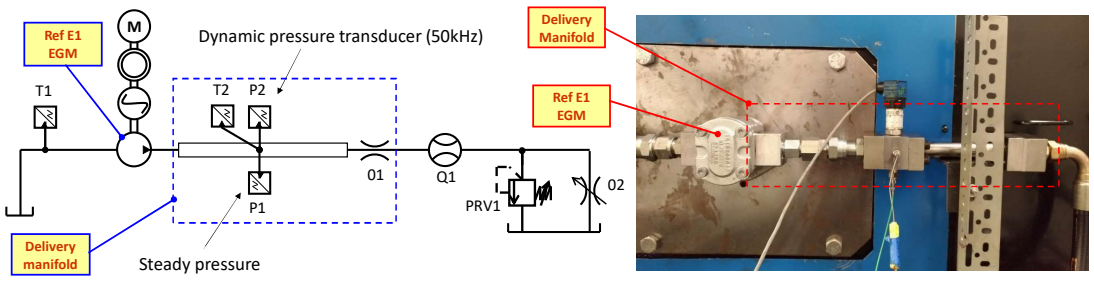

Figure 4.16. Experimental setup for measurement of Ref E1 EGM

Table 4.3.
Measurement devices for EGM validation schematic

Label	Sensor	Model	Specifications	Accuracy
P1	Pressure	Wika S-10	0 to 400 bar	±5% of span
P2	Pressure Ripple	Kistler	0 to 600 bar	
T1	Thermocouple	Omega K-type	-5 to 200 °C	±1°C
Q1	Flow Meter	VSE VS02	0.1 to 120 L/min	±0.3%

in both the time and frequency domains. These results highlight that the model shows good agreement with the first and second harmonics of the flow ripple, and matches higher for some operating conditions. The first harmonic of the ripple corresponds to the number of displacement chambers, in the case of the EGM to the number of teeth. The ripple at these frequencies corresponds to phenomenon which occur once per tooth span, including the cross-port flow permitted by the grooves in the meshing zone, pressure overshoot, and the pressurization of the TSV in the casing.

The second harmonic contains information about a unit acting in dual-flank operation, where contact between both flanks of the teeth in meshing effectively doubles the number of displacement chambers. After these two harmonics, the behavior of the ripple is more sensitive to manufacturing errors in the units and external factors such as the electric motor driving the unit.

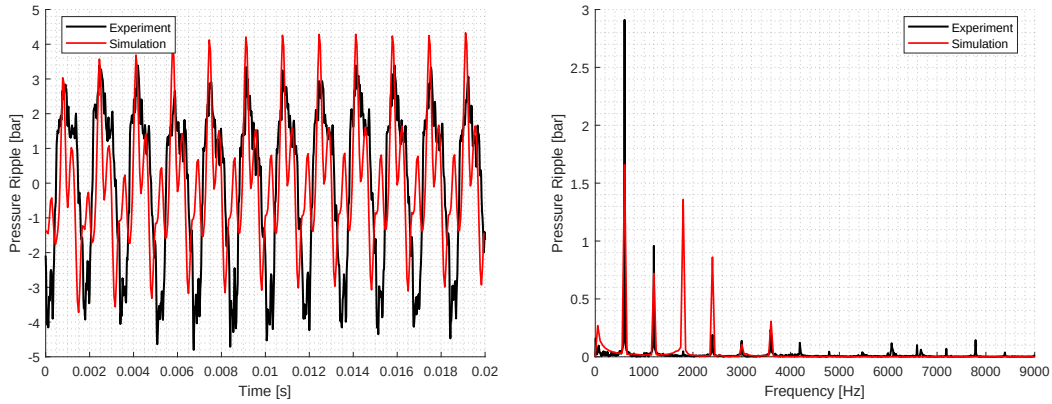

(a) Time Domain (b) Frequency Domain

Figure 4.17. Pressure ripple for $\Delta p/p_{\max}$=100%, shaft speed of 3000 rpm

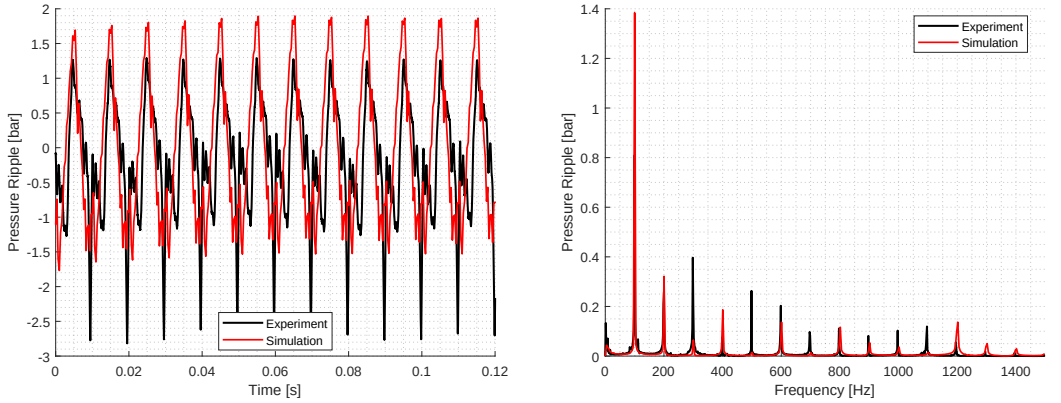

(a) Time Domain (b) Frequency Domain

Figure 4.18. Pressure ripple for $\Delta p/p_{\max}$=100%, shaft speed of 500 rpm

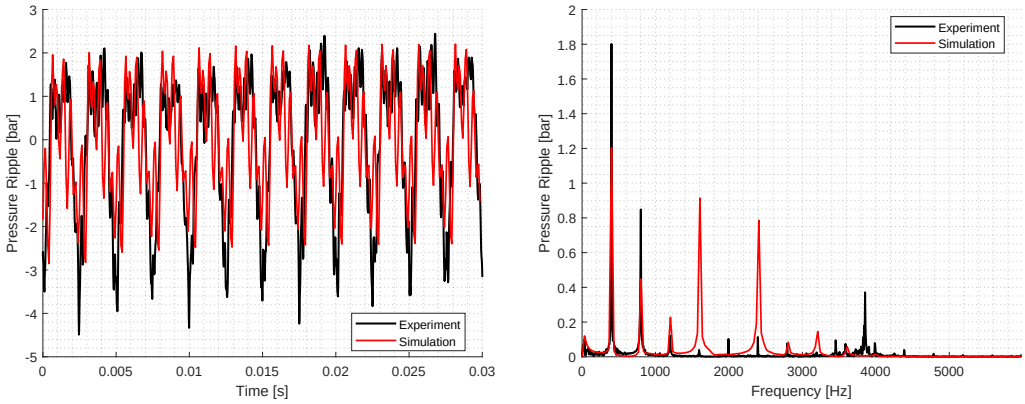

(a) Time Domain (b) Frequency Domain

Figure 4.19. Pressure ripple for $\Delta p/p_{\max}$=80%, shaft speed of 2000 rpm

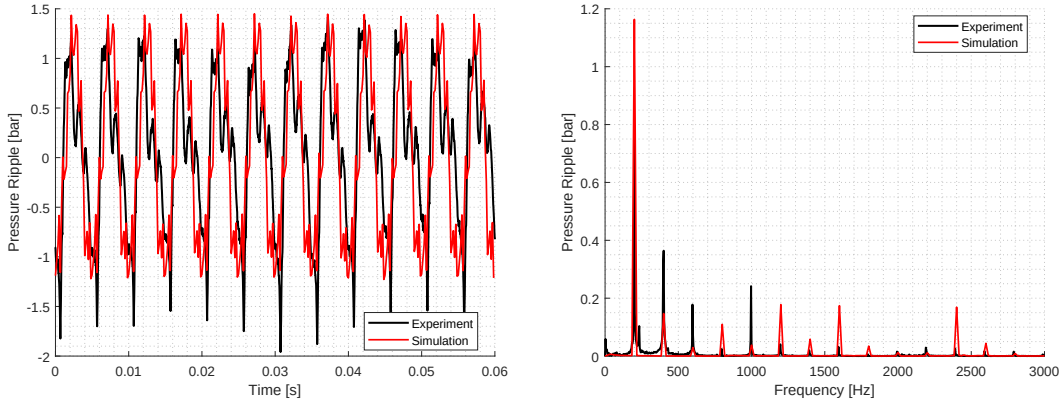

(a) Time Domain (b) Frequency Domain

Figure 4.20. Pressure ripple for $\Delta p/p_{\max}$=40%, shaft speed of 1000 rpm

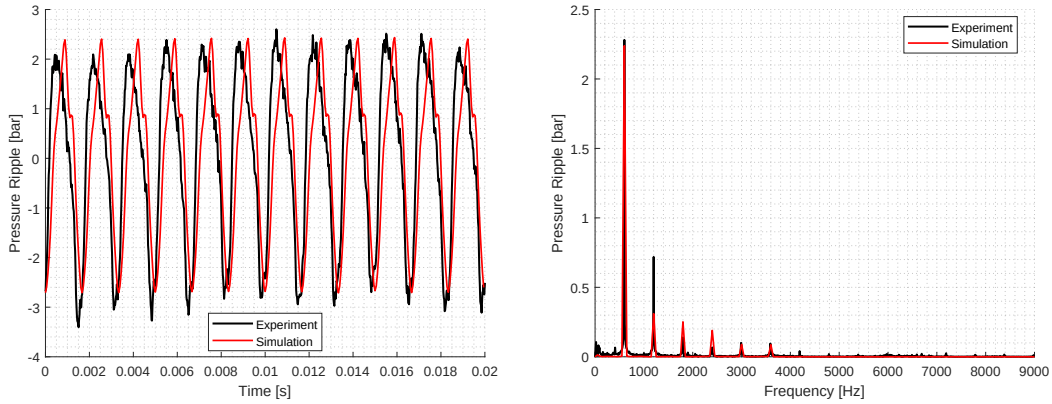

(a) Time Domain (b) Frequency Domain

Figure 4.21. Pressure ripple for $\Delta p/p_{\max}$=20%, shaft speed of 3000 rpm

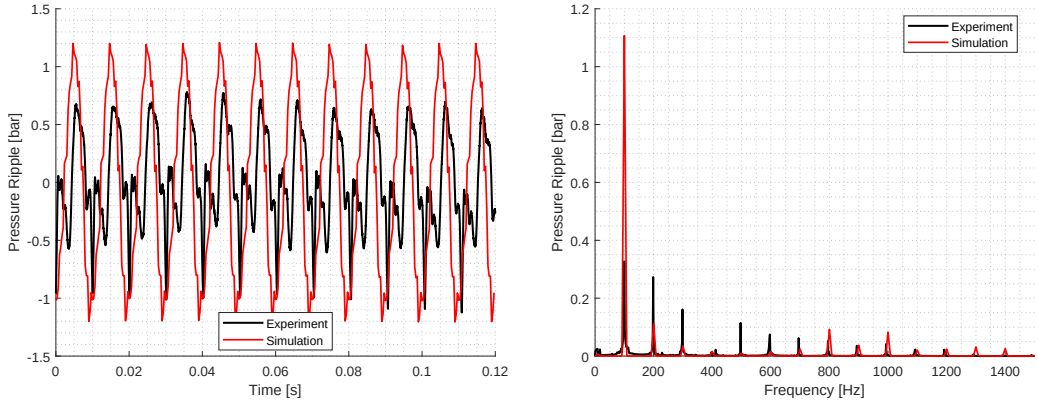

(a) Time Domain (b) Frequency Domain

Figure 4.22. Pressure ripple for $\Delta p/p_{\max}$=20%, shaft speed of 500 rpm

4.2.2 Reference Unit E2

The previous section showed the ability of the unit to capture the dynamic behavior of an EGP. Since these units contain only internal leakage paths, though, they provide no means for non-invasive validation of their interfaces. For this reason, additional tests were conducted with the Ref E2 EGM unit operating as a pump, again with an ISO VG 46 mineral oil as working fluid. The test circuit is very similar to that of Figure 4.16, with the addition of an external drain line. These tests were performed in the same test setup at Purdue University, using the same loading strategy and measurement devices shown in Table 4.3. As visible in Figure 4.23, the unit is externally drained, allowing for an isolated capturing of the drain flows of the unit.

The goal of this analysis is to demonstrate agreement of both the steady and transient behavior of the unit. Furthermore, by collecting the flow from an external drain port of the unit, validation of the lubricating interfaces in isolation can be performed through indirect flow prediction comparison.

First, the steady behavior of the reference unit is examined, with respect to the volumetric performance. Tests at different operating speeds and loads were conducted to construct the flow-pressure characteristics of the unit as shown in Figure 4.24(b). By recreating this procedure in Multics HYGESim, the resulting flow behavior is included for comparison in the same plots. Comparing this to the theoretical flow expected by the unit, the volumetric efficiency is given in Figure 4.24(a). Here, the efficiency is defined using the kinematic displacement of the unit V_{kin}, corresponding to the volume of fluid that is swept by the teeth of the gear as it rotates.

$$\eta_v = \frac{\overline{Q}}{\omega V_{\text{kin}}} \tag{4.9}$$

This study demonstrates the ability of Multics HYGESim to capture both the magnitude and trends of the efficiencies of an EGM over a wide range of operating conditions.

The delivery apparatus used for the tests allows for a straightforward comparison between the measured and the simulated pressure pulsations. As was discussed in

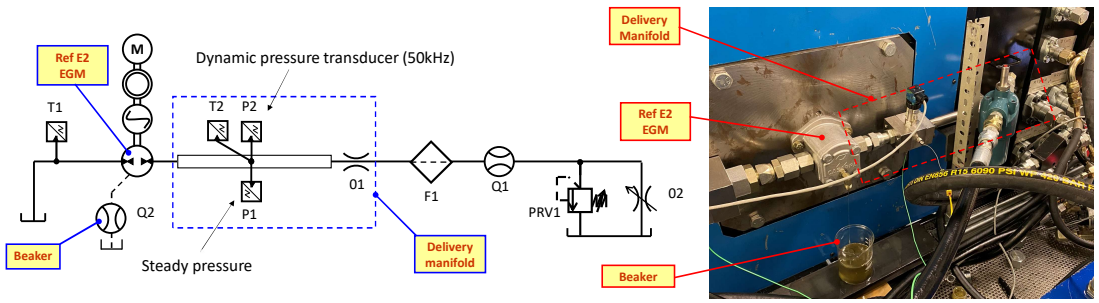

Figure 4.23. Experimental setup for measurement of Ref E2 EGM

Section 4.2.1, this pressure ripple is directly proportional to the flow ripple of the unit. In Figure 4.25, the resulting pressure oscillation at the pressure sensor used for pressure ripple measurements (P2, 50kHz) is shown. This result is compared to the predictions of Multics HYGESim, demonstrating agreement in both the time and frequency domains. It should be remarked that the pressure ripple in an EGM is highly sensitive to both the position and pressurization of the internal TSVs. This result, then, shows that the tool can capture not only the steady behavior of the unit, but also its dynamic pressure-flow characteristics as well as the main internal fluid dynamic features.

The choice of an externally drained EGM, shown in Figure 4.23, allows for a means of indirect measurement of the lubricating film behavior. As was highlighted in Figure 1.6, this drain flow must travel out of the TSVs into the lateral lubricating interface, and through the journal bearing before finally escaping through the drain port. Since these flow were demonstrated in Equation 3.18 to be cubic in gap height, the resulting flow is highly sensitive to the positions of the floating elements. While the volumetric efficiency of the unit also reflects these flows, comparison of the predicted drain-flow provides a further indirect validation of the lubricating interface models only. Figure 4.26 provides a reasonable agreement between the drain leakage predictions of Multics HYGESim as compared to the experimental measurement. It is worth noting that in this study, the nominal clearances of the unit were used. With this highly

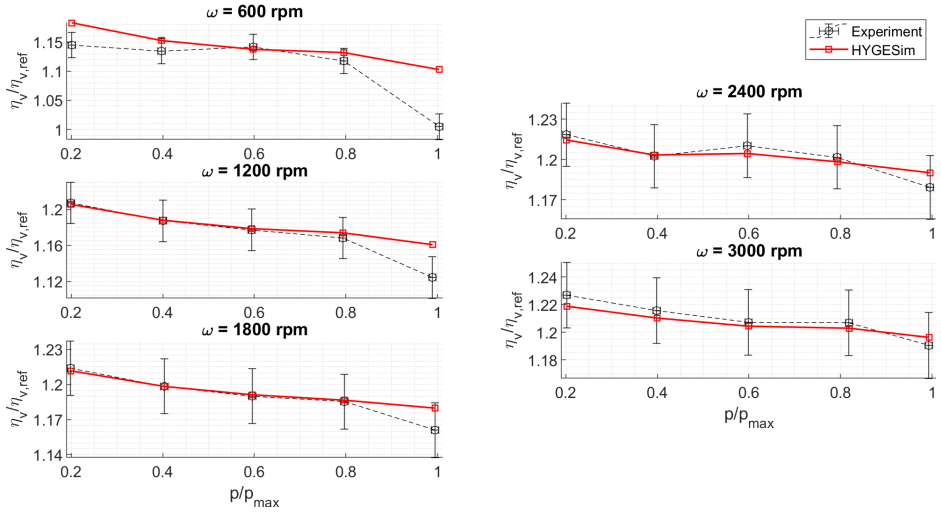

(a) Volumetric Efficiency

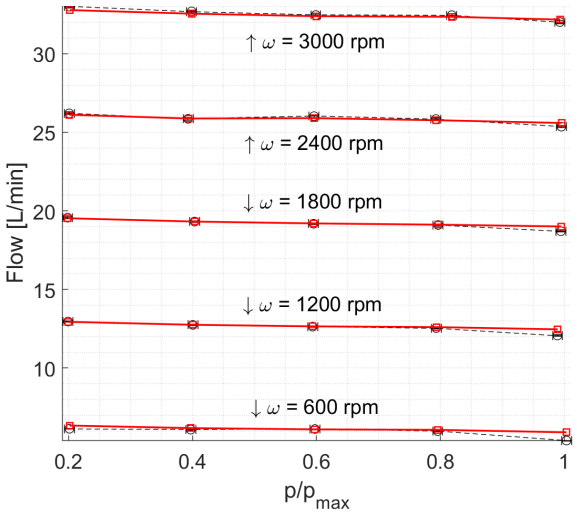

(b) Flow Characteristics

Figure 4.24. Steady State comparison of Multics HYGESim and experimental results (a) Volumetric Efficiency (b) Pressure-Speed Flow characteristics

sensitive cubic flow-gap relationship, agreement with experiment could be improved if the true clearances of the unit were taken and used as input to the model. However, since the goal of this study is to develop a tool which can be used in place of a manufactured prototype, the true clearance would not be known. Instead, it is elected

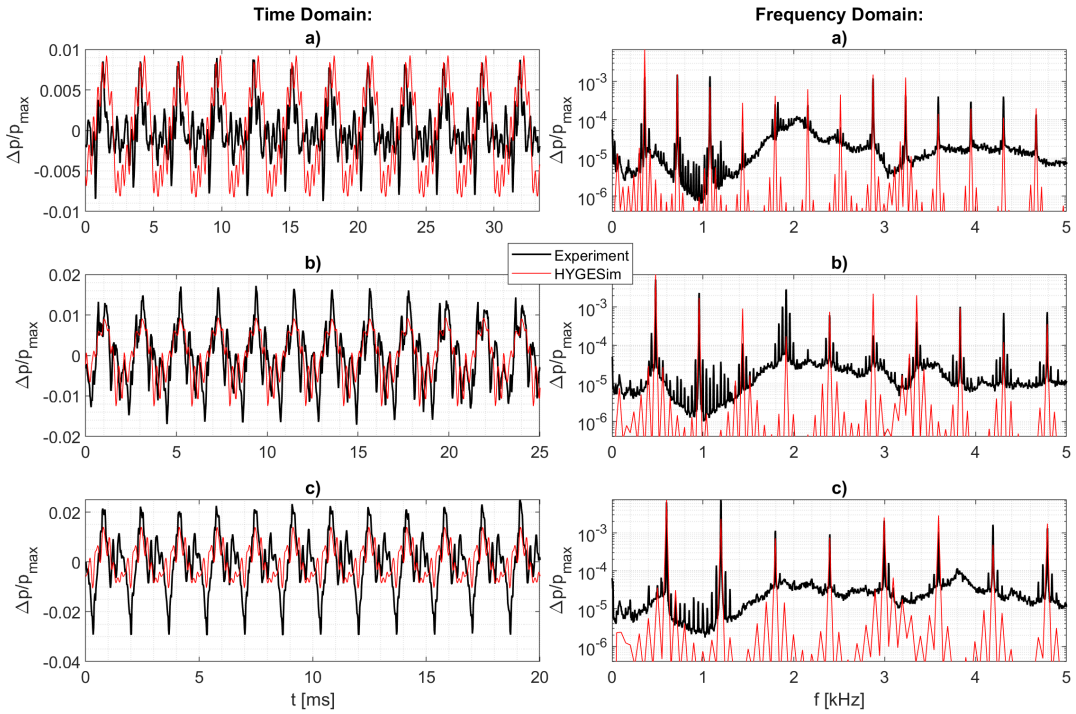

Figure 4.25. Pressure oscillation in both time and frequency domains a) $p/p_{\max} = 0.4$, $\omega = 1800$ rpm b) $p/p_{\max} = 0.6$, $\omega = 2400$ rpm c) $p/p_{\max} = 0.8$, $\omega = 3000$ rpm

here to demonstrate the ability of the tool to predict performance using only known design quantities. This result, then, confirms that the behavior of isolated lubricating interfaces of the machine can also be captured by the tool using only nominal geometry of the unit.

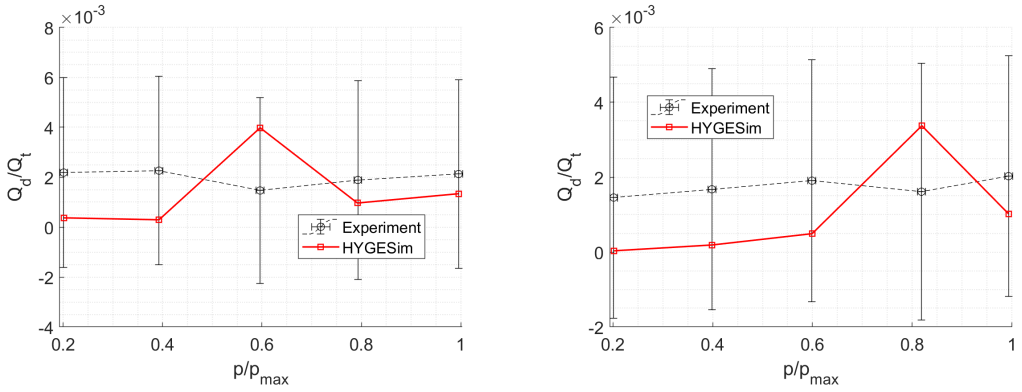

(a) 2400 rpm (b) 3000 rpm

Figure 4.26. Steady State comparison of Multics HYGESim and experimental results drain leakages at (a) 2400rpm (b) 3000rpm

4.3 Axial Piston Machine

A major goal of this thesis is to develop a modeling suite applicable to any PD machine. Similar to Multics HYGESim, the components of the simulation suite Multics developed in Chapters 2 and 3 can be used to construct the complete system of an APM. This model is referred to as Multics CASPAR, with all model components collected in Table A.1. Again for clarity, these components are represented graphically in Figure 4.27. Here the pistons, slippers, cylinder block, and swashplate are treated as inertial bodies, with dynamics and deformation captured by the respective modules of Multics. Based on these dynamics, the displacement chambers, hydrostatic pockets, and porting volumes are treated as lumped volumes with pressure dictates by the pressure buildup equation. Turbulent flow exchange between these lumped volumes is modeled using the orifice equation. The friction of the ball-socket interface of the piston-slipper pair is modeling using a Stribeck friction model. Finally the lubricating interfaces of the machine (piston-cylinder, slipper-swashplate, and valve plate - cylinder block) are modeled using Reynolds equation. For LP simulations these interfaces

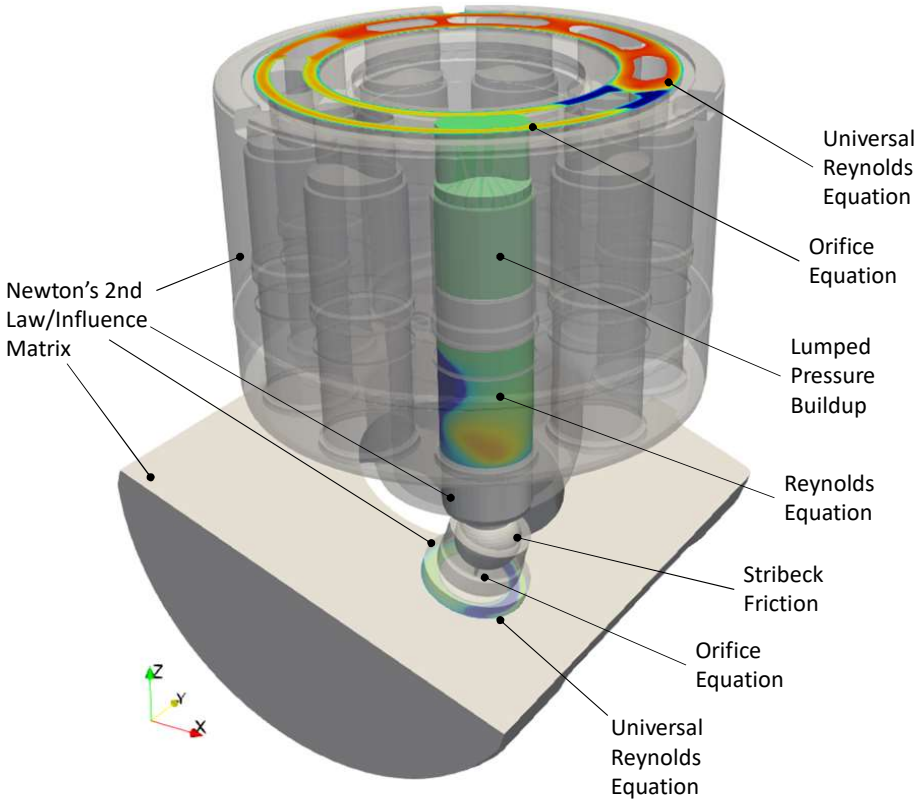

Figure 4.27. Modeling components for Multics CASPAR

are simplified, and for DP simulations they are modeled with the complete universal Reynolds solver.

The goal of this section, then, is to perform a similar non-invasive validation of the ability of Multics CASPAR to predict the behavior of a commercial APM during operation. In order to perform this validation, the steady state experiments performed by [138] on a reference commercial high pressure axial piston machine of swash-plate type are recreated (Ref P1).

The unit was loaded with the circuit demonstrated in Figure 4.28. By varying the operating speed and pressure relief (PRV1) setting, the pressure-flow characteristic of the unit was attained. In Figure 4.29(a), the resulting behavior of the unit is demonstrated with comparison against the proposed model. It is worth noting here,

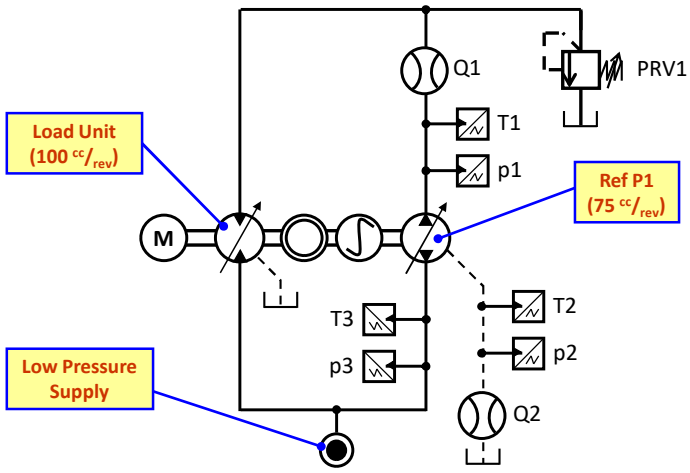

Figure 4.28. Experimental Setup of the reference unit performed by [138]

that the efficiencies are calculated using the shear and flow predictions of the Reynolds film model instead of the analytical approximations.

Following the approach discussed in [139], the total efficiency of the experiment is extracted from the steady state flow, pressure, and temperatures of the unit taking properties of the ISO VG 32 hydraulic oil used in this work. In Figure 4.29(b) this result is compared to the total efficiency prediction of Multics CASPAR, defined as the efficiency with which the unit converts mechanical power to useful hydraulic power [1]

$$\eta_t = \frac{Q_{\text{out}}\, p_{\text{out}} - Q_{\text{in}}\, p_{\text{in}} - Q_{\text{drain}}\, p_{\text{drain}}}{\tau_s\, \omega_s} \tag{4.10}$$

This figure confirms that the proposed model is able to accurately capture the efficiency of the unit over a wide range of operating speeds and pressures, with both the magnitude and trend of the experimental curve tracked.

For better understanding of the relative contributions of leakage and shear loses in the unit, Figure 4.30 shows comparisons of the volumetric and hydro-mechanical efficiency components of the total efficiency of the unit. Here volumetric efficiency η_v

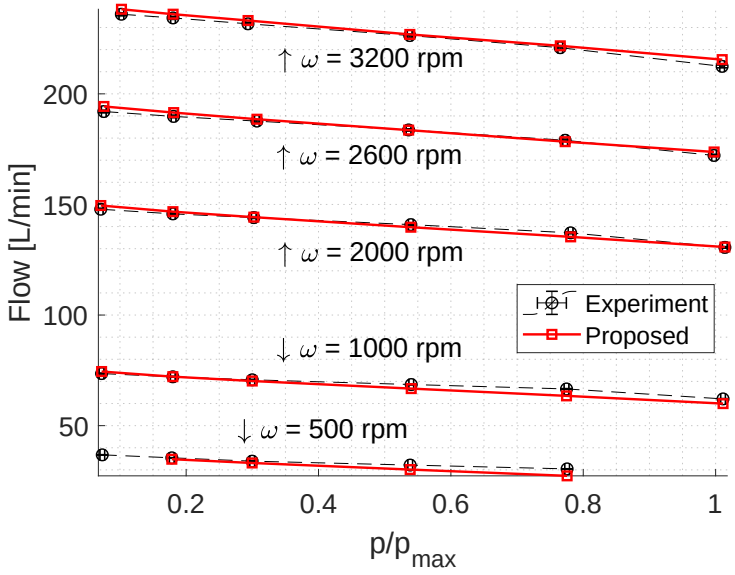

(a) Pressure-Flow Characteristic

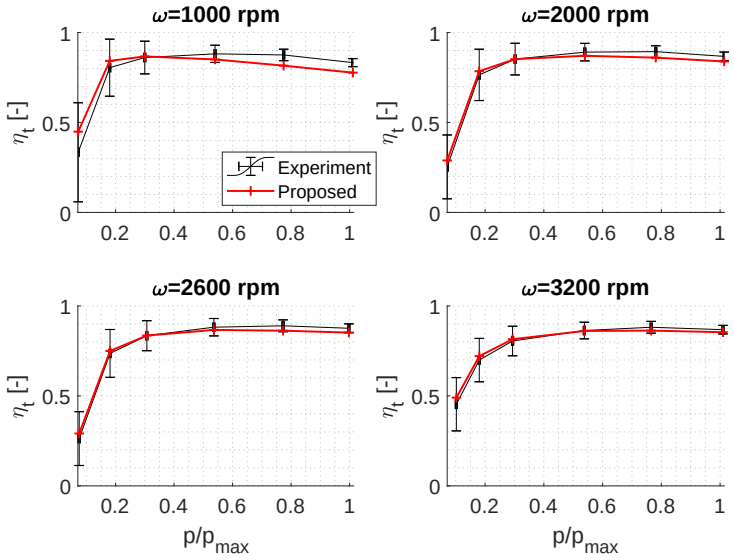

(b) Total Efficiency

Figure 4.29. Steady state performance of reference unit (a) Pressure-Flow Characteristic (b) Total Efficiency

is found using Equation 4.9 given the kinematic displacement of the unit, so that the corresponding mechanical efficiency must be

$$\eta_m = \eta_t/\eta_v \tag{4.11}$$

It is important to note that the major sources of both volumetric and shear losses in an APM are in its lubricating interfaces. These results, then, are only attainable with accurate modeling of the lubricating interfaces of the machine. Thus, these results act to indirectly validate both the flow and shear predictions of the lubricating interfaces. As was discussed for the case of the EGM, Equation 3.18 shows a cubic dependence of leakages on the gap height. Additionally, Equation 3.62 show how the shear losses shows reciprocal dependencies on the gap distribution in the interfaces. Thus since these functions are heavily dependant on the gap distribution, the matching of these results also indirectly validates the dynamics of the floating bodies in the unit.

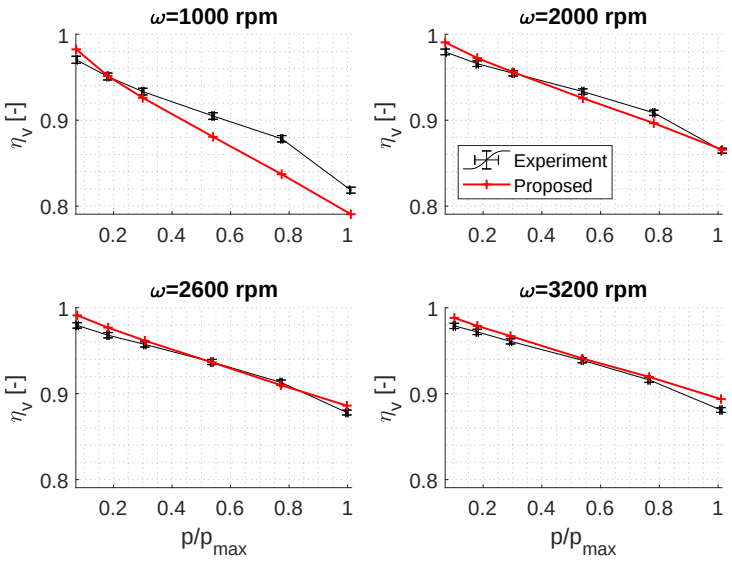

(a) Volumetric Efficiency

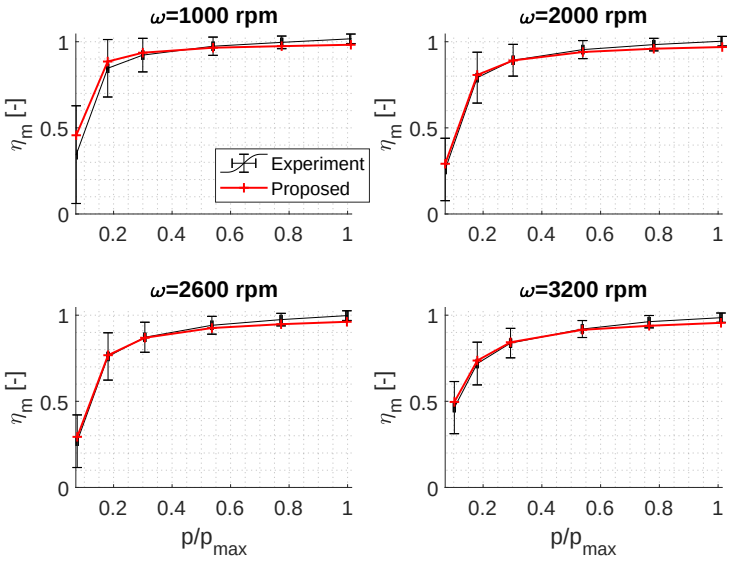

(b) Mechanical Efficiency

Figure 4.30. Steady state efficiency components of reference unit (a) Volumetric (b) Mechanical

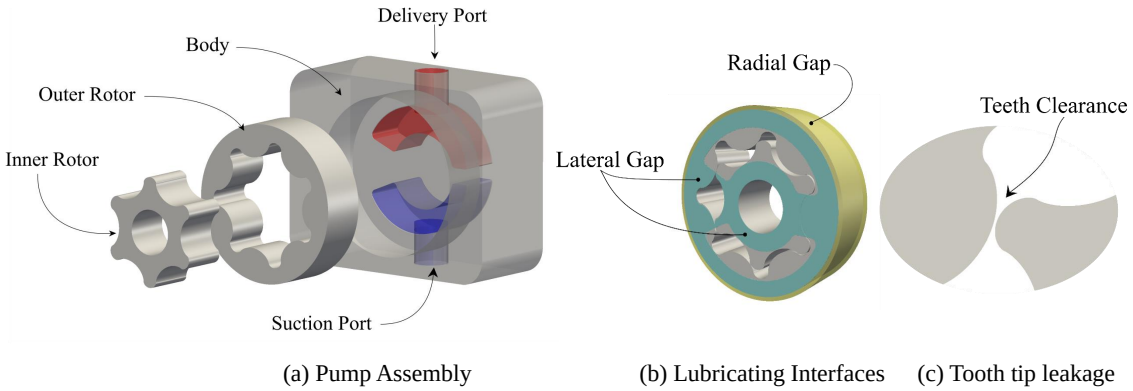

Figure 4.31. Demonstration of working principal of a Gerotor unit, highlighting loss sources in the machine (a) the assembly of a Gerotor (b) lubricating interfaces in the unit (c) flow constriction at tooth tips

4.4 Gerotor

The working principal of a Gerotor is similar to that of an EGM, where the meshing teeth form a contraction and expansion in the delivery and suction volumes respectively. This unit is demonstrated in Figure 4.31(a) from Mistry et al. [140]. The key difference here, is that an external gear rotates within an internal gear, with exactly one tooth difference such that sealing is maintained between adjacent volumes of fluid trapped by contact at each tooth shown in Figure 4.31(c). The lubricating films to be considered in this unit are the lateral gap interface, similar to the EGM except without a balancing element in this case, and the radial gap of the outer rotor which acts as a journal bearing. Both of these interfaces are shown in Figure 4.31(b).

Applying the modeling suite Multics presented in this thesis, Mistry et al. [140] simulated the Ref G1 Gerotor pump, validating against both the pressure and torque ripples of the unit against experimental results. These results act as both a validation of the tool in terms of accurately reflecting the physics, but also a proof of concept that the API can be directly applied to other units besides the EGM and APM for

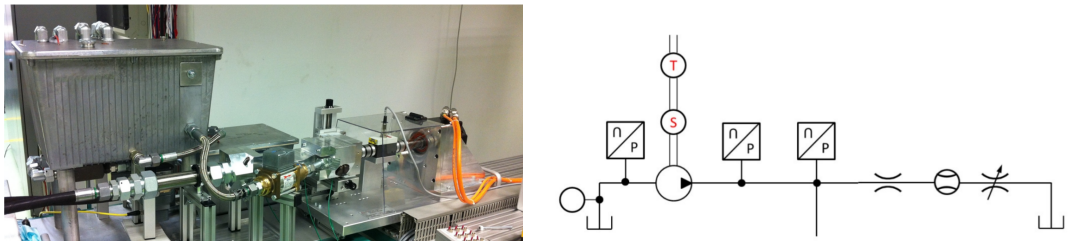

(a) Test Circuit (b) ISO Schematic

Figure 4.32. Experimental setup for Ref G1 Gerotor validation with (a) a picture of the test setup (b) the corresponding ISO schematic representation

which it is derived here. The following results are included here for completeness, but the reader is encouraged to refer to the original text for a more detailed explanation.

First in Figure 4.32, the experimental setup is shown both with an image and the corresponding ISO schematic. In this test, the input speed and torque of the drive shaft are recorded, as well as the flow across the pump. In addition, two pressure sensors are shown, where one is used for observing mean pressure and the other is a high frequency sensor for pressure ripple measurement.

Due to confidentiality, the true values of pressures and torques cannot be reported here, and are instead normalized by arbitrary values. Starting first with the pressure ripple, Figure 4.33(a) shows a comparison between the simulated and predicted flow ripple of the unit. Unlike the case of the EGM shown above, the shaft frequency of the unit is clear in the experimental flow ripple in this unit. This is typically caused by manufacturing errors present in individual teeth of the gears, so that the feature repeats only once with each shaft revolution. As a result, a low frequency wave over the 360° shaft rotation is visible. Since the geometry was assumed to be ideal in the simulations performed by [140], these affects were not captured. Excluding this, the results show good agreement with both the magnitude and shape of the resulting pressure ripple of the test circuit.

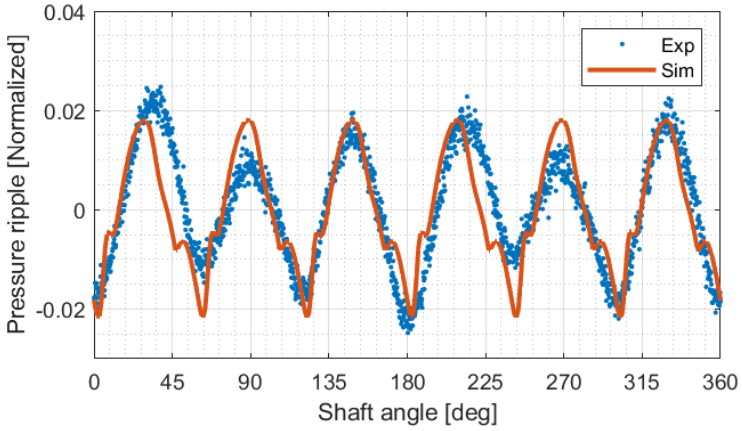

(a) Pressure Ripple

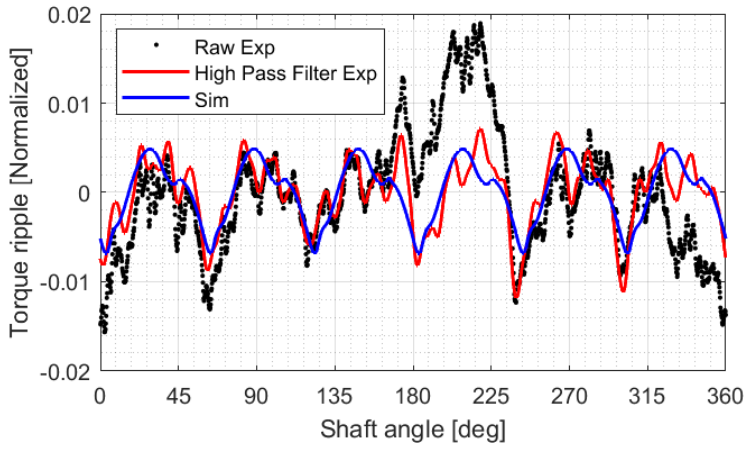

(b) Torque Ripple

Figure 4.33. Instantaneous pressure and torque ripple in unit over a full shaft revolution

Similarly, the torque ripple is considered. To avoid effects of manufacturing error and misalignment discussed with respect to the pressure ripple, the raw torque data was high-pass filtered. This acts to isolate the effects of the nominal Gerotor design. In Figure 4.33(b), the resulting filtered curve shows good agreement with the torque ripple predicted by simulation, where again values are normalized arbitrarily for confidentiality.

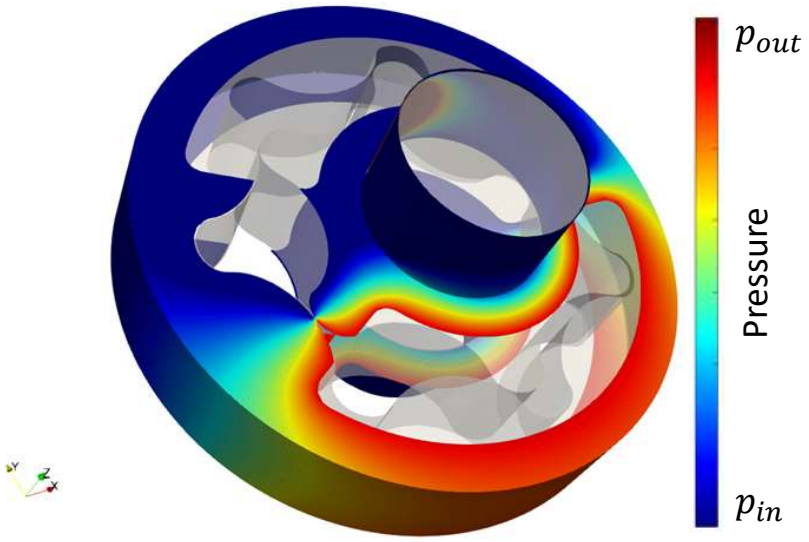

Figure 4.34. Net lubricating interface normalized pressure distribution over the DP domain of Ref G1

It is worth noting that these results were attainable only by considering the lubricating interfaces of the unit. In Figure 4.34 taken with permission from [140], an instant of the lubricating interfaces' pressure distributes are shown. This result demonstrates the applicability of Multics to markedly different geometries than the EGM and APM which this thesis discusses.

5. MODEL POTENTIALS

In Chapters 2 and 3, the various novel components of Multics were verified against relevant commercial software and analytical solutions. In Chapter 4, the core Universal Reynolds equation was validated against experimental and reference results in the state of the art. Additionally, the specific applications to EGM (Multics HYGESim) and APM (Multics CASPAR) were validated against experiments of the respective machines. With a verified and validated model, the present section will now go on to demonstrate some applications of the tool to highlight the model potentials. First in Section 5.1, the implications of each modeling feature will be studied using an EGM as reference. Next in Section 5.2, the use of this tool for a complete virtual prototyping will be shown. Finally, Sections 5.3 and 5.4 will perform detailed simulations of the mutual interactions present within EGMs and APMs respectively.

5.1 Detailed Analysis of a High Pressure EGP

To demonstrate the use of this tool on an existing unit, the following study is performed on the Ref E1 EGP. With this unit, the impact of each component of the tool can be discussed. For all simulations, the simplified loading circuit given in Figure 5.1 is used, where the line volume between the pump and load orifices is intentionally kept very small to exaggerate the resulting pressure ripple. Note here that the electric motor is assumed to be a perfect torque source, and introduces no variation of speed into the simulation. For confidentiality, the true values cannot be reported here, and all physical quantities are normalized with respect to representative quantities for the unit.

First, the fully lumped parameter model is demonstrated, both with fixed gears (F mode) or with the gears free to shift (FFI mode). In Figure 5.2, the delivery

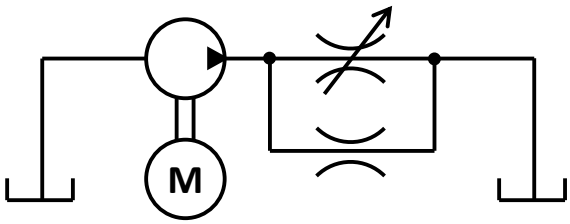

Figure 5.1. Hydraulic schematic for High Pressure EGP detailed simulation

flow of the unit is demonstrated, with comparison between both F and FFI mode to the kinematic flow of the unit. First comparing the F mode to the kinematic, the effect of the compressibility of the fluid is considered. Multiple drops in the flow, demonstrated by Figure 5.2(b), correspond to points in which the fluid that would have otherwise been delivered must instead be drawn into a TSV as it transitions from low to high pressure. Additionally, a drop occurs in the meshing zone, when the highly throttled relief grooves cannot deliver all of the volume displaced by the teeth. Finally, the capacitance of the outlet volume of the unit means that the flow does not drop as sharply in real operation as the kinematic curve predicts, with dynamics that lag the kinematic.

Also included in this figure is a comparison of the results obtained with and without the inclusion of macro-deformation of the bodies. While the difference is small, an additional benefit of the separation of macro and micro effects is the ability to consider the macro-scale deformation of the bodies without the necessity to use an influence matrix. To understand the reason for this difference, Figure 5.3 shows the instantaneous gear center distance in both the FFI simulations with and without macro deformation. This figure shows that due to the deformation of the bodies, the center distance of the gears perceived by the geometric module changes, reflecting a different net displacing and sealing action of the gears, and as a result the flow behavior (Figure 5.2) is changed.

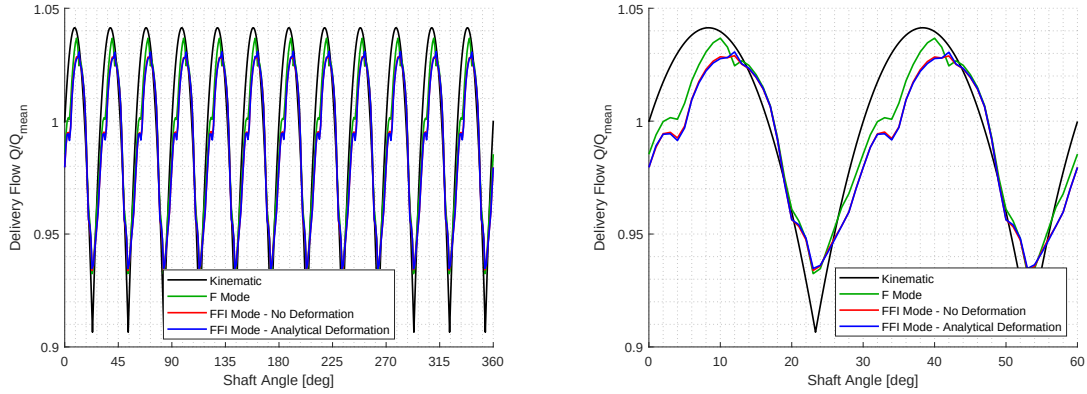

(a) Full Shaft Revolution

(b) 2 tooth spans

Figure 5.2. Instantaneous flow rate of the Ref E1 EGP using LP simulation (a) over a whole shaft revolution (b) zoomed in on 2 tooth spans

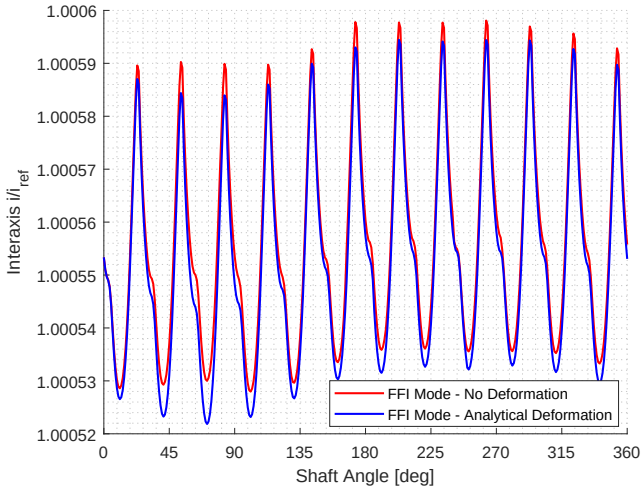

Figure 5.3. Instantaneous center distance of the two gears in LP simulation

Similarly to Figure 5.2, the instantaneous pressure of the drive TSV is given in Figure 5.4. In this figure, a key difference between the F and FFI modes is given, namely the fact that without considering the micro-motion of the gears, the radial gap

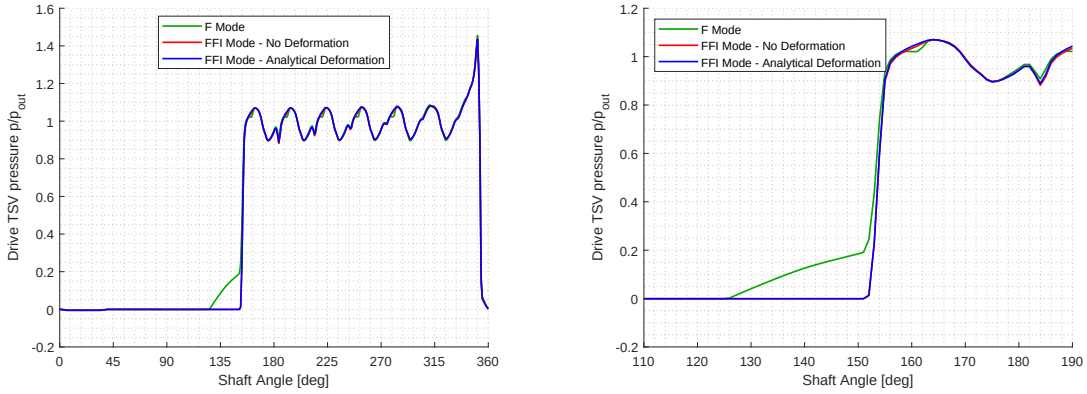

(a) Full Shaft Revolution

(b) TSV pressurization

Figure 5.4. Instantaneous drive TSV pressure of the Ref E1 EGP using LP simulation (a) over a whole shaft revolution (b) zoomed in on the TSV pressurization

sealing (at the teeth of the gears) is significantly different. This effect is highlighted in 5.4(b), where the leakage that is allowed in the F mode simulation due to an inadequate radial sealing allows for pressure to build well before the FFI simulation predict.

This claim is supported by Figure 5.5, comparing the instantaneous tooth tip gap over a full revolution of the shaft. By convention, the gap is equal to zero when the gear's tooth is not in the casing. This figure confirms that the F mode simulation allows non-zero gap in a region where the gears shift and seal in FFI mode. Furthermore, this figure shows that the shifting of the gears impacts not only the displacement of the unit, but its sealing as well.

If the impedance journal bearings are replaced with their corresponding Reynolds unwrapped films, Figure 5.6 demonstrates that the resulting shifting changes. Without the deformation of the bodies, this effect is subtle. Once the bodies are allowed to deform, a significant change in the quasi-steady position of the gears is achieved. This is expected since, by virtue of the fact that the Ockvirk solution neglects the

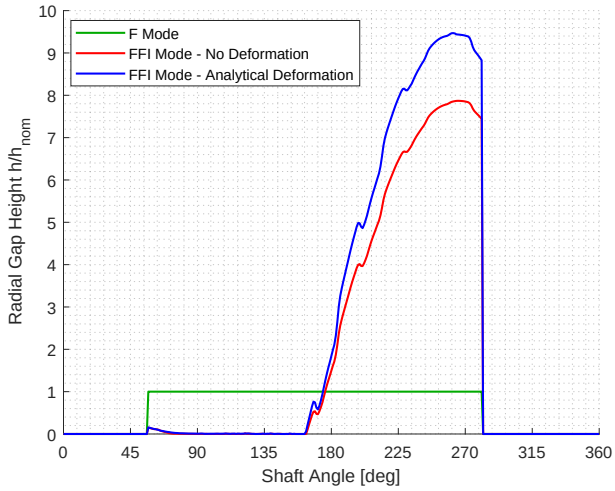

Figure 5.5. Instantaneous gap between tooth tip and casing in LP simulation

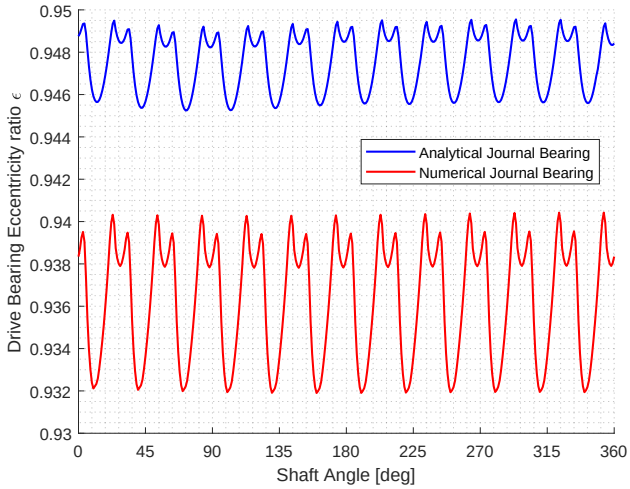

Figure 5.6. Instantaneous journal bearing eccentricity comparison between analytical impedance and numerical Reynolds simulations of the journal bearings without micro-deformation

pressure driven flow in the circumferential direction, it does not allow the pressure to diffuse circumferentially and under-predicts the load carrying capacity of the bearing.

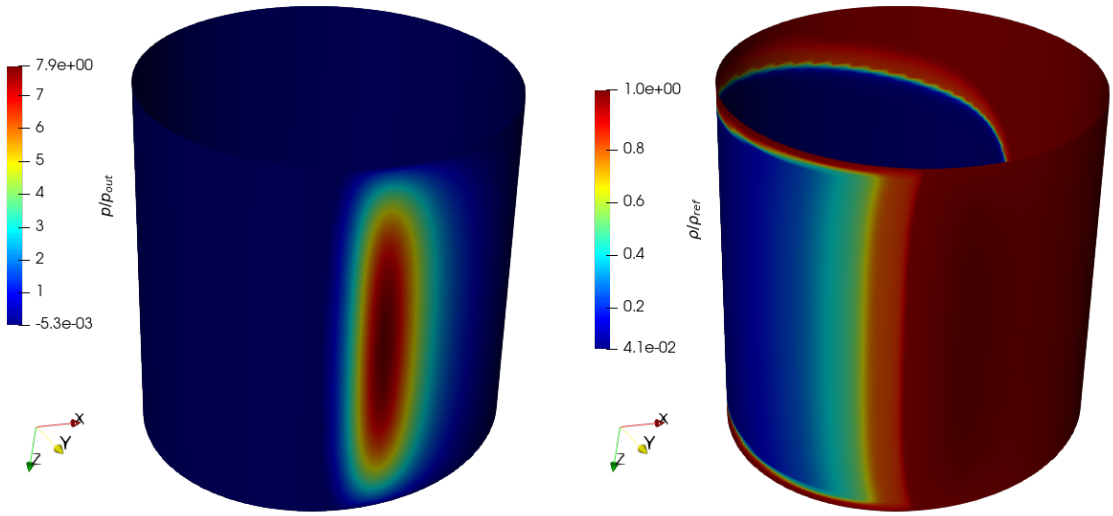

(a) Film Pressure (b) Film Density

Figure 5.7. Numerical distributed parameter Reynolds journal bearing result without micro-deformation showing (a) film pressure (b) film density

The resulting film pressure and density of the journal bearing are given in Figures 5.7(a) and 5.7(b) respectively. Figure 5.7(a) shows that a large pressure builds as the journal shifts to form a converging region in order to carry the applied load. As a result, Figure 5.7(b) shows the large scale cavitation that occurs in the expanding region of the bearing, with negligible effect on the pressure in this region.

Similarly Figure 5.8 compares the leakage out of a TSV using the analytical simplifications of the lateral flows as compared to the distributed parameter Reynolds film. For both, the same fixed gap is used, and no micro-deformation is present. It is worth noting that while the leakages are small for the low nominal gap taken here, this is not a general observation of all EGM units. Therefore, comparison should focus on the relative magnitude of the leakages, as opposed to comparison to the mean flow.

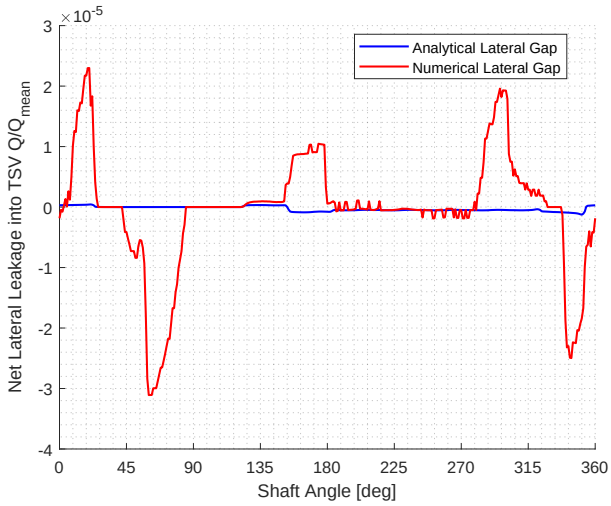

Figure 5.8. Instantaneous lateral leakage comparison between analytical simplifications and numerical Reynolds simulations of the fixed lateral gap without micro-deformation

The resulting film pressure and density of the lateral gap are given in Figures 5.9(a) and 5.9(b) respectively. Note that here and for all subsequent lateral gap plots for the sake of visualization, the results have been post-processed to snap the boundary points to the edges of the boundary polygon. This functionality is implemented within the films themselves, and is a user option that can be toggled. It has no effect on the internal field solution, but is helpful with the interpolated color filling employed by Paraview. This figure shows that without tilting or deformation, there is no wedge or squeeze terms to generate pressure, and pressure simply diffuses across the TSV boundaries. Unlike the journal bearing, Figure 5.9(b) shows that the lateral gap does not have large pockets of cavitation. It does, however, show the remnants of cavitated fluid, swept into the film from the cavitating TSV as the gears rotate. This shows a key strength of the DP approach outlined here, where it is able to capture the coupled effect of cavitation between the LP and DP volume. Even when the cavitated TSV has left the region, the low density and bulk modulus of the bulk fluid in that region

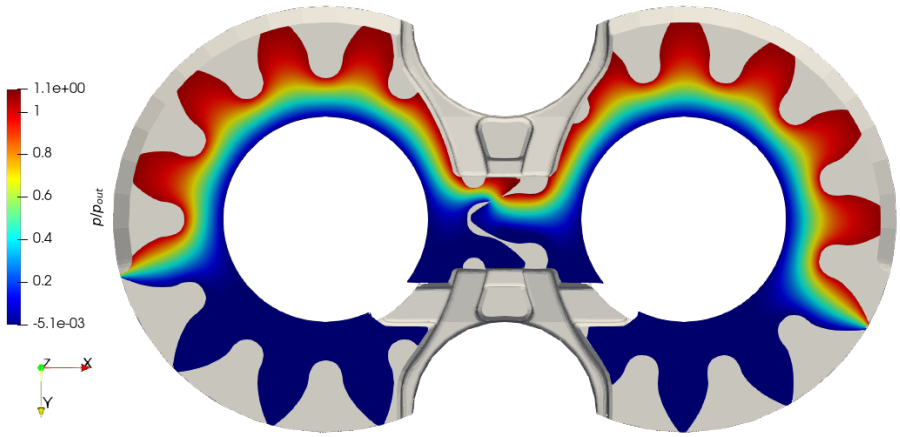

(a) Film Pressure

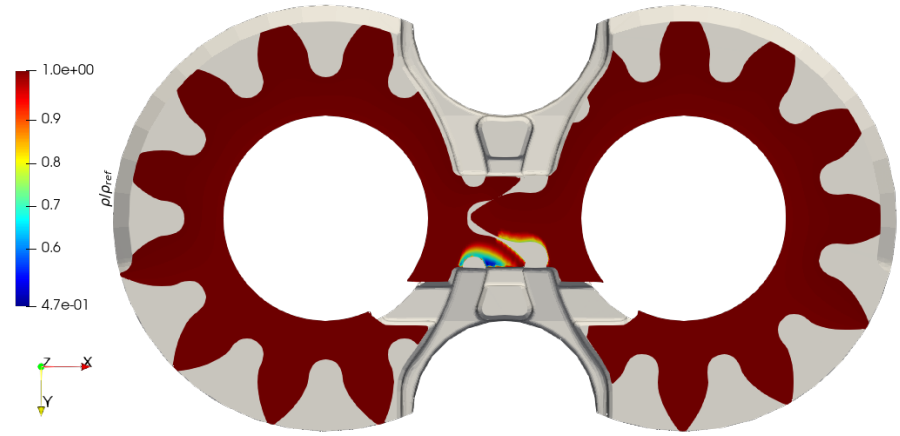

(b) Film Density

Figure 5.9. Numerical distributed parameter Reynolds lateral result without micro-deformation and fixed bushing showing (a) film pressure (b) film density

make it impossible for the film to recover before the next cavitated TSV deposits more cavitated fluid.

When the effect of micro-deformation is included, Figure 5.10 shows that the resulting eccentricity of the bearing increases. This erroneously makes the bearing appear to be able to carry less load, when in reality this increase in 'rigid' eccentricity

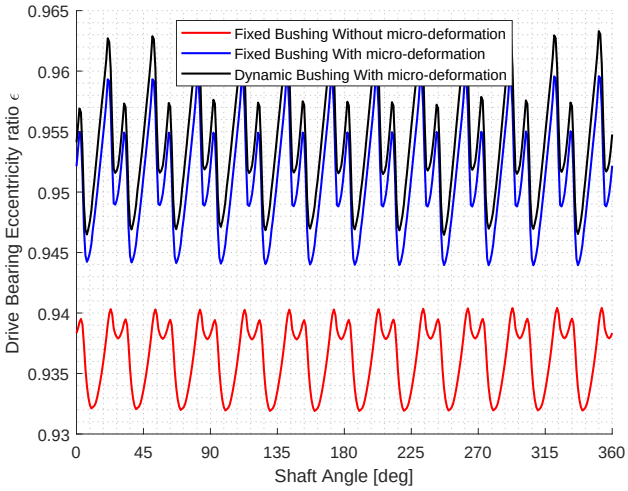

Figure 5.10. Instantaneous journal bearing eccentricity for the numerical Reynolds simulations with and without micro-deformation

is caused by the materials deforming and allowing the journal center to proceed further from the bearing's nominal center. As was shown in the previous plots, though, the LP model is sensitive to the position of the gears and therefore this change in position will have an effect on the performance of the unit.

Besides affecting the LP modeling, the effect of this deformation on the journal bearing is clearly demonstrated in Figure 5.11. Here, the deformation of the material allows the pressure to spread over a larger region of the bearing, thus decreasing the maximum pressure required to carry a given load. Figure 5.11(b) also shows an important aspect of the macro-deformation, where the bending of the shaft creates a gap that varies in the axial direction with the deformed gear. The result of this is shown in Figure 5.11(a), where the pressure peak concentrates on the gear side of the bearing, as was shown previously in Figure 3.12.

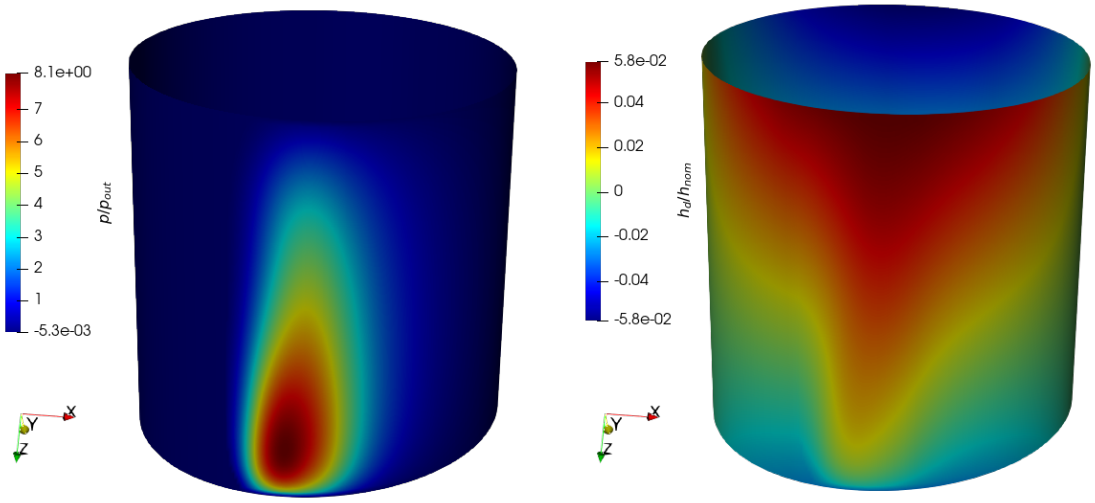

(a) Film Pressure (b) Gap Deformation

Figure 5.11. Numerical distributed parameter Reynolds journal bearing result with micro-deformation showing (a) film pressure (b) gap deformation

Similarly for the lateral leakage, the introduction of body deformation increases the gap heights and thus the leakages as is shown in Figure 5.12. In Figure 5.13, the corresponding film pressure and gap deformation is shown. These figures show that even without any axial motion of the gears or bushing, the deformation of the bodies forms a wedge shown in Figure 5.13(b) that builds pressure in the meshing zone, where the sweeping gears drag fluid into the converging wedge. This pressure build up is shown in Figure 5.13(a). As a result, the gap becomes more open on the high pressure side, but also the leakage dynamic changes entirely as the TSV pressurizes and in the meshing zone.

Finally, the complete model allows the bushing to move. Since the bearings are within the bushing of this unit, the effects of this bushing movement are found in both films, as is shown in Figure 5.14. This result justifies the need to couple the solving of all films and the lumped parameter model, where the tilting induced by

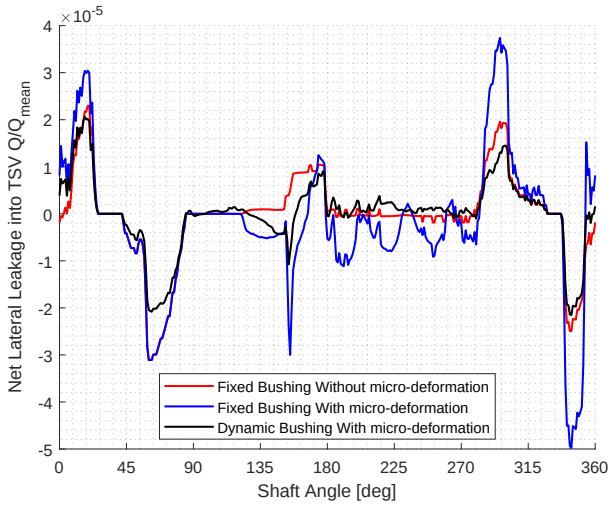

Figure 5.12. Instantaneous lateral leakages for the numerical Reynolds simulations with and without micro-deformation

the tooth space pressures causes a reactive pressure build-up in both the lateral and journal bearing interfaces in opposition. Note that here since the journal bearing film pressure are much higher than that of the lateral gap, the two are put on different color scales so that the trends can be seen in both. Returning to Figures 5.10 and 5.12, the inclusion of the movement of the plate changes the resulting eccentricity and leakage respectively. Note that in creating these figures, the simulation was first run with this complete model so that the quasi-steady position of the bushing was known. The fixed gap simulations were then run at this same gap so that a fair comparison could be made. It is worth noting that without the use of this complete model to determine the appropriate constant gap, the fixed gap simulations would not be able to achieve results even as close as those presented here.

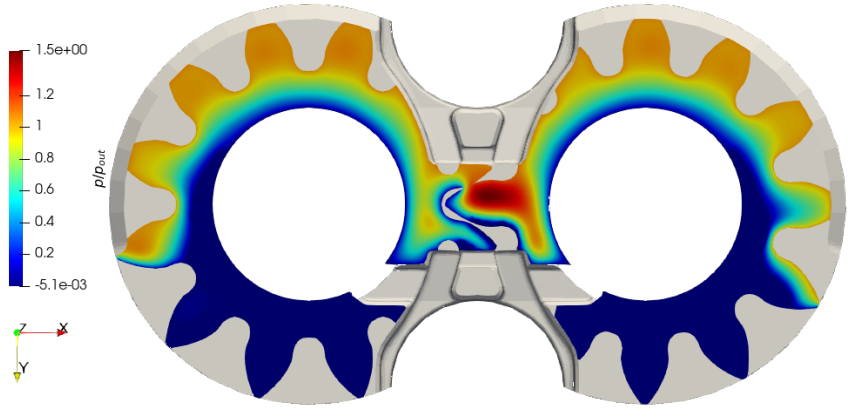

(a) Film Pressure

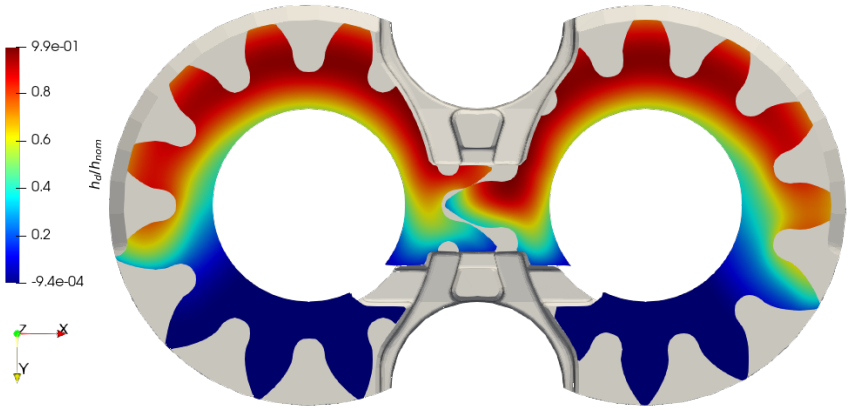

(b) Gap Deformation

Figure 5.13. Numerical distributed parameter Reynolds lateral gap result with micro-deformation and fixed bushing showing (a) film pressure (b) gap deformation

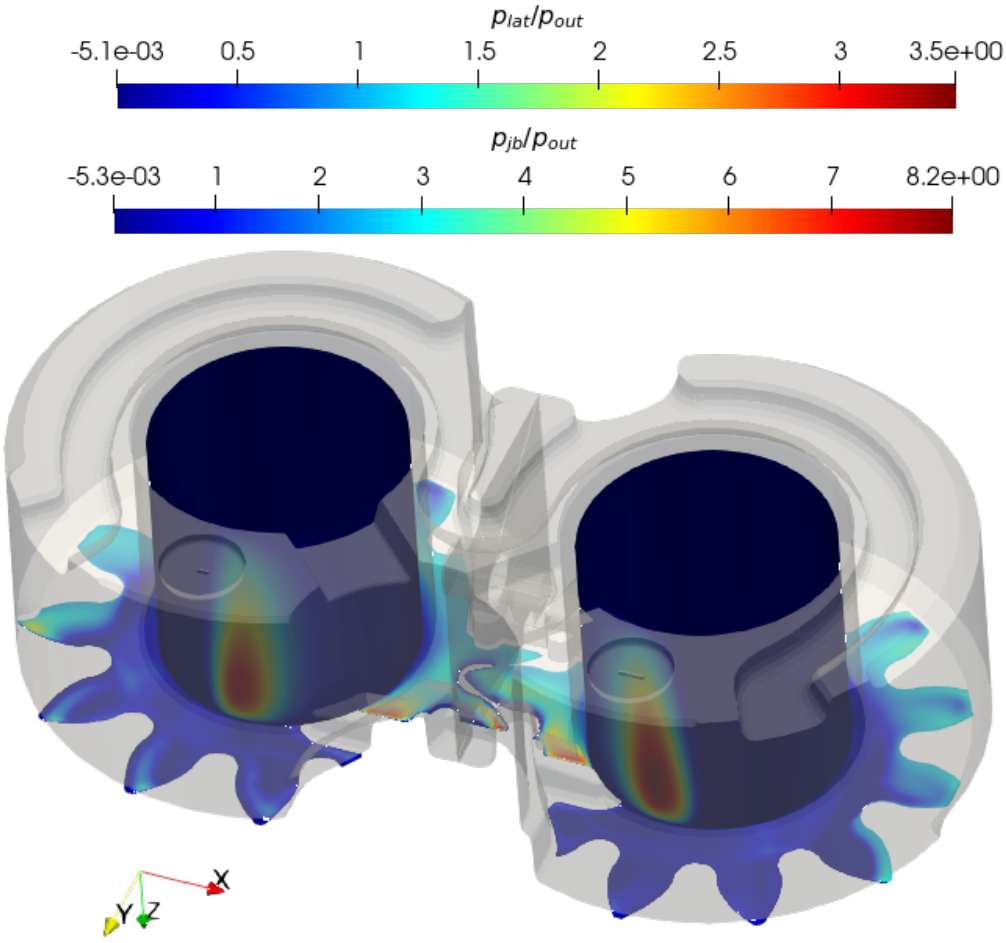

Figure 5.14. Numerical distributed parameter Reynolds lateral gap and journal bearing result with micro-deformation and dynamic bushing showing pressure distribution on all of bushing

5.2 Virtual prototyping of an EGM

A major goal of this work was to facilitate virtual prototyping of both existing PD concepts and new ones. However since most of these units will have many design parameters, and similarly the designer will have to balance many objectives, any optimization algorithm employed will require a large number of design evaluations. Considering this, the use of the complete DP model, with simulation time $>$ 10hrs is not feasible. Instead the lumped parameter model, with simulation time $\sim$ 50 seconds, can facilitate the exploration of a the solution space in significantly less time. For virtual prototyping, then, the present thesis proposes a 2-phased design procedure. First in Phase 1, the lumped parameter model is used, assuming ideal lubricating interface performance. In effect, this optimizes for the unit design with the highest potential performance. In reality, this ideal behavior is not attainable, and Phase 2 attempts to achieve as close to the ideal as possible.

The present section will demonstrate this virtual optimization procedure with the design of the Ref E3 EGM for application in an electro-hydraulic actuator (EHA). This design study is part of a larger effort (supported by the U.S. Department of Energy under grant no. DE-EE0008334.) with the overall goal of electrifying an entire machine as is highlighted in Figure 5.15. Here, each function of the machine is actuated by an isolated EHA, the core of which is the EH unit - the combination of the electric machine with a positive displacement machine. This application presents unique challenges to the design of the unit, which must be integrated directly with its electric machine, and virtual prototyping from zero is required. The working fluid considered for this machine is a typical ISO VG 46 hydraulic oil, with tabulated fluid properties used to model its behavior.

5.2.1 Phase 1: Lumped Parameter Optimization

As was mentioned above, it is not feasible to begin design optimization directly from the detailed distributed parameter model. This challenge can be overcome by

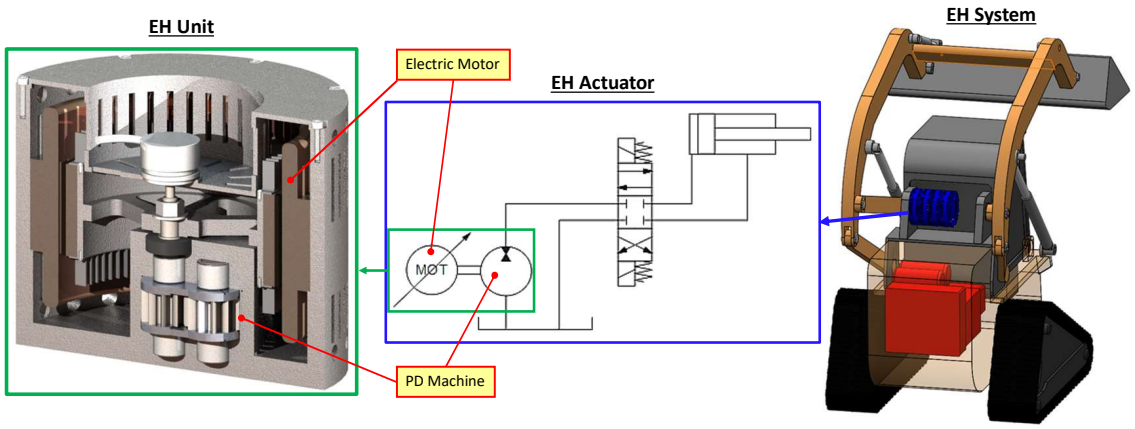

Figure 5.15. Definition of the Ref E3 EHA

observation that while the balance elements are driving factor in the performance of a unit, a poorly designed gear set with well designed balancing elements will still perform poorly. Thus the following procedure, using the LP implementation of Multics HYGESim as the core design evaluation function, optimizes the macroscopic design of the unit by identifying the optimal gear set and porting geometry. The optimization procedure is demonstrated in Figure 5.16.

This procedure is implemented in the commercial software modeFRONTIER. The modular nature of the software is well suited for this analysis, which relies on various tools with different software implementations. First, the optimization algorithm, based on an initial set of designs, will propose a new set of gear and groove parameters correspond to a single EGM design. This information is passed to a script which generates the gear and groove designs corresponding to these parameters if they are feasible. The constraints and conversion of these parameters to an EGM design will be discussed in the Design Generation section. This resulting EGM is then passed to the geometric model to extract the information necessary by the Multics HYGESim tool to simulate its performance using the lumped parameter EGM model discussed in Chapter 2. The post processing of these simulation results to extract the constraint and objective function results will be discussed in the Performance Evaluation section.

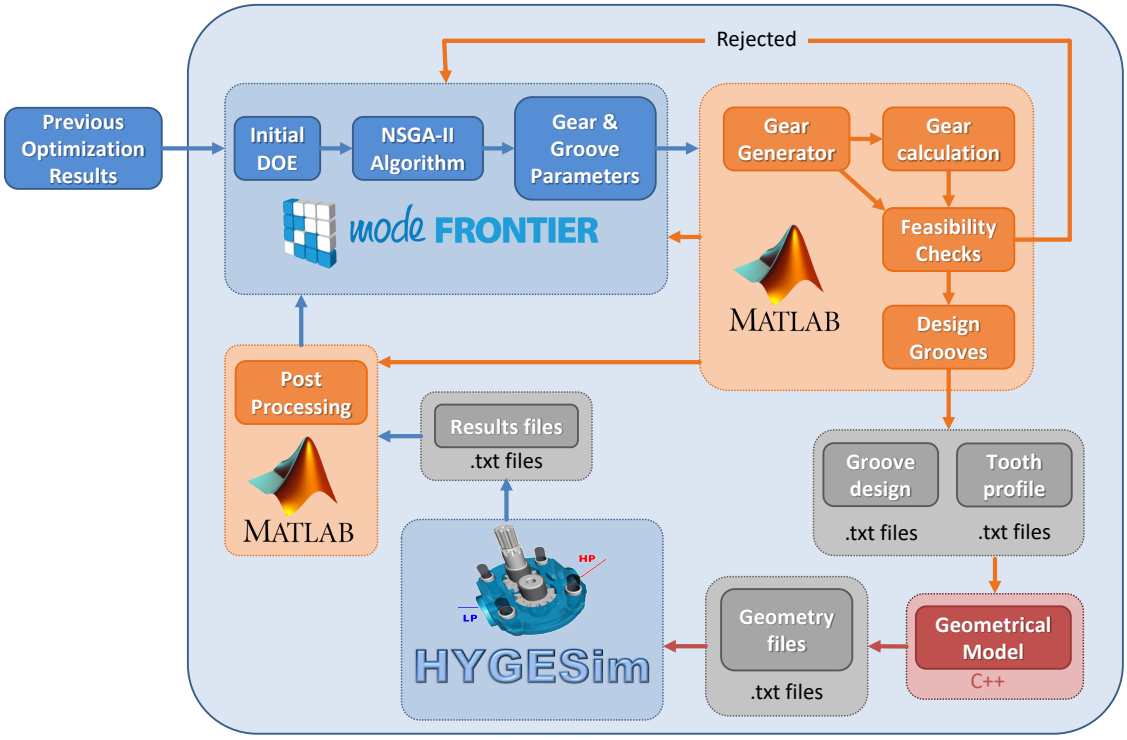

Figure 5.16. LP Optimization workflow

Finally, these are passed back to the optimization algorithm, which uses this feedback to adjust the EGM parameters appropriately. Selection of a design from these results will be discussed in Design Selection section.

Design Generation

The first step is to take a given set of design parameters and to generate an EGM. These parameters include information of not only the gear set, but the corresponding relief grooves which dictate the transition from high to low pressure. Note that throughout the parameterization, effort was made to parameterize using dimensionless values and angles. Doing this ensures that for a given set of parameters, changing a single quantity will cause all other dimensional quantities to scale accordingly. As a result, it is more likely that the new design given by this change will remain feasible

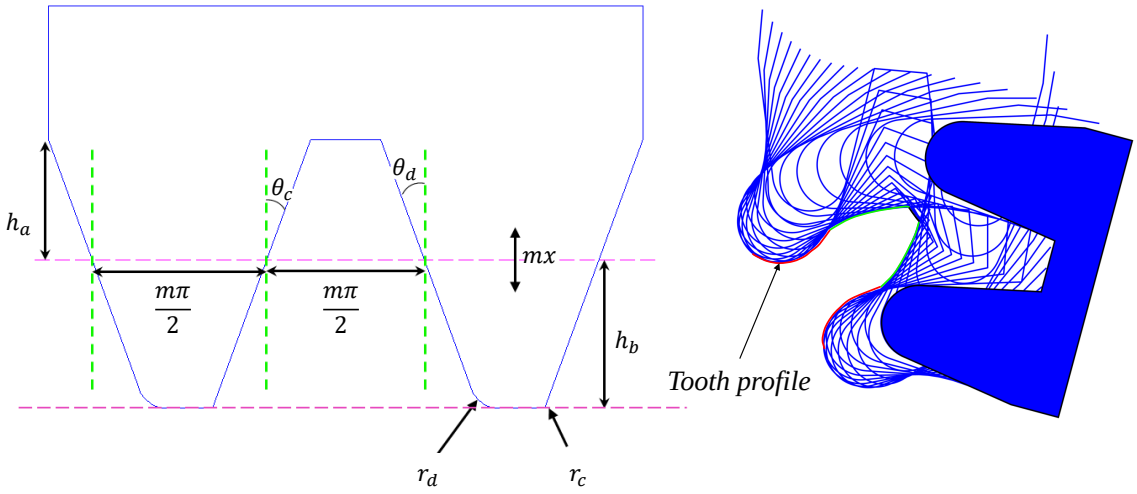

Figure 5.17. Symbolic cutting of the gear set using parametric rack cutter

such that the optimization can progress. Additionally, it can reveal relationships between the parameters that their dimensional counterparts would mask.

A gear design, then, is given by dimensionless quantities which define the shape of the involute EGM tooth. For example, the gear addendum h_a is related to its corresponding dimensionless parameter $\widetilde{h}_a$ and the gear module m through the relation

$$\widetilde{h}_a = \frac{h_a}{m} \tag{5.1}$$

and similarly for the parameters in Table 5.1, which collects all gear parameters. For this design, helical gears were not considered, and only asymmetric involute spur type units were considered, so that the gear generator developed by Zhao and Vacca [5] can be used to symbolically cut the gears. These design parameters, then, are the shape of the cutter which is used. In doing so, they control the resulting shape considering only gears that are physically possible for manufacturing. An example of this cutter, and the resulting symbolic cutting process, is given in Figure 5.17.

In order to determine if a given combination of gear parameters will lead to a physical gear set, a series of constraint functions are defined. The first constraints correspond to the cutter design, where again the reader is encouraged to consult [5]

Table 5.1.
Set of gear parameters and range of values considered

	Input	Min	Max
Number of teeth [-]	N_{teeth}	8	18
Gear depth [-]	$\widetilde{b}$	0.1	50
Addendum [-]	$\widetilde{h}_a$	0	3
Dedendum [-]	$\widetilde{h}_d$	0	3
Tool pressure angle, Drive [deg]	θ_d	10	40
Tool pressure angle, Coast [deg]	θ_c	10	40
Radius of curvature of root, Drive [-]	$\widetilde{r}_d$	0	1
Radius of curvature of root, Coast [-]	$\widetilde{r}_c$	0	1
Profile correction [-]	x_g	-1	1
Inter-axis percentage [-]	i_p	0.1	0.9

for a detailed derivation of the functions, which are reported here for completeness. First, the constraint

$$\left[(\widetilde{h}_b - \widetilde{r}_d)\tan\theta_d + \frac{\widetilde{r}_d}{\cos\theta_d}\right] + \left[(\widetilde{h}_c - \widetilde{r}_c)\tan\theta_c + \frac{\widetilde{r}_c}{\cos\theta_c}\right] \leq \frac{\pi}{2} \tag{5.2}$$

enforces that the tip of the cutter is flat so that the drive and coast side root fillets do not overlap. Next, the constraint

$$\frac{N_{\text{teeth}}}{2} + x_g + \widetilde{h}_a > \frac{N_{\text{teeth}}}{2}\max\left[\cos\theta_d, \cos\theta_c\right] \tag{5.3}$$

ensures that the involute profile exists for both the drive and coast flanks of the gear.

To form a physical gear, where the outer radius r_a satisfies its definition for involute gears

$$r_a = \frac{mN_{\text{teeth}}}{2} + mx + m\widetilde{h}_a \tag{5.4}$$

it is necessary to enforce a finite tip width L_t. Since the unit must perform a sealing action in its radial clearance, it is helpful to set some minimum value $L_{\text{t,min}}$ so that a

design that cannot meet the requirements of an EGM is not evaluated unnecessarily. The tooth tip width is then subject to constraint

$$L_t \geq L_{\mathrm{t,min}} \geq 0 \tag{5.5}$$

This work will focus on single flank gear pumps, where only the drive flanks make contact in meshing. This means that there is an opening between the corresponding volumes of both the drive and driven gears. In effect, the two TSVs act as a single combined volume while meshing. For single flank EGMs, the inter-axis at which they operate is a key design point in the behavior and porting of this single volume. In order to promote feasible designs, the optimizer is allowed to select only within the feasible inter-axis range. Again, this also works to generalize the parameters, meaning that a change to another input parameter scales the inter-axis accordingly. To place the inter-axis, it is first necessary to find the range of values that corresponding to a working gear set. For EGMs, this comes to two conditions. First, there is a geometric minimum after which there will be interference between the gears. This occurs either when the tip of one gear makes contact with the root of the other, or when both flanks make contact at dual flank inter-axis i_{df}. The maximum of these two is taken as the geometric minimum on inter-axis

$$i_{\mathrm{min,g}} = \max[r_a + r_r, i_{df}] \tag{5.6}$$

where the root radius r_r is given by

$$r_r = \frac{mN_{\mathrm{teeth}}}{2} + mx - m\widetilde{h}_b \tag{5.7}$$

Similarly, maximum geometric inter-axis is given when the gears no long make contact

$$i_{\mathrm{max,g}} = 2r_a \tag{5.8}$$

An additional geometric interference is possible, when the tooth tip of one gear makes contact with the root fillet of the other. The presence of this interference is checked in the range of geometric inter-axis numerically over one full angular pitch

of the gears, and the range $[i_{\min,g}, i_{\max,g}]$ is narrowed to exclude regions of i where interference between the root fillet and tip is found. Finally, the viable range of inter-axis values is further narrowed to the region where at least a single tooth is always in contact between the meshing gears, to form the viable inter-axis range $[i_{\min}, i_{\max}]$. As long as this range is at least as large as the possible inter-axis values that can occur based on the clearances of the bearings

$$i_{\max} - i_{\min} \geq C_{\text{jb}} \tag{5.9}$$

then the nominal inter-axis can be selected via the inter-axis percentage parameter

$$i_{\text{nom}} = i_{\min} + i_p \left(i_{\max} - i_{\min}\right) \tag{5.10}$$

With a gear set generated, it is necessary to generate its relief grooves. As was mentioned above, these grooves are used to direct the flow to either the delivery or suction volumes in the region, where the TSV is trapped between two contact points. In general, these grooves are designed such that the TSV is connected to the delivery port through this groove for as long as its volume is decreasing, and a pumping action is occurring. At the point where the volume is at its minimum, the volume should switch its connection from the delivery to the suction groove. As the volume is increasing, the suction action is connected to the unit's inlet. In practice, it is common to deviate from this ideal groove design, sacrificing some in volumetric efficiency to smooth the transition from high to low pressure. Many studies have focused on the design of these groove, including Gulati et. al. [81] searching for the optimum area curve and Wang et. al. [141] specifically focusing on the different possible morphologies.

In the present approach, a simple tilted rectangular groove morphology was selected. This approach is sufficient to compare the relative behavior of proposed designs, while minimizing the number of design variables required to describe its shape. The parametric definition of these grooves is demonstrated in Figure 5.18, where the delivery and suction grooves of both sides of the gears can be offset vertically X_i and

tilted θ_i. To define the position of these grooves, the angle of pressurization due to the back-flow groove θ_p is parameterized. As the back-flow groove sets the pressurization, the casing angle θ_s sets the radial sealing. Due to the net pressure force applied on the gears, they shift in their bearings as they carry the load. This shifting causes a variation in gap height as a function of angle which, along with the casing angle, defines the resistance of the EGM to flow over its tooth tips. The casing angle needs to be large enough to allow the volumes to fill, but small enough that this resistance is high after the gears have shifted. Since the shifting varies from gear to gear, so too must the casing angle and it is necessary to consider it as a defining design parameter.

Note that since this approach is for spur gears, the bottom face is a mirror of the image of the top, and there is no need to parameterize the design of both sides. In Table 5.2, a similar set of groove parameters is given, where again length scales are normalized by the gear module as demonstrated in Equation 5.1. Based on these parametrizations, it is possible to propose a design where the two grooves overlap each other. In this case, a direct connection will be formed through the grooves from the high pressure to low pressure volumes and the unit will not function. This condition can be avoided, however, by imposing the constraint

$$(X_1 - \frac{w}{2}\tan|\theta_1|) + (X_3 - \frac{w}{2}\tan|\theta_3|) > 0 \tag{5.11}$$

Similarly, it is possible to propose a design where the TSV is simultaneously open to the casing and the backflow groove. This situation introduces a direct bypass from the backflow grooves, through the TSV, and into the low pressure volume and must therefore be avoided. This situation is prevented by imposing the constraint

$$\theta_p - \theta_s \geq \frac{2\pi}{N_{\text{teeth}}} \tag{5.12}$$

which enforces that the angular difference between the casing and backflow groove is at least equal to one angular pitch of the gear.

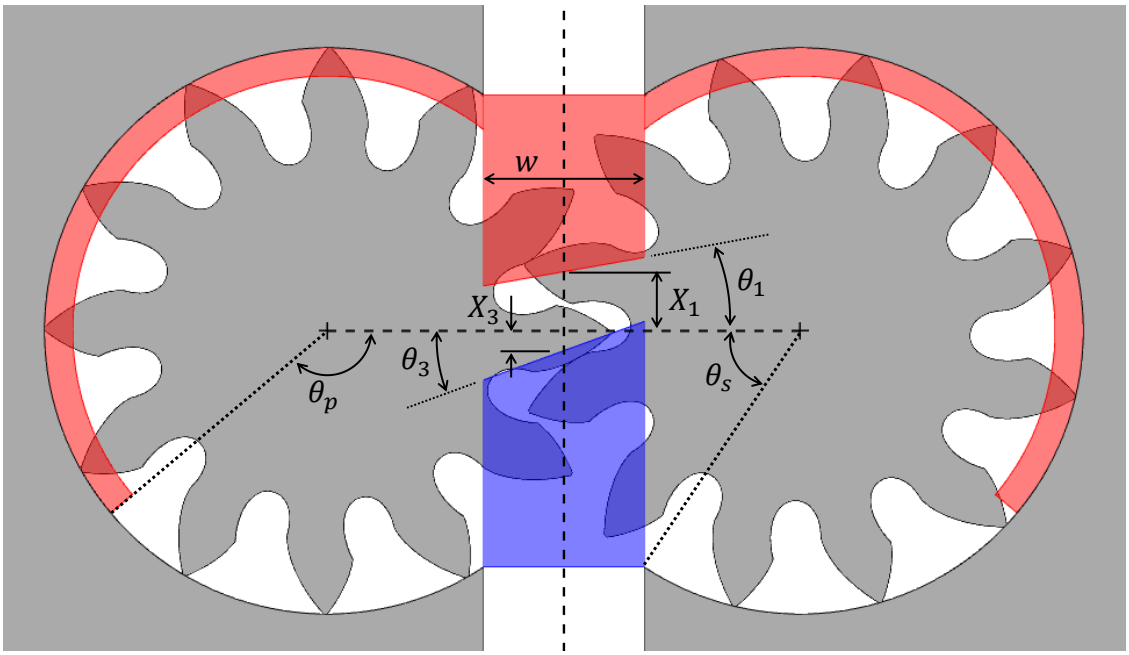

Figure 5.18. Relief Groove and pump body parameterization for given gear set

Table 5.2.
Set of groove parameters and range of values considered

	Input	Min	Max
Offset – Top Face Delivery Groove [-]	$\widetilde{X}_1$	-3	3
Offset – Top Face Suction Groove [-]	$\widetilde{X}_3$	-3	3
Tilt Angle – Top Face Delivery Groove [deg]	θ_1	-45	45
Tilt Angle – Top Face Suction Groove [deg]	θ_3	-45	45
Angle of Pressurization [deg]	θ_p	100	180
Starting angle of casing [deg]	θ_s	50	80

Performance Evaluation

In order to evaluate the feasibility of a proposed unit, its performance is simulated using the LP model over the representative simplified duty cycle and test circuit

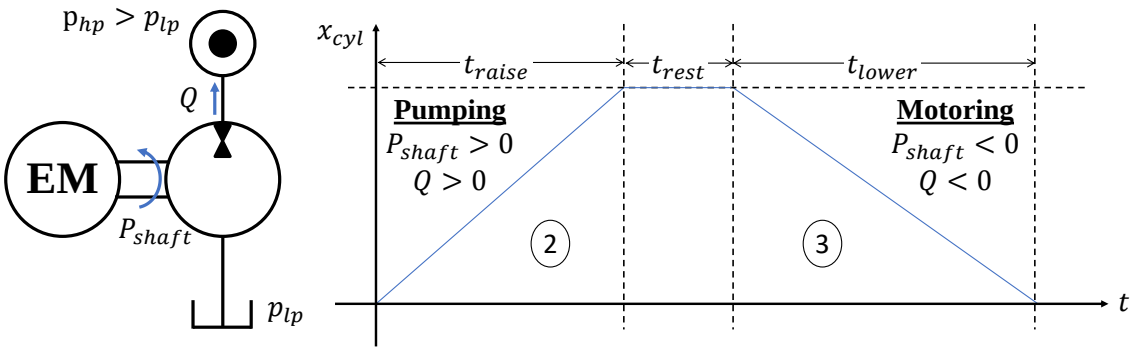

Figure 5.19. Simplified EGM loading circuit and corresponding duty cycle considered in optimization

demonstrated in Figure 5.19. In this circuit, the raising and lowering of the actuator is simplified to raising at constant load and speed, followed by lower at constant speed and load. This implies constant pumping and and energy recover phases respectively.

After running the Multics HYGESim simulation, the resulting pressure and flow characteristics are examined. First, Figure 5.20 demonstrates a typical pressure profile. From this profile, constraints can be defined that correspond to the pressure peaking and tendency of the unit to cavitate.

In order to avoid excessive pressure peaking in the tooth space volumes when the gears are meshing, a maximum allowable pressure difference between the tooth space volume pressure and the outlet pressure is taken for each condition. Consideration of this pressure peak captures both the resulting peak in loading on the lubricating interfaces of the pump, as well as the spike in torque required to compress the fluid. In doing so, the optimization can correlate with the mechanical performance of the pump, while not requiring a full design optimization of the bearing and lateral gap designs of each proposed pump design. The following contraint requires that the pressure peaking be no higher than that of a reference value

$$\Delta p = \max_t (p_{\mathrm{TSV}}(t) - p_{\mathrm{HP}}(t)) \leq \Delta p_{\max} \tag{5.13}$$

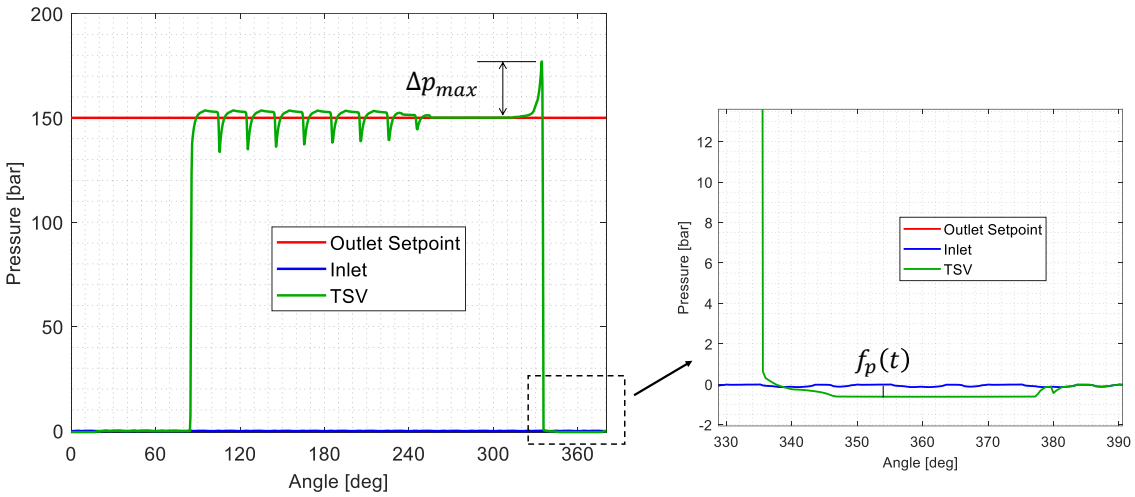

Figure 5.20. Pressure profile over a full shaft revolution in pumping mode, highlighting the resulting pressure overshoot and undershoot due to the relief groove design

While the volume is still trapped but starts expanding, the pressure will fall under that of the inlet tank pressure. When this happens, gaseous and vaporous cavitation will occur where trapped air will come out of the solution and in extreme cases the oil will evaporate. In order to quantify the tendency of a design to undergo this local aeration and cavitation, the region in which the tooth space volume pressure is under the inlet volume pressure is considered. This is accomplished by the parametric function

$$\psi_p = \begin{cases} p_{\text{inlet}} - p_{\text{TSV}}, & p_{\text{TSV}} < p_{\text{inlet}} \\ 0, & p_{\text{TSV}} \geq p_{\text{inlet}} \end{cases} \tag{5.14}$$

By integrating this function over a whole revolution, the local cavitation area A_c can be found. This function equally weights the magnitude of the pressure difference when $p_{TSV} < p_{\text{inlet}}$ and the time over which it occurs. While the result does not capture the magnitude of the gas release, it is effective in comparing the relative tendency of two pumps to release bubbles. Similar to the pressure constraint, this avoids the need to use a computationally expensive cavitation model online. Instead,

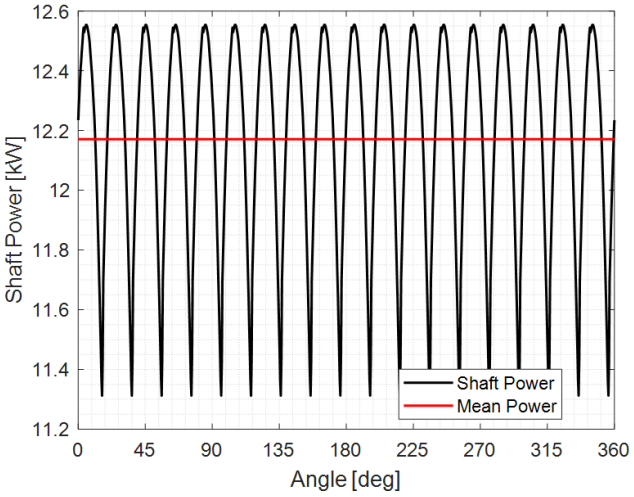

Figure 5.21. Instantaneous shaft power consumption in raise (pumping) mode of arbitrary EGM

this is avoided by requiring that the cavitation area be no higher than a limiting value, corresponding to a unit without aeration/cavitation issues

$$A_c = \int_0^{2\pi} \psi_p(\varphi)\, d\varphi \leq A_{\mathrm{c,max}} \tag{5.15}$$

A major goal of this design optimization is to minimize the total energy consumed over this representative cycle, including the energy consumed during pumping and the energy recovered during motoring where

$$\overline{P}_{\mathrm{shaft}} = \frac{P_{\mathrm{pumping}}\, t_{\mathrm{raise}} + P_{\mathrm{motoring}}\, t_{\mathrm{lower}}}{t_{\mathrm{raise}} + t_{\mathrm{rest}} + t_{\mathrm{lower}}} \tag{5.16}$$

The instantaneous shaft torque and speed of the unit is given by Multics HYGESim, as is demonstrated in Figure 5.21, and can be averaged during steady operation at both operating conditions to populate this equation.

Another important objective of this optimization is to generate a unit whose torque and flow ripples are low. This ripple, demonstrated in Figure 5.22, is inherent to all positive displacement machines with finite displacement chambers. Challenging the accepted assertion that outlet flow ripple leads to EGM noise, recent work [9] has

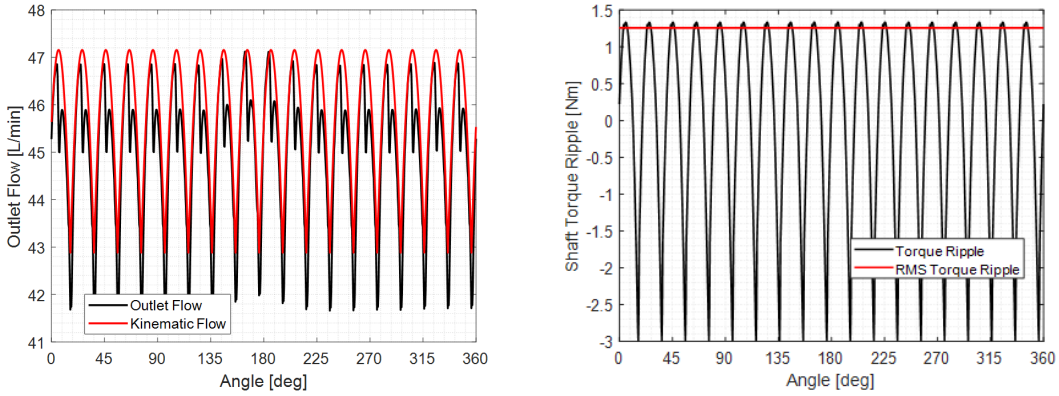

(a) Flow Ripple

(b) Torque Ripple

Figure 5.22. Ripple of both the flow and torque of the EGM during raise (pumping) mode of an arbitrary EGM

found that the contribution of the outlet pressure ripple (related to the outlet flow ripple) is not the most significant source to the generation of airborne noise of an EGM unit. Nevertheless, the flow ripple puts excessive vibration into the system that leads to noise in the downstream components and may lead to instability. Without detailed information on the design of the downstream system or the mounting of the unit, though, it is not possible to predict the exact resulting noise spectrum. Instead, this work attempts to minimize the noise sources which lead to perceived sound of the EGM. Figure 5.22(a) also demonstrates the necessity of using the full LP analysis, and not simply examining the kinematic behavior of the unit. In this figure the instantaneous flow predicted by the kinematic of the unit is compared to the flow from Multics HYGESim, where the operation with a real fluid leads to distinct deviation in the resulting ripple from the kinematic as discussed in Section 5.1.

For the sake of generality, it is assumed that the resonant frequencies of the structure are far from that of the fundamental frequency of the unit. Typically, the majority of the ripple energy of an EGM is in its first two harmonics of the fundamental frequency, and so this assumption is reasonable. While the magnitude

of the resulting noise cannot be predicted, when this is the case the system driven noise spectrum will tend to follow a similar trend to its sources'. Considering this, an A-weighting amplitude function $A(w)$ is applied to the ripple, so that the resulting oscillation will be evenly weighted as it is perceived by the human ear.

To accomplish this, a fast Fourier transform is first applied to the outlet flow and torque, offset by their mean values to isolate the ripple. Because the displacement of each unit will vary, the amplitude of the ripple also varies, and the use of the ripple power directly would not reasonably compare the tendency of two units. In order to quantify the magnitude of the outlet flow ripple of a proposed design, its signal power is calculated by summing the A-weighted power at each of the N spectral components. The flow and torque ripple objective functions

$$\begin{aligned} \widetilde{P}_Q &= \frac{1}{N\overline{Q}^2} \sum_{i=0}^{N-1} \left(A(w_i)|\hat{Q}(w_i)| \right)^2 \\ \hat{Q}(w) &= \mathcal{F}\left(Q(t) - \overline{Q} \right) \end{aligned} \tag{5.17}$$

$$\begin{aligned} \widetilde{P}_M &= \frac{1}{N\overline{M}^2} \sum_{i=0}^{N-1} \left(A(w_i)|\hat{M}(w_i)| \right)^2 \\ \hat{M}(w) &= \mathcal{F}\left(M(t) - \overline{M} \right) \end{aligned} \tag{5.18}$$

are then normalize by the mean flow and torque respectively. In effect, this quantifies the ripple power as a percentage of the mean simulated flow/torque of the unit $\overline{Q}/\overline{M}$. In the simulation phase, exactly one revolution of data is recorded. Since the fundamental frequency of a gear pump is given by its shaft speed, capturing exactly one period of the shaft rotation ensure that the ripple is periodic, and rectangular windowing is appropriate.

Finally, this machine must be mounted on mobile machinery, where space is heavily constrained. Considering this, the power density of the machine is important, and an objective function acts to minimize the total space occupied by the unit.

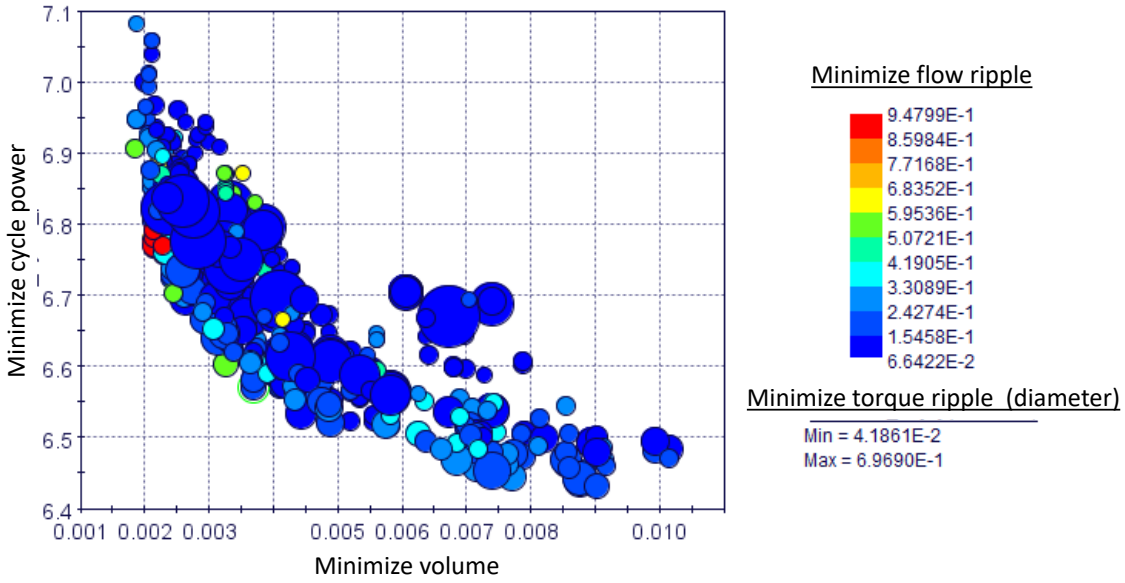

Figure 5.23. Pareto optimal front of hydraulic unit optimization, with all 4 objective functions demonstrated

Design Selection

With the problem well defined, design optimization was run with modeFrontier. Their built-in NSGA-II optimization algorithm is chosen primarily because it is inherently capable of handle discrete values (e.g. number of teeth), supports multi-objective optimization, and does not require determination of gradients. Since design evaluations are expensive, the latter is important for computational efficiency. Furthermore, because an entire generation is evaluated at once, a genetic algorithm is well suited for running multiple design evaluations in parallel. Finally, it is likely the solution space is non-convex and will contain local minimum, so the ability of the NSGA-II algorithm to promote exploration is desirable. The optimization was run for over 35,000 physical designs evaluated. 7 designs were run simultaneously, averaging around 1 design per minute on a Intel Core i7-6700 3.40GHz CPU.

This corresponds to 50 generations, allowing the optimizer ample opportunity to explore the solution space. After running this optimization, no single design that

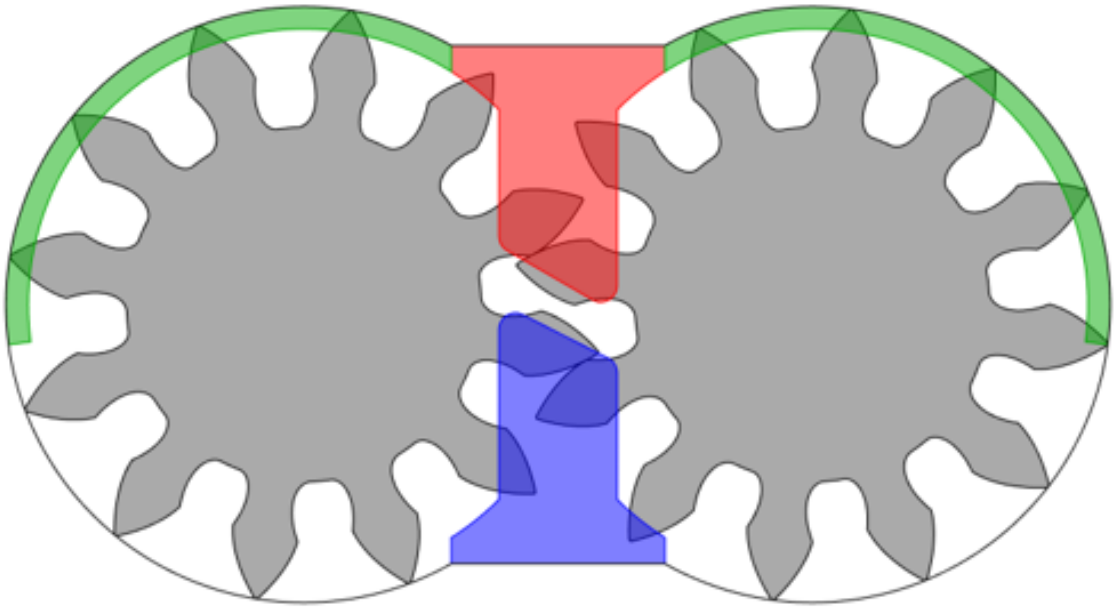

Figure 5.24. Selected gear/groove design from parallel coordinate chart

is optimal for all objectives was found. Instead a pareto optimal front is identified, demonstrated in Figure 5.23, correspond to the set of designs where in order to improve on one objective, at least one other must be harmed. This front demonstrates the benefit of this approach, namely the ability to understand the relative tradeoffs in designing a unit. By using a comprehensive EGM model, these relationships are not biased by the implicit assumptions of an analytical performance evaluation, and better reflect the true trade-offs of an EGM. Finally, the use of this procedure allows for detailed evaluation at a rate that cannot be matched by conventional manufacturing and experimental testing of prototypes. The selected design from this front is then given in Figure 5.24.

5.2.2 Phase 2: Distributed Parameter Design

With the nominal geometry of the unit identified, the assumptions inherent to the previous section must be relaxed so that detailed design of the unit can be performed.

Namely, this section will develop a procedure to design the balancing element of the Ref E3 EGM, which was assumed above to perform ideally. This unit must act as an EHA which can operate over a wide range of pressures and speeds, in both pumping and motoring modes. Over this range, there will be a large variation in the pressure distribution of the film. This is caused by the superposition of two effects – variation in the pressure boundaries of the TSVs and micromotion/deformation of the balancing element. To ensure that an optimal balance design is identified, operating conditions that span the entirety of the possible range of the unit must be considered. As was discussed in Section 3.4.2, the force and moment balance of the lateral balance element is given by the TSV and film pressures, the relief groove geometry, and the hydrostatic balance areas. Since the gear side of the unit is fixed from Phase 1, the only degree of freedom for Phase 2 is the delimitation of high and low pressures on the balance sides. The present section will discuss the method developed in this thesis to determine the optimal balance design of this given geometry.

Isolation of Hydrostatic and Hydrodynamic

First, the pressures of the TSVs diffuses over the film. For a parallel fixed plate, there is no pressure generation in the film and a hydrostatic pressure develops due only to diffusion. This is shown in Figure 5.25 for both a pumping and motoring case. The net force due to this pressure distribution can be resolved into a hydrostatic force, offset from the center of the plate thus inducing a moment. Because of the variation in pressurization of the TSVs over the range of operating conditions, the location and magnitude of this force depend on both speed and operating pressure.

In response to the discrepancy between this hydrostatic force and the opposing hydrostatic force of pressure on the balance side, the plate both tilts and translates. The resulting hydrodynamic wedge that forms, as well as any squeezing motion of the film, drastically changes the film distribution in the lateral gap and the resulting film force. If this hydrodynamic component is not sufficient to mitigate the force or

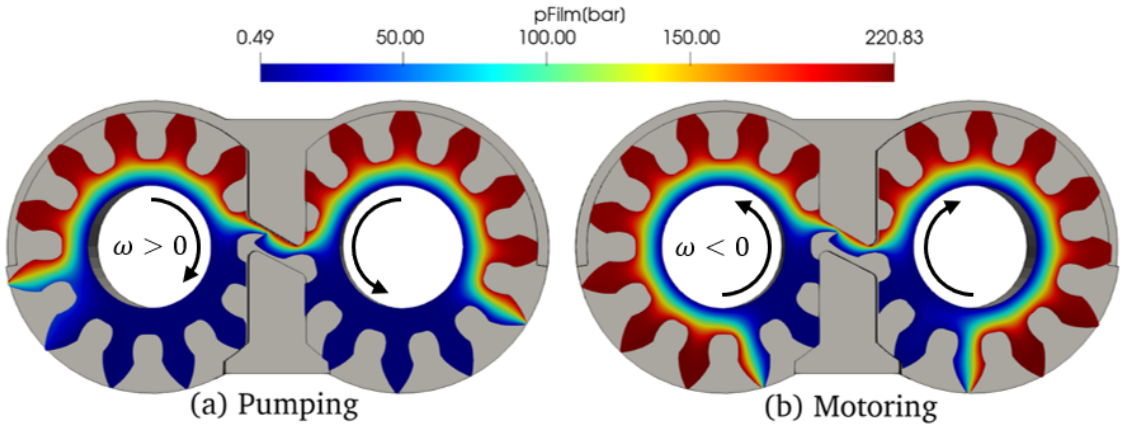

Figure 5.25. Comparison of pressurization for (a) a pumping mode (b) a motoring mode

moment imbalance, the plate will make contact with the gears. This leads to wear, decreasing both the life and efficiency of the unit, and must be avoided.

An important observation, though, is that the contact can occur only in response to an excess pressure imbalance between the balance and gap sides of the plate. Thus, the balance design which minimizes the hydrostatic force and moment imbalance will require the least response from the hydrodynamic effects, decreasing the likelihood of mechanical contact. Since the response is hydrodynamic, it is most effective at higher operating speeds. Considering this, priority in design of the hydrostatic balance must be given to the low speed operating conditions, relying on the hydrodynamic effects to carry the resulting imbalance at higher speeds.

The first step of the design procedure, then, is to quantify the hydrostatic force component which, in an ideal design, could be exactly counteracted by the balance areas. To do so, the simulation model is run over the entire operating range of the machine for a constant parallel gap. It is worth noting that in assuming an arbitrary fixed gap height, the resulting pressure distributions can only be treated as approximate. This is because the hydrostatic pressure distribution resulting from a different assumed gap would result in a differing leakage flow impacting the resulting

TSV boundary pressures. Considering this, a sufficiently small gap value must be selected which is close to the desired gap. In doing so, the hydrostatic design is optimized to realize this desired gap distribution.

Hydrostatic loading

The first step in this quantification, then, is to run simulations of the entire operating range of the unit with the balance element fixed in its ideal location. In this condition, Figure 5.26 shows a typical result of a pumping and motor mode, for both the net axial force and moments applied to the plate. First Figure 5.26(a) demonstrates significantly higher axial loading in the motoring condition as compared to pumping. Returning to Figure 5.25, this can be explained by the nature of a pumping mode where high pressure fluid that is displaced by the meshing of the gears is replaced with low pressure fluid from the inlet of the pump. Once the TSV enters the casing, it is isolated from the inlet and intermediate pressure forms. Since there is tight radial sealing in the unit, this pressure is very close to inlet. As a result, pressurization of the TSV occurs as it opens to the backflow groove. Instead in motoring mode, the displaced low pressure fluid is replaced with high pressure fluid. As the TSV enters the casing, it is still connected to the backflow groove and therefore maintains its high pressure. Once the TSV leaves the backflow groove, the tight radial sealing does not allow for enough the TSV pressure to drop due to leakage until it opens to the low pressure volume. As a result, a significantly larger area of the unit is at high pressure and applies significantly larger axial force than the pumping mode. In Figure 5.26(b), on the other hand, the motoring modes show significantly less tilting moment. Again returning to Figure 5.25, this can be explained by the same nature of the motoring mode bringing high pressure fluid throughout the entire casing, such that the tilting moment contributions of the TSVs cancel along the centerline of the plate. For the pumping mode, on the other hand, around half of the TSVs are at high pressure and apply significant tilting moment on the plate.

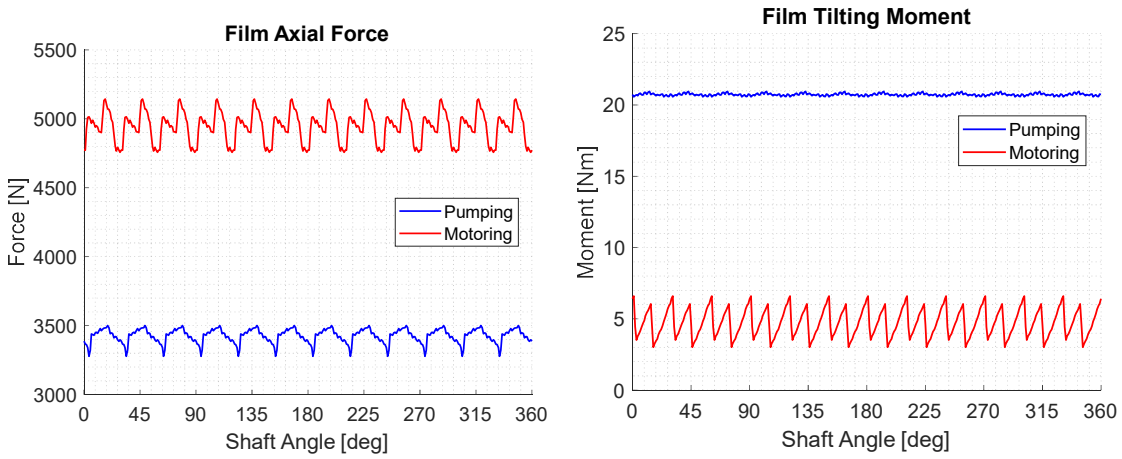

(a) Axial Force

(b) Tilting Moment (Toward LP)

Figure 5.26. Instantaneous loading from gap side due to fixed plate pressure diffusion (a) axial force (b) tilting moment

The resulting resolved force and moment are averaged and collected at each operating point, forming a map of the applied load on the plate over its operating range. These maps are given in Figure 5.27, demonstrating a drastic difference in the plate loading in motoring and pumping mode. From this figure, the effects of operating condition on the required balance force are highlighted. Most notably, there is a drastic change in the loading of the plate when the unit switches between pumping and motoring mode. Within a single quadrant, though, increase in the pressure difference of the unit yields a proportional increase in the gap forces. A change in loading with speed is also observed, with markedly less impact as compared to pressure difference and the sign of the speed. This variation is caused by the differing pressurization behavior of the sealing TSVs.

Balance design

With the loading defined, the next step is to formulate a design which minimizes the hydrostatic force and moment imbalances over the N_ω operating speeds and N_p

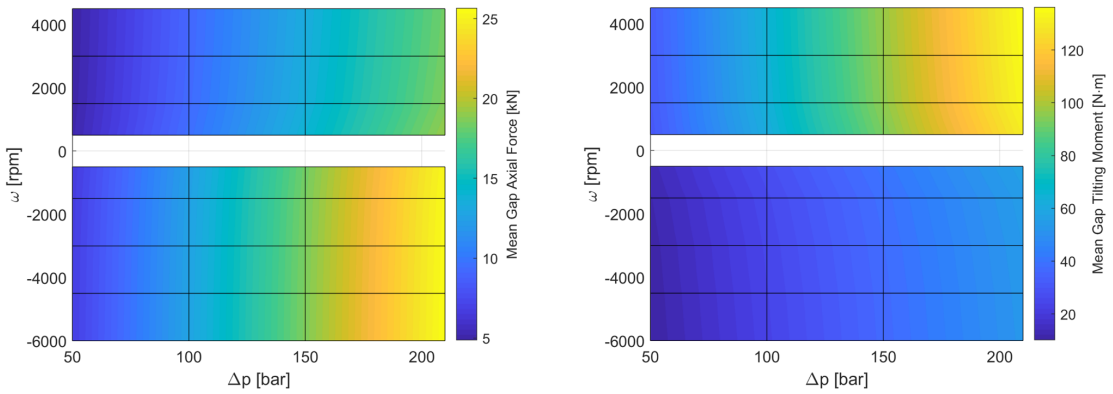

(a) Mean Axial Force

(b) Mean Tilting Moment (Toward LP)

Figure 5.27. Revolution averaged hydrostatic loading from gap side (a) axial force (b) tilting moment

operating pressures where performance is considered. To do so, the error over all operating points is collected into a single error function

$$\varepsilon_{\text{bal}} = \sum_{i=1}^{N_\omega} \sum_{j=1}^{N_p} \left[\left(w_{F,ij} \left| F_{\text{gap,ij}} - F_{\text{bal,ij}} \right| \right)^2 + \left(w_{M,ij} \left| M_{\text{gap,ij}} - M_{\text{bal,ij}} \right| \right)^2 \right] \tag{5.19}$$

As was discussed above, it is important to give priority to the lower operating speeds, since they rely most on hydrostatic balance. This is accomplished with the inclusion of weight functions $w_{F/M}$ for both the moment and force, scaling for the relative importance of each operating point. With an objective defined, the parameterization can then be developed.

In Figure 5.28 the balance side of the lateral plate is demonstrated, including parameters which define the delimiting point between the high and low pressure areas. This delimiter can be seen as the edge of the seal, which is commonly used to isolate the high pressure and low pressure sides. The first parameter is the radius of the seal r_{seal}, which must be greater than the bore r_{bore}, and less than the outer radius of the plate r_{plate}. At this radius, the high pressure area is then determined

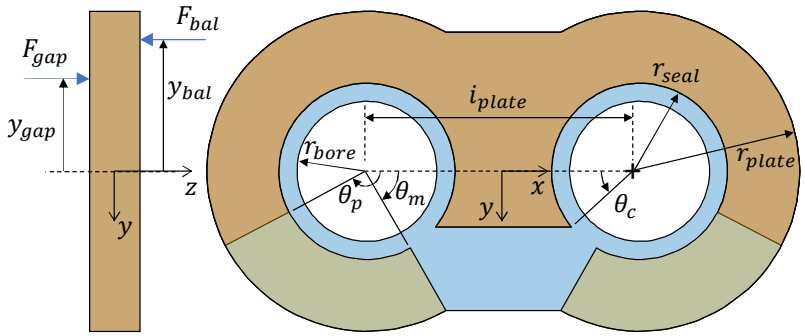

Figure 5.28. Balance side parameterization for Ref E3 design

by two angles defining the outer $\theta_{p/m}$ and central θ_c span of the plate. Notice here that this leaves an intermediate patch on the low pressure side which is isolated from both inlet and outlet. By connecting this patch to the TSVs, it is set to low pressure in pumping mode and high pressure in motoring mode. This strategy allows for the unique design of the balance for the pumping and motoring modes, to overcome the drastic change in TSV pressure distribution. The optimal balance design is then found via a single-objective optimization algorithm applied to optimization problem formalized in Table 5.3.

Table 5.3.
Optimization problem statement for Ref E3 hydrostatic balance design

Minimize	ε_{bal}
By Changing	r_{seal}, θ_c, θ_p, θ_m
Subject To	$r_{\text{seal}} \in (r_{\text{bore}}, r_{\text{plate}})$, $\theta_c < \theta_m$ $\theta_m < \theta_p$,

With an optimal hydrostatic design identified, detailed simulation of the dynamic performance of the plate is required to adjust the design. As was stated previous, this is because the imposition of an arbitrary constant gap yields a pressure solution which only approximates the true behavior. Furthermore, the inclusion of deformation induced wedge and squeezing effects changes the resulting TSV pressurization and thus the hydrostatic load to be balanced. Considering this, Figure 5.29 outlines the design procedure used in the present thesis. The approach begins with an educated initial guess given by the hydrostatic balance. By performing detailed simulations of this initial guess, its performance can be determined. It is likely that this design will suffer from either underbalance yielding excess gap height or overbalance yielding solid contact. Based on the magnitude of this discrepancy, the area can be heuristically adjusted to correct it. Since this can be adjusted in two ways, the choice of parameter to adjust depends on the behavior. If both the pumping and motoring modes exhibit the same imbalance behavior, the central element θ_c must be used to adjust the balance area of both configurations. Instead if the discrepancy occurs only in pumping or motoring, θ_p and θ_m respectively must be adjusted.

Optimal Performance

Following the procedure outline above, the initial design is generated using only the hydrostatic loading and is shown in Figure 5.28. For this design, the predicted load imbalance is shown in Figure 5.30. This figure demonstrates that by using the intermediate balance area on the balance side, the imbalance in force and moment at low speed can be kept below ± 200 N and ± 1 Nm respectively. As the speed is increased, though, the imbalance becomes more noticeable. Over all conditions, the imbalance is kept within 5% of the overall load.

In implementation, though, this design leads to a high contact force between the teeth and plate in the high pressure side of the gear. This discrepancy, as mentioned previous, is likely due to the fact that the pressurization is changed as soon as a tilt

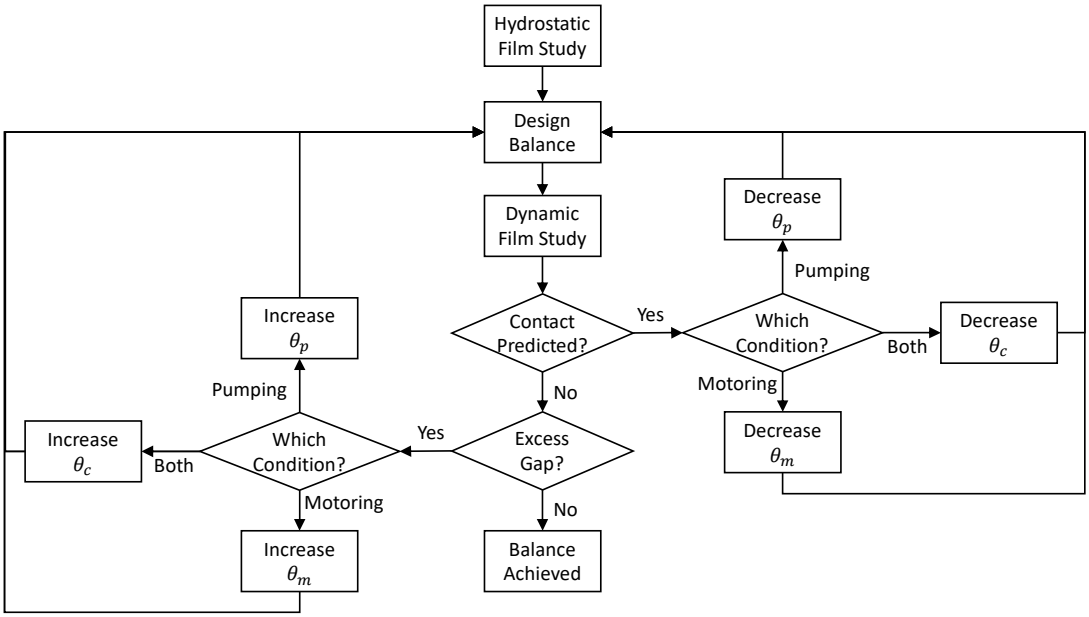

Figure 5.29. Heuristic design adjustment for balancing elements of EGMs

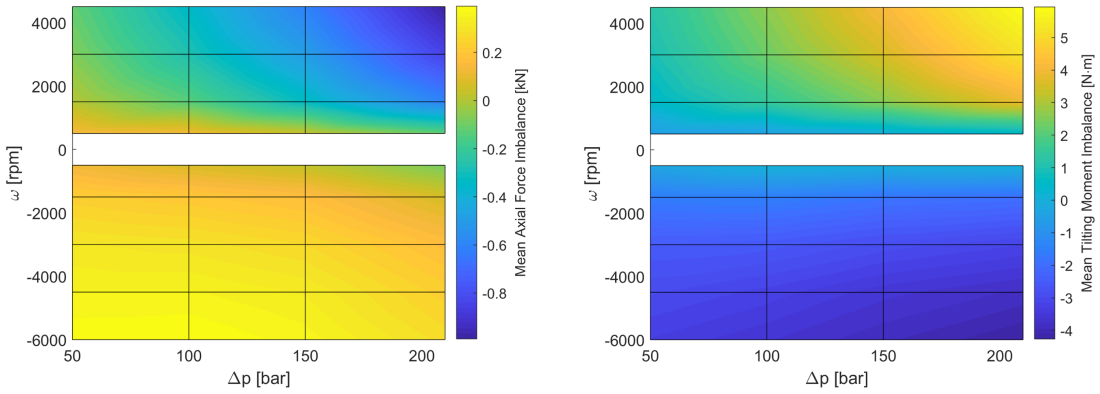

(a) Axial Force Imbalance

(b) Tilting Moment Imbalance

Figure 5.30. Revolution averaged hydrostatic loading from gap side (a) axial force (b) tilting moment

is introduced. Considering this, the high pressure area is adjusted to allow the high pressure area to reach lower in the plate, decreasing the resulting tilting moment and

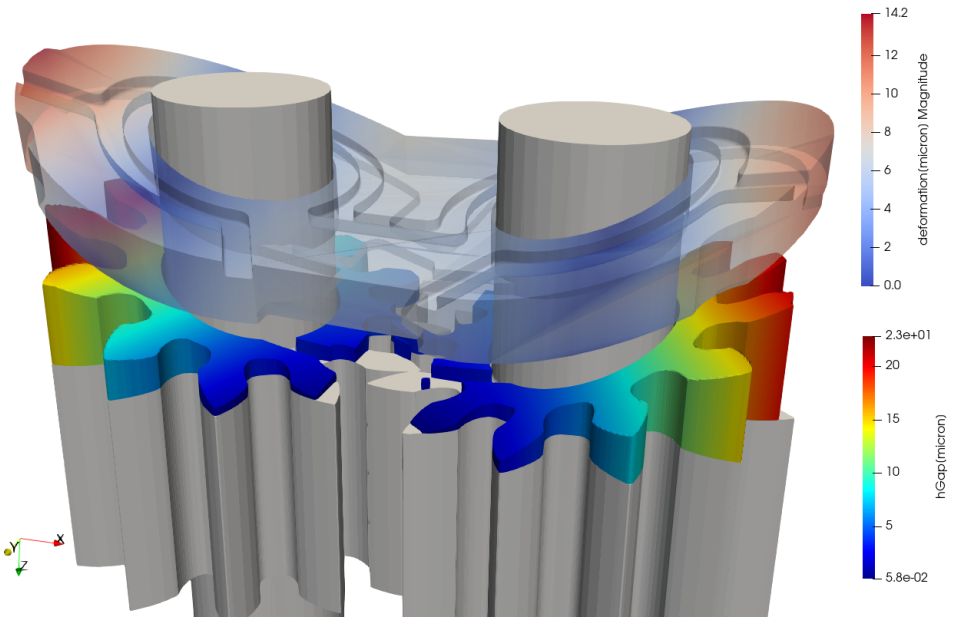

Figure 5.31. Gap Height distribution for Ref E3 EGm at 3000pm, 100bar outlet pressure

alleviating this contact. After iterating though the design adjustment phase, the final result is a balance design that maintains low gap height while avoiding contact of all operating conditions considered. To test this final optimized design, the following figures shows the performance of the finalized design at an operating condition for which it wasn't optimized - high speed (3000rpm) and moderate pressure (100bar) - that is a typical operating point of the unit.

First, Figure 5.31 demonstrates the gap height distribution over the lateral gap of the machine. Note that this distribution is the net effect of the plate and includes both its rigid motion as well as the surface deformations of plate and gears. As was discussed above, this figure shows how the deformation of the plate leads to a large deviation from the parallel gap assumption. Along with this deformation induced gap, there is quasi-steady oscillation in both the tilting and axial position of the plate, as is shown in Figure 5.32. From Figure 5.27(a) it is seen that there is an oscillation in the force applied on the plate as TSVs pressurizes or de-pressurizes. Figure 5.32(a)

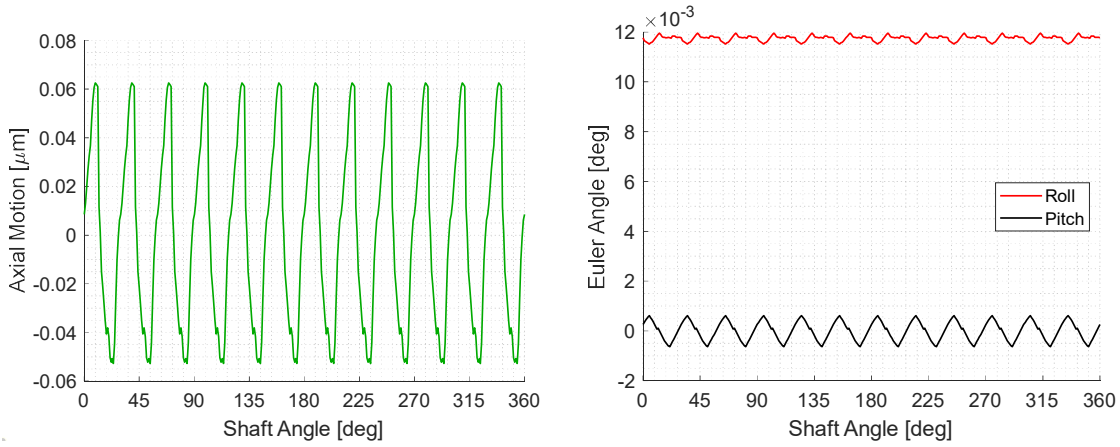

(a) Instantaneous Axial Position

(b) Instantaneous Tilting Angles

Figure 5.32. Revolution averaged hydrostatic loading from gap side (a) axial force (b) tilting moment

then shows that the plate responds to this oscillation with a qausi-steady oscilation about its equilibrium position. This same effect is present in Figure 5.27(b), where tilting moments about both x and y oscillate around their mean. Figure 5.32(b) then shows how both the roll (tilt from inlet to outlet) and pitch (tilt from drive to driven) show a qausi-steady oscillation. Because the hydrostatic balance is not sufficient at this operating point, a mean tilting toward the low pressure side is also demonstrated which allows a hydrodynamic wedge to form.

Together, these effects lead to a pressure profile throughout the gap that deviates drastically from the pressure diffusion solution of Figure 5.25. The design approach acknowledged this behavior, and identified designs that would deviate favorable. This effect is demonstrated in Figure 5.33, where the tilting observed in 5.32(b) leads to a hydrodynamic wedge that builds pressure on the low pressure side of the gear faces. While Figure 5.31 shows that this region does correspond to the minimum film thickness of the interface, this hydrodynamic buildup supports the imbalance so that the minimum gap is kept within 0.5 μm.

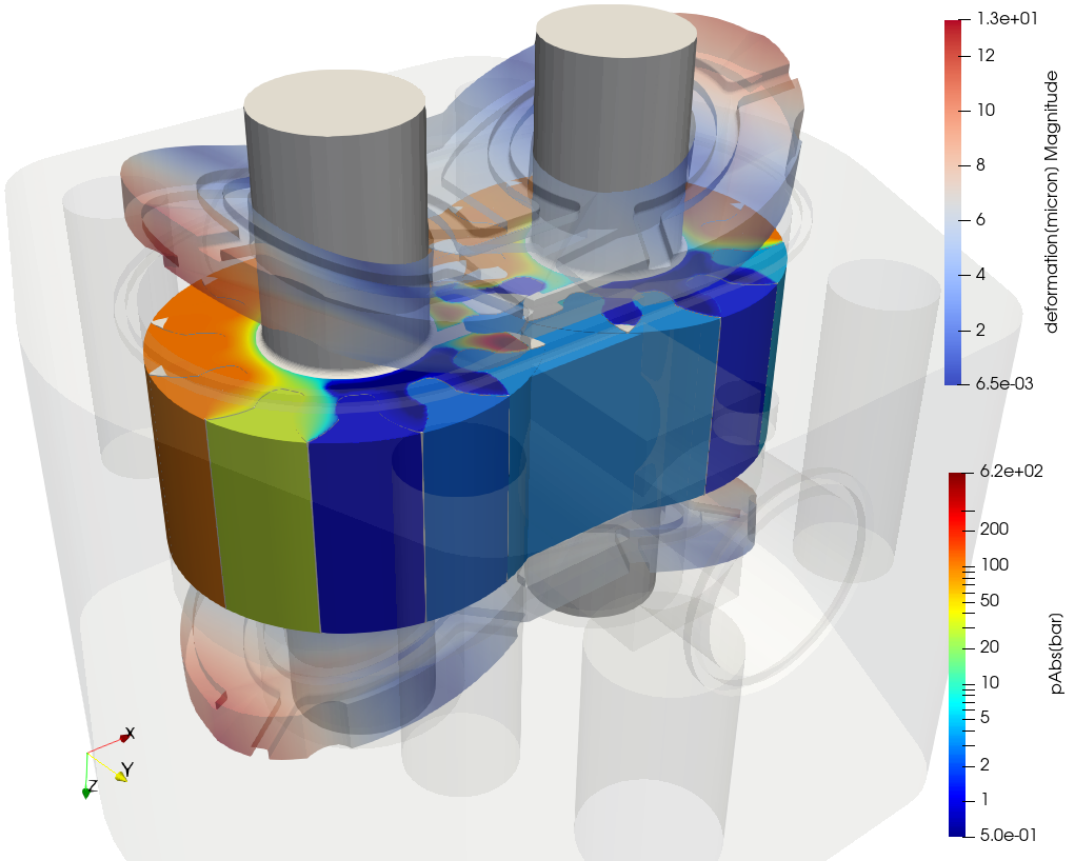

Figure 5.33. Fluid domain pressure distribution for Ref E3 EGM at 3000pm, 100bar outlet pressure

Since the roughness of the bodies is on the same order of magnitude as this minimum gap height, Figure 5.34 shows the resulting contact fraction of asperities in the film increases above null. As discussed in Section 3.4.3, this parameter corresponds to the fraction of the area occupied by contacting asperities. This contact will result in a small removal of material in the break-in process of the unit. Since this region is localized and small, the design performance is considered to be acceptable and is expected to perform well in this condition.

While this contact patch is fairly localized, Figure 5.35 shows how the impact of the asperities affects nearby regions outside of the contact. Here, regions that do not predict contact still show a pressure flow factor <1, corresponding to added flow

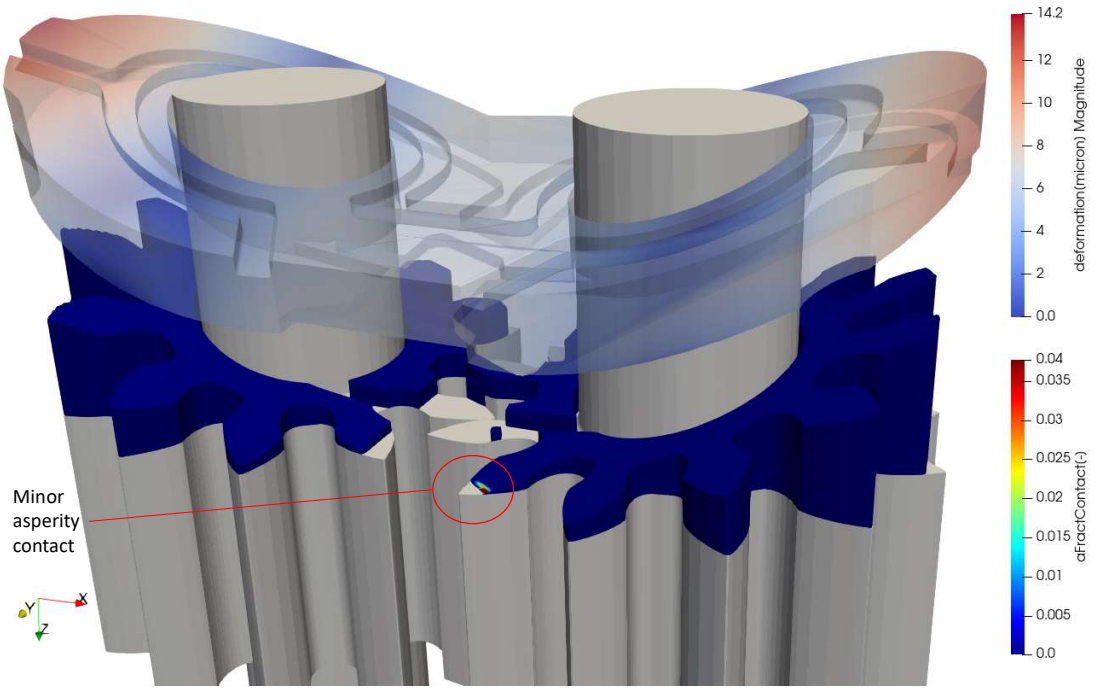

Figure 5.34. Asperity Contact Fraction for Ref E3 EGM at 3000pm, 100bar outlet pressure

resistances introduced by the asperities. This figure, then, highlights the need for accounting of mixed lubrication in the films, as a model that assumed full film would not be able to detect this affect outside of the contact patch.

Returning to Figure 5.33, a region of low pressure (below the inlet) is apparent in both the TSVs and film. To explain this Figure 5.36 shows the density over the domain, highlighting various forms of cavitation that occur during operation. First, the tilting of the rigid body induces a geometric wedge which drops the pressure. A similar effect can be seen due to wedges formed by the deformation of the plate and gears. In either case, the diverging regions that form work to separate the fluid and induces cavitation in response. Finally, consideration of the dynamics of the plate leads to regions that are instantaneously rising. Due to this separation, the film can only fill the void by releasing gas. Notice however that the density changes only slightly to meet these expansions. As a result of these cavitation effects in the film,

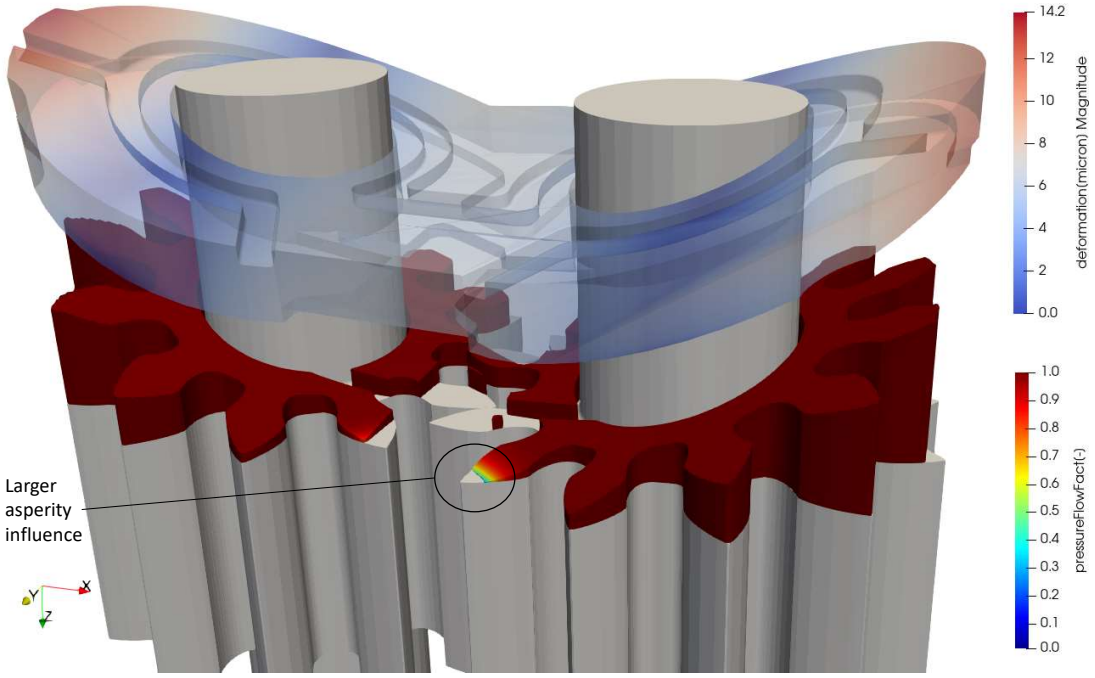

Figure 5.35. Pressure Flow Factor $\phi_{p,x} = \phi_{p,y}$ for Ref E3 EGM at 3000pm, 100bar outlet pressure

fluid must be taken from the displacement chamber. With this, cavitation information communicates across the boundary of the film, and the TSV pressure also decreases. Since the TSV is isolated in the low pressure region of the casing, the adjacent TSVs cannot provide enough flow to replace the lost mass and the TSV remains at low pressure until its radial gap opens enough to receive pressurized fluid. While local density drop is unavoidable due to the working principle of the balance element, this analysis confirms that the tendency of the film to cavitate is sufficiently small.

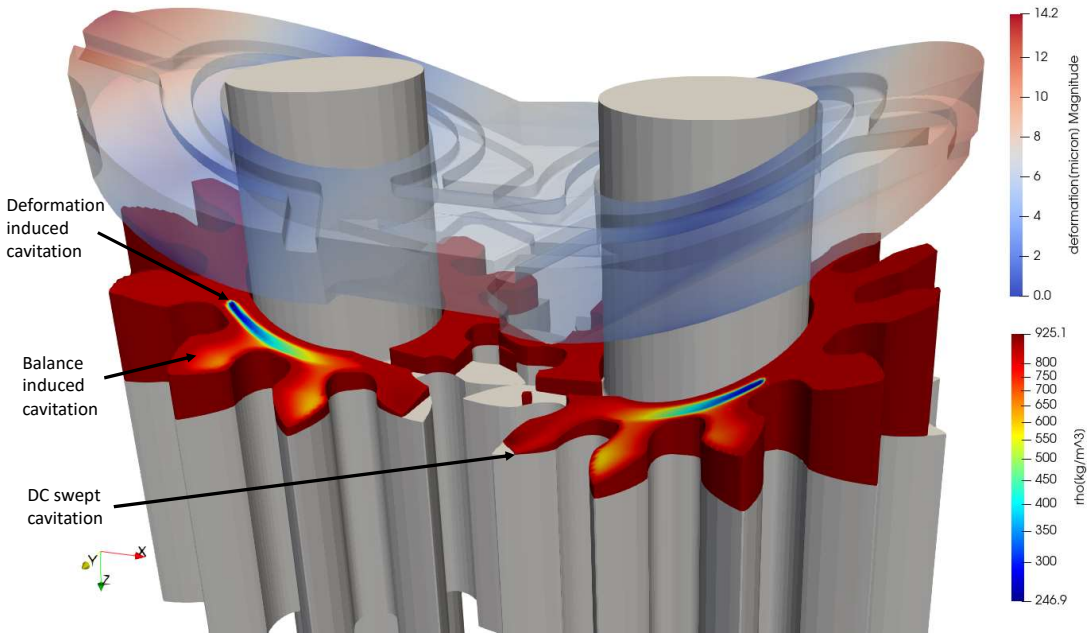

Figure 5.36. Film Density for Ref E3 EGM at 3000pm, 100bar outlet pressure

5.3 Study of interface mutual interaction in an EGM

In the section above, the design of the Ref E3 EGM was discussed. In this unit, a lateral balancing plate was used (Figure 1.4) due to external design constraints. The bearing block strategy demonstrated in Figure 1.5, however, is very common with EGM manufacturers. In these units, the journal bearings are housed within the same balancing element used for maintaining lateral sealing. This geometry inherently leads to a coupled behavior of the two interfaces, due to the coupled nature of the micromotion of the bearing block. Considering this, the present section performs a detailed study of these mutual interactions for the Ref E2 EGM, which employs this bearing block compensation strategy. In this study, the same circuit (Figure 4.23) which was used to load the unit in experiment is recreated here.

Similar to what was shown in Figure 5.33 for the Ref E3 EGM, Figure 5.37 demonstrates the ability of Multics HYGESim to capture the pressure distribution over the

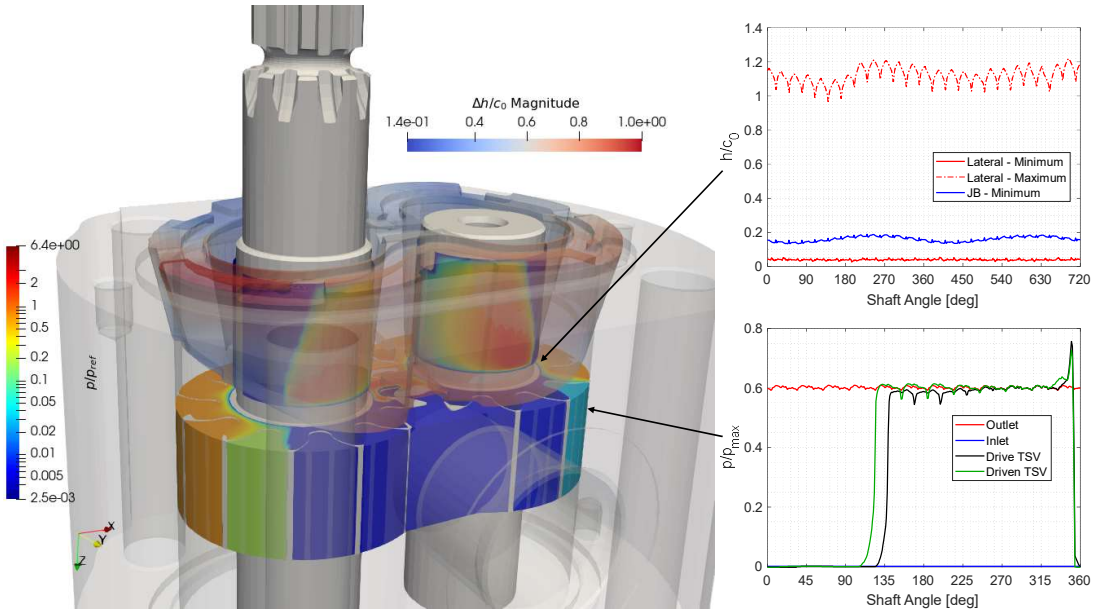

Figure 5.37. Pressure over the fluid domain and resulting floating element deformed position an instant for $p/p_{max} = 0.6$, $\omega = 3000$ rpm

whole fluid domain. Contrasting the lateral plate case, this figure shows the net deformation of the bearing block owing to all 4 lubricating interfaces it interacts with (i.e. the journal bearings and lateral gap). Due to this deformation, the pressure distribution is not symmetric about its axial center-line, as would be expected for a typical plain bearing. This effect was also observed in Section 5.1 for the Ref E1 EGM.

While existing tools [44, 54, 142] are able to capture the pressure distributions across domains that are demonstrated in Figure 5.37, the present work provides novel insight into local cavitation phenomenon across both the films and the displacement chambers. In Figure 5.38, the density distribution over the entire fluid domain is demonstrated. This figure highlights the capability of the tool to study geometry induced cavitation, such as the known tendency of an axially fed journal bearing to induce a void in the diverging region. Similar to Figure 5.36, strong coupling of the dynamics of the balances elements, allows for the wedge and squeeze induced

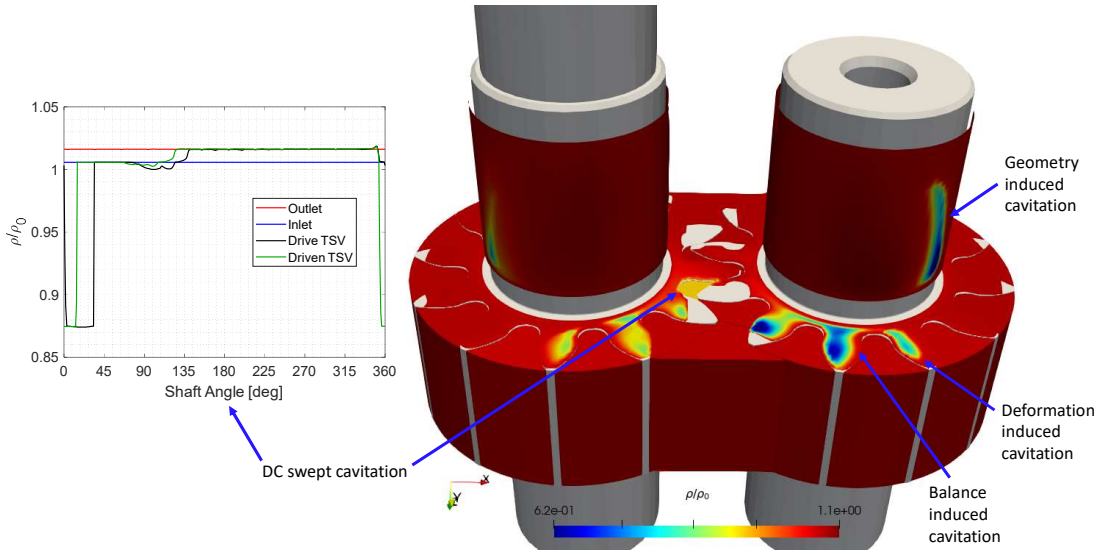

Figure 5.38. Density over the fluid domain at an instant for $p/p_{max} = 0.6$, $\omega = 3000$ rpm

cavitation by the balance of the body to be captured. This figure also shows a more prominent example of the exchange of cavitation information across the LP and DP domains in the meshing teeth. In this case, it is the TSV that undergoes cavitation due to throttling in the meshing zone. Because the gears rotate with respect to the plate, a portion of the cavitated fluid gets dragged into the film. The density of this fluid is low, so a given volume flow corresponds to a lower mass flow. Furthermore, the bulk modulus is very low for the cavitating fluid, so a large amount of mass is required to increase the pressure. As a result, the cavitated fluid gets caught in the film and cannot recover before the next TSV enters the meshing zone.

Again the flow factors (warped by film thickness) show that asperities contribute to the films' flow resistances in regions of minimum film thickness in Figure 5.39. This figure shows, as compared to Figure 5.35, that minimum film thickness regions occur in both the lateral and journal bearing interfaces of the unit. Since this occurs in the journal bearings in a region offset from the center-line of the bearings, this figure

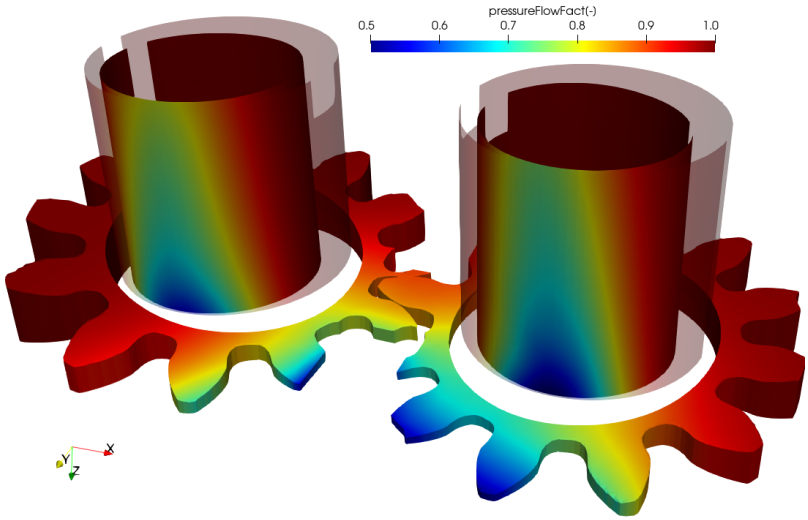

Figure 5.39. Pressure flow factor with films warped by gap height at an instant for $p/p_{max} = 0.6$, $\omega = 3000$ rpm

justifies the need to consider both interfaces in the moment balance of the bearing block.

Along with capturing more directly integrated physics, a major accomplishment of this thesis is the ability to study the mutual interactions of the lateral lubricating and journal bearing interfaces of an EGM. Due to the nature of the films, the major pressure contribution of their forces are orthogonal. As the body tilts and deforms, though, the pressure distributions develop in such a way that the net moment balance of the body is given by both interfaces. This is demonstrated in Figure 5.40, which shows how the journal bearings contribute a non-negligible moment, around 20% on average, to the net opposition to planar tilting of the body. In Figure 5.40(b), the magnitude of y-direction moment opposing the rocking from drive to driven is also shown. Since this value is centered around zero, this figure simply demonstrates that the bearing moment tends to be on the same order of the lateral gap contribution. In Figure 5.40(a), the contribution of the journal bearing opposition to the net tilting moment of the balance and TSV forces toward suction or delivery (x-direction) is included. Over the majority of operating conditions, this value is positive, cor-

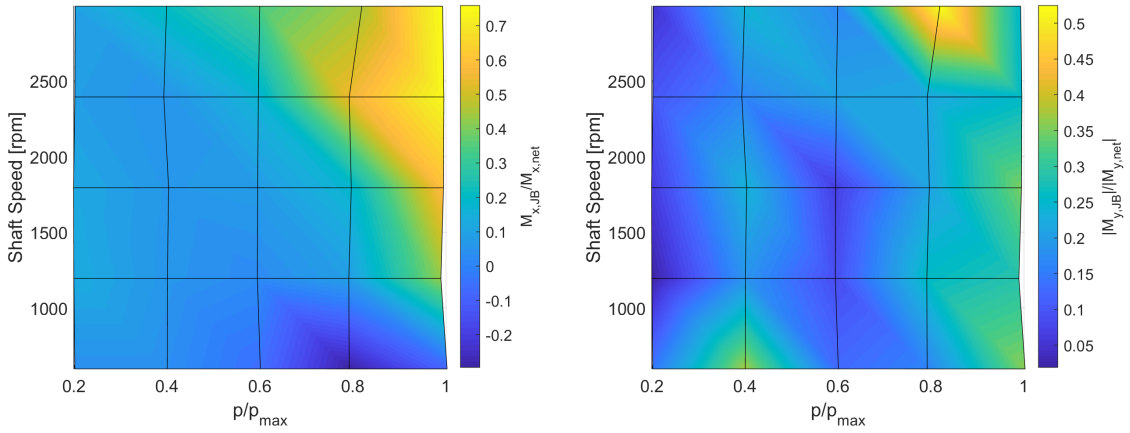

(a) Suction to Delivery

(b) Drive to Driven

Figure 5.40. Contribution of tilting moment opposition for the journal bearings on the bushing (a) Tilting from inlet to outlet (b) Tilting from drive to driven

responding to a condition where the bearing helps to prevent this tilting. For low speeds and high pressures, however, this figure demonstrates that the bearings tend to further tilt the bushing. This result justifies the need to couple the solution of these interface, as an interface in isolation does not capture the net dynamics of the bodies.

5.4 Study of piston-slipper spin in an APM

Similar to the section above, the dynamics of the piston-slipper assembly of an APM are determined by the net influence of the piston-cylinder and slipper-swashplate interfaces. Since most of the models for these machine discussed in Section 1.3 studied a single interface in isolation, though, they were not capable of capturing the coupled nature of the bodies' motions. For the first time, then, a detailed study of the sensitivity of the piston spin to various physical parameters of an APM is performed. Namely, this section will focus on the effects of the friction of the ball-socket

interface with operating condition – pressure difference, shaft speed, socket friction, and displacement angle. This study will take the commercial high pressure Ref P1 APM as reference.

Before entering this discussion it is worth clarifying, aided by Figure 5.41, the terminology used in this work. As was discussed in Section 2.2.4, the dynamics of each body are solved separately. This means that the block, piston, and slipper will each be rotating at unique velocities $\underline{\omega}_{block}$, $\underline{\omega}_{piston}$, $\underline{\omega}_{slipper}$ respectively. Since the block is mechanically connected to the drive shaft, its rotation speed is exactly equal to the shaft speed $\underline{\omega}_s$. Similarly, the swash-plate is fixed in this analysis and thus experiences $\underline{0}$ angular velocity. The piston and slipper, on the other hand, are free to rotate in response to the applied moments. The implications of this spin are two-fold; first the component parallel to the shaft (axial spin) acts to change the perceived average surface velocity of the piston-cylinder interface. The remainder of the angular velocity of the piston and slipper bodies lies in the plane perpendicular to the shaft axis (planar spin) and acts to change the gap height of the piston-cylinder interface. As will be discussed in this section, the central axis of the slipper is inclined with respect to the shaft, so that it must undergo both axial and planar spin in order to preserve a given gap height distribution.

The result of the differing spin of the two bodies is demonstrated for the piston-cylinder interface in the detail of Figure 5.41, but is equally applicable for the film between the slipper and swashplate. Here, the average velocity in the gap is determined by the rotation of both faces. Since the block and swashplate velocities are constant, this section will focus on the axial and planar spin of the piston and slipper bodies with variation in operating conditions. This figure also highlights how the velocity is not constant throughout the interface. This small variation is due to the linear translation of the bodies, which contributes a much smaller impact than the spin motion for typical machines.

With this terminology defined, Figure 5.42 first demonstrates a typical result of this tool with examples of the field data attained from the universal Reynolds

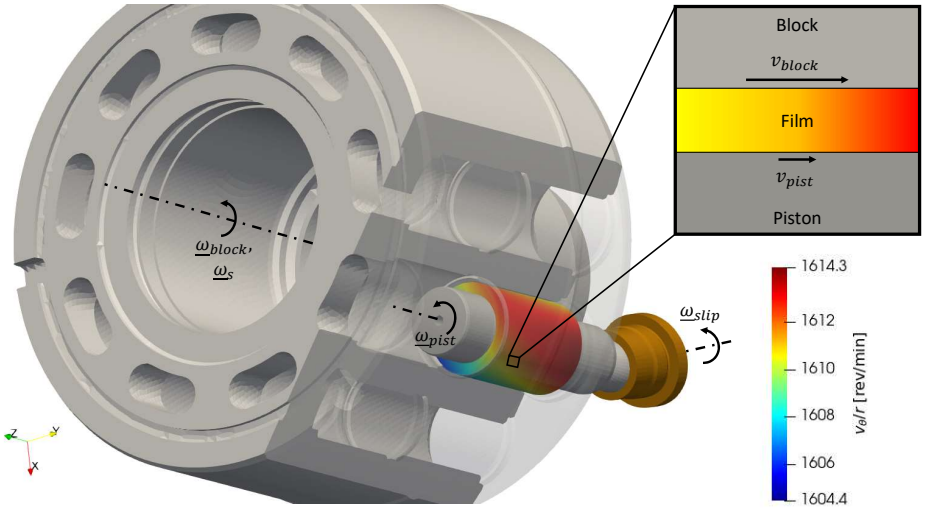

Figure 5.41. Body spin definitions

solution. Figure 5.42(a) demonstrates the film pressure distribution over the piston-cylinder, cylinder block - valve plate, and slipper-swashplate interfaces. This figure justifies the need to consider the detailed Reynolds solution as opposed to simplified analytical approximations, where there are high hydrodynamic pressures which build to oppose the tilted bodies. While these pressure results are attainable (in isolation) using existing models discussed above, the present work introduces the novel ability to describe the bulk fluid density over the domain. Due to the diverging wedge that forms in the piston-cylinder interfaces from this tilt, Figure 5.42(b) shows how the local density of the fluid drops drastically while the film pressure drops only slightly. Focusing on the interfaces of interest for this work, Figure 5.42(c) shows that the pressure peaks are not sufficient to hold the tilting moment on the piston-slipper body. As a result, the film thickness drops to a small enough value to allow for solid contact of the asperities and surfaces to share the loads. Figure 5.42(c) then shows how the asperities of the surface contribute a non-negligible resistance to flow in this region.

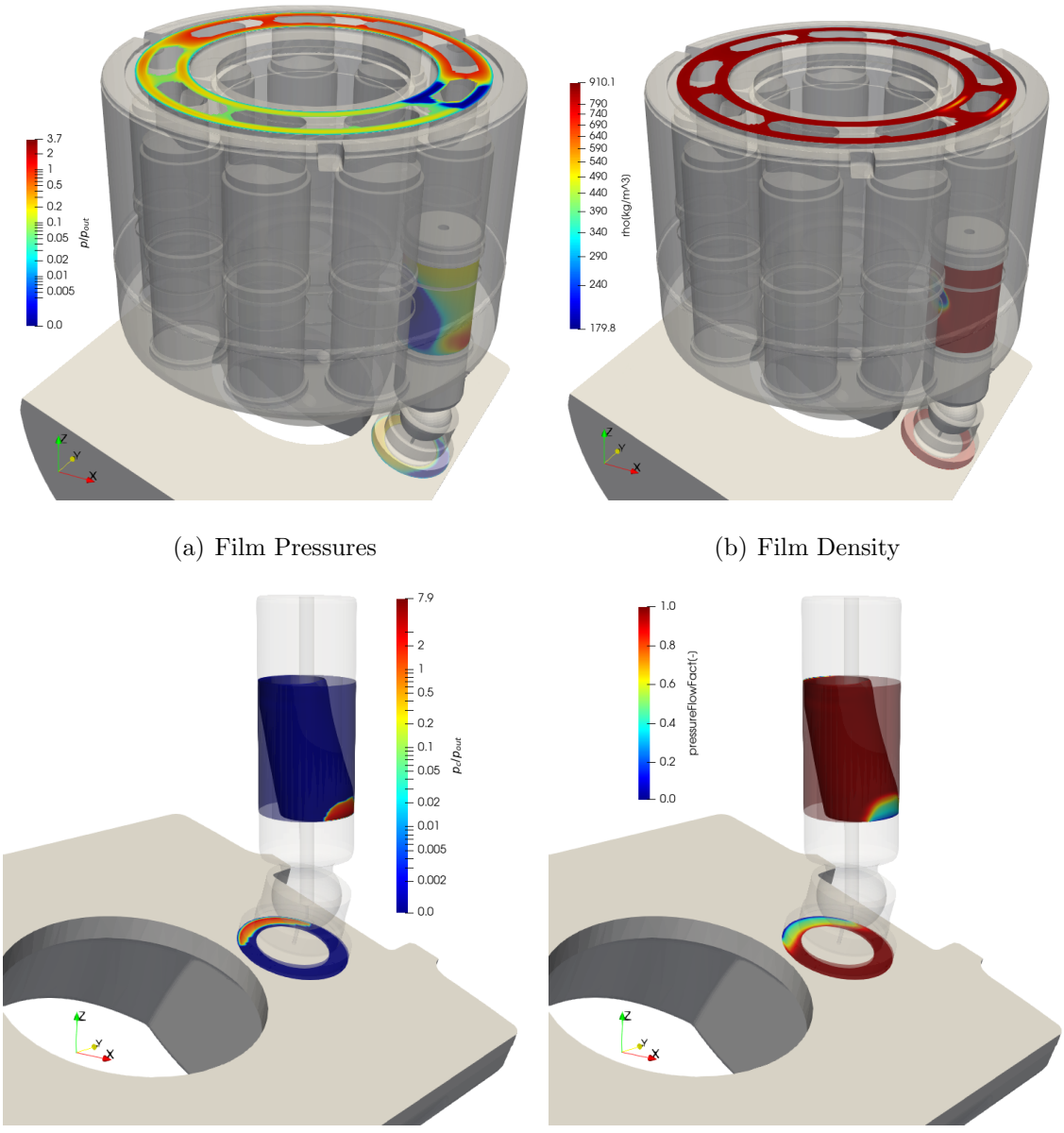

(a) Film Pressures

(b) Film Density

(c) Film Contact Pressure

(d) Film Pressure Flow Factor $\phi_{p,x} = \phi_{p,y}$

Figure 5.42. Field Data for High pressure high speed condition (a) Film Pressures (b) Film Density (c) Film Contact Pressure (d) Film Pressure Flow Factor $\phi_{p,x} = \phi_{p,y}$

To understand first a typical influence of the friction of the ball-socket, a moderate operating condition of the unit is considered. In this condition, Figure 5.43 shows

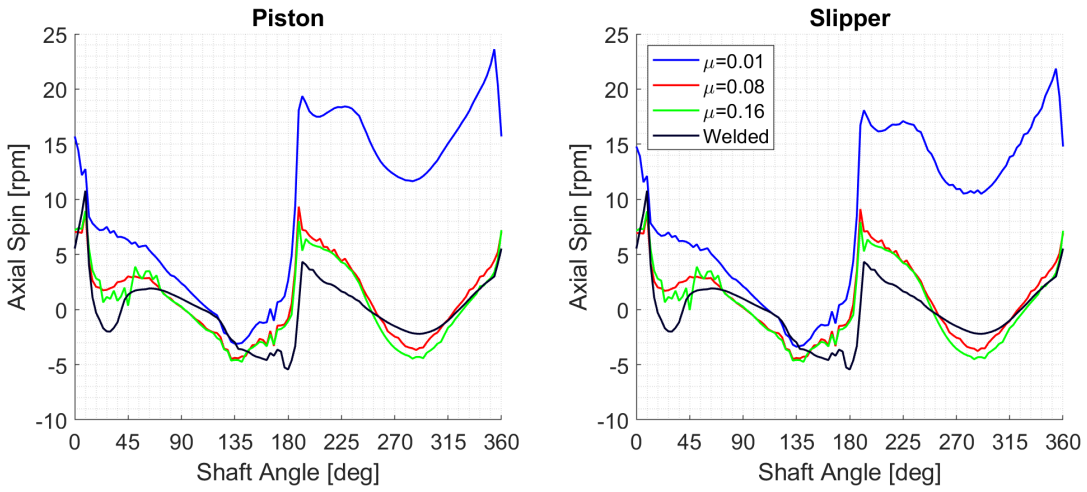

Figure 5.43. Axial spin at moderate operating condition for piston and slipper with varying socket friction

the component of spin aligned with the drive shaft for both the piston and slipper bodies. Here the static friction coefficient μ_s (and dynamic friction $\mu_d \approx \mu_s/2$) of the ball-socket is varied from its typical value 0.16 to adjust the effective resistance predicted with Equation 3.24. This plot investigates the variation versus half the typical friction (0.08), almost no friction (0.01), and infinite friction (welded).

It is worth noting, for clarity, the implication of a non-zero spin of the bodies. While the piston-cylinder interface is nominally aligned with the axis of the shaft, the slipper-swashplate interface is inclined by the swashplate angle. This means that as the slipper spins about the axial direction of the unit, it must also undergo planar rotation in order to maintain sealing of the hydrostatic pocket. This additional velocity, demonstrated in Figure 5.44, has a non-negligible contribution to the friction moment at the interface. For reference, the inclusion of a welded socket condition demonstrates the magnitude of planar tilting that is allowed only by the net motion of the two bodies.

As was discussed above, the resulting axial spin of the bodies is excited by the net imbalance of shear moments in the piston-cylinder and slipper-swashplate interfaces,

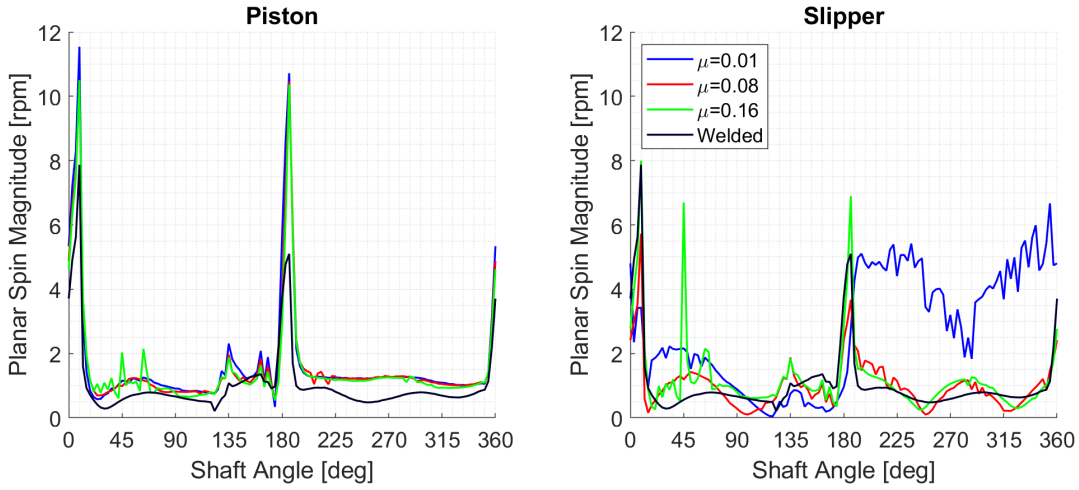

Figure 5.44. Planar spin at moderate operating condition for piston and slipper with varying socket friction

which is then opposed by the resulting friction in ball-socket interface. In effect, the piston-cylinder interface works to accelerate the body to the angular rotation of the block, while the slipper-swashplate interface works to decelerate the body to that of the stationary swashplate. In interpreting these results, then, it is important to understand the shear contribution of these interfaces. The dominant factor which determines the shear of the interfaces is their gap distribution, the minimum of which is demonstrated in Figure 5.45.

During the high pressure stroke of the unit, the pressure of both the displacement chamber and hydrostatic pocket yield sufficient normal force such that the socket behaves similarly to the welded interface. At the transition of the high to low pressure stroke of the unit, the force on the piston abruptly drops. With this drop, the shear at the piston-cylinder interface is able to overcome the friction force at the ball-socket interface, and the bodies accelerate. As the piston-slipper progresses through the low pressure stroke, though, the significantly lower pressure in the hydrostatic pocket tends to decrease the eccentricity of the piston-cylinder interface while simultaneously allowing the slipper to separate from the swashplate. As a result, the shear at both the

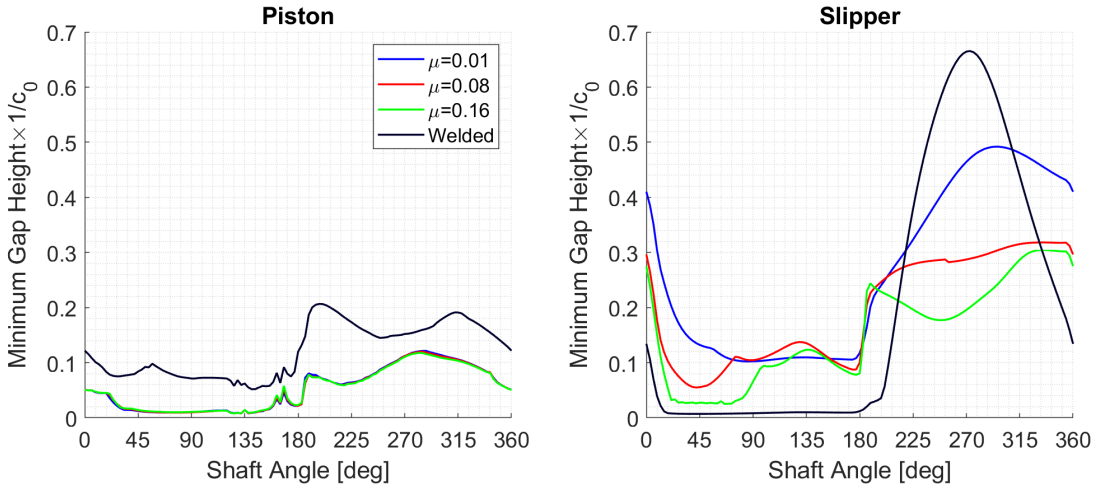

Figure 5.45. Minimum gap height at moderate operating condition for piston and slipper with varying socket friction

slipper-swashplate and piston-cylinder interface decreases, and the moment balances transitions to a steady spin velocity. Finally, as the piston-slipper object reaches the transition back from from low to high pressure, the force abruptly increases and the spin is halted.

Since the normal force on the socket that elicits this frictional force changes with operating conditions, it is also useful to examine the variation of this normal force. To do so, Figure 5.46 demonstrates the variation in axial spin as the pressure difference across the unit is varied. This result shows how increase in pressure, and therefore contact force, tends to decrease the spin of the piston. A counter-intuitive result is seen for the slipper, though, which teds to slightly increase in speed with increase in pressure. To explain the reasoning for this, Figure 5.47 demonstrates the change in minimum gap height with varying pressure. This figure demonstrates that while the piston's minimum gap changes, there is a much more significant variation in the slipper-swashplate gap. As the slipper lifts from the swashplate, its shear contribution to the moment balance of the body decreases and its speed is determined increasingly by the socket friction moment.

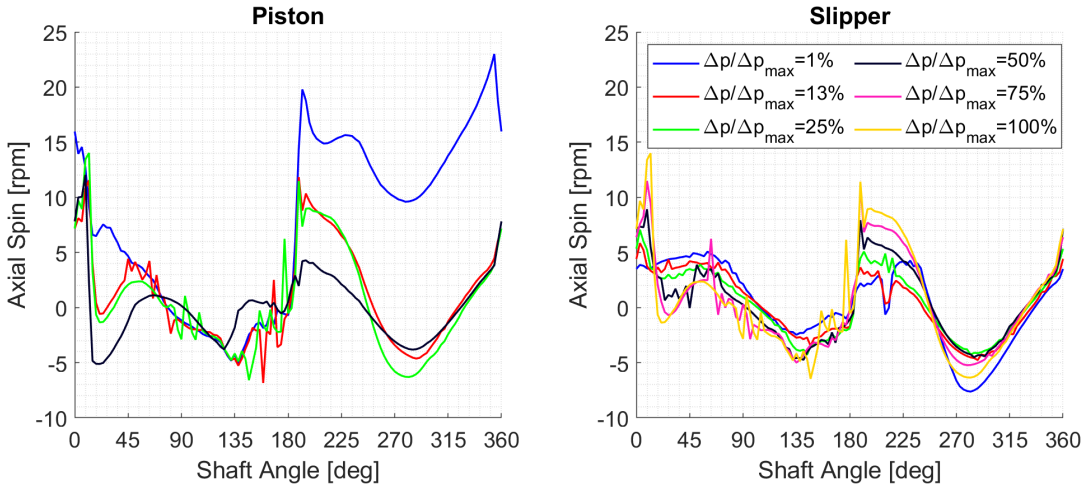

Figure 5.46. Axial spin at moderate operating condition for piston and slipper with varying operating pressure difference

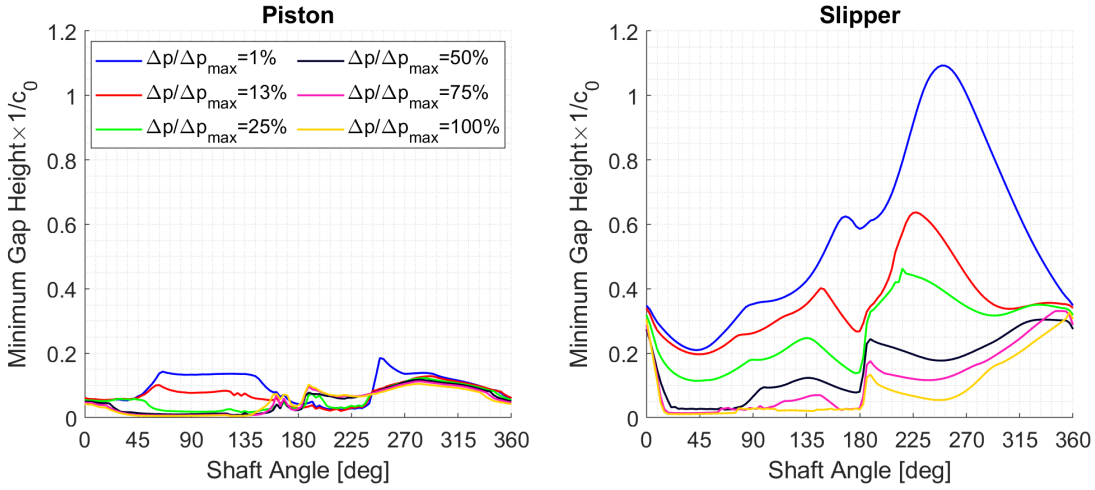

Figure 5.47. Minimum gap height at moderate operating condition for piston and slipper with varying operating pressure difference

The other factor which determines the spin of the piston is the shaft speed, as it is the rotation of the block that excites the piston spin. The effect of varying shaft speed is demonstrated in Figure 5.48, with the piston and slipper spins normalized by the shaft speed. Note that this figures shows an almost constant relative spin of the

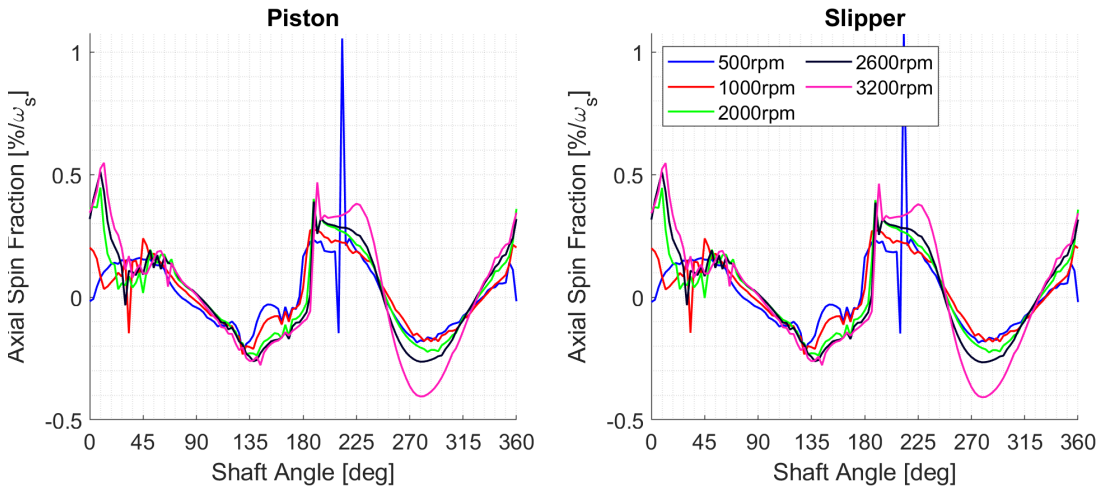

Figure 5.48. Axial spin at moderate operating condition for piston and slipper with varying shaft speed

bodies with the shaft speed. Due to the non-linearity of the shear term, as well as the difference in pressurization of the displacement chamber and hydrostatic pocket, the shape slightly varies across the operating conditions. Over all the operating ranges, though, the bodies rotate at no more than 1% of the shaft speed.

To explain this variation in shape, Figure 5.49 demonstrates the variation in pressure of both the displacement chamber and hydrostatic pocket at varying operating speeds. Due to the compressibility of the fluid, this figures shows how the higher operating speeds show a wider angular span of pressurization. As a result, they can maintain spin further into the high pressure stroke, while the lower speed conditions are stopped by the more immediate normal force.

The results discussed above justify the need for strong coupling of the films and body dynamics. To quantify this claim directly, a comparison of the overall moment sharing of the piston-slipper body loading by the piston-cylinder and slipper-swashplate interfaces is performed. Inherent to the kinematic of a swashplate type APM, the incline of the slipper will impart a large tilting moment (kinematic moment). In Figure 5.50, the projection of the slipper-swashplate moment (discluding

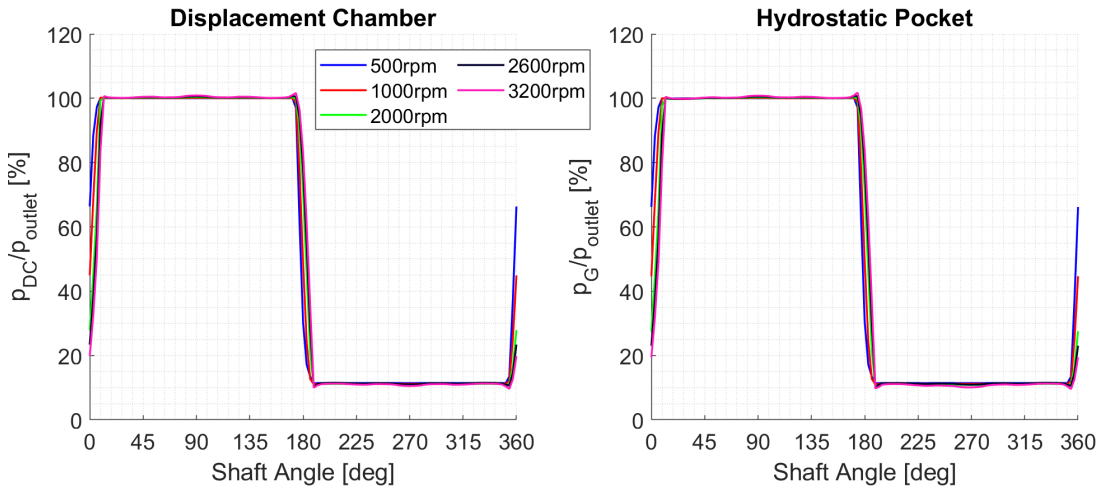

Figure 5.49. Pressure at moderate operating condition for piston and slipper with varying shaft speed

this contribution) and the piston-cylinder moment are normalized by the kinematic moment. In doing so, this figure demonstrates the relative contribution of each interface to the overall carrying of the kinematic moment. Over the high pressure stroke, the moment is carried primarily by the piston-cylinder interface. In the low pressure stroke the kinematic torque drops significantly, and an equilibrium is found with the two interfaces opposing one another. The strongest justification for the necessity of the coupled dynamics can be seen at the transitions between low and high pressure. Here, the transients of the DC and pocket pressures lead to a condition where the moments of the slipper-swashplate interface approach the same magnitude as the piston-cylinder interface. Consideration of the two in isolation, then, would mask this strongly coupled transitory response.

Further results can be offered to support the need for strong coupling of the films and body dynamics. Further results however, can be offered to support the need to strongly couple the solution to the displacement chambers of the unit with the films and dynamics. In Figure 5.51(a), the net leakage flow of the unit is plotted against the inlet and outlet port flow of a single DC. Since the magnitude of these

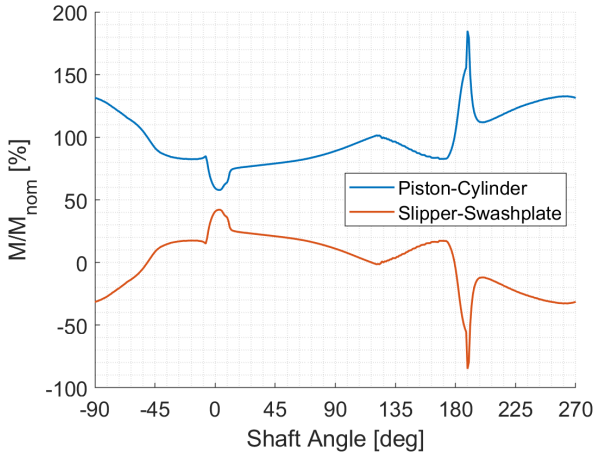

Figure 5.50. Moment Sharing of the Piston-Cylinder and Slipper-Swashplate interfaces at the moderate speed condition

port flows depends on the operating speed of the unit, a moderate middle point in speed is taken. From this figure it is clear that in the transitions between low and high pressure, the leakages are on the same order of magnitude as the overall flows into and out of the DC. Observing from the pressure buildup equation 2.4, this means that the leakages have comparable effects on the dynamics of the pressurization of the unit as the porting. As is shown in Figure 2.1, then, the sensitivity to pressure then propagates into both the boundaries of the Reynolds films as well as the loading of the bodies. Figure 5.51(b) then shows that each interface face contributes a non-negligible portion to the leakage flow, so that all must be considered in simulation.

Furthermore, it should be pointed out that this study was performed on a successful commercial unit. From the results presented in this section, it is clear that the porting is well designed. For a general use of the tool though, especially in a prototyping development, this porting need not be optimal and the strong coupling aspect is even more important. This is because in the absence of appropriate cross-port flows (a poorly designed porting), the effects of the films in the presence of cavitation and pressure peaking become increasingly prominent. This effect plays an increasing

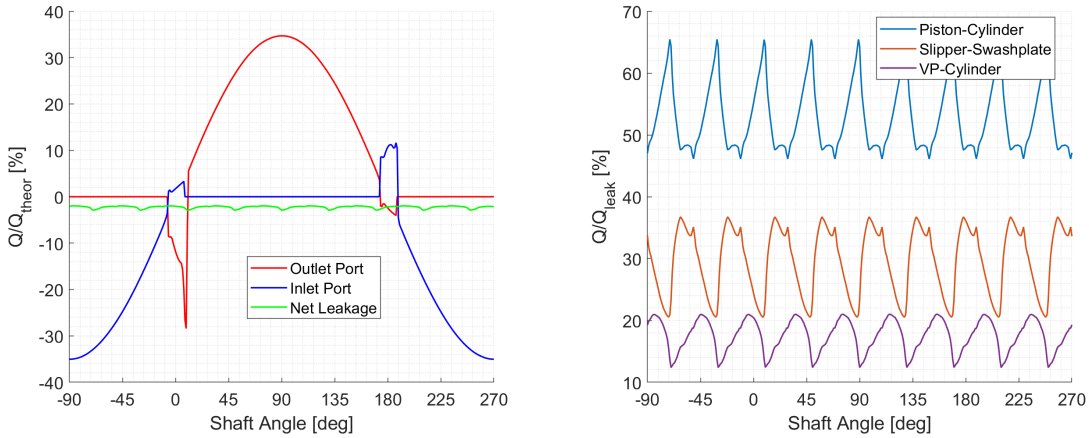

(a) Comparison with main flow

(b) Leakage contributions

Figure 5.51. Leakages over of the 3 main interfaces of the machine at the moderate speed condition (a) Comparison with main flow (b) Leakage contributions

role as the operating speed is decreased, where the pressure driven leakage magnitude approaches the magnitude of the speed-dependant flow of the unit. Thus, the use of a strongly coupled model protects against the potential for a weakly coupled model to mask these effects.

6. SUMMARY

This thesis presented a numerical model for the evaluation of performance of positive displacement machines. It included both a simple analytically approximated model implementation, as well as a detailed numerical model. In both, the motion of the floating bodies is considered, as well as its impact on the thin films of fluid within finite clearances of the unit, on the resulting performance. For the DP simulation model, the effects of cavitation in the films, mixed lubrication, fluid-structure interaction, and the impact of these features on both the body dynamics, LP model, and the adjacent films were captured. These models were implemented as a stand-alone toolbox Multics, which can be used to model the behavior of any PD machine with appropriate use of the toolbox. The models of an EGM, APM, and Gerotor created within this toolbox were validated again experimental results of the reference machines, with average error in predicted efficiency around 1% for both APMs and EGMs over their entire operating range. The lubricating films were independently validated against the relevant state of the art. Application of the EGM model Multics HYGESim was demonstrated by performing a virtual optimization of an EGM for an EHA, as well as detailed analysis of the implications of each modeling assumption on behavior. Similarly, the APM model Multics CASPAR was used to study the mutual interactions of the piston-cylinder and slipper-swashplate interfaces of an APM for the first time, showing as much as 50% of the load sharing carried by this mutual interaction.

In terms of floating body dynamics, this work improved the modeling capability by considering the inertia of the body, as well as the linear and angular accelerations that result from a given load. In addition to the pressure loading considered in the past, this work also included the effects of shear on the bodies as well as squeeze in both the analytical approximate and detailed numerical solutions. In DP simulation,

the dynamics of the bodies are given not only by a single film, but the collection of loading by all films that interface with the body. Using this updated model, the coupled response of the journal bearing and lateral lubricating interfaces of an EGM in response to a tilting of the bearing block was captured. It was confirmed in this analysis that the mutual interactions of these interface contributes an average of 20% to the overall load sharing. With this, the resulting flow ripple of an EGM and Gerotor, as well as the torque ripple of the Gerotor, were validated against experimental results.

Next with regard to cavitation in the films, this work derived a novel extension to the commonly used Elrod cavitation algorithm, removing the need for a discontinuous switch function that caused numerical instability. Furthermore, this approach provides for more detailed understanding of the makeup of the ruptured film in terms of gas and vapor content. The results of this model showed good agreement with simulation in literature of the Elrod method for both steady state and dynamic bearings.

In a related work, the commonly used Patir and Cheng average Reynolds mixed lubrication model was extended, applying the same flow factors derived in this model to the universal Reynolds equation. This formulation allows for the consideration of both the cavitation and mixed lubrication effects within the film automatically and with coupled solution.

The resulting pressure that comes as the solution to the mixed universal Reynolds equation is used with a novel analytically-derived influence matrix approach. Using either this novel form or FEM approaches, the transient responses of the deforming bodies was captured for the first time. These allow for consideration of the film deformation without or without the availability of external software or existing designs, and allows for consideration of the macro-deformation of the bodies in the lumped parameter modeling. The deformation models used in this thesis show good agreement with FEM results over varying loading and geometries, confirming their validity.

Finally, the entirety of the modelling aspects defined above were implemented into a stand-alone coupled simulation tool. By using thread-wise parallelization, this tool

can accomplish both low latency or high throughput simulation, with high efficiency for reasonable mesh resolution. As compared to existing approaches, the present work is able to accomplish a given simulation in at least 50% of the time. The API of this coupled tool was proven successful in its application to a third PD machine for which it was not derived, and in its matching with experimental simulation of the unit. This work has applicability as follows

- This work demonstrated how the LP tool could be used within an optimization workflow to identify an optimal EGM design without any user input once the objectives are defined. Therefore, PD manufacturers could use these approaches to develop similar virtual prototyping procedures to improve the efficiency of their next generation of units and to avoid the need to manufacture prototypes to evaluate their performance. This is especially true with the addition of the analytical deformation, removing the requirement for detail CAD of a unit to analyze its performance.

- Similarly, this tool could be used to study an existing unit, including diagnosis of unknown behavior of a unit, or design improvement of lubricating interfaces. Using the DP model, this tool could be used to predict failures such as wear in regions of mixed lubrication or pitting damage due to regions of high cavitation. This capability was demonstrated for both reference external gear machines and axial piston machines.

- By adjusting the inputs of the model, the resulting change in performance of the unit can easily be observed within a single model result. This tool, then, is helpful for understanding the sensitivity of a given unit to choice a parameter, which could be used to assist designers in decisions such as required tolerances and material selection.

7. FUTURE RESEARCH DIRECTIONS

7.1 Thermal Effects in Films

The author has put effort in adapting the compressible Reynolds equation to considering the effects of not only density variation with pressure, but with temperature

$$\rho = \rho(p, T) \tag{7.1}$$

Following the derivation of Section 3.1

$$\frac{\partial \rho}{\partial \psi} = \frac{\partial \rho}{\partial p}\bigg|_T \frac{\partial p}{\partial \psi} + \frac{\partial \rho}{\partial T}\bigg|_p \frac{\partial T}{\partial \psi} \implies \frac{\partial p}{\partial \psi} = \frac{\rho}{K_T}\frac{\partial \rho}{\partial \psi} - \frac{\partial \rho}{\partial T}\bigg|_p \frac{\partial T}{\partial \psi} \tag{7.2}$$

the density is related now to both the pressure and density. Applying this modification to the compressible Reynolds equation given in Equation 3.1

$$\underline{\nabla} \cdot \left(\frac{Kh^3}{12\mu} \left(\underline{\nabla}\rho - \frac{\partial \rho}{\partial T}\underline{\nabla}T \right) \right) = \underline{\nabla} \cdot (\rho h \underline{\overline{u}}) + \frac{\partial \rho h}{\partial t} \tag{7.3}$$

demonstrates that the distribution of temperature in film directly affects the diffusion of density, as well as varying the fluid properties within the film. Since the lumped parameter components of the model are already capable of solving for the temperatures, the model change requires only updating a non-constant film temperature with thermal boundary conditions given by the LP domain and the bodies. To that point, from the beginning of the fluid model derivation, it is assumed that the polytropic process given in Equation 2.20 does not include temperature change. In reality, information on the change in temperature over the film will improve not only the prediction of the cavitation from the universal Reynolds equation, but will allow the consideration of the state change of the liquid and gasses with temperature.

An important followup work could be to integrate a thermal solver of the fluid films and bodies into the Multics suite, using the thermal conditions of the lumped

parameter model as boundary conditions. In doing so, this model could be used to study the resulting fluid-structure-thermal problem and its impact on the dynamics and cavitation behavior of PD machines.

7.2 Choking conditions

In the present model, the effect of choking in the flow constriction is modeled simply by relating the flow to the speed of sound at a reference fluid state. While the author believes this is an adequate model, no further improvement was possible due to the lack of study of these flows for liquids in literature. A future research direction could be the refinement of this assumption by studying the behavior of a nozzle in sonic conditions with oil as a working fluid instead of an ideal gas.

7.3 Studying the impact of films on unit NVH

An important research direction in Dr. Vacca's research group, as well as in industry, is the study of the noise emissions of PD machines. Due to lack of availability of detailed models, these studies typically rely on experimental evaluation of prototypes. In Dr. Vacca's research group, a FEM/BEM model has been developed for EGMs [143], capable of mapping the instantaneous pressures and loading from the TSVs to the body of the pump, and tracking its propagation from fluid-borne noise to structure-borne and finally to air-borne noise. A limitation of this model is that, due to lack of information of the pressure distribution, the lateral lubricating and journal bearing interfaces are approximated with oscillating distributed forces. With a validated means for finding not only the instantaneous loading of these films, but their pressure distributions, a model expansion could be performed to better model these interfaces. With this revised model, a follow-up on the optimization procedure presented in Section 5.2 could also be performed, with focus on the modification of unit geometry to reduce the resulting noise radiation of the unit in response to these film loading.

7.4 Cavitation in films

In order to conserve computational resources in the present work, the transients of the gas release were neglected. While this is a safe assumption for steady operation, it is possible the consideration of the dynamics of individual bubbles, or even the homogeneous mixture, may lead to improvement in prediction of cavitation phenomena in these units. Additionally, it could be useful for predicting of damage in the unit caused by the individual bubbles. An extension to the model presented here, then, could illuminate more on the dynamic cavitation behavior in these units. It is also possible that the extension of this tool to employ larger-scale parallelism could be more effectively utilized with the additional workload this approach would imply.

7.5 Wear in balancing elements

It is common in PD machines to have a 'break-in' procedure, where the components wear so that they form to one another. This procedure is typically a closely guarded trade secret, and can be the difference between a functional and non-functional unit. Clearly, then, it is an important aspect for the design of these machines. Due to computational limitations, this effect is neglected in the lubricating films in the present model, where instead a measured worn profile would need to be fed directly into the solver to consider its impact on performance. A possible research direction could be to develop a wear model of the lubricating films, to provide machine designers with strategies to predict this wear and design 'break-in' procedures accordingly. This work would also be helpful to understand the extent to which the assumption of isotropic roughness in the fluid films is reasonable in PD machines, or to propose a more appropriate modeling solution.

REFERENCES

[1] J. Ivantysyn and M. Ivantysynova, *Hydrostatic pumps and motors*. New Dehli, India: Tech Books Int., 2003.

[2] L. J. Love and L. J, "Estimating the Impact (Energy, Emissions and Economics) of the US Fluid Power Industry," Oak Ridge National Laboratory (ORNL), Oak Ridge, TN (United States), Tech. Rep., 12 2012.

[3] M. Rundo, "Models for flow rate simulation in gear pumps: A review," *Energies*, vol. 10, no. 9, p. 1261, 8 2017.

[4] N. D. Manring and S. B. Kasaragadda, "The Theoretical Flow Ripple of an External Gear Pump," *Journal of Dynamic Systems, Measurement, and Control*, vol. 125, no. 3, p. 396, 2003.

[5] X. Zhao and A. Vacca, "Formulation and optimization of involute spur gear in external gear pump," *Mechanism and Machine Theory*, vol. 117, pp. 114–132, 2017.

[6] T. Ransegnola, X. Zhao, and A. Vacca, "A comparison of helical and spur external gear machines for fluid power applications: Design and optimization," *Mechanism and Machine Theory*, vol. 142, 2019.

[7] Y. Zhou, S. Hao, and M. Hao, "Design and performance analysis of a circular-arc gear pump operating at high pressure and high speed," *Proceedings of the Institution of Mechanical Engineers, Part C: Journal of Mechanical Engineering Science*, vol. 230, no. 2, pp. 189–205, 2016.

[8] S. Luo, Y. Wu, and J. Wang, "The generation principle and mathematical models of a novel cosine gear drive," *Mechanism and Machine Theory*, vol. 43, no. 12, pp. 1543–1556, 2008.

[9] K. A. Edge, B. R. Lipscombe, and P. Polak, "The Reduction of Gear Pump Pressure Ripple," *Proceedings of the Institution of Mechanical Engineers, Part B: Journal of Engineering Manufacture*, vol. 202, no. 1, pp. 61–62, 1988.

[10] H. Ding, F. C. Visser, Y. Jiang, and M. Furmanczyk, "Demonstration and Validation of a 3D CFD Simulation Tool Predicting Pump Performance and Cavitation for Industrial Applications," *Volume 1: Symposia, Parts A, B and C*, vol. 133, no. 1, pp. 277–293, 2009.

[11] E. Frosina, A. Senatore, M. Rigosi, E. Frosina, A. Senatore, and M. Rigosi, "Study of a High-Pressure External Gear Pump with a Computational Fluid Dynamic Modeling Approach," *Energies*, vol. 10, no. 8, p. 1113, 7 2017.

[12] A. S. Heisler, J. J. Moskwa, and F. J. Fronczak, "Simulated helical gear pump analysis using a new CFD approach," in *Proceedings of the ASME Fluids Engineering Division Summer Conference 2009, FEDSM2009*, vol. 1, no. PART A, 2009, pp. 445–455.

[13] P.-J. Gamez-Montero, R. Castilla, D. del Campo, N. Ertürk, G. Raush, and E. Codina, "Influence of the interteeth clearances on the flow ripple in a gerotor pump for engine lubrication," *Proceedings of the Institution of Mechanical Engineers, Part D: Journal of Automobile Engineering*, vol. 226, no. 7, pp. 930–942, 7 2012.

[14] E. Frosina, G. Marinaro, A. Senatore, and M. Pavanetto, "Effects of PCFV and Pre-Compression Groove on the Flow Ripple Reduction in Axial Piston Pumps," in *2018 Global Fluid Power Society PhD Symposium, GFPS 2018*. Institute of Electrical and Electronics Engineers Inc., 9 2018.

[15] X. Zhao and A. Vacca, "Numerical analysis of theoretical flow in external gear machines," *Mechanism and Machine Theory*, vol. 108, no. May 2016, pp. 41–56, 2017.

[16] F. Qi, S. Dhar, V. H. Nichani, C. Srinivasan, D. M. Wang, L. Yang, Z. Bing, and J. J. Yang, "A CFD study of an Electronic Hydraulic Power Steering Helical External Gear Pump: Model Development, Validation and Application," *SAE International Journal of Passenger Cars - Mechanical Systems*, vol. 9, no. 1, pp. 346–352, 2016.

[17] S. Kumar, J. M. Bergada, and J. Watton, "Axial piston pump grooved slipper analysis by CFD simulation of three-dimensional NVS equation in cylindrical coordinates," *Computers and Fluids*, vol. 38, no. 3, pp. 648–663, 2009.

[18] R. Castilla, P. J. Gamez-Montero, N. Ertrk, A. Vernet, M. Coussirat, and E. Codina, "Numerical simulation of turbulent flow in the suction chamber of a gearpump using deforming mesh and mesh replacement," *International Journal of Mechanical Sciences*, vol. 52, no. 10, pp. 1334–1342, 2010.

[19] K. Riemslagh, J. Vierendeels, and E. Dick, "Arbitrary Lagrangian-Eulerian finite-volume method for the simulation of rotary displacement pump flow," *Applied Numerical Mathematics*, vol. 32, no. 4, pp. 419–433, 2000.

[20] M. G. Mithun, P. Koukouvinis, I. K. Karathanassis, and M. Gavaises, "Numerical simulation of three-phase flow in an external gear pump using immersed boundary approach," *Applied Mathematical Modelling*, vol. 72, pp. 682–699, 8 2019.

[21] K. Foster, R. Taylor, and I. M. Bidhendi, "Computer prediction of cyclic excitation sources for an external gear pump," *Journal of Engineering Manufacture*, vol. 199, 1985.

[22] M. Eaton, P. S. Keogh, and K. A. Edge, "The Modelling, Prediction, and Experimental Evaluation of Gear Pump Meshing Pressures with Particular Reference to Aero-Engine Fuel Pumps," *Proceedings of the Institution of Mechanical Engineers, Part I: Journal of Systems and Control Engineering*, vol. 220, no. 5, pp. 365–379, 8 2006.

[23] S. Manco' and N. Nervegna, "Simulation of an External Gear Pump and Experimental Verification," *Proceedings of the JFPS International Symposium on Fluid Power*, vol. 1989, no. 1, pp. 147–160, 1989.

[24] A. Corvaglia and M. Rundo, "Comparison of 0D and 3D Hydraulic Models for Axial Piston Pumps," in *Energy Procedia*, vol. 148. Elsevier Ltd, 2018, pp. 114–121.

[25] N. D. Manring, "Valve-plate design for an axial piston pump operating at low displacements," *Journal of Mechanical Design*, vol. 125, no. 1, pp. 200–205, 2003.

[26] B. O. Helgestad, K. Foster, and F. K. Bannister, "Pressure Transients in an Aaxial Pistion Hydarulic Pump," *Inst Mech Eng (Lond) Proc*, vol. 188, no. 17, pp. 189–199, 2 1974.

[27] K. G. Weddfelt, M. E. Pettersson, and J. O. S. Palmberg, "Methods of reducing flow ripple from fluid power piston pumps - An experimental approach," in *SAE Technical Papers*, vol. 100, 1991, pp. 158–167.

[28] A. M. Harrison and K. A. Edge, "Reduction of piston pump pressure ripple," in *Proceedings of the Institution of Mechanical Engineers, Part I: Journal of Systems and Control Engineering*, 2000, pp. 53–64.

[29] P. Casoli, A. Vacca, G. Franzoni, and G. L. Berta, "Modelling of fluid properties in hydraulic positive displacement machines," *Simulation Modelling Practice and Theory*, vol. 14, no. 8, pp. 1059–1072, 2006.

[30] R. M. Harris, K. A. Edge, and D. G. Tilley, "Predicting tlie beliavior of slipper pads in swashplate-type axial piston pumps," *Journal of Dynamic Systems, Measurement and Control, Transactions of the ASME*, vol. 118, no. 1, pp. 41–47, 1996.

[31] J. M. Bergada, S. Kumar, D. L. Davies, and J. Watton, "A complete analysis of axial piston pump leakage and output flow ripples," *Applied Mathematical Modelling*, vol. 36, no. 4, pp. 1731–1751, 4 2012.

[32] M. Borghi, B. Zardin, and E. Specchia, "External gear pump volumetric efficiency: Numerical and experimental analysis," in *SAE Technical Papers*, 10 2009.

[33] M. Battarra and E. Mucchi, "A method for variable pressure load estimation in spur and helical gear pumps," *Mechanical Systems and Signal Processing*, vol. 76-77, pp. 265–282, 2016.

[34] A. Roccatello, S. Mancó, and N. Nervegna, "Modelling a variable displacement axial piston pump in a multibody simulation environment," *Journal of Dynamic Systems, Measurement and Control, Transactions of the ASME*, vol. 129, no. 4, pp. 456–468, 2007.

[35] F. Fornarelli, A. Lippolis, P. Oresta, and A. Posa, "A computational model of axial piston swashplate pumps," in *Energy Procedia*, vol. 126. Elsevier Ltd, 9 2017, pp. 1147–1154.

[36] A. Vacca and M. Guidetti, "Modelling and experimental validation of external spur gear machines for fluid power applications," *Simulation Modelling Practice and Theory*, vol. 19, no. 9, pp. 2007–2031, 2011.

[37] J. F. Booker, "Dynamically-Loaded Journal Bearings: Numerical Application of the Mobility Method," *Journal of Lubrication Technology*, vol. 93, no. 1, p. 168, 1971.

[38] T. M. Ransegnola, A. Vacca, M. A. Morselli, A. Kowalski, and R. Muizelaar, "A Simulation Model for a Tandem External Gear Pump for Automotive Transmission," in *2018 WCX World Congress Experience*, Detroit, 4 2018.

[39] X. Zhao and A. Vacca, "Analysis of continuous-contact helical gear pumps through numerical modeling and experimental validation," *Mechanical Systems and Signal Processing*, vol. 109, pp. 352–378, 2018.

[40] R. Rituraj, T. Ransegnola, and A. Vacca, "An Investigation on the Leakage Flow and Instantaneous Tooth Space Pressure in External Gear Machines," in *2018 Global Fluid Power Society PhD Symposium, GFPS 2018*, 2018.

[41] F. Rituraj, A. Vacca, and M. A. Morselli, "Modeling of manufacturing errors in external gear machines and experimental validation," *Mechanism and Machine Theory*, vol. 140, pp. 457–478, 2019.

[42] Rituraj, A. Vacca, and M. A. Morselli, "Thermal Modelling of External Gear Machines and Experimental Validation," *Energies*, vol. 13, no. 11, 2020.

[43] S. Dhar and A. Vacca, "A novel CFD - Axial motion coupled model for the axial balance of lateral bushings in external gear machines," *Simulation Modelling Practice and Theory*, vol. 26, pp. 60–76, 2012.

[44] ——, "A novel FSI-thermal coupled TEHD model and experimental validation through indirect film thickness measurements for the lubricating interface in external gear machines," *Tribology International*, vol. 82, no. PA, pp. 162–175, 2015.

[45] D. Thiagarajan, "Investigation of Hydro-Mechanical Losses in External Gear," in *BATH/ASME 2016 Symposium on Fluid Power and Motion Control*, Bath, UK, 2016, pp. 1–10.

[46] M. Pellegri and A. Vacca, "A Simulation Approach for the Evaluation of Power Losses in the Axial Gap of Gerotor Units," *JFPS International Journal of Fluid Power System*, vol. 11, no. 3, pp. 55–62, 2019.

[47] U. Wieczorek and M. Ivantysynova, "Computer aided optimization of bearing and sealing gaps in hydrostatic machines—the simulation tool caspar," *International Journal of Fluid Power*, vol. 3, no. 1, pp. 7–20, 2002.

[48] M. Pelosi and M. Ivantysynova, "A novel fluid-structure interaction model for lubricating gaps of piston machines," *WIT Transactions on the Built Environment*, vol. 105, pp. 13–24, 2009.

[49] ——, "Heat transfer and thermal elastic deformation analysis on the Piston/Cylinder interface of axial piston machines," *Journal of Tribology*, vol. 134, no. 4, pp. 1–15, 2012.

[50] ——, "The impact of axial piston machines mechanical parts constraint conditions on the thermo-elastohydrodynamic lubrication analysis of the fluid film interfaces," *International Journal of Fluid Power*, vol. 14, no. 3, pp. 35–51, 2013.

[51] A. Schenk and M. Ivantysynova, "A transient thermoelastohydrodynamic lubrication model for the slipper/swashplate in axial piston machines," *Journal of Tribology*, vol. 137, no. 3, 2015.

[52] M. Zecchi and M. Ivantysynova, "A novel approach to predict the cylinder block / valve plate interface performance in swash plate type axial piston machines," in *Bath/ASME Symposium on Fluid Power and Motion Control*, Bath, UK, 2012.

[53] D. Thiagarajan and A. Vacca, "Mixed lubrication effects in the lateral lubricating interfaces of external gear machines: Modelling and experimental validation," *Energies*, vol. 10, no. 1, p. 111, 1 2017.

[54] D. Thiagarajan, A. Vacca, and S. Watkins, "On the lubrication performance of external gear pumps for aerospace fuel delivery applications," *Mechanical Systems and Signal Processing*, vol. 129, pp. 659–676, 8 2019.

[55] D. Morgridge, H. P. Evans, R. W. Snidle, and M. K. Yates, "A Study of Seal Lubrication in an Aerospace Fuel Gear Pump Including the Effects of Roughness and Mixed Lubrication A Study of Seal Lubrication in an Aerospace Fuel Gear Pump Including the Effects of Roughness and Mixed Lubrication," *Tribology Transactions*, vol. 54, pp. 657–665, 2011.

[56] Yi Fang and M. Shirakashi, "Mixed lubrication characteristics between the piston and cylinder in hydraulic piston pump-motor," Tech. Rep. 1, 1995.

[57] S. Hashemi, A. Kroker, L. Bobach, and D. Bartel, "Multibody dynamics of pivot slipper pad thrust bearing in axial piston machines incorporating thermal elastohydrodynamics and mixed lubrication model," *Tribology International*, vol. 96, pp. 57–76, 4 2016.

[58] L. Shang and M. Ivantysynova, "Scaling Criteria for Axial Piston Machines Based on Thermo-Elastohydrodynamic Effects in the Tribological Interfaces," *Energies*, vol. 11, no. 11, p. 3210, 11 2018.

[59] R. Ivantysyn, A. Shorbagy, and J. Weber, "Investigation of the Wear Behavior of the Slipper in an Axial Piston Pump by Means of Simulation and Measurement," in *12th International Fluid Power Conference*, 2020, pp. 315–326.

[60] R. M. Harris, K. A. Edge, and D. G. Tilley, "The spin motion of pistons in a swashplate-type axial piston pump," in *3rd Scandinavian International Conference Fluid Power*, Linkoping, Sweden, 1993.

[61] A. Faraz and S. Payandeh, "Towards approximate models for Coulomb frictional moments in: (I) revolute pin joints and (II) spherical-socket ball joints," *Journal of Engineering Mathematics*, vol. 40, no. 3, pp. 283–296, 2001.

[62] J. Kang, "Theoretical Model for Friction-Induced Vibration of Ball Joint System under Mode-Coupling Instability," *Tribology Transactions*, vol. 58, no. 5, pp. 807–814, 2015.

[63] C. Weiss, A. Hothan, M. Morlock, and N. Hoffmann, "Friction-induced vibration of artificial hip joints," *GAMM Mitteilungen*, vol. 32, no. 2, pp. 193–204, 2009.

[64] N. Fan and G. X. Chen, "Numerical study of squeaking suppresses for ceramic-on-ceramic hip endoprosthesis," *Tribology International*, vol. 48, pp. 172–181, 2012.

[65] C. Weiss, P. Gdaniec, N. P. Hoffmann, A. Hothan, G. Huber, and M. M. Morlock, "Squeak in hip endoprosthesis systems: An experimental study and a numerical technique to analyze design variants," *Medical Engineering and Physics*, vol. 32, no. 6, pp. 604–609, 2010.

[66] C. Weiss, M. M. Morlock, and N. P. Hoffmann, "Friction induced dynamics of ball joints: Instability and post bifurcation behavior," *European Journal of Mechanics, A/Solids*, vol. 45, pp. 161–173, 2014.

[67] B. Armstrong and C. de Wit, *Friction Modeling and Compensation*. CRC Press, 1995.

[68] S. R. Brown, "Fluid flow through rock joints: The effect of surface roughness," *Journal of Geophysical Research*, vol. 92, no. B2, p. 1337, 1987.

[69] N. Patir and H. S. Cheng, "An Average Flow Model for Determining Effects of Three-Dimensional Roughness on Partial Hydrodynamic Lubrication," *Journal of Lubrication Technology*, vol. 100, no. 1, p. 12, 1 1978.

[70] ——, "Application of Average Flow Model to Lubrication Between Rough Sliding Surfaces," *Journal of Lubrication Technology*, vol. 101, no. 2, p. 220, 4 1979.

[71] W. Chengwei and Z. Linqing, "An Average Reynolds Equation for Partial Film Lubrication With Contact Factor," *Journal of Tribology*, vol. 111, no. January, pp. 2–5, 1989.

[72] F. Meng, Q. J. Wang, D. Hua, and S. Liu, "A simple method to calculate contact factor used in average flow model," *Journal of Tribology*, vol. 132, no. 2, pp. 1–4, 4 2010.

[73] S. C. Lee and N. Ren, "Behavior of elastic-plastic rough surface contacts as affected by surface topography, load, and material hardness," *Tribology Transactions*, vol. 39, no. 1, pp. 67–74, 1996.

[74] S. M. Chun, "Wear Analysis of Engine Bearings at Constant Shaft Angular Speed during Firing State - Part II: Calculation of the Wear on Journal Bearings," *Tribology and Lubricants*, vol. 34, no. 4, pp. 146–159, 2018.

[75] ——, "Wear Simulation of Engine Bearings in the Beginning of Firing Start-up cycle," *Tribology and Lubricants*, vol. 35, no. 4, pp. 244–266, 2019.

[76] C. Gu, X. Meng, S. Wang, and X. Ding, "Modeling a hydrodynamic bearing with provision for misalignments and textures," *Journal of Tribology*, pp. 1–29, 11 2019.

[77] Z. Xie and H. Liu, "Experimental research on the interface lubrication regimes transition of water lubricated bearing," *Mechanical Systems and Signal Processing*, vol. 136, 2 2020.

[78] R. S. Devendran and A. Vacca, "Theoretical analysis for variable delivery flow external gear machines based on asymmetric gears," *Mechanism and Machine Theory*, vol. 108, pp. 123–141, 2017.

[79] ——, "A novel design concept for variable delivery flow external gear pumps and motors," *International Journal of Fluid Power*, vol. 15, no. 3, pp. 121–137, 2014.

[80] P. Casoli, A. Vacca, and G. Berta, "Optimization of Relevant Design Parameters of External Gear Pumps," in *The Seventh JFPS International Symposium on Fluid Power*, 2008.

[81] S. Gulati, A. Vacca, and M. Rigosi, "A General Method to Determine the Optimal Profile of Porting Grooves in Positive Displacement Machines: the Case of External Gear Machines," *10th International Fluid Power Conference (IFK2016)*, vol. i, pp. 453–464, 2016.

[82] R. Chacon and M. Ivantysynova, "Virtual prototyping of axial piston machines: numerical method and experimental validation," *Energies*, vol. 12, no. 9, 2019.

[83] M. J. Braun and W. M. Hannon, "Cavitation formation and modelling for fluid film bearings: A review," *Proceedings of the Institution of Mechanical Engineers, Part J: Journal of Engineering Tribology*, vol. 224, no. 9, pp. 839–863, 2010.

[84] M. S. Plesset and A. Prosperetti, "Bubble Dynamics and Cavitation," Tech. Rep., 1977.

[85] A. C. Rust and M. Manga, "Bubble Shapes and Orientations in Low Re Simple Shear Flow," *Journal of Colloid and Interface Science*, vol. 249, pp. 476–480, 2002.

[86] A. K. Singhal, M. M. Athavale, H. Li, and Y. Jiang, "Mathematical Basis and Validation of the Full Cavitation Model," *Journal of Fluids Engineering*, vol. 124, no. 3, pp. 617–624, 9 2002.

[87] S. Dabiri, W. A. Sirignano, and D. D. Joseph, "Interaction between a cavitation bubble and shear flow," *Journal of Fluid Mechanics*, vol. 651, pp. 93–116, 2010.

[88] A. Jaramillo, G. Bayada, I. Ciuperca, and M. Jai, "On the well-posedness of Reynolds-Rayleigh-Plesset coupling," Tech. Rep., 2018.

[89] T. A. Snyder, M. J. Braun, and K. Pierson, "On Rayleigh-Plesset based cavitation modelling of fluid film bearings using the Reynolds equation," in *Journal of Physics: Conference Series*, vol. 656, no. 1, 2015.

[90] B. J. Hamrock, S. R. Schmid, and B. O. Jacobson, *Fundamentals of Fluid Film Lubrication*, 2nd ed. Boca Raton: CRC Press, 3 2004.

[91] D. del Campo, R. Castilla, G. Raush, P. Gamez-Montero, and E. Codina, "Pressure effects on the performance of external gear pumps under cavitation," *Proceedings of the Institution of Mechanical Engineers, Part C: Journal of Mechanical Engineering Science*, vol. 228, no. 16, pp. 2925–2937, 11 2014.

[92] J. Zhou, A. Vacca, and B. Manhartsgruber, "A Novel Approach for the Prediction of Dynamic Features of Air Release and Absorption in Hydraulic Oils," *Journal of Fluids Engineering*, vol. 135, no. 9, p. 091305, 9 2013.

[93] J. Zhou, A. Vacca, and P. Casoli, "A novel approach for predicting the operation of external gear pumps under cavitating conditions," *Simulation Modelling Practice and Theory*, vol. 45, pp. 35–49, 2014.

[94] Siemens, "HYD Advanced Fluid Properties, Technical bulletin 117," Siemens, Tech. Rep., 2017. [Online]. Available: https://www.plm.automation.siemens.com/global/en/products/simcenter/simcenter-amesim.html

[95] Y. Shah, A. Vacca, S. Dabiri, Y. G. Shah, A. Vacca, and S. Dabiri, "Air Release and Cavitation Modeling with a Lumped Parameter Approach Based on the Rayleigh–Plesset Equation: The Case of an External Gear Pump," *Energies*, vol. 11, no. 12, p. 3472, 12 2018.

[96] B. Jakobsson and L. Floberg, "The finite Journal Bearing, considering vaporization," *Trans. Chalmers University Tech.*, p. 190, 1957.

[97] K. Olsson, "Cavitation in Dynamically Loaded Bearing," *Trans. Chalmers University Tech.*, p. 308, 1965.

[98] H. G. Elrod and M. L. Adams, "A Computer Program for cavitation and Starvation Problems Cavitation and Related Phenomena in Lubrication," in *1st Leeds-Lyon Symposium on Tribology*, 1975, pp. 37–42.

[99] H. G. Elrod, "A Cavitation Algorithm," *Transactions of the ASME*, vol. 103, no. July 1981, pp. 350–354, 1981.

[100] C. M. Woods, "Use of multigrid techniques in the solution of the Elrod algorithm for a dynamically loaded journal bearing." Ph.D. dissertation, Case Western Reserve University, 1988.

[101] R. F. Ausas, M. Jai, and G. C. Buscaglia, "A mass-conserving algorithm for dynamical lubrication problems with cavitation," *Journal of Tribology*, vol. 131, no. 3, pp. 1–7, 2009.

[102] F. Dimofte, "Fast Methods to Numerically Integrate the Reynolds Equation for Gas Fluid Films," in *STLE-ASME Joint Tribology Conference*, St. Louis, Missouri, 1991.

[103] D. Vijayaraghavan and T. G. Keith, "Development and Evaluation of a Cavitation Algorithm Development and Evaluation of a Cavitation Algorithm," *Tribology Transactions*, vol. 32, no. 2, 1989.

[104] M. Miraskari, F. Hemmati, A. Jalali, M. Y. Alqaradawi, and M. S. Gadala, "A Robust Modification to the Universal Cavitation Algorithm in Journal Bearings," *Journal of Tribology*, vol. 139, no. 3, 5 2017.

[105] M. Fesanghary and M. M. Khonsari, "A modification of the switch function in the elrod cavitation algorithm," *Journal of Tribology*, vol. 133, no. 2, 2011.

[106] S. Nitzschke, E. Woschke, D. Schmicker, and J. Strackeljan, "Regularised cavitation algorithm for use in transient rotordynamic analysis," *International Journal of Mechanical Sciences*, vol. 113, pp. 175–183, 7 2016.

[107] W. Chong, M. Teodorescu, and N. Vaughan, "Cavitation induced starvation for piston-ring/liner tribological conjunction," *Tribology International*, vol. 44, no. 4, pp. 483–497, 4 2011.

[108] D. Vijayaraghavan and T. G. Keith, "Analysis of a Finite Grooved Misaligned Journal Bearing Considering Cavitation and Starvation Effects," *Journal of Tribology*, vol. 112, no. 1, p. 60, 2008.

[109] S. Kango, R. K. Sharma, and R. K. Pandey, "Comparative analysis of textured and grooved hydrodynamic journal bearing," *Proceedings of the Institution of Mechanical Engineers, Part J: Journal of Engineering Tribology*, vol. 228, no. 1, pp. 82–95, 1 2014.

[110] D. E. Brewe, "Theoretical modeling of the vapor cavitation in dynamically loaded journal bearings," *Journal of Tribology*, vol. 108, no. 4, pp. 628–637, 1986.

[111] X.-L. Wang, J.-Y. Zhang, and H. Dong, "Analysis of bearing lubrication under dynamic loading considering micropolar and cavitating effects," *Tribology International*, vol. 44, no. 9, pp. 1071–1075, 8 2011.

[112] Rituraj, "Numerical Methodologies for Modelling the Key Aspects Related to Flow and Geometry in External Gear Machines," Ph.D. dissertation, Purdue University, 2020.

[113] C. Barus, "Isothermals, Isopiestics and Isometrics relative to Viscosity;," *American Journal of Science*, vol. 45, no. 3, pp. 87–96, 1893.

[114] C. Roelands, "Correlational aspects of the viscosity-temperature-pressure relationship of lubricating oils," Ph.D. dissertation, Technical University of Delft, 1966.

[115] D. Dowson and G. R. Higginson, *Elasto-hydrodynamic lubrication: The fundamentals of roller and gear lubrication.* Oxford: Pergamon Press, 1966.

[116] H. E. Merritt, *Hydraulic control systems.* John Wiley and Sons, 1967.

[117] G. K. Batchelor, *An Introduction to Fluid Dynamics.* Cambridge: Cambridge University Press, 2000.

[118] D. Childs, H. Moes, and H. van Leuwen, "Journal Bearing Impedance Descriptions for Rotordynamic Applications." *Journal of Tribology*, vol. 99, pp. 198–210, 1976.

[119] H. Moes and R. Bosma, "Mobility and Impedance Definitions for Plain Journal Bearings," *Journal of Tribology*, vol. 103, pp. 468–470, 1981.

[120] F. Rituraj, A. Vacca, and M. Rigosi, "Modeling and Validation of Hydro-Mechanical Losses in External Gear Machines," *Mechanism and Machine Theory*, p. In Press, 2021.

[121] K. L. Johnson, *Contact Mechanics*. Cambridge: Cambridge University Press, 1985.

[122] M. Ivantysynova, C. Huang, and S.-K. Christiansen, "Computer Aided Valve Plate Design - An Effective Way to Reduce Noise," *SAE Technical Paper*, 2004.

[123] L. R. Petzold and A. C. Hindmarsh, "LSODA–livermore solver for ordinary differential equations, with automatic method switching for stiff and non-stiff problems." 1997.

[124] M. Galassi, J. Davies, J. Theiler, B. Gough, G. Jungman, P. Alken, M. Booth, F. Rossi, and R. Ulerich, "GNU Scientific Library Release 2.6," Tech. Rep., 2019.

[125] L. Shang and M. Ivantysynova, "International Journal of Fluid Power A temperature adaptive piston design for swash plate type axial piston machines A temperature adaptive piston design for swash plate type axial piston machines," *InternatIonal Journal of fluId Power*, vol. 18, no. 1, pp. 38–48, 2017.

[126] A. H. Shapiro, *The Dynamics and Thermodynamics of Compressible Fluid Flow*. New York, NY: John Willey & Sons, 1953, vol. I.

[127] D. K. Shin and J. J. Lee, "Theoretical analysis of the deflection of a cantilever plate for wirebonding on overhang applications," *IEEE Transactions on Components, Packaging and Manufacturing Technology*, vol. 2, no. 6, pp. 916–924, 2012.

[128] A. E. H. Love, "The stress produced in a semi-infinite solid by pressure on part of the boundary," *Philosophical Transactions of the Royal Society of London. Series A, Containing Papers of a Mathematical or Physical Character*, vol. 228, no. 659-669, pp. 377–420, 1929.

[129] E. Pan, M. Bevis, F. Han, H. Zhou, and R. Zhu, "Surface deformation due to loading of a layered elastic half-space: A rapid numerical kernel based on a circular loading element," *Geophysical Journal International*, vol. 171, no. 1, pp. 11–24, 10 2007.

[130] J. Tilak Ratnanather, J. H. Kim, A. M. J Davis, and S. K. Lucas, "IIPBF: a MATLAB toolbox for infinite integrals of product of Bessel functions: a MATLAB toolbox for infinite integrals of product of Bessel functions," *ACM Trans. Math. Softw. V, N, Article A*, 2011.

[131] S. K. Lucas and H. A. Stone, "Evaluating infinite integrals involving Bessel functions of arbitrary order," *Journal of Computational and Applied Mathematics*, vol. 64, no. 3, pp. 217–231, 12 1995.

[132] J. ORourke, *Computational Geometry in C*. Cambridge: Cambridge University Press, 1998.

[133] B. Armstrong and C. de Wit, *Friction Modeling and Compensation*. CRC Press, 1995.

[134] A. A. Raimondi and J. Boyd, "A solution for the finite journal bearing and its application to analysis and design: I," *ASLE Transactions*, vol. 1, no. 1, pp. 159–174, 1958.

[135] M. J. D. Powell, "A hybrid method for nonlinear equations," in *Numerical methods for nonlinear algebraic equations*, P. Rabinowitz, Ed. New York, NY: Gordon and Breach Science Publishers, 1970, ch. 6, pp. 87–114.

[136] T. Ransegnola, F. Sadeghi, and A. Vacca, "An Efficient Cavitation Model for Compressible Fluid Film Bearings," *Tribology Transactions*, p. In Press, 2020.

[137] A. Vacca, G. Franzoni, and P. Casoli, "On the Analysis of Experimental Data for External Gear Machines and Their Comparison With Simulation Results," in *ASME International Mechanical Engineering Congress and Exposition, Proceedings (IMECE)*, 2007, pp. 45–53.

[138] A. Busquets, "An Investigation of Micro-Surface Shaping on the Piston/Cylinder Interface of Axial Piston Machines," Ph.D. dissertation, Purdue University, 2018.

[139] P. Casoli, F. Campanini, A. Bedotti, M. Pastori, and A. Lettini, "Overall Efficiency Evaluation of a Hydraulic Pump with External Drainage Through Temperature Measurements," *Journal of Dynamic Systems, Measurement and Control*, vol. 140, no. 8, 2018.

[140] Z. Mistry, M. H. Babu, A. Vacca, E. Dautry, and M. Petzold, "A Numerical Model for the Evaluation of Gertotor Torque Considering Multiple Contact Points and Fluid-Structure Interactions," in *12th International Fluid Power Conference*, Dresden, 2020.

[141] S. Wang, H. Sakurai, and A. Kasarekar, "The optimal design in external gear pumps and motors," *IEEE/ASME Transactions on Mechatronics*, vol. 16, no. 5, pp. 945–952, 2011.

[142] M. Borghi and B. Zardin, "Axial balance of external gear pumps and motors: Modelling and discussing the influence of elastohydrodynamic lubrication in the axial gap," in *ASME International Mechanical Engineering Congress and Exposition*, vol. 15-2015. Houston, Texas, USA: ASME, 2015.

[143] S. Woo, T. Opperwall, A. Vacca, and M. Rigosi, "Modeling Noise Sources and Propagation in External Gear Pumps," *Energies*, vol. 10, no. 7, pp. 1–20, 2017.

[144] P. Nowell, "Mapping a Square to a Circle," 2005. [Online]. Available: http://mathproofs.blogspot.com/2005/07/mapping-square-to-circle.html

PUBLICATIONS

Journal Articles

Ransegnola, T., Vacca, A., 2021, "A Study of Piston and Slipper Spin in Axial Piston Machines subject to Ball-Socket Friction and Fluid-Structure induced Cavitation and Mixed Lubrication," **In Preparation**

Ransegnola, T., Vacca, A., 2020, "A Strongly Coupled Simulation Model for External Gear Machines considering Fluid-Structure induced Cavitation and Mixed Lubrication," *Applied Mathematical Modelling* **In Review**

Ransegnola, T., Sadeghi, F., Vacca, A., 2020, "An efficient cavitation model for fluid film bearings with compressible lubricants," *Tribology Transactions* **In Press**

Ransegnola, T., Zhao, X., Vacca, A., 2019, "A comparison of helical and spur external gear machines for fluid power applications: Design and optimization," *Mechanism and Machine Theory*, 142, DOI:10.1016/j.mechmachtheory.2019.103604

Patents/Copyrights

Vacca A., Sudhoff S., Ransegnola T., Zappaterra F., December 2019, "Integrated Electro-hydraulic Machine," **Provisional Patent Application**

Vacca A., Ransegnola T., Zhao X., Rituraj, March 2019, "HYGESim HYdraulic GEar Simulator," **Copyright for source code filed**

Conference Papers

Ransegnola, T., Vacca, A., 2020, "Virtual design and analysis of the balancing element of an external gear machine considering cavitation and mixed lubrication effects," *IEEE Global Fluid Power Society PhD Symposium* October 19-21, 2020, Guilin, China

Ransegnola, T., Vacca, A., Morselli, M.A., Kowalski, A., Muizelaar, R., 2018, "A Simulation Model for a Tandem External Gear Pump for Automotive Transmission," *SAE WCX World Congress Experience*, Apr. 10–12, 2018, Detroit, MI, USA, DOI:10.4271/2018-01-0403

Rituraj, Ransegnola, T., Vacca, A., 2018, "An Investigation on the Leakage Flow and Instantaneous Tooth Space Pressure in External Gear Machines," *IEEE Global Fluid Power Society PhD Symposium*, July 18-20, 2018, Samara, Russia, DOI:10.1109/gfps.2018.8472358

A. MODEL EQUATIONS

This chapter collects the flow assumptions applied to each flow term depicted in Chapter 2. First, Table A.1 collects the model assumptions for the APM.

Table A.1.
Pressure/Flow/Force Models for Multics CASPAR

Gap	**Analytical Model**	**Distributed Model**
Piston-Cylinder Block Q_{SK}, $\underline{F}_{SK}$	Eccentric Annular Flow Long Impedance Bearing	Unwrapped Film
Valve Plate-Cylinder Block Q_{SB},$\underline{F}_{SB}$	Cylindrical Couette-Poiseuille	Cylindrical Film
Slipper-Swashplate Q_{SG}, $\underline{F}_{SG}$	Cylindrical Couette-Poiseuille	Cylindrical Film
Slipper pocket p_G, $\underline{F}_G$	Pressure build-up, Pressure projection	
Displacement Chamber p_{DC}, $\underline{F}_{DC}$	Pressure build-up, Pressure projection	
DC - Slipper pocket Q_{PG},$\underline{F}_{PG}$	Orifice Equation, Stribeck Friction	
Inlet/Outlet Chamber $p_{LP/HP}$	Pressure build-up	
Inlet/Outlet flow $Q_{r,LP/HP}$	Variable Orifice Equation	

Similarly, the model assumptions for the EGM are collected in Figure A.2.

Table A.2.
Pressure/Flow/Force Models for Multics HYGESim

Gap	**Analytical Model**	**Distributed Model**
Journal Bearing $Q_{l,JB}$, $\underline{F}_{JB}$	Eccentric Annular Flow Short Impedance Bearing	Unwrapped Film
Inter-TSV Lateral Leakage $Q_{l,LL}$,$\underline{F}_{LL}$	Cylindrical Couette-Poiseuille	Cylindrical Film
TSV-Drain Leakage $Q_{l,DL}$,$\underline{F}_{DL}$	Cylindrical Couette-Poiseuille	Cylindrical Film
Tooth Lip Leakage $Q_{l,RL}$,$\underline{F}_{RL}$	Cartesian Couette-Poiseuille	
Displacement Chamber p_{DC}, $\underline{F}_{DC}$	Pressure build-up, Pressure projection	
Inlet/Outlet Chamber $p_{LP/HP}$, $\underline{F}_{LP/HP}$	Pressure build-up, Pressure projection	
Inlet/Outlet port flow $Q_{t,LP/HP}$	Fixed Orifice Equation	
Inlet/Outlet depth-wise flow $Q_{t,LV/HV}$	Variable Orifice Equation	
Inlet/Outlet groove-wise flow $Q_{t,LG/HG}$	Variable Orifice Equation	
Back-flow groove flow $Q_{t,HS}$	Variable Orifice Equation	

B. PERTURBED UNIVERSAL REYNOLDS DERIVATION

B.1 Governing Equation

The derivation begins by perturbing the normal-velocity of a given solution to the mixed universal Reynolds Equation 3.28 by $\dot{h}'$ so that the density solution is perturbed by ρ'. By assuming a sufficiently small deviation in time from the known solution, it can be observed that this velocity perturbation contributes negligible change in the gap height $h \approx h_0$ and thus the flow factors remain constant. By linearizing the universal Reynolds equation about the given nominal solution ρ_0, then, this perturbation can be described locally by

$$\underline{\nabla} \cdot \left(\underline{\phi}_p \circ \left(\frac{h_0^3}{12} \frac{K}{\mu}\bigg|_{\rho_0+\rho'} \underline{\nabla}(\rho_0 + \rho') \right) \right) = \underline{\nabla} \cdot \left((\rho_0 + \rho') \overline{\underline{v}} (\phi_R R_q + \phi_c h_0) \right) + \underline{\nabla} \cdot \left((\rho_0 + \rho') \frac{\phi_s}{2} R_q \left(\underline{v}_t - \underline{v}_b \right) \right) + (\phi_R R_q + \phi_c h_0) \left[\frac{\partial \rho_0}{\partial t} + \frac{\partial \rho'}{\partial t} \right] + (\rho_0 + \rho')(\dot{\overline{h}}_0 + \phi_c \dot{h}') \tag{B.1}$$

With the assumption of a sufficiently small perturbation, $\rho' \ll \rho_0$ such that change in compressibility and viscosity is negligible, and the diffusivity of the film can be taken as a constant at the reference state

$$\frac{K}{\mu}\bigg|_{\rho_0+\rho'} \approx \frac{K_0}{\mu_0} + \frac{\partial}{\partial \rho}\left(\frac{K}{\mu}\right)\bigg|_0 \rho' = \left[\frac{\rho_0}{\mu_0} \left(1 - \frac{\rho'}{\mu_0} \frac{\partial \mu}{\partial \rho}\bigg|_0 \right) + \frac{\rho'}{\mu_0} \right] \frac{\partial p}{\partial \rho}\bigg|_0 \approx \frac{K}{\mu}\bigg|_{\rho_0} \tag{B.2}$$

Since the velocity perturbation is applied only along the gap-normal direction, density wedge effects are negligible as compared to the squeeze response. Furthermore, the squeeze response of the perturbed density is approximated using backward differencing against the reference solution with known 0 perturbation. With this simplification, and by removing the reference state, this equation reduces to describe the perturbation response directly

$$\underline{\nabla} \cdot \left(\underline{\phi}_p \circ \left(\frac{K_0 h_0^3}{12\mu_0} \underline{\nabla} \rho' \right) \right) = \frac{\overline{h}_0}{\Delta t} \rho' + \rho_0 \phi_c \dot{h}' + \dot{\overline{h}}_0 \rho' \tag{B.3}$$

As a notational convenience, the constant terms can be collected to form the perturbed universal Reynolds equation

$$\underline{\nabla} \cdot \left(\underline{\underline{D}} \, \underline{\nabla} \rho' \right) = \gamma + \kappa \rho' \tag{B.4a}$$

$$\underline{\underline{D}} = \frac{K_0 h_0^3}{12\mu_0} \underline{\underline{I}} \, \underline{\phi}_p \tag{B.4b}$$

$$\gamma = \rho_0 \phi_c \dot{h}' \tag{B.4c}$$

$$\kappa = \dot{\overline{h}}_0 + \frac{\overline{h}_0}{\Delta t} \tag{B.4d}$$

with definition of the local diffusivity tensor $\underline{\underline{D}}$ as well as the constant and linear forcing γ and κ respectively. By neglecting the change in gap height, the change in volume and thus pressure of the CVs at the boundaries due to this perturbation can also be neglected. With this, a homogeneous Dirichlet boundary condition is applied to the density perturbation along the edges of the domain.

B.2 Domain-Specific Maps

B.2.1 Rectangular Film

First, this problem is solved for the case of a rectangular domain. Here, the arbitrary rectangular shape is mapped linearly to the unit domain

$$\begin{aligned} x_1(\xi) &= \frac{\xi L_1}{2} \\ x_2(\eta) &= \frac{\eta L_2}{2} \end{aligned} \tag{B.5}$$

In this domain, a basis of Chebyshev polynomials of the first kind $T_i(\xi)$ is applied. Rather than imposing boundary conditions expressly, this basis is modified to inherently satisfy the homogeneous boundary condition

$$\hat{T}_k(\xi) = T_k(\xi) + \frac{\xi - 1}{2} T_k(-1) - \frac{\xi + 1}{2} T_k(1) \tag{B.6}$$

In effect, the constant $T_0(\xi)$ and linear $T_1(\xi)$ polynomial weights are predetermined to satisfy the boundary conditions, such that they need not be included in the linear system. With these functions applied in both the ξ and η directions, the basis used here is given by the product of each combination of one-dimension functions. This basis is unwrapped into the single basis vector used in Equation 3.85

$$N_j(\xi,\eta) = \hat{T}_k(\xi)\,\hat{T}_i(\eta) \tag{B.7}$$

From the solution of Equation 3.86, the pressure throughout the film is known. The net loading on the bodies due to the film is given by the integral of this pressure solution. Since these integrals do not change with time, they need only to be computed once so that

$$F_z = \left(\iint_{\Gamma'} \underline{N}\,\left|\underline{\underline{J}}\right|\,d\Gamma'\right)^T \underline{a} \tag{B.8a}$$

$$M_x = \left(\iint_{\Gamma'} x_2\,\underline{N}\,\left|\underline{\underline{J}}\right|\,d\Gamma'\right)^T \underline{a} \tag{B.8b}$$

$$M_y = \left(\iint_{\Gamma'} -x_1\,\underline{N}\,\left|\underline{\underline{J}}\right|\,d\Gamma'\right)^T \underline{a} \tag{B.8c}$$

B.2.2 Circular Film

In the circular film, the boundary of the film is given only at the outer radius r_o. The solution to the circular film can be exactly recovered from the solution of the rectangular film, where the circular domain is mapped to a rectangular domain using Nowell's elliptical grid mapping [144]

$$\begin{aligned} x_1(\xi,\eta) &= r_o\,\xi\sqrt{1-\eta^2/2} \\ x_2(\xi,\eta) &= r_o\,\eta\sqrt{1-\xi^2/2} \end{aligned} \tag{B.9}$$

This map was chosen because its simplicity yielded the lowest condition number of the resulting stiffness matrix, as compared to the other square-circle maps consid-

ered. With this map, the same basis function definitions of Equation B.7 and force calculations of Equation B.8 used for the rectangular film can be applied.

B.2.3 Annular Film

Unlike the circular film, the annular film has a non-zero inner radius r_i. At this additional boundary, the homogenous Dirichlet boundary condition must also be applied, and the circular film solution cannot be used. Instead in this case, the domain is mapped using a cylindrical coordinate system where

$$\begin{aligned} x_1(\xi,\eta) &= \left[\frac{r_i + r_o}{2} + \eta\left(\frac{r_i - r_o}{2}\right)\right]\cos\pi\xi \\ x_2(\xi,\eta) &= \left[\frac{r_i + r_o}{2} + \eta\left(\frac{r_i - r_o}{2}\right)\right]\sin\pi\xi \end{aligned} \tag{B.10}$$

Unlike the previous two cases, the homogenous boundary condition in this case must only be applied along the edges of the radial η direction. In the tangential ξ direction, symmetry about $\xi = \pm 1$ must be respected. Thus, a Fourier basis is applied with complex wave number ν_k

$$\hat{F}_k = \Re\left(\exp\left[\nu_k \xi\right]\right) \tag{B.11}$$

along this direction. With appropriate choice of wave numbers, these functions inherently satisfy the symmetry requirements of both the function value and its derivatives. For an arbitrary film state, this basis must be capable of representing a general function including both phase and magnitude. These two degrees of freedom can be expressed as linear weights using Euler's formula, with choice of wave number ν_k imposing the symmetry boundary condition so that

$$\hat{F}_k = a_k \cos k\pi\xi + b_k \sin k\pi\xi \tag{B.12}$$

Similar to above, this basis is unwrapped into the single basis vector used in Equation 3.85

$$N_j(\xi,\eta) = \hat{F}_k(\xi)\,\hat{T}_i(\eta) \tag{B.13}$$

Again once the pressure solution is found from Equation 3.86, the forces can be determined using Equation B.8.

B.2.4 Cylindrical Film

Finally, the cylindrical film of radius r_c is mapped by unwrapping the cylinder into the unit domain where

$$\begin{aligned} x_1(\xi) &= \xi \pi r_c \\ x_2(\eta) &= \frac{\eta L_2}{2} \end{aligned} \tag{B.14}$$

Similar to above, Equation B.13 describes the Fourier basis applied in the tangential direction and the Chebyshev basis applied along the axis of the cylinder. Unlike the other domains, the act of unwrapping the film means that the force calculations must be modified. Here, the pressure solution obtained with Equation 3.86 is integrated to find the net force projected onto the plane normal direction, where again the integrals can be evaluated off-line with their result stored

$$F_x = \left(\iint_{\Gamma'} \underline{N} \cos(\xi\pi) \left| \underline{\underline{J}} \right| d\Gamma' \right)^T \underline{a} \tag{B.15a}$$

$$F_y = \left(\iint_{\Gamma'} \underline{N} \sin(\xi\pi) \left| \underline{\underline{J}} \right| d\Gamma' \right)^T \underline{a} \tag{B.15b}$$

$$M_x = \left(\iint_{\Gamma'} -x_2 \underline{N} \sin(\xi\pi) \left| \underline{\underline{J}} \right| d\Gamma' \right)^T \underline{a} \tag{B.15c}$$

$$M_y = \left(\iint_{\Gamma'} x_2 \underline{N} \cos(\xi\pi) \left| \underline{\underline{J}} \right| d\Gamma' \right)^T \underline{a} \tag{B.15d}$$

VITA

Thomas Ransegnola was born and raised in New Jersey, USA. After graduating high school in 2011, he attended Boston University where he received a Bachelor of Science degree in Mechanical Engineering in 2015. In August 2016, he joined the Maha Fluid Power Research Center as a direct Ph.D. student of Mechanical Engineering at Purdue University. He received a Master of Science degree in Mechanical Engineering in May 2020, and has continued his graduate research at Purdue. His research focused on the development and application of a universal simulation library for positive displacement machines, the result of which is laid out in the present document. His graduate research has lead to a patent, copyright, several publications in international journals and conferences, and a startup company.